Biophysics of Extracellular Action Potentials

Thesis by

Carl Gold

In Partial Fulfillment of the Requirements

for the Degree of

Doctor of Philosophy

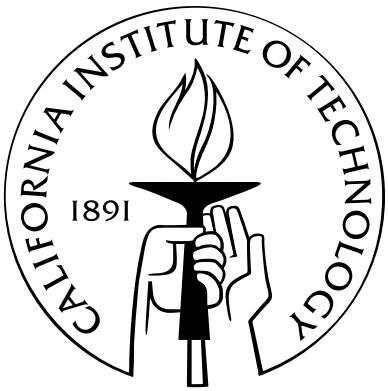

California Institute of Technology

Pasadena, California

2007

(Defended May 18, 2007)

Loka Samasta Sukhino Bhavantu

May all beings everywhere be happy and free...

Acknowledgements

I would like to thank all of those who collaborated on this project, without whom it could never have been successful: John Anderson, György Buzsáki, Rodney Douglas, Cyrille Girardin, Darrell Henze, Kevan Martin; and of course my thesis adviser Christof Koch.

This work was supported by National Institute of Mental Health (NIMH) Fellowship 1-F31-MH-070144-01A1 and Grant MH-12403, National Institute of Neurological Disorders and Stroke Grants NS-34994 and NS-43157, the NIMH-supported Conte Center for the Detection and Recognition of Objects, and the National Science Foundation.

Abstract

The goal of this thesis is to analyze the generation of single unit extracellular action potentials (EAPs), and to explore pertinent issues in the interpretation of EAP recordings. I use the line source approximation to model the EAP produced by individual neurons. I compare simultaneous intracellular and extracellular recordings of CA1 pyramidal neurons *in vivo* with simulations using the same cells' reconstructions. The model accurately reproduces both the waveform and the amplitude of the EAPs. The composition of ionic currents is reflected in the features of each cell's EAP, while dendritic morphology has little impact.

I compared constraining a compartmental model to fit the EAP with matching the intracellular action potential (IAP). I find that the IAP method underconstrains the parameters. The distinguishing characteristics of the EAP constrain the parameters and are fairly invariant to electrode position and cellular morphology. I conclude that matching EAP recordings are an excellent means of constraining compartmental models.

I recorded spikes from cat primary visual cortex (V1) and recreated them in the model. I calculated the distance at which an electrode could record the EAPs given the prevalent background noise. My analysis suggests that in the superficial cortical layers 50%–80% of the neurons were active, while in deeper layers only 10%–20% were active. I analyzed the bias towards recording the large neurons in the deep layers. If the detection and clustering algorithm is sensitive enough to include low-amplitude spikes then bias is moderate. If only high amplitude units ($> 200\ \mu$V) are picked up, then recording will be significantly biased towards the deep layers.

The majority of spikes in cortex had a negative peak with a mean of -0.11 mV, but a minority of units (<10%) had a large positive peak of up to 1.5 mV. Simulations demonstrate that a pyramidal neuron may generate a negative spike with amplitude greater than 1 mV, but a positive spike of at most 0.5 mV. I conclude that high-amplitude positive spikes cannot result from a single neuron EAP. I suggest that they may result from synchronized action potentials in groups of L5 pyramidal neurons.

Contents

List of Figures

List of Tables

Chapter 1

Introduction

Extracellular action potential (EAP) recordings form one of the primary means for studying the activity of the intact brain. Multi-electrode arrays and spike sorting algorithms have advanced to the point where hundreds of neurons can be reliably recorded in a single experiment (see, e.g., [Csicsvari et al., 2003]). Yet despite the widespread reliance on EAP recordings, there remain several aspects of EAPs that are poorly understood. For example, why do EAPs waveforms show so much variability when viewed at a short (e.g., millisecond) time scale, while intracellular action potentials (IAPs) are so stereotyped? And is this variability essentially random, or can it be used to identify different neuron classes or intracellular phenomenon? Other important and largely unanswered questions have to do with the use of EAPs for detection and classification of neural units: How does the amplitude of the EAP depend on factors like the size of the neuron and the distance of the recording electrode, and at what range can an electrode reliably record different types of neurons? How likely is it that different neurons in range of the electrode produce similar amplitude spikes and thus create multi-unit clusters? Are extracellular recordings biased toward different classes of cells due to differences in their resultant EAP amplitudes? And what portion of neurons in the brain are actually active during recordings?

These questions persist despite the fact that the *physics* of extracellular potentials has been well understood for decades. By the *physics* of EAPs I mean the way the laws of electromagnetism work within the neuropil to generate potentials as a result of ionic currents. These were explained in the work of pioneering computational neuroscientists such as Wilfrid Rall (e.g. [Rall, 1962]) and Robert Plonsey (e.g. [Plonsey, 1969]). When I speak of the *biophysics* of EAPs I mean the practical consequences of the physics for the extracellular recording of neurons, primarily *in vivo*, exemplified by the questions listed above. The biophysics of EAPs is the subject of this dissertation. It has received relatively little attention in the computational neuroscience literature (e.g., analysis of CA1 population spikes in [Varona et al., 2000].)

The paucity of studies probably resulted from inadequate techniques with which to model EAPs in a meaningful way. Due to the variety of EAPs waveforms and the difficulty of modeling them,

it has been generally assumed that EAP variability across different recordings is due to random positioning of the electrode and the morphology of the neuron; a relationship that does not provide useful information about the intracellular state of the cell — I will show that this assumption is entirely incorrect.

The main advance that makes the current study possible is the development during the 1980's and 1990's of the techniques for detailed neuronal modeling, culminating in the availability of efficient, flexible, and easily programmable neural simulators such as the NEURON Simulation Environment [Hines and Carnevale, 1997]. By *detailed* neuronal modeling I mean models based on complete neuronal reconstructions and including models for the wide variety of ionic channels present in real neurons. Without such a high level of detail it would not be possible to interpret which aspects of the real neurons are significant in generating the various aspects of EAPs, or to have confidence that there is not some missing aspect of the model that has an important consequence on the result. (Indeed, although my models are currently state of the art, the next generation of computational neuroscientists will no doubt find some aspects of them entirely inadequate to explain phenomena I have not considered.)

This thesis is divided into six chapters: an introduction and conclusion, and four chapters which correspond to manuscripts that are (at the time of this writing) published (chapter 2), in press (chapter 3), in preparation (chapter 4), and submitted (chapter 5) respectively. Chapter 2 deals with recreating simultaneous intra- and extracellular recordings made in the CA1 region of the rodent hippocampus *in vivo*. Because the data include detailed information about all the conditions of the recording (i.e. the reconstruction of the recorded neuron and the position of the extracellular electrode, as well as both intra- and extracellular recording) they serve to verify that the modeling technique can in fact accurately reproduce EAPs. Chapter 3 further analyzes the generation of EAPs as explained by the model with the goal of demonstrating that EAPs contain a large amount of information about the neurons which generate them. I therefore conclude that if a detailed model accurately reproduces EAPs from an unknown population of neurons, then it does in fact provide an accurate picture of those neurons' EAP-generating process.

In chapters 4 and 5, I turn my attention to modeling EAPs in neocortex, using recordings from the primarily visual cortex (V1) of the cat. Chapter 4 focuses on analyzing the factors influencing the range at which an extracellular electrode can record an EAP and derives answers for important related questions like the probability of multi-unit recording, the fraction of units which are active, and the extent of bias towards larger neurons. The final chapter, chapter 5, is more speculative in nature: it characterizes and then attempts to explain the phenomenon of high amplitude positive polarity spikes in cortex. I show that some explanations are physically impossible or inconsistent with the data, and I suggest a new explanation (synchronized spiking) and demonstrate it to be plausible. However, the final hypothesis would require further experiments to confirm or deny.

Chapter 2

Modeling Simultaneous Intra- and Extracellular Recordings of CA1 Pyramidal Cells *In Vivo*

2.1 Introduction

Typically, EAP recordings are used only to determine whether and when neurons have spiked, under the assumption that the actual waveform of individual action potentials does not convey any information. At the same time, average EAP waveforms are known to exhibit a range of characteristic features when observed on a millisecond time scale, and these variations can be used to distinguish between different neuronal classes [Mountcastle et al., 1969, Csicsvari et al., 1999]) as well as individual neurons within classes (e.g., [Quiroga et al., 2004])). However, there have been only a few attempts to systematically study the causes of the variability in EAP waveforms either through experimental work or through computer modeling [Rall, 1962, Buzsáki et al., 1996, Quirk et al., 2001, Holt and Koch, 1999].

I show that an accurate computational model of the EAP can shed light on the source(s) of variability in recorded EAP waveforms and can contribute to the analysis of some outstanding questions in the interpretation of EAP recordings. I investigate the effects of cellular morphology, the cell's spatial dimensions, and differential expression of various ionic channels on the waveform of the EAP. I take advantage of recent developments in computational modeling to predict EAPs resulting from simulated neurons at a high level of detail [Holt, 1998] and the massive increase in available computing power since the theory was developed in the 1960s ([Rall, 1962]; [Plonsey, 1969]). I use an unique data set [Henze et al., 2000] to reproduce the precise conditions for the generation of a set of intra- and extracellular action potentials recorded *in vivo*.[1]

[1]The material presented in this chapter is based on that published as [Gold et al., 2006].

2.2 Methods

2.2.1 Computational Methods

The extracellular potential induced by a spike in a neuron was calculated in two distinct stages. First, I computed the transmembrane currents for a pyramidal neuron model on the basis of standard 1D cable theory, e.g., [Koch, 1999]. Second, I used those currents to compute the extracellular potentials as described below.

2.2.1.1 Calculation of Extracellular Potentials and the Line Source Approximation

It has been previously demonstrated that the neuropil is well modeled by an isotropic volume conductor in which the capacitive effects of the media are negligible in the frequency range of interest to me (1– 3000 Hz). That is, I can satisfactorily describe the extracellular milieu by a purely ohmic conductivity, ρ (units of Ωcm). (see, e.g., [Plonsey, 1969, Holt, 1998].) Under these circumstances, the electric potential in the extracellular space is governed by Laplace's equation,

$$\nabla \cdot (\frac{1}{\rho}\nabla\Phi) = 0 \tag{2.1}$$

where Φ is the extracellular potential. At the boundaries, $(1/\rho)\nabla\Phi = J_m$, where J_m is the transmembrane current density and ρ is the extracellular resistivity. For a single point source of amplitude I in an unbounded isotropic volume conductor, the solution is dual to the classical physics problem of point charges in free space (Coulomb's law),

$$\Phi = \frac{\rho I}{4\pi r} \tag{2.2}$$

where r is the distance from the source to the measurement. Multiple current sources combine linearly via the superposition principle. In real neurons, membrane currents are distributed over elongated cylindrical processes, whose length considerably exceeds their width. The Line Source Approximation (LSA) [Holt and Koch, 1999] makes the simplification of locating the transmembrane net current for each neurite on a line down the center of the neurite. By assuming a line distribution of current, the resulting potential from equation 2.2 has a straightforward analytic 2D solution in cylindrical coordinates. For a single linear current source having length Δs, the resulting potential $\Phi(r,h)$ is given by:

$$\begin{aligned} \Phi(r,h) &= \frac{\rho}{4\pi}\int_{-\Delta s}^{0} \frac{I}{\Delta s}\frac{ds}{\sqrt{r^2+(h-s)^2}} \\ &= \frac{\rho I}{4\pi\Delta s}\log|\frac{\sqrt{h^2+r^2}-h}{\sqrt{l^2+r^2}-l}| \end{aligned} \tag{2.3}$$

where r is the radial distance from the line, h is the longitudinal distance from the end of the line, and $l = \Delta s + h$ is the distance from the start of the line. [Holt, 1998, Holt and Koch, 1999] analyzed the accuracy of the LSA and found it to be highly accurate except at very close distances (i.e., 1 μm) to the cable (see also [Rosenfal, 1969] and [Trayanova and Henriques, 1991]). Because extracellular recording electrodes are typically many μms away from neurons, I can use the LSA to calculate extracellular potentials. The steps in the model are as follows. First, I computed transmembrane currents for a particular neuron with its complement of ionic currents (see below) using the NEURON Simulation Environment [Hines and Carnevale, 1997], assuming that the extracellular potential was constant and equal to zero. In a second step, I used the LSA to compute the extracellular potential at a select number of locations from the transmembrane currents using a custom written Matlab program. I assumed that the previously calculated transmembrane currents would not be affected by the small changes in extracellular potential (<1 mV). One could refine this estimate on the basis of an iterative procedure, but this does not significantly affect the numerical results [Holt, 1998].

2.2.1.2 Calculation for Inhomogeneous Resistivity

The LSA assumes an extracellular medium that is homogeneous. However, recent measurements of CA1 have found that the pyramidal cell body layer has approximately double the resistivity of the surrounding stratum radiatum and stratum oriens (ρ = 640, 260, 290 Ωcm respectively) [López-Aguado et al., 2001]. Furthermore, these baseline resistivities may be increased by as much as 50% during periods of high activity. Because the inhomogeneity comprises an approximately planar layer, I can use the Method of Images ([Maxwell, 1881]; [Weber, 1950]) to calculate its impact. Three layers of differential conductivities (ρ_1, ρ_2, and ρ_3), separated by two parallel planes, is exactly solved by an infinite series of images with decreasing magnitudes of the form:

$$I_{\text{image}} = I_{\text{original}}\left(\frac{\rho_1 - \rho_2}{\rho_1 + \rho_2}\right)^n \left(\frac{\rho_3 - \rho_2}{\rho_2 + \rho_3}\right)^m \tag{2.4}$$

where the positive integers n and m increase for the more distant images. The magnitude of the images decline rapidly at the same time as the distance to the images increases; in practice, the infinite series is well approximated by the first few terms (results shown here use n, $m < 5$). The impact of the high resistance layer was found to be relatively modest, as described in section 2.3.6. Complete details of the solution are given in appendix A.

2.2.2 Experimental Methods

Simultaneous intracellular and extracellular recordings of CA1 neurons *in vivo* were reported previously in [Henze et al., 2000] and I briefly review the methods here. The extracellular electrodes were of three types: (1) single, 60 μm diameter wires, (2) "tetrodes" as described in [Gray et al., 1995],

or (3) planar silicon electrode arrays with 6 recording sites spaced 25 μm apart, as described in [Henze et al., 2000]. During numerous attempts to obtain stable intracellular recordings from cells also recorded by the extracellular electrode, [Henze et al., 2000] obtained recordings from 38 neurons: 3 recorded with single wire electrodes, 22 recorded with tetrodes, and 13 recorded with silicon probe arrays.

Recordings were wideband filtered at either 1 Hz-3 KHz or 1 Hz-5 KHz. Averages of the EAPs were made by sampling from the extracellular recording at times triggered by the intracellular spike. In preparing averages for comparison to the model, I used only recordings from the beginning of the session until the cell started to depolarize significantly (>5-10 mV) due to the shunt current from electrode impalement. The number of spikes available for the average range from a few hundred to a few thousand. After intracellular recordings were complete, cells were injected with biocytin, the rats were sacrificed and the brains sliced, stained at 60 μm and preserved in slides. Of the 38 recorded cells, 17 cells were stained well enough for reconstruction. In these cases the complete 3-D structure of recorded cells was measured using the Neurolucida System and then used as the basis for compartmental simulations. In cases where the extracellular electrode track left some visible mark of its location (i.e., blood or debris) this was also measured and used to estimate the electrode location for comparison with the computer simulations. Visible electrode tracks were found in the CA1 area for 7 cells, and tracks were found in the overlying cortex only for another 3 cells.

I also used a larger sample of EAP recordings (N=307) with no coincident intracellular electrode recordings as a reference set for comparison (methods similar to [Csicsvari et al., 2003]), to more accurately estimate the frequency of EAP features observed in the small sample of simultaneous recordings, and to confirm that observed features in the simultaneous recordings were not artifacts of intracellular impalement.

2.2.3 Simulation Methods

Single trials of standard 1-D compartmental simulations were performed for each reconstructed cell within NEURON [Hines and Carnevale, 1997]. and compared to the average simultaneous intra- and extracellular recordings. The average number of compartments was around 250, based on a 3-D reconstruction that contained around 2,500 measurements of dendrite diameters and locations. The time steps of the simulation were varied by the CVODE method [Hines and Carnevale, 2001]. During the simulation, membrane currents for all compartments of the cell were saved at intervals of about 0.05-0.1 ms to calculate extracellular potentials. Note that many of the parameters described in this section, with the exception of active current conductance densities tuned to indivual cells, are listed in appendix B.

2.2.3.1 Passive Parameters and Spines

The intracellular resistivity was set to R_I=70 Ωcm [Stuart and Spruston, 1998]. The value of this parameter had an important impact on the resulting extracellular potential amplitude. Simulations with higher values for R_I resulted in potentials that were too small to match the recording and histology data. The membrane resistance was set to R_m=15k Ωcm^2 [Spruston and Johnston, 1992], to account for the net effect of *in vivo* synaptic conductances in reducing the membrane resistance without actually modeling detailed synaptic activity [Destexhe and Paré, 1999]. The specific capacitance was set to C_m=1μF/cm^2 [Koch, 1999]. The reversal potential for the passive leak mechanism was set to V_{rest}=-65mV.

Dendritic spines are accounted for by adjusting the passive membrane parameters R_m and C_m, decreasing the former and increasing the latter by a factor f given by the normalized spine area [Major et al., 1994]. Specific spine density estimates are taken from [Megias et al., 2001] but here I modify the passive properties of the compartment directly without modifying the compartment length or diameter as that would also impact the properties of active ionic currents. That is:

$$f = \frac{A_{\text{spines}}}{A_{\text{comp}}} \tag{2.5}$$

$$C_m^f = C_m(1+f) \tag{2.6}$$

$$R_m^f = \frac{R_m}{1+f} \tag{2.7}$$

where A_{spines} is the estimated spine surface area for the compartment and A_{comp} is the actual surface area of the compartment derived from the histological reconstruction that ignores spines. A_{spines} is given by

$$A_{\text{spines}} = L \times \delta \times \alpha \tag{2.8}$$

where L is the length of the compartment, δ is the density of spines at the compartment location, in spines/μm, and α is the average area of a spine, assumed to be 0.83 μm^2 [Harris and Stevens, 1989]. The spine densities, δ, used in the model are specific to different sections of the cell as described in [Megias et al., 2001]. The classification of compartments to the categories described in [Megias et al., 2001] was based on the compartment diameter, d, and path distance from the soma, Δ. Both the spine densities and criteria for compartmental classification are listed in table B.1.

These choices resulted in average somatic input resistances of 31.8 +/- 6.5 MΩ which is in agreement with previous measurements of CA1 input resistances *in vivo* (48.4 +/- 11 MΩ [Henze and Buzsáki, 2001]) and compatible with the notion that due to constant synaptic bombardment *in vivo*, the input resistance is as much as 80% lower [Destexhe and Paré, 1999] compared to

in vitro [Spruston and Johnston, 1992].

2.2.3.2 Active Ionic Currents

The model includes Hodgkin-Huxley style kinetic models for 12 different voltage-dependent ionic currents carried by Na^+, K^+, and Ca^{2+} ions. The ionic currents included in the model were:

- Fast inactivating Na^+ (axonal and soma/dendritic varieties $I_{Na^+Ax.}$and I_{Na^+SD}) [Magee and Jonston, 1995, Martina and Jonas, 1997, Colbert and Pan, 2002];
- A type K^+ (proximal and distal varieties, I_{K^+AProx}, I_{K^+ADist}) [Klee et al., 1995] [Hoffman et al., 1997];
- AHP type Ca^{2+} dependent K^+ (I_{K^+AHP}) [Williamson and Alger, 1990];
- C type voltage and Ca^{2+} dependent K^+ (I_{K^+C}) [Lancaster and Nicoll, 1987] [Yoshida et al., 1991];
- D type K^+ (I_{K^+D}) [Storm, 1988];
- K type K^+ (also known as "DR" type, I_{K^+K}) [Klee et al., 1995];
- M type K^+ (I_{K^+M}) [Halliwell and Adams, 1982];
- H type mixed cation (somatic and distal varieties, I_{HSoma}, I_{HDend}) [Magee, 1998];
- L type Ca^{2+} ($I_{Ca^{2+}L}$) [Fisher et al., 1990, Christie et al., 1995, Magee and Jonston, 1995];
- N type Ca^{2+} ($I_{Ca^{2+}N}$) [Fisher et al., 1990, Christie et al., 1995, Magee and Jonston, 1995];
- R type Ca^{2+} ($I_{Ca^{2+}R}$) [Magee and Jonston, 1995];
- T type Ca^{2+}($I_{Ca^{2+}T}$) [Fisher et al., 1990, Magee and Jonston, 1995].

The formalism used for the active current models is that described in [Borg-Graham, 1999], with the exception of the Na^+ current: while [Borg-Graham, 1999] used a new Markov model, I use the traditional Hodgkin-Huxley formulation. The parameters for the kinetics of non-Ca^{2+}dependent currents are listed in table B.2. There are many differences between the parameter values determined by [Borg-Graham, 1999] and the values I have chosen for the model of simultaneous *in vivo* intra- and extra-cellular recordings. Perhaps the most important differences are the significantly faster time course of activation used for the primary K^+ currents active in repolarization, I_{K^+AProx}, I_{K^+ADist}, I_{K^+C}, I_{K^+D}, and I_{K^+K}. As described in section 2.3.3 these changes were required to match the variety of extracellular potential waveforms. Other differences between the two models have lesser significance, such as the differences between the properties of Ca^{2+} currents.

For the Ca^{2+} dependent currents, I_{K^+C} and I_{K^+AHP}, I adopt the Markov model formalism, also from [Borg-Graham, 1999]. The parameters used are listed in tables B.3 and B.4. I have again changed the model parameters to match the simultaneous intra- and extracellular recordings by speeding up the activation rates, and increasing the sensitivity of the channels to changes in the Ca^{2+}concentration.

For calcium buffering and diffusion I used the Cadifus mechanism included with NEURON [Hines and Carnevale, 2001]. The mechanism models Ca^{2+} diffusion in 4 concentric shells for all compartments. The rates of buffering and diffusion have been adapted to approximately match the results described in [Jaffe et al., 1994]; [Christie et al., 1995]: the average Ca^{2+} concentration in the central shells is on the order of 50-100 nM, and a single action potential increases the concentration by 2-10 nM. To achieve these results I altered the parameter for the initial calcium concentration (cai) from 50 nM to 75 nM to model a cell that has been recently active, although I simulated only a single action potential. I also changed the Total Buffer concentration parameter from 3 nM to 5 nM, and the forward buffering rate (k1Buf) from 100 /mM-ms to 250 /mM-ms.

Several active currents in the model had non-uniform conductance density distributions in the compartmental model. While the properties of all of the ion currents are studied primarily in the soma and thick apical dendrites I have assumed similar properties occur in basal dendrites. The general approach is similar to that described in [Poirazi et al., 2003] and the precise distributions used are described below. Current types not listed had a uniform density in every compartment. The peak conductance densities used for each cell along with parameters used to define the non-uniform densities are listed in tables 2.1, 2.2, and 2.3. Densities for the currents that were held constant for all cells are listed in table B.5.

1. $I_{Na^+Ax.}$. The density at the axon initial segment and at nodes of Ranvier is a multiple (<5) of the density on the soma, $\bar{g}_{init-seg} = \bar{g}_{soma} \times \alpha_{iseg}$, $\bar{g}_{node} = \bar{g}_{soma} \times \alpha_{node}$. (Colbert and Pan, 2002) The values used for α_{iseg} and α_{node} were varied for each cell in order to match the simultaneous intra- and extracellular recordings, as listed in table 2.1.

2. I_{Na^+SD}. The density is the same on the soma and axon hillock [Colbert and Johnston, 1996] and the current is subject to slow inactivation which tends to increase with distance from the soma [Colbert et al., 1997]. Peak conductance density in dendritic compartments is defined as a percentage of the somatic density with a linear decrease from the proximal dendrites to distal dendrites. The conductance density for a given compartment is defined by the equation: $\bar{g}_{dendrite} = \bar{g}_{soma} \times \{\gamma_{min} + (\gamma_{max} - \gamma_{min}) \times (\frac{300-\Delta}{300})\}$, where γ_{max} and γ_{min} indicate the maximum dendritic conductance density ratio (in the proximal dendrites) and the minimum dendritic conductance density ratio (in the distal dendrites) respectively, Δ is the path distance from the soma to the compartment, and 300 μm is the distance at which the the conductance

density reaches its minimum. At distances beyond 300 μm the conductance density for all compartments is given by $\bar{g}_{dendrite} = \bar{g}_{soma} \times \gamma_{min}$. The axon initial segment and nodes of Ranvier had conductance densities higher than the soma, $\bar{g}_{axon} = \bar{g}_{soma} \times \alpha_{axon}$. The values used for γ_{min}, γ_{max}, and α_{axon} where varied for each cell in order to match the simultaneous intra- and extracellular recordings, as listed in table 2.1.

3. $I_{K^+ADist/Prox}$. The conductance density for currents in distal dendrites are significantly higher and exhibit shifted activation kinetics to be more active at lower voltage. Due to their low activation threshold, a non-trivial fraction of these channels are active at rest. Results in [Frick et al., 2003] suggest that there are even higher conductance densities for these current in narrow dendrites off the apical trunk and I found this assumption consistent with reproducing the simultaneous intra- and extracellular recordings. In the proximal dendrites closer than 100 μm to the soma, the I_{K^+AProx} current has a fixed conductance density. In the distal dendrites, the I_{K^+ADist} current replaces the I_{K^+AProx} current, and the peak conductance density increases linearly with distance from the soma. The peak conductance density in a given distal compartment is defined by the equation: $\bar{g}_{distal} = \bar{g}_{proximal} \times \{1 + 6 \times (\frac{\Delta - 100}{350 - 100})\}$, where the factor of 7 defines the ratio of the maximum conductance density (in the far distal dendrites) to the minimum conductance density (in the near distal dendrites), 100 μm is the maximum distance considered to be proximal, and 350 μm is the distance from the soma at which the conductance density reaches the maximum value. For compartments further than 350 μm the conductance density is fixed at $\bar{g}_{dendrite} = \bar{g}_{proximal} \times (\gamma_{min} + \gamma_{max})$. In narrow dendrites (basal, apical oblique, and apical tuft) the peak conductance density is boosted by a further multiplicative factor over whatever the conductance density would be in a similar thick dendrite. That is, the distal conductance density in narrow dendrites is given by $\bar{g}_{distal}^{dendrite} = \bar{g}_{distal} \times \alpha_{dendrite}$. The values used for $\alpha_{dendrite}$ where varied for each cell in order to match the simultaneous intra- and extracellular recordings. The values used are listed in table 2.2.

4. I_{K^+C}. This current has a high conductance density and contributes to repolarization in the soma and proximal dendrites only [Poolos and Johnston, 1999]. Density of I_{K^+C} current is greatest at the soma and decline to zero outside of the proximal dendrites. The conductance density for compartments within the proximal dendrites is given by the equation $\bar{g}_{proximal} = \bar{g}_{soma} \times \alpha \times (\frac{\Delta_{prox} - \Delta}{\Delta_{prox}})$, where Δ is the path distance from the soma to the compartment, Δ_{prox} is the maximum distance from the soma considered to be proximal, and α (≤ 1) defines the maximum conductivity density in the proximal dendrites. For compartments further from the soma than Δ_{prox} the conductance density of the I_{K^+C} current is zero. The values used for Δ_{prox} and α where varied for each cell in order to match the simultaneous intra- and extracellular recordings. The values used are listed in table 2.3.

5. $I_{HSoma/Dend}$. The conductance density of this current is greatest in the distal dendrites, where the activation requires somewhat more hyperpolarized potentials. The conductance density of I_{HDend} current is defined as a multiple of the I_{HSoma} conductance density, with the multiplicative factor increasing linearly with distance from the soma. For a dendritic compartment the conductance density of I_{HDend} current is defined by the equation $\bar{g}_{dendrite} = \bar{g}_{soma} \times \{1 + 6 \times [1.0 - (\frac{300-\Delta}{300})]\}$, where 1 and 6 are ratios defining the minimum (proximal) and maximum (distal) density of I_{HDend} in relation to the somatic density, Δ is the path distance from the soma to a given compartment, and 300 μm is the distance at which the I_{HDend} conductance reaches its maximum density. For compartments at distances beyond 300 μm from the soma the density is fixed at $\bar{g}_{dendrite} = \bar{g}_{soma} \times 7$.

6. I_{K^+AHP}. This current is located in dendrites only. The conductance density of I_{K^+AHP} is highest in the proximal dendrites and lower in distal dendrites. For dendrites with a distance $\Delta < 100$ μm, the conductance density is set to $\bar{g}_{high}$, while for dendrites with distance $\Delta \geq 100$ μm the conductance density is set to $\bar{g}_{low}$ (listed in table B.5.)

7. $I_{Ca^{2+}L}$. This current is located in dendrites only. The conductance density of $I_{Ca^{2+}L}$ is highest in the proximal dendrites and lower in distal dendrites. For dendrites with a distance $\Delta < 50$ μm the conductance density is set to $\bar{g}_{high}$, while for dendrites with distance $\Delta \geq 50$ μm the conductance density is set to $\bar{g}_{low}$ [Fisher et al., 1990, Magee and Jonston, 1995].

8. $I_{Ca^{2+}T}$. This current is located in dendrites only and has a conductance density that increases with distance from the soma. For a dendritic compartment the conductance density is given by the equation $\bar{g}_{dendrite} = \bar{g}_{distal} \times \frac{\Delta}{150}$, where $\bar{g}_{distal}$ is the maximum conductance density in distal dendrites, Δ is the path distance from the soma to the compartment, and 150 μm is the distance from the soma at which the conductance density reaches its peak value. For compartments with $\Delta > 150$, μm the conductance density $\bar{g}_{dendrite} = \bar{g}_{distal}$ [Fisher et al., 1990, Magee and Jonston, 1995].

9. $I_{Ca^{2+}N/T}$. Ca^{2+} currents of the N and T type are located in the soma only. The density is zero in dendritic compartments. [Christie et al., 1995]

The sodium reversal potential, E_{Na^+}, was set to 70 mV. Ca^{2+} currents were modeled using a conductance (not permeability) based formalism with $E_{Ca^{2+}}$=140 mV. I used E_{K^+}=-140 mV to accurately account for perfusion of K^+ from the intracellular electrode. This is based on using the Nernst equation where the extracellular concentration of K^+ is 5 mM. Normally, the intracellular K^+concentration is 140 mM. However, the sharp pipette contains 1 M K^+ and given the fact that larger molecules like biocytin effectively perfuse from a pipette during current injection (which was applied throughout the recording) the soma and apical shaft will most likely approach this level.

Cell	$\bar{g}_{soma}$	γ_{min}^{apical}	γ_{max}^{apical}	γ_{min}^{basal}	γ_{max}^{basal}	α_{node}	α_{iseg}
d037	45.0	0.5	0.80	0.30	0.71	3.0	2.0
d056	35.0	0.1	0.51	0.31	0.72	3.0	4.0
d068	35.3	0.2	0.41	0.30	0.71	2.0	1.5
d081	33.0	0.3	0.70	0.32	0.70	3.0	3.0
d112.1	30.0	0.7	0.90	0.70	0.87	3.0	2.0
d112.2	28.3	0.56	1.02	0.78	1.03	3.1	2.0
d128	39.1	0.3	0.60	0.50	0.94	3.0	2.0
d135	42.0	0.3	0.53	0.30	0.69	3.0	2.0
d137	40.8	0.81	0.95	0.30	0.65	3.0	1.9
d145	40.0	0.30	0.70	0.30	0.71	3.0	3.0
d147	25.1	0.35	0.70	0.76	1.06	3.0	2.0
d149	25.2	0.75	0.75	0.55	0.95	3.0	2.0
d151	50.1	0.15	0.86	0.05	0.85	1.0	1.0
d163	35.0	0.30	0.86	0.51	1.0	3.0	2.0
d180	38.0	0.3	0.35	0.90	1.0	1.5	1.1
d187	43.8	0.10	0.50	0.10	0.50	2.0	5.0
d188	40.0	0.70	0.90	0.70	0.90	3.0	2.0
d189	25.0	0.42	0.90	0.40	0.50	3.0	1.5
Average	36.1	0.4	0.72	0.45	0.80	2.7	2.2
Std. Dev.	7.3	0.22	0.2	0.24	0.17	0.6	1.0

Table 2.1: Conductance density parameters for Na^+ current.

Units for $\bar{g}$ are mS/cm^2. Other quantities are dimensionless.

While the concentration will be normal in oblique and distal dendrites as a result of active membrane processes, it is the soma and apical shaft that make the largest contribution to the generation of observable EAPs. Consequently, I simplify the model by assuming a constant 1 M intracellular K^+ concentration. My experiences tuning the model, as described in the results section, led me to the conclusion that any inaccuracies resulting from this assumption are small in comparison to other sources of uncertainty in the biophysical parameters. (The most likely consequence being slightly different tuned active current conductance densities, as compared to a model incorporating details of K^+ perfusion and active K^+ membrane pumps.)

The exact kinetics and densities of the currents were tuned to match the simultaneous intra- and extracellular recordings taken *in vivo* while remaining faithful to the qualitative properties that have been established by *in vitro* studies. This includes the non-uniform distribution of active ionic current conductances as detailed in above. In general, the time constants were found to require values significantly faster than those measured *in vitro* and when necessary activation/inactivation curves were modified as well. The peak conductance densities associated with each current were treated as variables that needed to be tuned to match the simultaneous intracellular and extracellular recording, leaving the passive parameters and active ionic current kinetics fixed for all cells. The parameters tuned were those listed in tables 2.1, 2.2 and 2.3.

Cell	I_{K^+AProx}	I_{K^+ADist}				I_{K^+D}	I_{K^+K}	I_{K^+M}
	$\bar{g}_{proximal}$	$\bar{g}_{dendrite}$	α_{basal}	$\alpha_{oblique}$	α_{tuft}	$\bar{g}$	$\bar{g}$	$\bar{g}$
d037	25	41.9	2.0	2.0	3.0	0.5	49.9	0.5
d056	7.0	9.8	2.0	2.0	3.0	0.5	1.0	0.7
d068	10.1	9.7	3.0	3.0	4.0	1.0	49.9	0.7
d081	5.0	5.0	2.0	2.0	3.0	1.0	8.0	0.9
d112.1	35	35.0	5.0	4.0	6.0	1.0	1.5	1.0
d112.2	2.5	20.2	3.0	3.0	4.9	0.5	0.5	0.5
d128	9.9	11.1	2.0	2.0	3.0	1.0	9.0	0.2
d135	10.3	15.2	2.0	3.1	4.0	4.0	8.3	0.5
d137	5.1	4.8	3.1	2.0	3.0	4.0	70.6	1.5
d145	15.0	24.9	3.0	3.0	4.0	0.5	3.0	0.8
d147	2.5	21.0	3.0	3.0	4.0	0.5	0.5	0.8
d149	2.5	22.0	1.0	3.0	4.0	0.5	0.5	0.3
d151	5.0	8.0	3.0	3.0	5.0	2.0	12.0	0.2
d163	7.5	12.6	2.0	2.0	3.0	0.5	14.6	0.8
d180	10.0	47.0	2.0	2.0	3.0	1.0	0.5	0.5
d187	5.0	10.7	2.0	2.0	3.0	1.0	10.0	1.0
d188	41.2	40.1	2.0	2.0	3.0	2.0	0.5	0.5
d189	2.5	22.5	2.6	2.0	3.0	0.5	0.5	0.5
Average	11.2	20.1	2.5	2.5	3.7	1.2	13.4	0.7
Std. Dev.	11.3	13.1	0.9	0.6	0.9	1.1	20.9	0.3

Table 2.2: Conductance density parameters for A, D, K and M type K^+currents.

Units for $\bar{g}$ are mS/cm^2. Other quantities are dimensionless.

2.2.3.3 Model Axon

The axon for each cell was modeled with a structure similar to that described in [Mainen et al., 1995]: The diameter of the axon is 1/20th of the diameter of a sphere having the same surface area as the measured soma. An axon hillock 10 μm long connects the soma to the initial segment, beginning at 4$\times$ the axon diameter and tapering to the axonal diameter. The initial segment is 15 μm long. Following the initial segment the axon for pyramidal cells consists of alternating myelinated sections (100 μm long) and nodes of Ranvier (1 μm long.) The axon for the interneuron is un-myelinated and 500 μm in length.

While [Mainen et al., 1995] used a very high conductance density of Na^+ currents to create axonal initiation (1,000x the somatic density), I used a model similar to that suggested by [Colbert and Pan, 2002]. The initial segment and nodes of Ranvier have an Na^+ current conductance density that is only moderately higher than the soma (2-3x) but the Na^+ current in the initial segment and nodes of Ranvier ($I_{Na^+Ax.}$) has kinetics that activates at more depolarized potentials than the Na^+ current in the soma and dendrites (I_{Na^+SD}). This resulted in an action potential that usually initiates at the first node of Ranvier 0.5-1 ms before spreading to the soma via the initial segment.

Cell	I_{K+C} $\bar{g}_{soma}$	α_{apical}	Δ_{prox}^{apical}	α_{basal}	Δ_{prox}^{basal}
d037	1.0	0.75	100	0.75	50
d056	10.0	0.97	100	0.75	100
d068	1.0	0.75	25	0.76	25
d081	12.0	0.75	50	0.76	50
d112.1	3.0	0.75	50	0.75	50
d112.2	8.9	1.0	99	0.74	99
d128	22.1	0.75	150	0.75	99
d135	5.9	1.0	101	0.78	97
d137	30.4	0.76	101	0.76	50
d145	9.0	1.00	75	0.78	50
d147	19.9	0.99	99	0.76	99
d149	25.6	1.0	50	1.0	101
d151	13.5	1.0	126	0.5	101
d163	6.1	0.98	101	1.01	101
d180	12.0	0.25	50	0.75	100
d187	8.0	0.50	50	0.75	100
d188	40.0	0.25	25	1.0	100
d189	7.5	0.75	100	0.75	50
Average	13.1	0.79	81	0.78	79
Std. Dev.	10.6	0.25	35	0.12	27

Table 2.3: Conductance density parameters for C type K^+ currents.

Units for $\bar{g}$ are mS/cm^2. Other quantities are dimensionless.

2.2.3.4 Electrode Shunt and Driving Inputs

The cell was stimulated by a relatively low amplitude tonic current injection, 1 nA [Henze et al., 2000]. An electrode shunt, R_{shunt} between 50 and 200 MΩ, modeled the impact of the sharp electrode on the cell. The shunt was located at either the soma or in an apical trunk compartment in cases where the height of the action potential and lack of pronounced AHP in the intracellular recording suggested it was distal from the soma [Kamondi et al., 1998].

Synaptic input was mimicked by varying the leak resistance and reversal potential for the more distal compartments assumed to be receiving synaptic input. Typically, this meant reducing R_m by a factor of 3 to 5, and applying a reversal potential to the leak current of between -50 and -30 mV to mimic a mixed excitatory and inhibitory synaptic input. Under these conditions the action potential typically initiated in the axon initial segment.

2.2.4 Performance

Simulations were 25 ms long: The first 10 ms were used to establish the stability of the rest potential (between -70 and -60 mV) given by the combination of active currents without synaptic input. Simulated synaptic input was switched on to depolarize the cell for 1-5 ms until an action potential was triggered and the cell repolarized and returned to a stable rest potential as judged by remaining stable for the final 10 ms of the simulation. In addition, a 4 ms extracellular spike trace at 100

locations was computed. All the above took 1-2 minutes (on 2.5 GHz Intel-based computer running the Linux operating system), long enough that a brute force automatic search for optimal parameters to match the simulation was not feasible. Consequently, the primary method for tuning the channel density parameters of the model was manual trials guided by my intuition and knowledge of the parameter dependencies, supplemented by an automated local search of the parameter space (section 2.3.4).

2.3 Results

2.3.1 Membrane Currents and the Extracellular Potential Waveform

The simultaneous intra- and extracellular recording along with the model simulation matching the recording for cell D151 is shown in Figure 2.1. As can be seen by comparing the total membrane current (I_{Total}) to the EAP, the shape of the waveform is proportional to the time profile of I_{total} across the membrane of the perisomatic compartments. This is a straightforward consequence of the basic equation of the extracellular potential, equation 2.2, and the superposition principle. Note that while the apical trunk compartment in the figure has a net current peak amplitude approximately 1/5 that of the soma, there are several other proximal dendritic compartments with virtually identical current vs. time profiles. This gives the proximal dendrites about equal weight to the soma in determining the shape of the waveform. An additional consequence of equation 2.2, that will be further analyzed below, is that distal dendritic compartments make virtually no contribution to the EAP in the perisomatic region (i.e., the waveform detectable by an extracellular recording electrode.) This is because the smaller diameter of the individual distal dendrites results in smaller net currents and the greater distance further reduces the impact.

2.3.2 Electrode Position and Capacitive Phase of the EAP

Another example of an EAP is illustrated in cell D068, Figure 2.2. As in most recordings, the EAP lacks a prominent capacitive current phase. The capacitive phase peak for cell D151 (Figure 2.1) is 9% of the amplitude of the Na^+ phase peak; in all 34 recordings in [Henze et al., 2000] only 4 have a capacitive phase peak that is comparable or larger. I compared these results to the sample of 307 EAPs recorded without a simultaneous intracellular recording and found that 73% of the waveforms had a capacitive peak that was less than 5% of the amplitude of the Na^+ peak, while 95% of the recordings had a capacitive peak amplitude that was less than 10% of the amplitude of the Na^+ peak. The overall average ratio was 6%, and the distribution had a long tail including a handful of recordings for which the ratio of the capacitive phase peak to the Na^+ peak was close to 100% (recordings from [Henze et al., 2000] contained two such waveforms.)

The reason why the majority of the recordings exhibit little or no capacitive current in the EAP is demonstrated in Figure 2.2. During a perisomatic action potential initiation, the membrane potential change at the soma is driven by local Na^+ current, and therefore there is no significant capacitive current until after the Na^+ current is already active. Because the inward Na^+ current is of greater amplitude than the outward capacitive current, the total current lacks an initial positive peak. In contrast, in the more distant dendrites there is a brief interval between the initial, passive, depolarization and the active regeneration of the action potential through local Na^+ channel openings. Also, the Na^+conductance density is typically lower in the dendrite than at the soma (due to slow inactivation, as described in section 2.2.3.2) and consequently the capacitive current is relatively larger. As a result of these factors, at the start of the AP the positive capacitive current is the largest membrane current and a positive capacitive dominant phase is present in the total current. This explains the previously observed phenomena that an initial, positive, capacitive phase is usually visible in EAP waveforms recorded from CA1 pyramidal cells when the tip of the recording electrode is situated along the apical trunk at some distance from the soma [Buzsáki and Kandel, 1998]. Simulations suggest that waveforms with a capacitive phase of the same size as the Na^+ phase may result from a distal dendritic action potential initiation that then propagates forward to the soma: the reversal of the initiation process described above leads to the disappearance of the capacitive phase of the EAP in the distal apical region and the appearance of an enlarged capacitive phase around the soma and the basal dendrites.

Cell DO68 (Figure 2.2) also illustrates the contribution of the axon to the EAP: due to the lower threshold of activation, the axon initial segment Na^+ current activates before the soma current, beginning at the time of the action potential in the first node of Ranvier. This creates a slight depolarization approximately a millisecond before the start of the more prominent 3-phase EAP described above. The myelinated axon and nodes of Ranvier make no contribution to the EAP. The myelinated axon lacks active channels and has only a capacitive current which is very small relative to the perisomatic currents, while the nodes of Ranvier are too small and isolated to create a significant amplitude EAP of their own.

While the model does predict significant variation in the shape of the EAP waveform at distal locations, practically all of the significant variability occurs at amplitudes below the threshold of detectability. In Figures 2.1-2.3 only the red and orange traces are above the typical detection and sorting threshold, about 60 μV, in CA1 [Henze et al., 2000]. Aside from the aforementioned increase in the capacitive phase of the waveform along the apical trunk, in the region around the soma where an extracellular electrode would detect the spike above the background noise there is relatively little variation in the shape of the waveform, only an increase in amplitude as the electrode is moved closer to the soma.

2.3.3 Active Current Conductance Density and the EAP Waveform

The recording of cell D112.1 (Figure 2.3) illustrates two other sources of variability seen in average EAPs of CA1 pyramidal cells: the width of the Na^+ dominant phase may vary and show inflection points in the transition to the K^+ dominant phase, and also the amplitude and shape of the K^+ dominant phase varies. The model suggests that this variability reflects differences in the conductance densities of active ionic currents, rather than electrode position.

Figure 2.3 illustrates how the width of the Na^+ dominant phase of the EAP is influenced by the timing of the K^+ currents. Variability in the timing of the net K^+ current can occur because there are at least five different K^+ currents (A, C, D, K and M type) that make a contribution to the repolarization of the action potential and each type has unique properties with respect to the onset time and duration of the K^+ current it generates. The A current is fast and inactivating; the C current is slower to activate and also inactivates slowly due to Ca^{2+} dependence; the D current is slow but has a low threshold of activation being active at rest; the K current is fast but has a relatively high activation threshold; and the M current is the slowest but has a low threshold of activation, though not low enough to be active at rest. Although the C and K currents tend to dominate repolarization at the soma, the M and A currents make a larger contribution in the distal dendrites where the C current is not present (as described in section 2.2.3.2) and where the AP amplitude is too low to trigger significant K current.

Reproducing the simultaneous intra- and extracellular recordings with the model led me to the conclusion that it was necessary to assume significant variation in the conductance density levels of the K^+currents in order to achieve reasonable matches between recording and simulation. This was particularly the case when trying to match the width of the Na^+ phase, and the shape of the K^+ phase in the extracellular waveform. Evidence for varying levels of expression of ionic channels in pyramidal cells has also been found in the analysis of gene expression profiles [Toledo-Rodriguez et al., 2004]. The peak conductance densities used to match the waveforms are given in tables 2.1, 2.2 and 2.3. While the variability in the peak Na^+ conductance density (as measured by a single standard deviation) is only on the order of 25% of the mean, for the four primary K^+ currents the variability is of the same order of magnitude as the average.

For the model to match the narrow Na^+ dominant phase (0.35 ms, measured as the width at 25% of peak amplitude) and rapidly decaying K^+ phase in the EAP of cell D068 (Figure 2.2) requires a dominant K type K^+ current to rapidly counteract the Na^+ current and achieve repolarization. Cell D151 (Figure 2.1) has a somewhat longer duration Na^+ phase and a K^+ phase that decays more slowly, and the best match with the model is achieved by assuming a balanced combination of C, D, and K type K^+ currents. Cell D112.1 (Figure 2.3) is relatively unusual in that it has a sharply peaked Na^+ phase in which the transition to the K^+ phase slows significantly midway, leading to a relatively long duration Na^+ phase that lasts 0.95 ms. Only 3 out of 38 of the waveforms

[Henze et al., 2000] had a similar shape and in a larger sample of EAP recordings (with no associated intracellular recording) the proportion having such a waveform was similar (27 out of 307). This type of waveform was best matched by a repolarization consisting of primarily A and C type currents.

Although the amplitude of the waveform varies (generally getting smaller as a recording session progresses), there is little change in the waveform of the EAP during recording sessions that last up to two hours. This suggests that the conductance density differences between cells are stable on this time scale.

2.3.4 Estimation of Simulated EAP Accuracy

The quality of the fit between the simulation and recording achieved by these methods are listed in table 2.4. The measure of error used is the square root of the mean square error (SMSE) between the recording and the simulation. The SMSE is then normalized by the peak amplitude to enable comparison of the error on intra- vs. extracellular recordings and on cells with different amplitude EAPs. For comparison of the model with the extracellular recording, I also weighted the mean square error to emphasize an accurate match for the samples at the peak amplitude: the sample for the negative (Na^+) peak was weighted 10x the non-peak sample points, the points immediately before and after the peak were weighted 5x, and the points two samples distant from the peak were weighted by 2.5x (weights on all sample points were then normalized). Due to the longer duration of the intracellular AP peak, weighting was not necessary to insure that the SMSE reflected a close match to the peak amplitude. For single wire and tetrode recordings, I compare the simulated EAP to the largest amplitude channel. For silicon probe recordings, I calculate the SMSE for all channels with peak amplitudes greater than 20 μV and report the average.

The comparison between model and recording was made at the best spatial estimate of the electrode location whenever possible, or at a plausible location if there was no electrode track. In all cases where the electrode location could be estimated, the model produced a good estimate of the amplitude of the EAP at that location. Unfortunately, due to their low profile, none of the silicon probe recordings produced a visible electrode track in the CA1 area. Nevertheless, the model produced a good match to the sequence of EAP amplitudes on the different recording sites at plausible electrode positions, i.e., nearly parallel with the apical trunk, coming within a reasonable distance of the soma as suggested by the maximum amplitude recording (Figure 2.8).

The method used to tune the conductance densities of the active ionic current was a combination of manual tuning and automated search. Manual tuning of the parameters was directed by two main principals: (1) the net Na^+ current for the perisomatic region must produce the observed peak amplitude in the intracellular and extracellular action potentials; (2) the net combination of K^+ current on the entire cell must repolarize at the rate shown in the intracellular recording, while K^+ conductance densities may be shifted to match the shape of the EAP waveform. The flow of

significant axial currents in the cell (an order of magnitude greater than the membrane current in a typical compartment) means that M and A type K^+ in the distal dendrites, can result in significant repolarization to the soma and proximal dendrites while having virtually no contribution to the routinely recorded EAP.

After a reasonably good fit was achieved by manual exploration of the parameter space (i.e., normalized SMSE close to 5% for a recording with amplitude greater than 20 μV), an additional local search in the parameter space was performed using the Nelder-Mead Simplex algorithm. Improvements to the match were relatively modest, typically <1% for both the intracellular and extracellular waveform. The parameter values tested by the search were typically within a few percent of the values at the initial starting point. When I attempted to tune the conductance density parameters solely with the automated search (starting from average values for the parameters) the resulting error was invariably larger than those achieved by manual tuning. This suggests that the performance landscape in the parameter space is non-convex, with many local optima.

Despite this obstacle and the high degree of variability in my data, I succeeded to model both intra- and extracellular data to within 10%. This could be achieved because the degree of non-convexity due to parameter variations at a fine scale is less significant than the relatively constrained choices available for a few dominant parameters. For a given recording, the choice of Na^+ conductance density is well constrained by the simultaneous recording amplitudes and only the precise balance between somatic and dendritic densities leads to local optima in performance. At the same time, the choice of which K^+ currents dominate is constrained by the shape of the EAP: a cell with a K^+ phase that begins and ends rapidly will always have dominant K type conductance, while one with a K^+ phase that begins and ends slowly will always have a dominant C type conductance. It is fine tuning the exact trade off between the K^+ currents that are less significant that creates many local optima. These observations lead me to conclude that the tuned parameters for conductance densities do, in fact, represent qualitatively unique combinations of dominant current types. Better results from automated search may result from methods designed to escape from very small local optima, such as simulated annealing.

While it is possible to match simultaneous intra- and extracellular recordings with a compartmental simulation, it is actually exceedingly difficult to simultaneous achieve low errors on both. Interestingly, I find that matching the EAP seems to be a tighter constraint on the model parameters than matching the intracellular action potential. Table 2.4 shows that lower errors were achieved for the match to the intracellular recording than the extracellular recording in nearly every case, despite equal weight being assigned to both errors in the manual and automated parameter tuning. Figure 2.4 illustrates this point further by demonstrating that a model cell can have virtually identical membrane potentials despite significant changes in the distribution of active current densities. The extracellular waveform varies to a much greater degree when the distribution of active currents is

changed. Consequently, it would be very unlikely to have significant changes in the intracellular AP (peak amplitude, duration or size of AHP) due to conductance density changes without having a significant impact on the EAP. This results from the fact that the membrane potential in any given compartment combines membrane currents with axial currents while the EAP results directly from the active membrane currents in the perisomatic region alone, giving the membrane potential additional degrees of freedom compared to the extracellular potential. This result will be examined in much greater detail in chapter 3.

	Intracellular			Extracellular			
Cell	Recording Amplitude (mV)	Simulation $\sqrt{\text{MSE}}$ (mV)	% Error	Recording Amplitude (μV)	Simulation $\sqrt{\text{MSE}}$ (μV)	% Error	Number of Sites >20 μV
D037	52.7	2.3	4.4	15.6	1.9	12.2	NA
D056	48.3	1.7	3.5	95.1	5.8	6.1	NA
D068	17.5	1.6	9.1	41.0	1.6	3.9	NA
D081	60.9	1.9	6.1	66.7	2.2	3.3	NA
D128	65.5	3.7	2.9	30.3	1.5	4.9	NA
D112.1	28.9	1.9	6.4	64.4	4.7	7.3	NA
D112.2	55.8	2.9	5.2	40.0	2.8	7.0	NA
D135	50.5	1.6	3.2	21.9	0.9	4.3	NA
D137	70.8	3.6	5.1	4.7	0.7	15.0	NA
D145	79.5	2.1	2.7	110.0	4.4	4.0	NA
D147	42.0	1.6	4.3	21.7	1.7	7.7	NA
D149	57.3	4.8	8.4	10.9	1.8	16.5	NA
D151	72.7	4.3	5.9	109.1	3.6	3.3	NA
D163	75.6	2.6	3.5	64.0	5.7	8.9	3
D180	72.1	3.0	4.2	36.6	3.4	9.3	4
D187	53.1	4.1	7.7	58.6	8.9	15.2	5
D188	78.5	4.2	5.4	48.3	19.0	39.3	3
D189	35.8	3.7	10.4	35.6	2.9	8.0	2
Average	56.5	2.9	5.5	48.6	4.1	9.8	NA
SD	17.6	1.1	2.2	31.8	4.3	8.5	NA

Table 2.4: Measure of the error between the data and the model.

Square root of the mean square error (SMSE) at the recording sample points over a 4 ms window beginning 1 ms before the peak of the AP. The SMSE is normalized by the height of the intracellular AP and by the amplitude of the extracellular peak respectively to obtain percentage error.

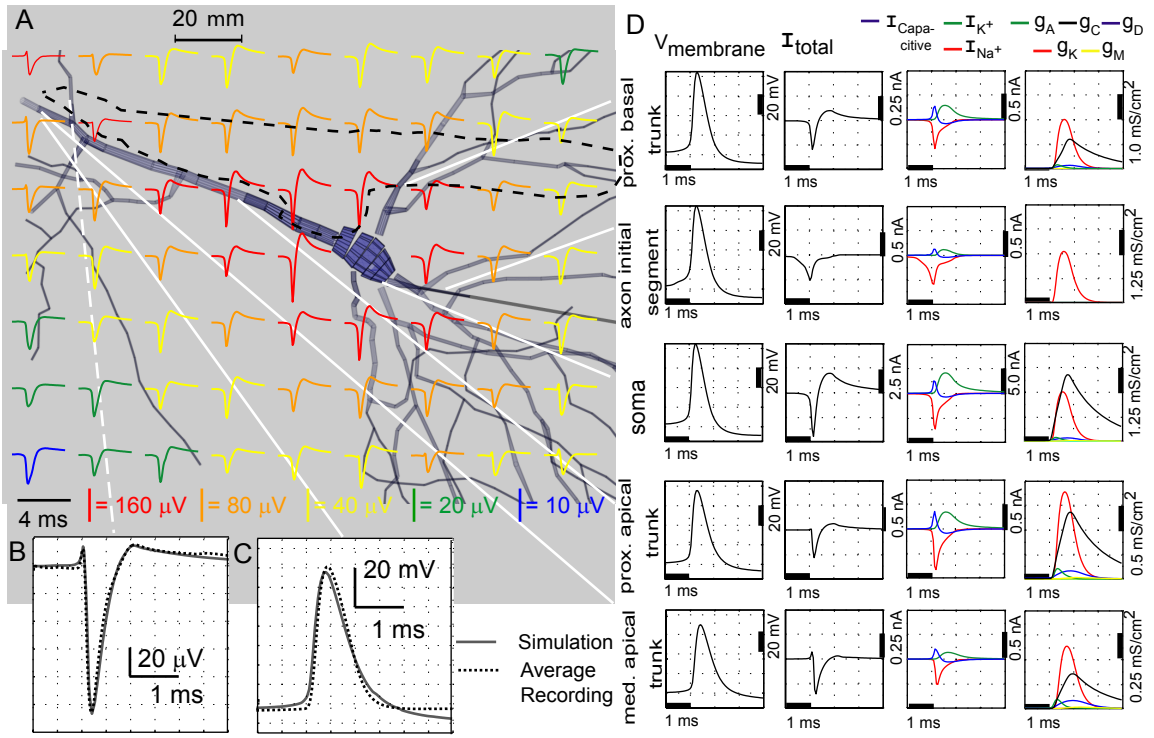

Figure 2.1: Recording and simulation D151.

A: EAPs in the transverse section containing the soma and the tip of the electrode track (dotted line). B: Enlargement of the EAP at the estimated electrode position, and comparison to the recording (strongest channel of the tetrode). The EAP is made up of three distinct phases: (1) a brief, positive peak; (2) a much larger negative peak; and (3) a positive period of longer duration and slowly decaying amplitude. C: Comparison of the average intracellular recording with the simulated spike in the proximal apical trunk. The lack of pronounced AHP suggests the intracellular electrode was not at the soma. D: Details of the simulation in the indicated compartments. The shape of the EAP waveform is given by the shape of the net membrane current across the membrane at the soma and proximal dendrites (second column). The third column shows the makeup of the membrane current in terms of Na^+, K^+ and mixed-ion capacitive current. All three currents are simultaneously active throughout the AP; the three phases of the EAP correspond to the current that is dominant at that time: the brief positive peak at the start of the waveform is due to the positive capacitive current; the main negative peak is due to the influx of Na^+current driving the action potential; the final positive phase results from repolarizing K^+ current flowing out of the cell. The last column shows the corresponding conductivity densities of the A, C, D and K type K^+ currents.

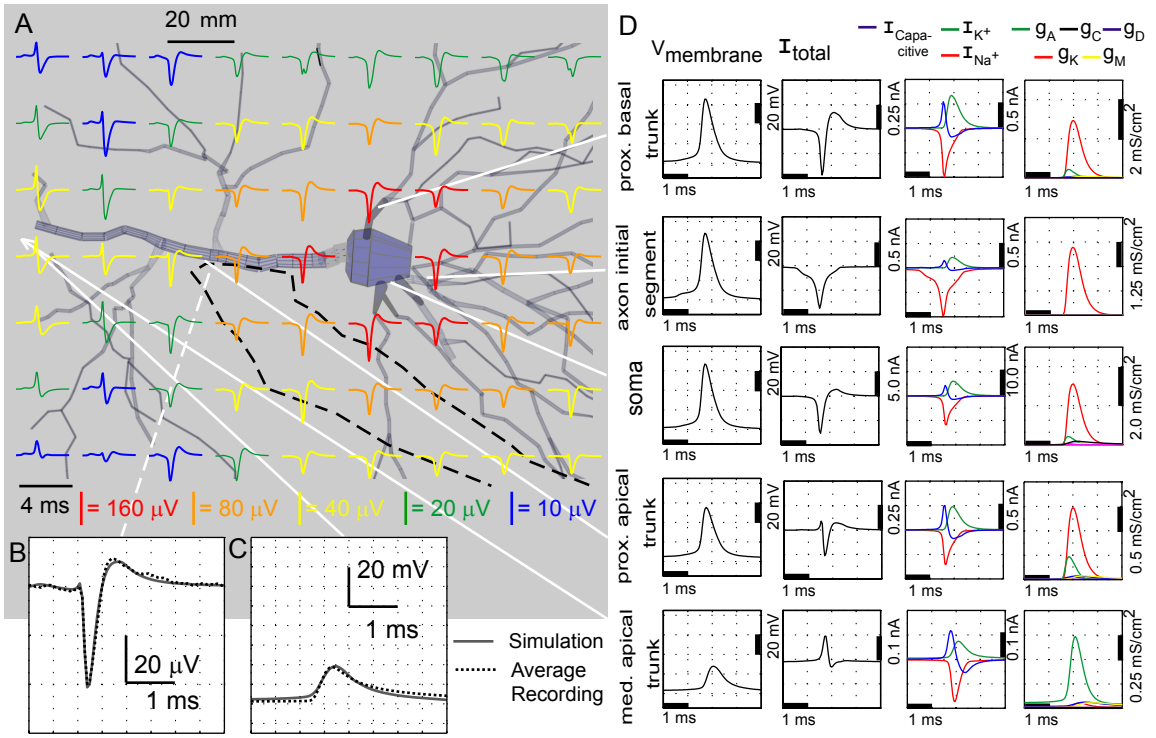

Figure 2.2: Recording and simulation D068 .

A: EAPs in the transverse section containing the tip of electrode track (dotted line), 5 μm caudal to the soma and apical trunk. (the Z-axis is the axis perpendicular to the plane of the section.) Close to the soma, there is no initial, positive peak in the EAP. At locations along the apical trunk, the initial peak becomes pronounced. B: Comparison of extracellular recording (strongest channel of the tetrode) and simulation at the estimated electrode position. There is only a slight hint of a positive deflection before the negative Na^+dominant phase of the waveform. C: Comparison of intracellular recording and the simulation in the apical trunk 120 μm from the soma. D: Further simulation details. In the soma (middle row) the positive capacitive current, proportional to the change in membrane potential coincides with the larger Na^+ current (third column) because the membrane potential change is driven by local Na^+current. In dendritic compartments (first, fourth and fifth rows) the membrane depolarization is initially driven by Na^+ current from the soma, until local Na^+ currents are activated and the action potential regenerates. In the brief time before the local Na^+ currents activate, the positive capacitive current is the dominant membrane current and a capacitive dominant phase is visible in the net current (second column). Consequently, the EAP has a more pronounced capacitive phase close to the apical trunk. Also shown, the Na^+ current starts to enter the axon initial segment (2nd row) in a gradual way, driven by the action potential in the first node of Ranvier (not shown) and before the start of the main action potential at the soma. This results in a gradually sloped negative phase before the start of the main EAP.

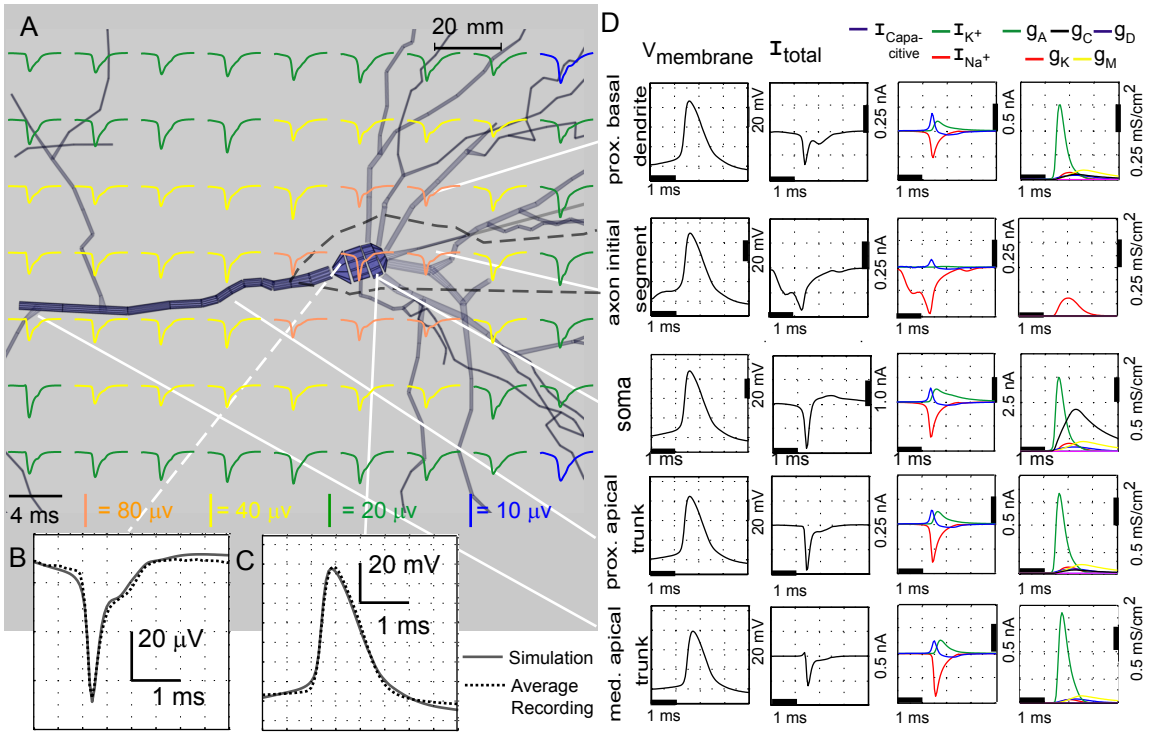

Figure 2.3: Recording and simulation D11221.

A: EAPs in the transverse section containing the electrode track (dotted line), 25 μm caudal to the soma and apical trunk (the Z-axis is the axis perpendicular to the plane of the section; i.e., soma is at Z=-25 μm, with respect to the plane of the EAPs.) B: Enlargement of the EAP at the estimated electrode position, and comparison to the recording (strongest channel of the tetrode). An initial positive peak is completely absent, and the Na^+ dominant negative phase is made up of a narrow peak followed by a period of slower repolarization. The K^+ dominant phase is of minimal amplitude. C: Comparison of intracellular recording and simulation at the soma. D: Selected details of the simulation. The duration of significant Na^+ channel activation is longer than the Na^+dominant phase seen in the EAP. The width of the Na^+ dominant phase in the EAP is therefore determined by the timing of the K^+ currents: a strong A and C type current (rightmost column.) The very fast A current shapes the sharp peak of the Na^+ phase by quickly counteracting the Na^+ current. However, the A current rapidly inactivates. C current continues the repolarization in the somatic compartment, but has a much lower density in the dendritic compartments. This leads to the widening of the Na^+ phase and the negligible amplitude of the K^+ phase. The shape of the EAP (B) is similar to the current profile of the proximal dendrites (first and fourth rows, second column).

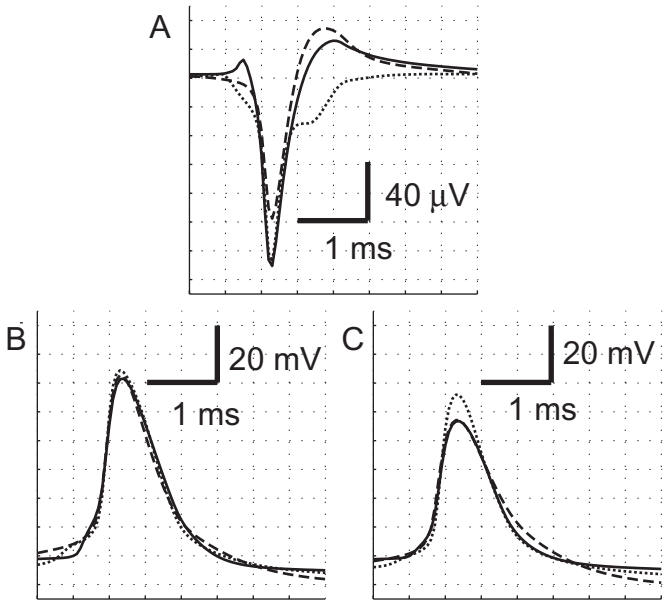

Figure 2.4: EAP as a constraint on the model parameters.

A: An EAP at (X=-20, Y=20, Z=0) for cell D151 simulated with three different distributions of active currents. The EAP changes significantly as a result of the change in parameters: the EAPs each have normalized error(an SMSE) of approximately 12.5% with each other. B: Intracellular membrane potentials at the soma for the same simulations. The parameters have been tuned so that the membrane potentials are virtually identical, despite the very different EAPs: the average SMSE is 3.5%. C: Intracellular membrane potentials in the apical trunk at a distance of approximately 100 microns from the soma: the average SMSE is 5.5%. While at this distance the membrane potential shows more variability than at the soma, the introduction of a second membrane potential measurement as a constraint does not provide as much of a measure of error as a single EAP measurement. Due to the high dependence of the EAP on the precise active current conductance density the reverse result, similar EAPs for different intracellular membrane potentials, would be exceedingly unlikely. This point will be further examined and explained in chapter 3.

2.3.5 Electrode Position and Width of the Na^+ Phase

In sections 2.3.2 and 2.3.3 I presented evidence that the main impact of electrode position (other than on the amplitude of the EAP) was on the presence or absence of a positive capacitive dominant peak in the waveform, and that the main determinant of the width of the Na^+ dominant phase is the balance of ionic currents. However, the position of the extracellular electrode makes a secondary contribution to the duration of the Na^+ dominant phase of the waveform, as shown in Figure 2.5: the more distant the electrode from the cell, the longer the duration of the Na^+ dominant phase. It follows that the duration of the Na^+ phase of the EAP should be negatively correlated to the amplitude of the EAP. This relationship was analyzed in the sample of 307 EAP recordings made by silicon probes. The resulting correlation coefficient between the duration of the Na^+ phase (as measured as the width at 25% peak amplitude) and the amplitude was -0.246 ($p = 1.4 \times 10^{-5}$).

The phenomenon occurs because action potentials take time to back-propagate, and because voltage amplitudes decay with distance from the current source (as in equation 2.2). A recording electrode close to the soma, will effectively "see" only the somatic and most proximal dendritic current sources. This is not only because of the larger currents, but also because any contribution from a distal source will be scaled by a much greater distance. But if the electrode is moved away from the cell, it effectively sees both the currents from the somatic initiation of the action potential and also the back-propagation of the action potential into the dendrites as they will have similar scaling due to distance. Because the backpropagation along the main dendrites takes a significant fraction of a millisecond, to a distant recording electrode it looks like the extracellular potential results from a continuous current source of longer duration when in fact it is produced by moving current sources of short duration.

2.3.6 Impact of the High-Resistivity Cell-Body Layer

Including the exact calculation for the impact of the high resistivity cell body layer had only a modest impact on extracellular voltages compared to the assumption of homogeneous conductivity equal to that of the stratum oriens or the stratum radiatum. This is illustrated in figure 2.6 which shows the percentage change in the peak amplitude of the EAP waveform (i.e., the negative Na^+ phase peak) in comparison to homogeneous resistivity at the level of the stratum radiatum. The illustration is calculated for the heightened resistivity that would occur in a period of intense activity (baseline resistivity of 350Ωcm, high resistivity layer of 750 Ωcm. [López-Aguado et al., 2001]) While very close to the cell the amplitude changes by nearly 100% (nearly doubling), the impact decreases rapidly with distance and outside of the high resistance layer there is only around a 10% increase. I also compared how the impact depends on the thickness of the high resistance layer: If the layer were only 20 μm thick (rather than the usual 40 μm) the impact is dramatically decreased, showing

virtually no change outside of the high resistivity layer and at most around a 50% increase in amplitude very close to the cell. If the high resistivity layer were 60 μm thick, the impact increases somewhat, projecting a 20% increase in amplitude up to distances around 50 μm from the soma. All in all, I conclude that for realistic resistivity levels and thicknesses of the layer the impact is rather modest. Still, I included the high resistivity layer in all of my CA1 simulations in order to be as realistic as possible.

2.3.7 Cell Morphology

A salient aspect of the reconstruction and simulations that had very little impact on the EAP waveform was the details of each cell's dendritic morphology. To demonstrate this relative indifference, I performed simulation using the reconstructed morphology of a CA1 basket cell [Gulyas et al., 1999] with the conductance density parameters tuned to match one of my recordings from a pyramidal cell (Figure 2.7). While a pyramidal cell has a single apical dendrite and a skirt of basal dendrites extending from opposite ends of a conical soma, the basket cell has an approximately spherical soma with two thick dendrites and an assortment of narrow dendrites extending at more irregular angles. However, the resulting EAP matches the original recording very closely. I also observe that given the freedom to choose the electrode distance from the soma (to match the amplitude of the waveform), I can match virtually any EAP waveform using an arbitrarily chosen CA1 pyramidal cell for the simulation. This results from the fact that the observable waveform is determined by the net current profiles of the perisomatic compartments: if the distribution of active currents in the perisomatic region is similar for two cells, then the EAP waveform will be similar regardless of the precise location and branching pattern of the dendrites. These observations suggest that the major determinant of the EAP waveform depends primarily on the unique distribution of channel densities and considerably less on the morphological details of the cell.

At the same time, I found that the size of the neuron from each recording session was strongly correlated with the amplitude of the resulting EAPs. For example, I compared the peak amplitude predicted by the simulations at a reference position 20 μm from the soma (in a direction perpendicular to the apical trunk) and found that amplitude ranged from 80 μV for the smallest cell up to 130 μV for the largest (cell size was measured by total membrane surface area.) The correlation coefficient between amplitude and cell size was 0.67 ($p=2.2 \times 10^{-4}$). However, there are multiple factors contributing to the peak amplitude of the EAP (e.g., Na^+ current density and the assumptions regarding the resistivity, etc.) which will be discussed in much greater detail in chapter 4.

2.3.8 Contribution of the Basal Dendrites

As mentioned in section 2.3.2, the model predicts a variety of EAP waveforms in the subthreshold region of the basal dendrites, as in Figure 2.8. Note that the pyramidal cell recorded in the session was not stained sufficiently for reconstruction, and so simulations were performed with a cell reconstructed from another session. As the simulation demonstrates, a "W" shaped waveforms can result from an AP in a single cell and does not require coincident firing in two nearby cells. The EAP is produced by superposition of the waveform resulting from somatic AP currents with the waveform resulting from AP backpropagation into the basal dendrites. The amplitude of the Na^+ phase peak in "W" waveform is <10 μV. While they appear clearly in an average of several hundred spikes, such waveforms would not be detected if it were not for the fact that the six-site probe also had recording sites close to the soma. Five out of 13 silicon probe recordings from [Henze et al., 2000] revealed similar waveforms on distal recordings sites. Recordings and modeling experiments prove that a variety of waveforms can occur depending on the exact proximity to the local basal dendrite(s). In rare cases "W" waveforms occur at high amplitude. One recording in the data from [Henze et al., 2000] was of a large amplitude ($>50\mu$V negative peak amplitude) "W" waveform at a proximal site, which I have not been able to reproduce in the model.

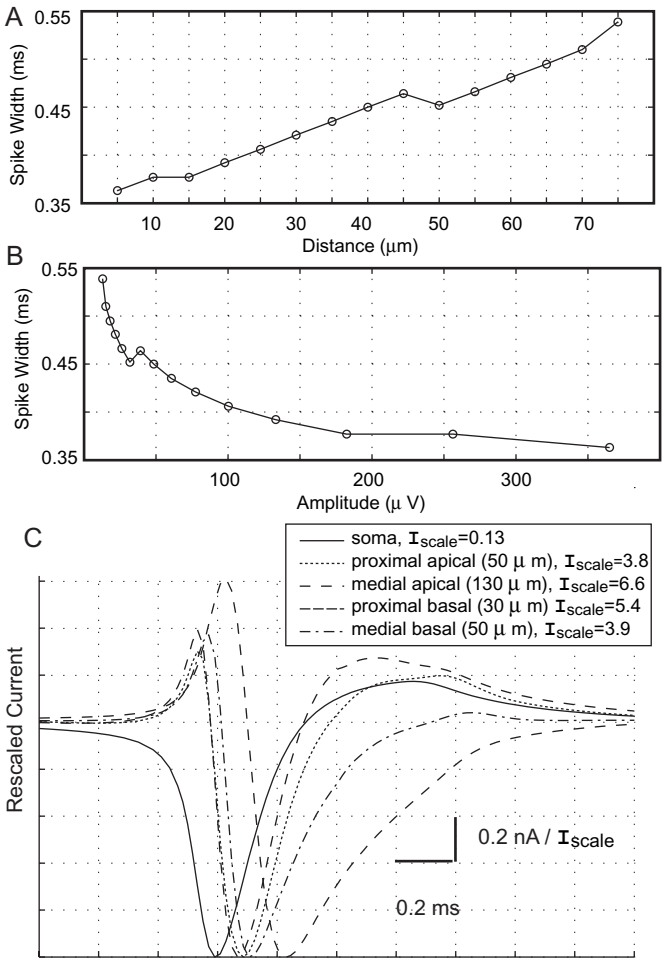

Figure 2.5: Analysis of the duration of the Na+ phase.

A: Duration of EAP Na^+ phase vs. the simulated electrode position when moving away from the soma in a direction perpendicular to the apical trunk. Duration is measured as the width at 25% peak amplitude of the Na^+ dominant (negative) phase. There is a nearly linear relationship between the duration of the Na^+ dominant phase and the distance from the electrode to the soma. B: The same data as in A, plotted vs. the amplitude of the waveform. C: Membrane current vs. time at different locations illustrates the time required for the action potential to propagate back into the dendrite. The combined inward current phase of the soma and proximal dendrites (solid curves) makes a reasonably close prediction for the apparent duration of the Na^+ phase observed at 45 μm, around 0.4 ms.

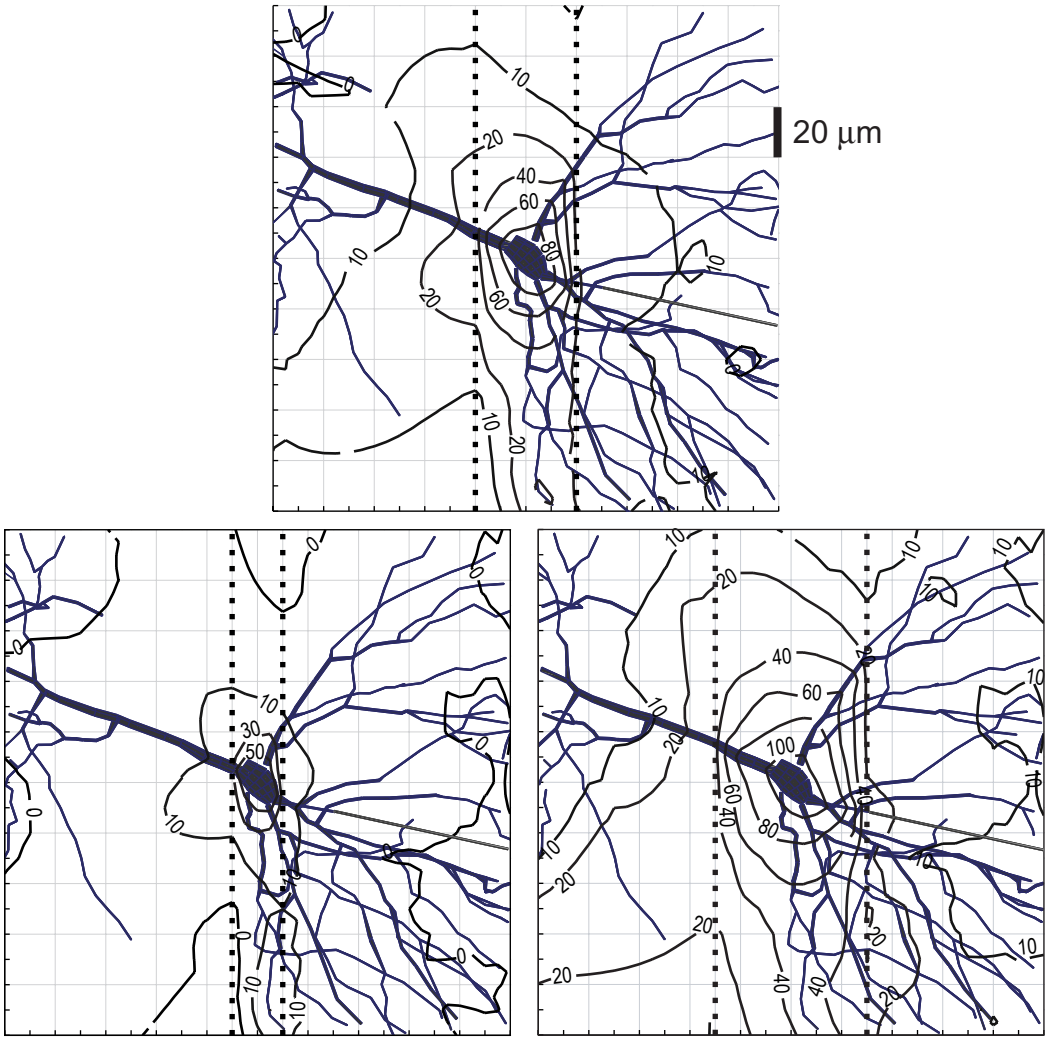

Figure 2.6: Impact of the high-resistivity cell body layer

Percentage change in the peak amplitude of the EAP waveform in comparison to homogeneous resistivity. Top: Assuming the high resistivity layer is 40 μm thick. Bottom, left: Assuming the high resistivity layer is 20 μm thick. Bottom, right: Assuming the high resistivity layer is 60 μm thick

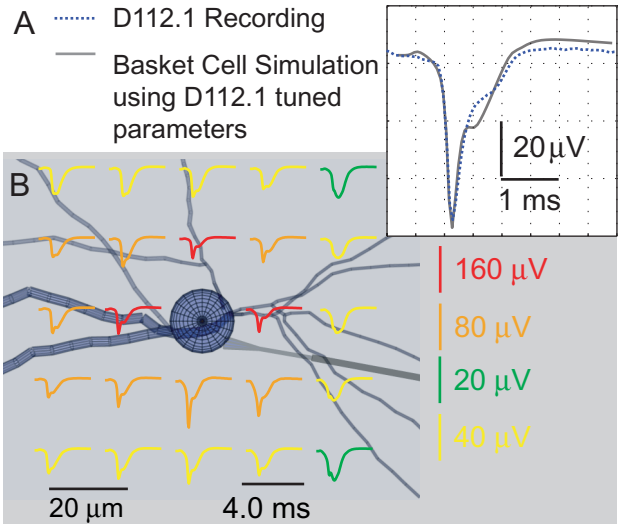

Figure 2.7: CA1 basket cell simulated with the conductance densities tuned for pyramidal cell recording D112.1.

The basket cell is PV08D from [Gulyas et al., 1999] The simulation of D112.1 is shown in Figure 2.3). A: The extracellular waveform is virtually the same as that for neuron D112.1. This suggests that the dendritic morphology makes little direct contribution to the waveform. B: The EAPs around the simulated basket cell in the plane of the soma. The EAPs below threshold are somewhat different than those for D112.1, but the above threshold EAPs are very similar.

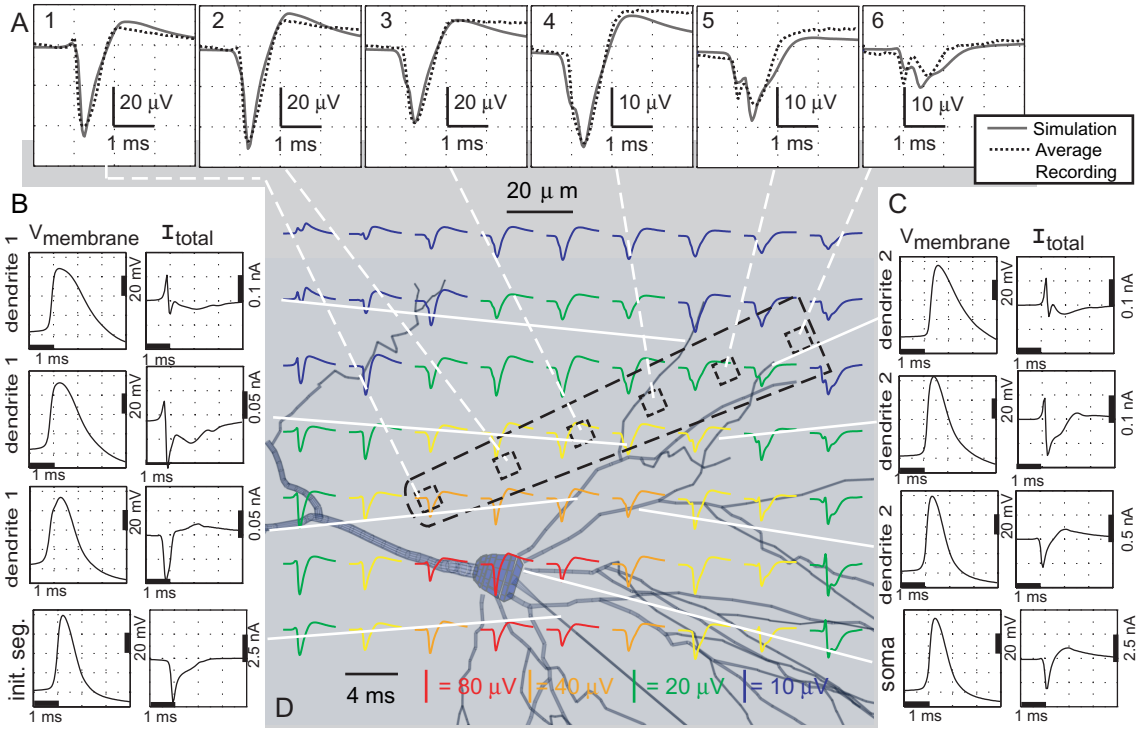

Figure 2.8: Extracellular recording and simulation D180.

The recording was made with a six-site silicon probe with 25μm spacing between individual taps. The sites closest to the cell body have a typical waveform, including the presence of the capacitive phase on the deepest recording site (site 1) but not on the site with the strongest recording, presumably closest to the soma (2). In the shallower sites in the stratum oriens (4-6) the waveform is of smaller amplitude and the Na^+ phase of the waveform has longer duration (see section 3.5). The two recording sites, most distant from the cell (5-6), show unusual waveforms similar to a letter "W" in appearance. B: Extracellular potential waveforms in a transverse section 10 μm caudal to the soma and apical trunk (i.e., soma is at Z=-10 μm, with respect to the plane of the EAPs.) The assumed position of the recording electrode is indicated (dotted line.) C: Details of the simulation. The somatic current (last row, second column) is two orders of magnitude larger than the basal dendritic currents; but at distal recordings sites it is scaled by distance. The current profile in the basal dendrite (first two rows, second column) exhibits a large capacitive dominant phase and in the more distal site there is virtually no Na^+ dominant phase due to the increasing density of A type K^+ currents (middle and right columns.) The "W" waveform results when a recording site is close to the basal dendrite (<10μm.) The waveform first reflects the current due to a distant somatic AP initiation followed by the local dendritic currents. The capacitive phase of the dendritic current creates the brief positive "notch" in the negative Na^+ phase.

2.4 Discussion

My main finding is that a detailed compartmental model combined with the LSA can accurately reproduce both the waveform and amplitude of recorded EAPs. Further, the model provides precise explanations for many of the features observed experimentally in EAPs. Despite the high degree of variability typical of biological measurements, the complexity of the system under investigation – a single, highly nonlinear nerve cell embedded into non-uniform neuronal tissue – the remoteness of distal dendritic events and uncertainty about the exact electrode position, my model yields less than 10% average normalized error (table 2.4). This reasonable close match validates the simplified assumptions I made to describe the extracellular milieu in my domain of interest (i.e., at frequencies <3kHz) using ohmic but no capacitive components. It is known that action potentials in CA1 tend to fire in synchrony with local field potential (LFP) oscillations [Csicsvari et al., 1999]. As a result, EAP waveforms do in fact seem to contain an average LFP component of a few (typically <10) μV. These factors may significantly increase the error in matching low amplitude EAPs.

An important observation of present experiments is that exact channel distributions, rather than the details of the dendritic arbors, are the main determinants of the EAP wave form. The implication of finding is that CA1 pyramidal cells that are usually regarded as a homogeneous set of neurons do have substantial variability in their biophysical properties and that such variability may be identified with proper analysis of the extracellularly recorded spikes.

2.4.1 Variability of Conductance Density

I demonstrated that for neurons to produce significantly different EAP waveforms in the perisomatic region, it is necessary for the net current profiles in the soma and proximal dendrites to be different, and that the source of this difference is most likely a varied balance of repolarizing K^+ currents. I assumed that variability of the K^+current contributions made by different ionic current types on different cells is due solely to differences in conductance densities (i.e. ionic channel densities) rather than to variability in channel behaviors (i.e. kinetics.) However, it is known that the activation curves of some ionic channels may shift by several mV under various conditions in slice preparations (e.g. LTP [Frick et al., 2004].) It seems possible that if I allowed the kinetics of ion current activation/inactivation to vary from cell to cell, I could match the simultaneous intra- and extracellular recordings with less variability in the conductance density levels.

In this light, I consider the choice to fix active current kinetics to be a pragmatic decision based on the need to manage the complexity of the model. In fact, several other important aspects of ionic current behavior were also effectively "lumped" into the conductance density. For example, Na^+ channels and K and D type K^+ channels in CA1 pyramidal cells are all known to suffer from slow, activity-dependent inactivation [Colbert et al., 1997, Klee et al., 1995, Storm, 1988]. Because

an average recording is modeled with a single simulated spike, what may, in fact, be slow inactivation of these channels is represented in the model as a reduced peak conductance density level. Similarly, the activity of the I_{K^+C} current is strongly dependent on the intracellular $[Ca^{2+}]$ which may vary from cell to cell in real neurons but does not vary in the model. Consequently what may in fact be variation in $[Ca^{2+}]$ are also reflected in the model as differences in the density of the I_{K^+C} conductance. Finally, a variety of neuromodulators affect the activation and inactivation of ionic channels in pyramidal neurons; for review see, e.g., [Tsubokawa, 2000]. Any impact of these various factors are all folded into the parameter controlling the peak conductance density. Consequently, I consider conductance density as a single parameter that actually reflects a large number of factors contributing to the currently available number of any particular ionic channel.

2.4.2 Extracellular Recording as a Model Constraint

I performed extensive and laborious manual and automated tuning of the peak conductance densities to minimize the error between the model and the recordings. However, these results do not prove that I have found a globally optimal solution for all of the parameters. In particular, I have not exhaustively searched the large number of parameters controlling the kinetics of ionic current activation and inactivation. Even without relaxing my assumption that active current kinetics are constant across different cells, it may be that an alternative formulation of the channel kinetics may provide a better match to the recording data.

While the example of Figure 2.4 is admittedly contrived, it suggests that EAPs have been an underutilized resource for constraining compartmental models. Combining extracellular recordings with intracellular recordings is a useful technique even for *in vitro* physiology experiments as it will add precision to the analysis of events involving active ionic currents. If the general properties of the intracellular action potential are known (i.e., typical amplitude and duration), EAP measurements made at specified locations is a further source of information for constraining a compartmental model. In turn, this feature may provide a useful technique for studying the properties of active ionic currents *in vivo* as will be analyzed more fully in chapter 3.

2.4.3 Impact of Cell Morphology on EAP

My results predict that while size of the soma and proximal dendrites are important factors determining the amplitude of the EAP, the details of cell morphology make relatively little impact on the EAP waveform However, a few caveats apply to this result: In the example of figure 2.7 the axonal and spine properties appropriate to a CA1 pyramidal cell were mapped onto a basket neuron. Therefore the example only shows that the location and size of the dendrites do not have a important impact on the EAP, but does not suggest that other properties of specific cell types will not be

significant. In fact,modeling a spineless cell with an unmyelinated axon would significantly alter the input resistance and AP initiation properties of the model cell and conductance density parameters tuned to match a CA1 pyramidal cell would need to be significantly altered just to produce a stable action potential, let alone a particular EAP waveform. Also, I have not ruled out the possibility that the cell morphology may be indirectly related to the shape of the EAP waveform via a feedback mechanism through which morphological details control the conductance density levels.

2.4.4 Expected Developments

Because the model accurately predicts the amplitude of the EAP, I can use it to predict the distance at which an electrode would detect cells not only in the hippocampus but wherever there is sufficient data available to constrain the model. This LSA method is applied to investigate the relative importance of different factors in determining at what distance EAPs may be detected by a recording electrode, and to analyze how sampling bias due to cell size may influence EAP recordings, in chapter 4.

To date, extracellular unit recordings have been used mainly to monitor the spike output of neurons. However, multiple-site high-resolution extracellular recordings can also provide useful information about intracellular features of the recorded neurons. For example, the extent of soma-dendritic backpropagation of action potentials can be monitored in the intact brain as a function of behavior; e.g., [Buzsáki et al., 1996, Quirk et al., 2001]. My findings suggest that accurate and high-resolution monitoring of EAP can provide information about alteration of conductance densities in single neurons as a function of state changes and plasticity. Because subcortical neuromodulators and use-dependent activation of neurons are known to modulate the various conductances, my results imply that by monitoring the waveforms, EAPs can provide access to this valuable information in behaving animals. Finally, models consisting of large numbers of geometrically arranged neurons can provide the tool needed for the perfection of unit classifying algorithms and for the development of ideal recording electrode configurations without the need of simultaneous extracellular and intracellular recordings from various cell types and brain regions.

Chapter 3

Using Extracellular Action Potential Recordings to Constrain Compartmental Models

3.1 Introduction

Compartmental neuron models are one of the most useful computational methods in modern neuroscience. This is because they allow conjectures based on physiological data to be tested for biophysical plausibility and then generate additional predictions which can be tested by further physiological experiments (for review see, e.g., [Koch and Segev, 1999, Stuart et al., 2001].) A common difficulty with the application of compartmental models is constraining the many parameters controlling their properties [Vanier and Bower, 1999, Keren et al., 2005, Hayes et al., 2005, Huys et al., 2006]. This is particularly the case with compartmental models based on complete cell reconstructions and including the variety of ionic channels known to occur on different neuronal cell types and their corresponding non-uniform conductance densities [Migliore and Sheperd, 2002]. Such models can easily possess 100 or more degrees of freedom.

A variety of data is used to tune *in vitro* compartmental models, principally membrane potential traces, spike times in response to current injection, and subthreshold current vs. voltage (I-V) curves; see, e.g., [Vanier and Bower, 1999, Keren et al., 2005]. However, [Keren et al., 2005] found that both membrane potential traces and spike times yield non-optimal performance as the model constraint for a genetic algorithm search. They proposed the additional constraint of the voltage vs. the first derivative of the voltage. [Hayes et al., 2005] came to a similar conclusion, arguing for the cumulative voltage integral as a model constraint. [Huys et al., 2006] demonstrated that if the membrane potential is known or can be closely estimated for all compartments of a neuron then optimal model parameters can be determined directly. This approach would rely on optical imaging of the membrane potential.

If a modeling study aims to reproduce *in vivo* conditions the choices are more limited by the difficulty of applying these protocols. The most abundant measurements of *in vivo* neuronal activity are extracellular recordings. Yet, surprisingly, there have been few attempts to tune compartmental models with these data [Varona et al., 2000]. If compartmental models are to be widely used to match *in vivo* conditions, it would be advantageous if there was a practical method to tune them using extracellular recordings in the absence of additional protocols.

I already performed a detailed simulation study recreating simultaneous intra- and extracellular recordings of CA1 pyramidal neurons *in vivo* as described in chapter 2. Action potentials were simulated based on morphological reconstructions of the recorded cells and the resulting extracellular potentials were calculated based on the membrane currents predicted by the model. I tuned the model parameters for each cell until a plausible match was achieved for both the intracellular action potential (IAP) and the extracellular action potential (EAP). The tuned model allowed detailed explanation of a variety of features of the EAPs. An interesting finding was that variation of cell morphology within the class of CA1 pyramidal neurons made only minimal impact on the EAP waveform, while different distributions of active conductance densities have predictable impacts on the EAP waveform. This finding suggests that EAPs recorded *in vivo* may be used to analyze the intracellular state of the neuron, including active ionic conductance kinetics and conductance densities, the parameters that must typically be tuned when constraining a compartmental model.

In the process of tuning the model I observed that it was significantly easier to tune the model to closely match the IAP waveform than to match the EAP waveform. It has previously been observed that single IAP traces are a weak constraint on the compartmental model [Keren et al., 2005]. My own observations suggest the novel possibility that EAP waveforms may have significantly greater power as a model constraint.

To further investigate this, I analyzed cases where a compartmental model could have significantly different conductance density parameters but still produce the same IAP waveform. For these cases, I analyzed the influence that the conductance density parameters had on the EAP. One potential drawback of using EAP measurements to tune a compartmental model is the sensitivity of the EAP to the position of the measuring electrode: if the position is not known with a high degree of accuracy it may introduce uncertainty which cancels any benefit. Also, if a model is tuned from EAP recordings made *in vivo* then the morphology of the neuron will also be unknown. I addressed these issue by analyzing the sensitivity of EAP features to electrode position and morphological variation as predicted by the model.[1]

[1]The material presented in this chapter is based on material now in press: [Gold et al., 2007].

3.2 Methods

3.2.1 Compartmental Model Simulations

3.2.1.1 Overview

The standard circuit model for a compartmental model is shown in Figure 3.1. The intracellular potential for a typical compartment is derived from current conservation,

$$I_m = I_{a,in} - I_{a,out} \tag{3.1}$$

The membrane current, I_m, is given by the sum of the ionic currents, the membrane capacitive current, and any leak current. The axial currents, $I_{a,in}$ and $I_{a,out}$, are given by the difference between the voltage in neighboring compartments divided by the axial resistivity, R_a, which is assumed here to be constant as would be the case for neighboring compartments of identical size. This leads to the first order differential equation:

$$\begin{aligned} -C\frac{dV_m(x)}{dt} &= G_{Na^+}(x)[V_m(x) - E_{Na^+}] + \sum_n G_{K^+n}(x)[V_m(x) - E_{K^+}] \\ &\quad -\frac{[V_m(x-1) - V_m(x)]}{R_a} + \frac{[V_m(x) - V_m(x+1)]}{R_a} + \dots \end{aligned} \tag{3.2}$$

where G_{Na^+} and the G_{K^+n} are understood to have the usual non-linear voltage-time dependence (see e.g. [Koch, 1999]), and ... refers to leak and Ca^{2+} conductances which are orders of magnitude smaller than the Na^+ and K^+ conductances during an action potential. I performed my compartmental simulations using the NEURON Simulation Environment [Hines and Carnevale, 1997].

The parameters of the model that must be estimated can include both the passive parameters, C, and R_a, as well as the maximum conductance densities and kinetics parameters of the time varying resistances G_{Na^+} and the G_{K^+n} (usually referred to as $\bar{g}$.) In practice the densities of the different conductances vary greatly across different classes of neurons [Migliore and Sheperd, 2002] and even between different cells [Toledo-Rodriguez et al., 2004] while the expected values for the passive parameters are expected to be in a more confined range [Koch, 1999]. For this reason I focus my attention on the parameters of the active conductance densities.

3.2.1.2 Active Conductances and Passive Properties

The model includes Hodgkin-Huxley style kinetic models for 15 different voltage or $[Ca^{2+}]$ dependent ionic conductances known to be present on CA1 pyramidal cells (for review, see [Borg-Graham, 1999]). Several of the conductances had non-uniform distributions densities as suggested by previous *in*

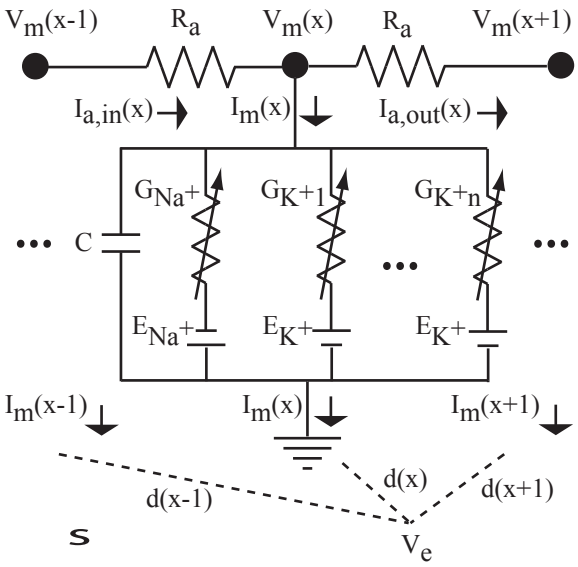

Figure 3.1: Circuit model of intracellular and extracellular potentials

vitro research (for review, see [Migliore and Sheperd, 2002]). The conductances were fast inactivating Na^+ (somatic and axonal varieties), A type K^+ (proximal and distal varieties), AHP type Ca^{2+}dependent K^+, C type voltage and Ca^{2+} dependent K^+, D type K^+, K type K^+, M type K^+, H type mixed cation (somatic and distal varieties), L type Ca^{2+}, N type Ca^{2+}, R type Ca^{2+}, T type Ca^{2+}. The active conductance kinetics were modeled with the formalism of [Borg-Graham, 1999], with somewhat different parameter choices as detailed in section 2.2.3.2.

As I focused in this study on reproducing the shape of the EAP, I treated the maximal conductance densities ($\bar{g}$) for the Na^+ and A, C, D, K and M type K^+ conductances as variables that could be tuned, leaving the remaining parameters (including the passive parameters and active ionic conductance kinetics) fixed for all simulations. Current due to the Ca^{2+}, H and AHP conductances as well as the passive leak were much smaller and consequently do not play a significant role in the generation of the EAP waveform (although $[Ca^{2+}]$ plays an important role in the control of the C type K^+ conductance.) The values used for the tunable conductance densities are listed in table 3.3 in section 3.3.1, below. The values used for the fixed conductances are the same as those listed in table B.5, in section 2.2.3.2. The system of the non-uniform distribution of conductances are also described in section 2.2.3.2, albeit based on the conductance parameters given in table 3.3. The passive parameters and model for spines are the same as described in section 2.2.3.1.

Synaptic input was mimicked by reducing the leak resistance and assigning a reversal potential above threshold in the compartments receiving synaptic input, as described in section 2.2.3.4. Usually the simulated synaptic input was applied to all dendritic compartment >50 μm from the soma for a short time (<5ms) until an action potential was initiated. For complete details of the

compartmental model see section 2.2.3.

3.2.1.3 Cell Morphologies

The cells used for simulation are reconstructed CA1 pyramidal cells from the experiments described in [Henze et al., 2000]. Most of the simulations described were performed on a single morphology, while in section 3.3.8 I consider results comparing 17 different neuronal reconstructions. The size of the cells in the sample is described in section 3.3.8.

The axon for each cell was modeled similar to that described in [Mainen et al., 1995]: An axon hillock 10 μm long connects the soma to the initial segment which is 15 μm long. After the initial segment the axon consists of five alternating myelinated sections (100 μm long) and nodes of Ranvier (1 μm long). The active Na^+ conductance in the initial segment and nodes of Ranvier is modeled based on the results of [Colbert and Pan, 2002]: it is active at a lower threshold than the active Na^+ conductance in the soma and dendrites. The Na^+ conductance in the initial segment has a somewhat higher density than that in the soma. The initial segment repolarizes actively with K and D type K^+conductance only, while the nodes of Ranvier repolarize passively. The fifth (final) node terminates with a sealed end.

I also performed simulations of single, long cylinder to analyze the spatial derivatives of the membrane potential in a simplified geometry as described in section 3.3.4. These models consisted of 101 compartments, each 3 μm in diameter and 10 μm in length (total length of 1010 μm). The passive parameters and active conductances were the same as for the detailed morphological reconstructions, although the conductance densities used were slightly modified. The simplified models contained no axon and were excited to action potential by means of a simulated current injection using the standard ICClamp mechanism provided with the NEURON Simulation Environment [Hines and Carnevale, 1997].

3.2.2 Calculation of Model Extracellular Action Potentials

The EAP is calculated in two stages. First, I computed the transmembrane potential and currents for a pyramidal neuron model using the NEURON simulation environment [Hines and Carnevale, 1997]. Second, I used those currents to compute the extracellular potentials with the Line Source Approximation (LSA) [Holt and Koch, 1999].

It has been previously demonstrated that the neuropil is well modeled by an isotropic volume conductor and that the electric potential in the extracellular space is governed by Laplace's equation [Plonsey, 1969]. For a single point source in an unbounded isotropic volume conductor, the solution is dual to the classical physics problem of point charges in free space (Coulomb's law):

$$V_e = \frac{I}{4\pi d\sigma} \tag{3.3}$$

where I is the amplitude of a point source of current (A), d is the distance from the source to the measurement (m), and σ is the conductivity (S/m) of extracellular space (I assume $\sigma = 0.3$ S/m, or $R_e = 333$ Ωcm.)

For intuition purposes, a simplified (point source) model for the extracellular potential resulting from a multi-compartment model is given by:

$$\begin{aligned} V_e &\approx \frac{1}{4\pi\sigma}\sum_x \frac{I_m(x)}{d(x)} \\ &\approx \frac{1}{4\pi\sigma}\sum_x \frac{1}{d(x)}\{G_{Na^+}(x)[V_m(x) - E_{Na^+}]... \\ &\quad + \sum_n G_{K^+n}(x)[V_m(x) - E_K{}^+] + C\frac{dV_m(x)}{dt}\} \end{aligned} \tag{3.4}$$

as illustrated in Figure 3.1. In practice such an approximation would give inaccurate results if the compartment size were not extremely fine.

The LSA uses a simplified continuous distribution of membrane currents by locating the net current for each neurite on a line down the center of the neurite. The current for each compartment is distributed over the three dimensional line segments (from the morphological reconstruction) that it spans. By assuming a line distribution of current the resulting potential has a straightforward analytic solution [Holt, 1998, Holt and Koch, 1999]. For a single linear current source having length Δs, the resulting potential is given by:

$$\begin{aligned} V_e &= \frac{1}{4\pi\sigma}\int_{-\Delta s}^{0} \frac{I}{\Delta s}\frac{ds}{\sqrt{r^2 + (h-s)^2}} \\ &= \frac{I}{4\pi\sigma\Delta s}\log|\frac{\sqrt{h^2+r^2} - h}{\sqrt{l^2+r^2} - l}| \end{aligned} \tag{3.5}$$

where r is the radial distance from the line, h is the longitudinal distance from the end of the line, and $l = \Delta s + h$ is the distance from the start of the line. [Holt, 1998, Holt and Koch, 1999] analyzed the accuracy of the the LSA and found it to be highly accurate in comparison to a continuous cylindrical distribution, except at very close distances (i.e., $\sim 1\mu m$) to the cable. Because extracellular recording electrodes are typically many μms away from neurons, I can use the LSA to calculate extracellular potentials from a model with high accuracy regardless of the interior compartmentalization of the model neuron.

This approach assumes that the extracellular medium is a homogeneous and isotropic volume

Compartment	Length (μm)	Diameter (μm)	Area (μm^2) S	C	N_m	N_a	Nsegs
Standard	10	2.5	78.5	4.9	1	1	1
Soma	18.8	9.5	560	71	0.14	0.07	1
Axon Initial Segment	3.0	0.67	6.3	0.35	12.46	13.9	5
Apical Trunk @ 25 μm	16.8	3.2	169	8.04	0.46	0.61	3
Apical Trunk @ 100 μm	8.0	2.0	50.5	3.14	1.55	1.56	3
Apical Trunk @ 200 μm	10.7	2.0	67	3.14	1.17	1.56	5

Table 3.1: Comparison of model compartments.

For comparison in Figures 3.4, 3.5, 3.6 and 3.7 membrane currents, I_m, and axial currents, I_a are multiplied by the normalization factors N_m and N_a respectively. Normalization factors are calculated from the ratio of the surface area, S, and cross-sectional area, C, in comparison to the standard compartment size. Nsegs gives the total number of compartments in the same section.

conductor. I am therefore not considering the fact that the CA1 region is, in fact, inhomogeneous [López-Aguado et al., 2001], although the impact of this inhomogeneity is not great, as discussed in section 2.3.6. This approach also does not analyze filtering effects that may be caused by the extracellular medium, as suggested in [Bédard et al., 2006].

3.2.3 Comparison of Model Currents

In order to facilitate comparison of membrane and axial currents in compartments of unequal sizes I present current data for the reconstructed neuron *normalized* to a fixed compartment size of 10 μm length and 2.5 μm diameter. Membrane current is normalized by a factor of $N_m = S_{actual}/S_{standard}$, where S is the membrane surface area of the compartment. Axial currents are normalized according to $N_a = C_{actual}/C_{standard}$ where C indicates the compartment cross sectional area. Table 3.1 lists the compartments used for comparison, their actual size and the normalization factor used in converting their currents to the equivalent "standard" size compartment. Table 3.1 also lists the number of compartments ("Nsegs") in the same unbranched length of neurite as the compartment that is presented for analysis. Because neighboring compartments in the model have nearly identical active conductances they will make virtually identical contributions to the nearby extracellular potentials.

3.2.4 Comparison of EAP Waveforms

To compare intra- and extracellular spike shapes across models, I computed the minimum normalized square root of the mean square error (SMSE) between aligned waveforms. To calculate the SMSE, the waveforms are first interpolated to a regular sampling of 20,000 Hz from the variable step integration used for the simulations [Hines and Carnevale, 2001].

The peak amplitude of the EAP waveform is of particular interest because of its close relationship to the Na^+ conductance density, but the brief duration of the EAP peak means a mismatch at the

peak will make only a small contribution to an unweighted error measure. To remedy this, I weighted the error at the peak amplitude sample by a factor of 10 and the error at the surrounding samples by factors of 5, 2.5, and 1.25 respectively (all other samples received a weight of 1) and then normalized the resulting error. In calculating the error on a 4 ms waveform this method gives roughly 27% of the weight to the 9% of the sample points centered around the peak. For consistency, the same method was applied to the IAP waveforms, although the longer duration of the peak meant that the weighting method was relatively less consequential.

The waveforms were voltage offset and shifted in time in order to determine the minimal SMSE. Samples of a waveform being shifted enter and leave the comparison window while the other waveform stays constant, making the measure asymmetric. To remedy this I calculated the error between two waveforms twice, shifting each in turn, and took the average of the two errors. Finally, the SMSE is normalized by the peak amplitude (of the smaller of the two waveforms) to enable comparison of errors on the IAP and the EAP, and on EAPs with different amplitude.

3.2.5 Measurement of EAP Waveform Features

I measured the features of the EAP waveforms produced by the model as illustrated in Figure 3.2. I focused on 7 measures:

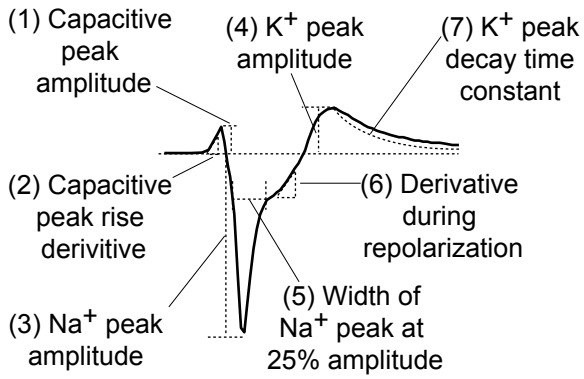

Figure 3.2: Measurements of EAP waveforms.

1. The amplitude of the initial, positive peak associated with the capacitive current (if present).
2. The first derivative of the waveform in the rising phase to the capacitive peak. The derivatives are approximated simply as $\Delta V/\Delta t$ at each (inhomogeneous) time step in the simulation.
3. The amplitude of the large, negative peak due to the Na^+ current.
4. The amplitude of the positive peak following the negative peak from the combined repolarizing K^+ current (if present).

5. The width (duration) of the Na^+ peak measured at 25% of peak amplitude.

6. The first derivative during the repolarization phase of the Na^+peak. The repolarization phase is defined as the portion of the waveform between the (negative) Na^+ peak, including the first 2/3 of the samples until the K^+ peak (or the end of the waveform if there is no K^+ peak).

7. The decay time constant of the K^+ peak. For waveforms with no K^+ peak (no local maxima in the EAP after the negative Na^+ peak), the exponential is fit to the final 1/3 of the samples between the Na^+peak and the end of the window; the negative value resulting from the fit for the exponent indicates that the waveform is increasing during this window.

Because of the decay in the amplitude of the waveform with increasing distance from the neuron, as described in section 3.3.7, I normalize the amplitude of the capacitive and K^+ peaks by that of the Na^+ peak and interpret them as a percentage. The amplitude of the Na^+peak is not used as a feature by itself.

EAPs were calculated on a 50 μm $\times$ 50 μm grid in the plane of the soma and apical trunk at a spacing of 10 μm. I considered only waveforms with peak amplitude greater than 40 μV. The required amplitude for detection and clustering EAPs in CA1 is around 60 μV [Henze et al., 2000] and I have observed a similar threshold in cortical recordings, as discussed in chapter 4. I have chosen the somewhat lower threshold of 40 μV for these tests because the level of background noise in extracellular recordings is dependent on the recording equipment and protocol. My previous results modeling CA1 neurons, described in chapter 2 suggested that lower amplitude waveforms will be more varied in shape. Consequently I felt it best to err on the side of caution by including waveforms that may be detectable with a very low noise configuration. In that way my analysis in section 3.3.7 presents a greater range of variability in waveform shape than may be commonly observed.

3.3 Results

3.3.1 Dependence of EAP Waveform on Active Conductance Distributions

In order to analyze how the EAP waveform depends on the density of active ionic conductances I created a small number of simulations with significantly different active conductance densities but with very similar IAPs at the soma. Forcing the simulations to have (nearly) identical IAPs illustrates the different way in which intracellular and extracellular potentials are generated. Parameters were tuned manually and the results for four simulations are shown in Figure 3.3. For the four simulations, the IAPs are virtually indistinguishable at the soma and remain very similar at a location on the

apical trunk 100 μm from the soma. Only beyond 200 μm from the soma do the differences between the four simulations becomes apparent. Yet the four simulations produce very different EAPs at three measurement locations near the soma and along the apical trunk (table 3.2).

The conductance densities used for the simulations are shown in table 3.3. The main features of the four simulations are as follows: (**A**) The axon initial segment has a significantly larger Na^+conductance density than the soma, in comparison to the simulations **B**-**D**, and repolarization depends primarily on the C type K^+ conductance; (**B**) repolarization depends primarily on the K type K^+ conductance; (**C**) repolarization depends primarily on the A type K^+conductance; (**D**) similar to **B**, except that the conductance density is uniform in the dendrites (whereas in **A**-**C** the density decreases with distance in the dendrites) and the cell is stimulated only in distal compartments (>500 μm from the soma) so that the action potential initiates in the distal apical trunk rather than in the axon.

As described in section 2.3.4, manual tuning of the parameters was guided by three principles: (1) the net Na^+ conductance for the perisomatic region (including the axon initial segment) is tuned to determine the peak amplitude of the IAP and the EAP; (2) K^+conductance densities dominant in the perisomatic region (primarily C and K type) are tuned to determine the shape of the K^+ dominant phase of the EAP waveform; (3) K^+ conductances dominant in the distal sections (primarily A, D and M type) are tuned so the IAP repolarizes at the desired rate. Based on these principles I had little difficulty engineering the four simulations to have nearly identical IAPs at the soma despite the significant differences in the conductance densities.

Details of the model for the simulations of Figure 3.3 are shown in Figures 3.4, 3.5, 3.6 and 3.7. In each simulation the extracellular waveforms at positions near the soma and along the apical trunk around 50 μm and 100 μm from the soma (Figures 3.4(ii), 3.5(ii), 3.6(ii) and 3.7(ii)) are almost exactly rescaled versions of the net currents for the soma and sample apical trunk compartments close to the measurement sites (Figures 3.4(i), 3.5(i), 3.6(i) and 3.7(i), bottom row). As will be discussed further in section 3.3.3, the extracellular potential described by equations 3.3 and 3.4 is dominated by the most proximal parts of the neuron.

The first difference between the EAPs is in positive peak due to capacitive current at the start of the EAP waveform. For **A** the capacitive peak is evident at all positions, while in **B** and **C** the capacitive peak is only visible in the most distal EAP. For **D**, the capacitive peak is clearly observable only at the location closest to the soma. As described in section 2.3.2, capacitive current appears in the EAP when the section proximal to the electrode is strongly depolarized by axial current from another section. For **A**, the axon initial segment has a much higher density of Na^+conductance than the soma while the difference is more modest for **B**, **C** and **D** (12 times and 2-3 times the somatic value respectively, see table 3.3.) Consequently, in **A**, the spike initiates more strongly in the axon and the initial depolarization of the soma results from axial currents originating in the axon: note

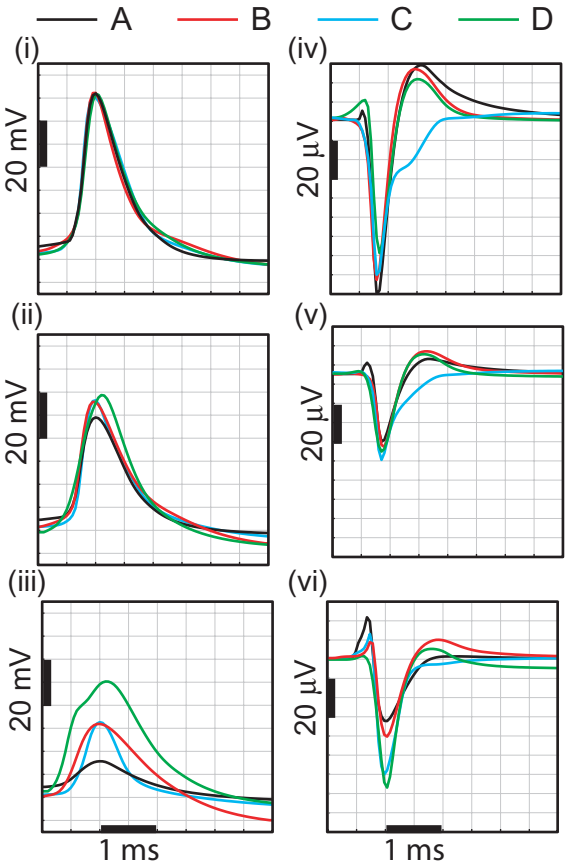

Figure 3.3: Comparison of intra- and extracellular action potentials for four conductance density models.

Left column: IAP at the soma (i), and on the apical trunk at 100 (ii) and 200 μm (iii). The IAPs at the soma are virtually indistinguishable, and the difference does not become significant until the measurement at 200 μm. Right column: EAP measurements near the soma (iv), near the apical trunk 50 μm (v), and near the apical trunk 100 μm from the soma (vi). The EAPs produced by the four simulations are significantly different at all locations. The pairwise error between the simulations are listed in table 3.2.

the large positive peak at the beginning of the inward axial current for the soma in **A** (Figure 3.4(i) 3rd row.) In **B** and **C** the somatic and axonal initiation is more nearly simultaneous and the capacitive current at the soma is masked by simultaneous Na^+ current (Figures 3.4(i), 3.5(i) and 3.6(i), 4th row.)

In **D** (Figure 3.7), the action potential initiates in the distal dendrites and then propagates to the soma, resulting in a capacitive peak that is larger than that of **A** but only in the region of the soma. In this case the soma is initially depolarized by axial current from the apical trunk. The capacitive peaks of **A** and **D** can be further distinguished by whether the rise to the peak is abrupt, as in **A**, or gradual, as in **D**. This is related directly to the abruptness with which the AP begins, as can be seen in the first millisecond of Figure 3.3(i). However, the difference between the EAPs of Figure 3.3(iv)

	Intracellular			Extracellular		
Trials	Soma	Apical Trunk, 100 μm	Apical Trunk, 200 μm	x=0 μm, y=20 μm	x=50 μm y=30μm	x=100 μm, y=40μm
A/B	3.2	7.1	45.8	8.3	7.1	17.7
A/C	2.7	4.7	30.1	17.8	14.1	26.5
A/D	3.2	11.1	53.1	15.6	9.4	25.4
B/C	3.6	4.9	29.8	16.8	17.3	20.7
B/D	2.8	7.1	27.9	10.1	5.5	14.7
C/D	2.8	10.0	57.2	18.1	17.1	16.7
Average	3.1	7.5	40.7	14.5	11.8	20.3

Table 3.2: Measure of between-trial difference.

The error measure is expressed as a percentage, the Normalized Square Root of the Mean Square Error (NSMSE), as described in section 3.2.4. The location of the measurements are the same as those compared in Figure 3.3 and detailed in Figures 3.4, 3.5, 3.6 and 3.7

provides a larger error signal with which to tune a model. These observations show that the presence or absence of a capacitive peak near the soma and its shape are useful measurements for constraining the relative Na^+ conductance densities in the soma, axon and dendrites and for determining the site of AP initiation. One weakness of this approach is that capacitive peaks similar to that of **A** are produced near to the apical trunk following a somatic AP initiation ([Buzsáki and Kandel, 1998] and section 2.3.2), as illustrated in Figure 3.3(vi) (trace **C** and **D**).

A second difference in the measured EAPs is the amplitude of the main negative peak – this is determined by two factors: The first is the density of the Na^+ conductance, which is similar for the the four simulations. A second factor is the density of fast repolarization conductance, particularly the A and K type K^+ conductances, which counteract the peak Na^+ current (see Figs. 3.4(i), 3.5(i), 3.6(i) and 3.7(i), 2nd and 4th rows for the time course of the K^+ conductances and the Na^+ and K^+ components of the membrane current.) Thus, **B**- **D**, which have higher densities of fast K^+ conductances than **A** have somewhat smaller negative peaks in the EAP near the soma. This suggests that using the amplitude of the EAP peak near the soma may not satisfactorily constrain the Na^+ conductance density, without a means to constrain the A and K type K^+ conductances. However, the density of K^+ conductances is further constrained by the shape of the final positive peak of the EAP waveform. For the *in vivo* case, the amplitude of the negative peak is also made ambiguous by uncertainty about the morphology and electrode position as discussed in sections 3.3.7 and 3.3.8.

The shape of the waveform during the repolarization phase is determined by which K^+ conductances dominate in the repolarization close to the electrode (see Figs. 3.4(i), 3.5(i), 3.6(i) and 3.7(i), 2nd row.) In **A** the repolarization is dominated by the C type K^+conductance, which is restricted to the soma and the proximal dendrites. The C conductance is Ca^{2+} dependent and consequently has a slow decay time, leading to the slower decay of the repolarization phase of the proximal EAP

for **A**. In **B** and **D**, the dominant K^+ conductance is the K type with a secondary contribution from the M type. The K type K^+ conductance is uniform throughout the cell, but has high V_m threshold for activation making it most active proximal to the soma where the IAP peak is the highest. The K type K^+conductance deactivates as soon as the IAP is complete, leading to the short duration of the repolarization phase in the EAPs of **B** and **D**. In **C**, the repolarization is dominated by the A type conductance which has a higher density in distal dendrites. Consequently the EAP proximal to the soma shows no significant K^+ dominant phase.

3.3.2 Axial Currents and the Membrane Potential

The differential equation for V_m, equation 3.2, contains both membrane and axial current contributions. If the membrane current contribution due to active conductances can be different but the resulting $V_m(t)$ is the same then the axial current must make up the difference. As illustrated in Figs. 3.4(i), 3.5(i), 3.6(i) and 3.7(i), 3rd row, the axial currents are in fact much larger than the membrane current in all compartments except the soma and axon initial segment.

The soma is mainly a source of current to the apical dendrites throughout simulations **A**, **B** and **C**. The initial positive spike in inward axial current at the soma is due to current flowing from the axon, while at the peak of the somatic AP current is pushed into the basal dendrites (not shown) producing the negative spike in the inward current to the soma (negative according to the sign convention of Figure 3.1). During the depolarization phase of the AP the apical trunk compartments shown are also sourcing axial current to more distal compartments (not shown).

The behavior during repolarization is different for each simulation: in simulations **A** and **B**, the soma and proximal apical trunk have significant repolarizing currents due to proximally activated K^+conductances which leads to the reversal of the axial current in the apical trunk: the soma is contributing to repolarization of the distal dendrites. This is more the case in **B**, Figure 3.5(i) than in **A**, Figure 3.4(i). In **C**, Figure 3.6(i), the net repolarizing current in the perisomatic region is much smaller and distal compartments are self repolarizing through the local A type K^+ conductances. Consequently there is almost no reversal of axial currents, only a slowing of the outward axial current (which is never as large as in **A** and **B**.) Simulation **D**, in which the AP initiates in the distal dendrites, is approximately the reverse of **B**: axial current flows inward from the apical dendrites to the soma and then reverses during the repolarization phase.

As a result of the large axial currents, the IAP in any given compartment is shaped by the pattern of activity over the entire cell. The depolarization at the soma is created from the pooled Na^+ current from the soma, axon and dendrites. K^+ conductances which are active in distal sections like the A and M type can make a significant contribution to repolarization even at the soma. Of course, axial currents merely reflect differences in V_m between different compartments, or taken collectively they can be seen as resulting from the spatial gradients in V_m. However it is viewed,

	Maximal Conductance, $\bar{g}$ (mS/cm^2)			
Conductance	**A**	**B**	**C**	**D**
I_{Na^+} Soma	37.5	36	32.5	20
I_{Na^+} Iseg	450	72	130	20
I_{Na^+} $Dend_{max}$	18.75	23.4	29.25	20
I_{Na^+} $Dend_{min}$	3.75	7.2	22.75	20
I_{K^+AProx}	5	1	50	0.5
I_{K^+ADist}*	10	1	50	0.5
I_{K^+ADist} Basal*	20	2	250	0.5
I_{K^+ADist} Oblique*	20	2	300	0.5
I_{K^+ADist} Tuft*	30	2	400	0.5
I_{K^+C} Soma	25	0.5	5	0.5
I_{K^+C} Dend	18.75	0.25	3.75	0.25
I_{K^+D}	15	2.5	2	2.5
I_{K^+K}	20	40	2	40
I_{K^+M}	1	4.5	1	4.5

Table 3.3: Maximal conductance densities ($\bar{g}$) for the four simulations.

All numbers are in units of mS/cm^2. * indicates $\bar{g}$ 100 μm from the soma; distal sections have densities that are several times greater as described in section 2.2.3.2.

the dependence of the IAP on the overall pattern of activation seems to gives it additional degrees of freedom in comparison to the EAP.

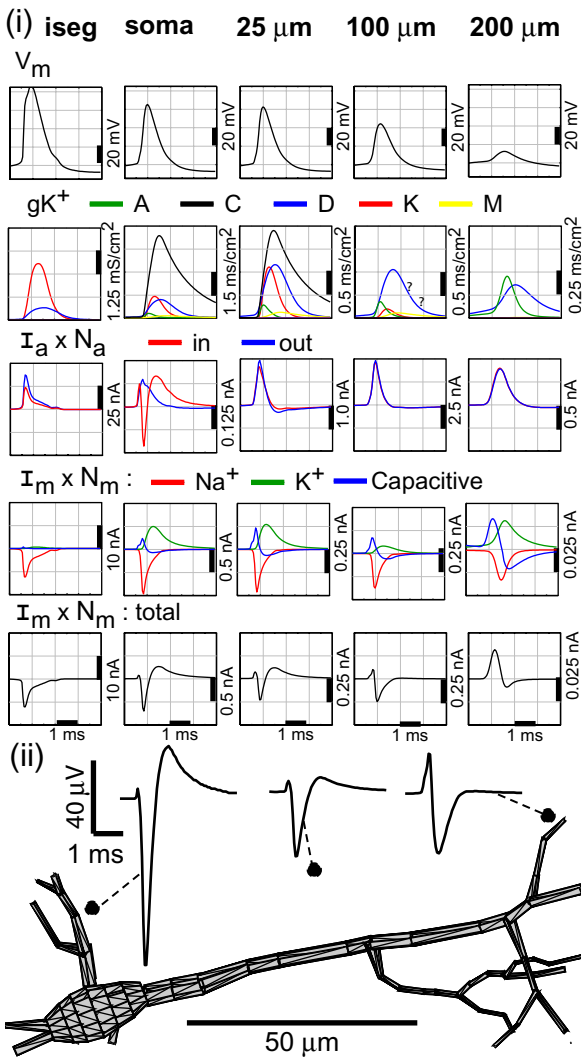

Figure 3.4: Details of simulation **A**.

(i) Intracellular details. Each column shows data from a single compartment: Axon Initial Segment (iseg), Soma, and apical trunk compartments 25, 100 and 200 μm distance from the soma. *First row:* Membrane potential. *Second row:* Time course of the conductance density for the various types of K^+ conductances. *Third row:* Normalized axial currents flowing into (i.e., from the direction of the basal dendrites and axon) and out of (i.e., towards the distal apical dendrites) each compartment. See section 3.2.3 for details of normalization procedure. All compartments obey $I_m = I_{in} - I_{out}$. The notation agrees with that of Figure 3.1, although note that the soma has multiple compartments to the left: the axon and all basal dendrites (not shown). *Fourth Row:* Breakdown of the membrane current into Na^+, K^+ and capacitive components. The membrane current is normalized for compartment size, as described in section 3.2.3. *Fifth Row:* Normalized total membrane current. **(ii)** Extracellular potentials at the indicated positions, the same positions compared in Figure 3.3 and table 3.2. **A** has a high density of Na^+ conductance in the axon initial segment in comparison to **B** and **C**, and the C type K^+ conductance is dominant in the repolarization. As a result, a large positive capacitive peak is visible in the EAP near the soma, before the negative Na^+ peak. This is due to the soma being driven by axial current from the axon before the somatic Na^+ conductance fully activates. The K^+ dominant positive phase at the end of the EAP has a relatively slow decay due to the slow inactivation of the C current.

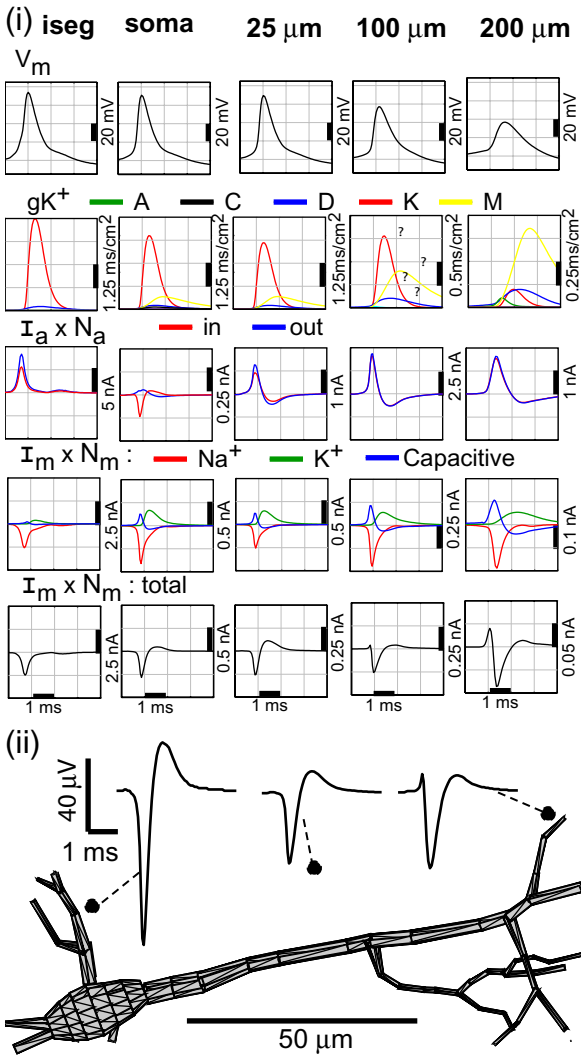

Figure 3.5: Details of simulation **B**.

For general description see Figure 3.4. The simulation has similar Na^+ conductance densities in the axon and soma and the repolarization is dominated by K type K^+conductance. As a result, the positive capacitive dominant peak in the EAP manifests only near the distal apical dendrite which is driven by axial current from the soma and axon. The K^+ dominant peak of the EAP decays quickly because the K type K^+ conductance deactivates as soon as the membrane potential repolarizes. Due to the strong repolarizing current produced by the K conductance the axial current shows a reversal as the soma and apical trunk contribute to the repolarization of more distal dendrites.

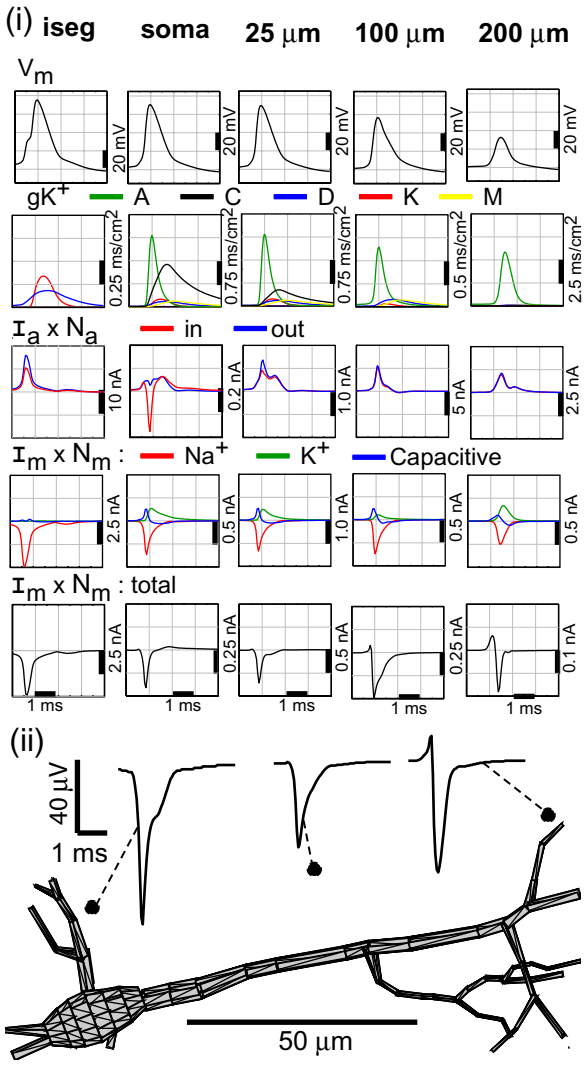

Figure 3.6: Details of simulation **C**.

For general description see Figure 3.4. The simulation has similar Na^+conductance densities in the axon and soma and the repolarization is dominated by A type K^+ conductance which is most dense in the distal dendrites. As a result, much of the repolarizing current is provided by the distal dendrites and the EAP shows virtually no K^+ dominant phase. The inactivation of the A conductance occurs when the Na^+ conductance is still active, creating an inflection point in the repolarization of the EAP.

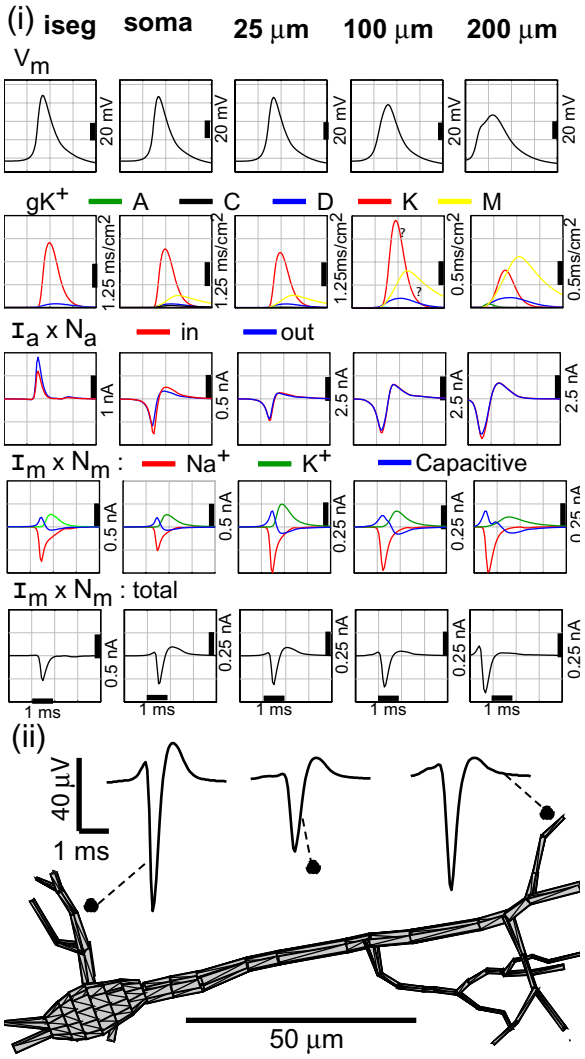

Figure 3.7: Details of simulation **D**.

For general description see Figure 3.4. The Na^+ conductance density is uniform throughout the soma and dendrites and the simulated synaptic input is concentrated in the distal dendrites. Consequently the action potential initiates in the distal apical dendrites and then propagates to the soma. The resulting axial currents in the apical trunk are the inverse of simulation **B**, with the distal dendrites first sourcing current to and then sinking current from the perisomatic region. As a result the capacitive dominant peak of the EAP is most visible near the soma and basal dendrites. The K^+ conductances are similar to those of **B** leading to a fast decay of the K^+ dominant phase of the EAP.

3.3.3 V_m Compared to V_e as a Model Constraint

Inspection of equations 3.2 and 3.4 suggests that both $V_m$and V_e introduce possible confounding factors if they are used to estimate the active conductance densities in a model. The membrane potential, V_m, is made ambiguous by the contribution of both the local membrane current and axial currents from other compartments. As described in section 3.3.2, the axial currents are large relative to the membrane currents and reflect the *overall* pattern of activation in the neuron. Consequently different overall distributions of active membrane currents can lead to very similar V_m waveforms in any given compartment.

The extracellular potential, V_e, is made ambiguous by the summation of membrane current contributions from multiple compartments at different (possibly unknown) distances. However, in realistic neuron models the active conductance densities in neighboring compartments and the resulting total membrane current, $I_m(x)$, is quite similar for neighboring compartments. Furthermore, the distance dependence for contributions to the extracellular potential is such that compartments that are more than a few tens of microns from the measurement site make little contribution. Therefore, for the purposes of intuition the extracellular potential equation may be approximated as

$$V_e \approx \frac{a \ \langle I_m \rangle_{proximal}}{4\pi\sigma(\langle d \rangle_{proximal})^b} \tag{3.6}$$

where $\langle ... \rangle_{proximal}$ indicates averaging over the most proximal compartments to the recording site. The scaling constant a accounts for the number and size of neighboring compartments. The constant exponent for the distance term in the denominator, $1 < b < 3$, accounts for the fact that in reality the net membrane current for the whole cell is zero and decay will be somewhat faster than inversely proportional to distance, as discussed in detail in section 3.3.7. [2]

Equation 3.6 says that V_e at a given location will be in direction proportion to the typical I_m in the most proximal portion of the cell. This makes it depend very directly on the conductance density parameters that I am interested in estimating. Given this constraint on the conductance densities proximal to the electrode, the conditions of biological plausibility and facts provided by studies performed *in vitro* extend the usefulness of the constraint to the entire neuron. For example, conductance densities are expected to vary smoothly with location on the neuron and the density of the A type K^+ current should be much greater in the distal dendrites than the soma [Hoffman et al., 1997]. The examples **A**-**D** all obey these and other similar conditions.

In contrast, I have seen that V_m measured in a single compartment (typically the soma) is not even a good constraint for the conductance densities in that portion of the cell because it depends so strongly on the overall pattern of activity in the neuron. Consequently a model tuned to match a single V_m measurement effectively has additional degrees of freedom in comparison to a model

[2] The constant a must have units of $\mathrm{m}^{(1-b)}$ to render equation 3.6 dimensionally consistent.

tuned to match V_e. This is true even when using conditions of biological plausibility and facts from *in vitro* studies as additional constraints.

My examples suggest that this is true despite the fact that I_m is in fact a function of V_m. In the case of the Na^+ current channel inactivation makes the Na^+ conductance relatively decoupled to the details of V_m: as long as a reasonable size action potential occurs the Na^+ conductance will open and then close over the same time course. Variation in the V_m peak will only change the driving force for a brief period. This is also true of the A current which inactivates on a time scale similar to the Na^+ conductance. The other K^+ conductances (C, D, K and M type), on the other hand, do not inactivate and they are extremely sensitive to the precise peak amplitude and duration of the action potential. However, the ways in which they vary are similar, so that for any typical AP they can still be distinguished. For example, a higher V_m peak will increase both the C type and K type K^+ conductance and which is dominant may still be judged by the decay time of the K^+ peak in the EAP, as described in section 3.3.1.

3.3.4 The relationship between V_m and V_e

By combining eqs. 3.1 and 3.2 with eq. 3.4 I can actually write the point source approximation for the extracellular potential as a function of the axial currents instead of the membrane currents:

$$V_e = \frac{1}{4\pi\sigma}\sum_x \frac{1}{d(x)}\frac{[V_m(x-1) - 2V_m(x) + V_m(x+1)]}{R_a}$$

Recalling the simplest central difference approximation for the second derivative (accurate to within $O(h^2)$),

$$f''(x) = (1/h^2)[f(x-h) - 2f(x) + f(x+h)]$$

I can write the equation for V_e in terms of the second derivative of V_m:

$$V_e = \frac{l^2}{4\pi\sigma R_a}\sum_x \frac{V_m''(x)}{d(x)} \tag{3.7}$$

where l is the compartment length, assumed to be uniform as is the intracompartment resistance, R_a. This shows that the extracellular potential at any location is proportional to a weighted sum of the second derivatives of the membrane potential with respect to position.

The proportionality of V_e to the $V_m''(x)$ is more concise than describing V_e in terms of active membrane currents, but the connection to the active conductance densities is obscured. This relationship is exact for all types of membrane currents, in contrast to the approximation that V_e is proportional to the first time derivative of the membrane potential, $V_m'(t)$, as it would be for a

passive membrane. The relationship between the extracellular potential and the second derivative of the membrane potential has been previously noted in the literature although its implications for model tuning have not been analyzed; see, e.g., [Malmivuo and Plonsey, 1995] where a continuous formulation is derived.

The second derivative of any function highlights regions of rapid change and for this reason forms the basis of many edge detection algorithms in image processing; see, e.g., [Forsyth and Ponce, 2003]. At the presence of an "edge," or as an action potential moves past a particular location, the second derivative goes positive, returns to zero and then goes negative: the center of the edge coincides with the zero crossing of the second derivative.

In Figures 3.8, 3.9 and 3.10 I illustrate the membrane potential and its derivatives as a function of position in simulations of long, single cylinders with parameters tuned to be similar to those of simulations **B**, **C** and **D** of section 3.3.1.[3] In the simulation based on **B**, the action potential initiates at the center and propagates fully to both ends of the cylinder, Figure 3.8(ii). In contrast, in the simulation based on **C** the action potential initiates in the center but fails to propagate fully, Figure 3.9(ii). In the simulation based on **D** the action potential initiates at one end of the cylinder and propagates to the other end, Figure 3.10(ii). Despite these very different spatio-temporal patterns of V_m, I show that $V_m(t)$ in a central compartment can be nearly the same: The average NSME for V_m measured at the center of the cylinders is less than 3%. (Figures 3.8, 3.9, 3.10, (i)).

Comparing Figures 3.8, 3.9 and 3.10 I observe that V_e is negative when a local peak in $V_m(x)$ occurs near the recording location (i.e., the second derivative test for a local maximum). This corresponds to the activation of the Na^+conductance. A positive V_e occurs in when there is a local minimum in $V_m(x)$. This would be the case when an AP initiates in the center of the neuron (the soma) and spreads outward followed by the center leading in the repolarization, corresponding to the activation of the repolarizing K^+ conductances.

Alternatively, if the AP initiates far from the location of the V_e measurement and then passes the measurement location the situation is analogous to edge detection in image processing: as the slope increases second derivatives become positive, corresponding to a positive capacitive phase of the EAP. The mid point of the rising slope in $V_m(x)$ corresponds to a zero crossing of the second derivative and the beginning of the negative, Na^+ dominant phase of the EAP (a local maximum in $V_m(x)$). As the EAP passes the measurement location the falling slope of $V_m(x)$ will produce a second zero crossing and positive second derivatives corresponding to activation of the K^+ conductances near the recording site.

As V_e depends on the second spatial derivatives of V_m it is much more sensitive to the overall pattern of activation than V_m itself, even when measured only at a single point. Consequently the

[3]The result of simulation **A** relies on an additional axonal cylinder and so it is less suitable for this simplified experiment. The conclusions derived from the **D** type cylinder are also applicable to the **A** scenario.

resulting V_e waveforms have features which clearly distinguish the different processes at work in each simulation. Figures 3.8(v), 3.9(v) and 3.10(v), showing $\frac{1}{d(x)}\frac{d^2V_m}{dx^2}$, clearly illustrate the extent to which V_e is dominated by contributions from the most proximal regions of the cell. Nevertheless, the weighted average of second derivatives measured from the central sections of the cylinder are informative about the overall pattern of activation. In this light I view V_e as a local measure that reflects the global pattern of activation. While considering the spatial gradients of V_m do not allow direct conclusions about the active conductance densities, this approach provides a more rigorous basis for understanding why such conclusions are possible.

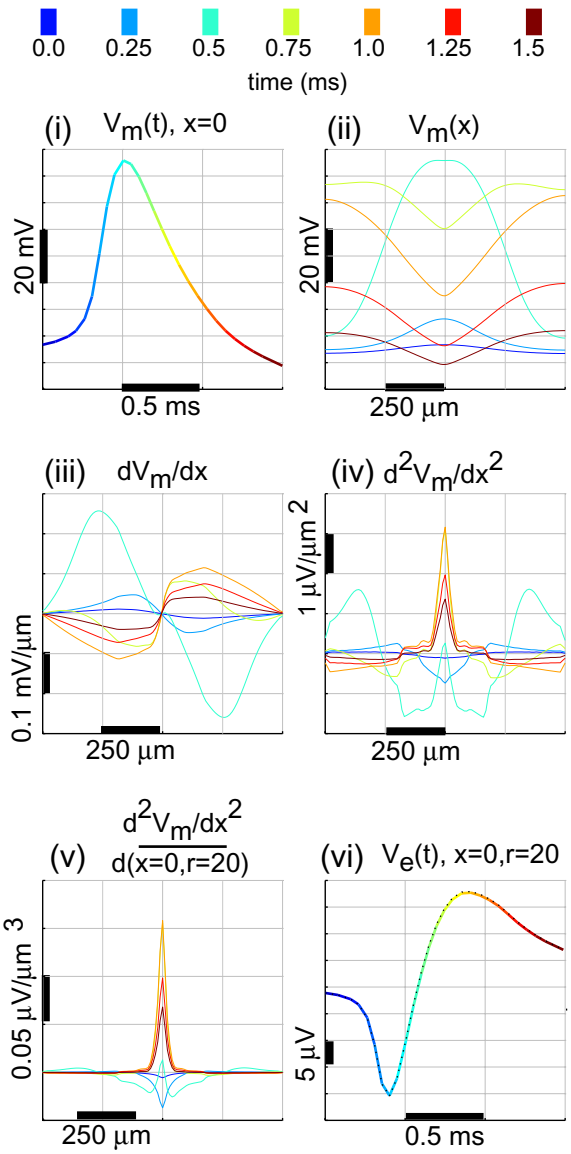

Figure 3.8: V_m, spatial derivatives of V_m, and V_e for a cylinder model based on simulation **B**

(i) $V_m(t)$ at the center of the cylinder; (ii) $V_m(x)$ at different times during the simulation, according to the color coded time scale: The action potential initiates in the center of the cylinder and then spreads at nearly full strength to both ends. Note that the x-axis scaling is shown in terms of distance, not in terms of the compartment index ; (iii) dV_m/dx : Note that the center of the cylinder is defined as $x = 0$ leading to the opposite sign for the first derivative on either side of the center; (iv) d^2V_m/dx^2; (v) d^2V_m/dx^2 scaled by distance, as in eq. 3.7, for a location aligned with the center of the cylinder ($x = 0$) at a radial distance of 20 μm ($r = 20$ μm). After d^2V_m/dx^2 is scaled by the distance to a location V_e at any given time is the sum (or integral, in the continuous case) of d^2V_m/dx^2 multiplied by a constant factor. While the AP is rising the second derivatives at the center is negative corresponding to the local maximum in $V_m(x)$. This leads to a negative V_e, corresponding to the Na^+ dominant phase of the EAP. After the AP spreads the center is the minimum and the second derivative becomes positive. This leads to a positive V_e, corresponding to the K^+ dominant phase of the EAP. (vi) $V_e$calculated with the approximate eq. 3.7 (color) and the LSA (dotted line). For this simplified geometry, the two are indistinguishable.

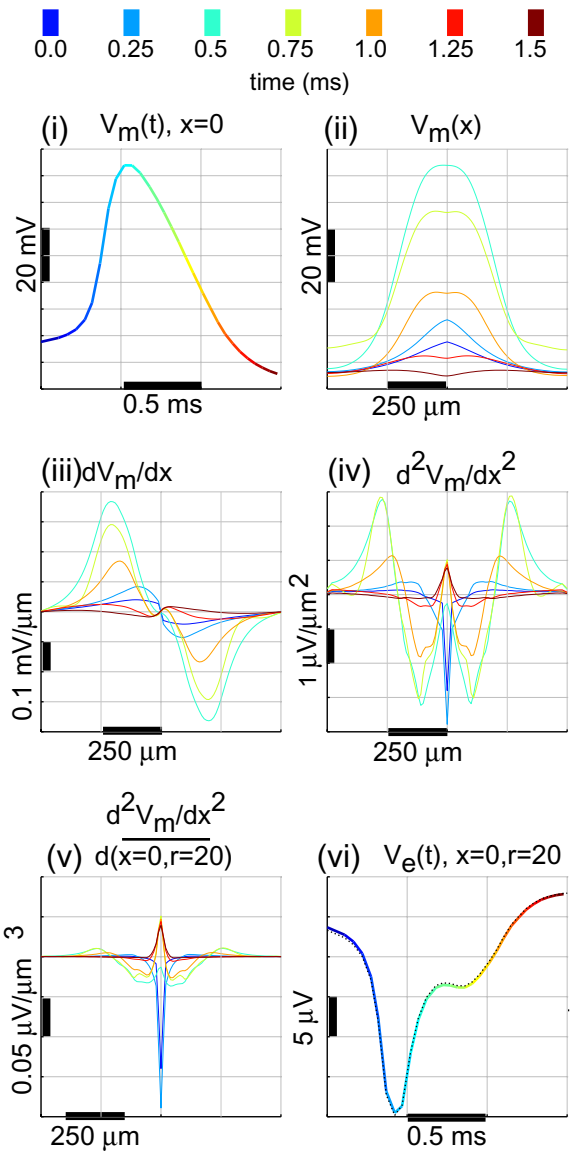

Figure 3.9: V_m, spatial derivatives of V_m, and V_e for a cylinder model based on simulation **C**

For a general description, see Figure 3.8. After initiating at the center of the cylinder the action potential fails to propagate to the far ends of the cylinder. The second derivatives are most negative during the early rise of the AP and becomes less negative as the AP spreads, to the extent that it does, and the amplitude begins to fall. The amplitude at the center is not less than in surrounding cylinder until late in the AP and consequently the second derivative and V_e stay negative for longer than in simulation B. The inflection point, or pause, in the repolarization corresponds to a time when the spatial extent of the AP is narrowing just as the peak declines: the narrowing of spatial extent of the depolarization and flattening of distal voltages tends to eliminate positive contributions to the second derivative, just as the falling amplitude is reducing negative contributions. This coincides to the inactivation of the A type K^+current, after it has blocked the backpropagation of the action potential. At the end of the process the center of the cylinder is finally somewhat hyperpolarized relative to the rest, due to the localized presence of the C current. This makes net positive second derivatives in the center of the cylinder, corresponding to the small amplitude K^+ dominant phase.

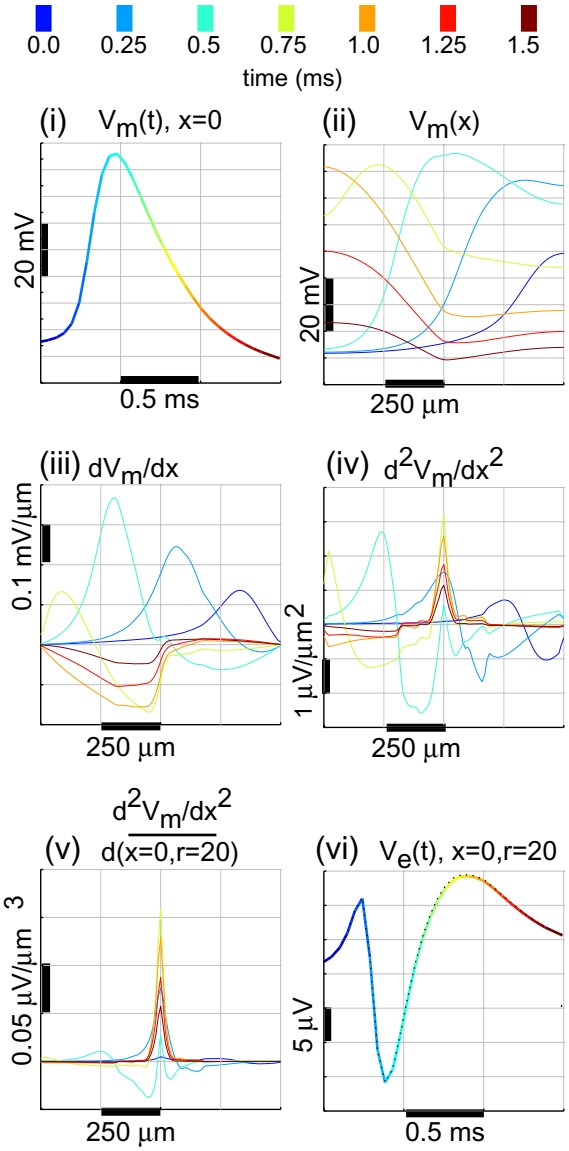

Figure 3.10: V_m, spatial derivatives of V_m, and V_e for a cylinder model based on simulation **D**

For a general description, see Figure 3.8. The action potential initiates at one end of the cylinder and propagates to the far end. When the action potential initiates at the end of the cylinder V_m at the center of the cylinder begins to rise and the second derivative is positive, corresponding to the capacitive phase of V_e. As the rising phase of the AP passes the center of the cylinder the second derivative crosses zero and goes negative, corresponding to the maximum V_m at the center and the Na^+ dominant phase of the EAP. The passage of the repolarizing slope of the AP causes another zero crossing of the second derivative and a return to positive values of V_e, corresponding to the K^+ dominant phase of the EAP.

3.3.5 Impact of Conductance Density Noise

The second derivative is a mathematically ill-conditioned operation. It therefore has the property of amplifying any noise. This raises the question of whether the EAP remains useful for estimating active conductance densities in the case that they are perturbed by noise from constant or continuously varying values. That there is variability in the conductance density is suggested by patch-clamp results, see, e.g., [Hoffman et al., 1997], but it is difficult to say how variability at the level of a patch translates into variability at the level of a compartment which is much larger. I assessed the impact of noise in the conductance densities by repeating the simulations of sections 3.3.1 and 3.3.4 with the $\bar{g}$ value for every conductance a random variable in every compartment except the soma. Somatic conductances were left fixed: the assumption of the model is that the soma provides the "true" base value for conductances in the rest of the neuron which follow noisy rules to determine the local densities.

The $\bar{g}$ value for each conductance in each compartment was chosen separately from a uniform distribution having a minimum of 50% and a maximum of 150% of the value used for the fixed conductance simulation. That is, $\bar{g} = \hat{g} + \hat{g} \times U(-0.5, 0.5)$, where $\hat{g}$ is the values for $\bar{g}$ determined by the rules described in section 2.2.3.2, and the parameters in table 3.3, and $U(a, b)$ describes a uniform random variable with minimum a and maximum b. This gives each conductance density variable a standard deviation of approximately $0.3\hat{g}$. Note that the kurtosis for a uniform random variable is $-6/5$, indicating that the variance is due to frequent modest size deviations from the mean rather than infrequent large deviations (the kurtosis of a Gaussian is 0).

Figure 3.11 shows the results for 10 trials each of simulations based on the parameter sets **A**, **B**, **C** and **D** of section 3.3.1. The experiments show that the overall shape of the waveform is consistent despite noise in the conductance densities. The greatest impact is in changes to the peak negative amplitude which results from the changes to the Na^+ density in the thick, proximal dendrites and the axon.

Figure 3.12 presents details of a single trial of the long cylinder simulation of Figure 3.8, section 3.3.4 with noise in the $\bar{g}$ values. Noise in the conductance densities does in fact lead to significant noise in dV_m/dx and d^2V_m/dx^2. This suggests that the smoothly varying values for d^2V_m/dx^2 (and the membrane current) in the simulations of Figures 3.8, 3.9 and 3.10 is due to the imposition of constant or continuously varying conductance densities. Nevertheless, because the noise in the conductance densities is uncorrelated from compartment to compartment, it tends to cancel out and results in only minor changes to the EAP measured at the center of the cylinder. Results for simulations of cylinders based on parameter sets **C** and **D** with noise in the conductance densities were similar.

These results suggest that the EAP is a reliable indicator of the average distribution of conductance densities even if there is considerable variability from compartment to compartment. The

biggest difficulty is in estimating the Na^+ conductance density for the perisomatic region from the peak negative amplitude, a measurement I have already noted as ambiguous due to the presence of various fast K^+ currents which may counteract the peak Na^+ current. As will be discussed below, this measurement is made more ambiguous if the location of the electrode and the morphology of the neuron are unknown as in the case of modeling from *in vivo* EAP recordings.

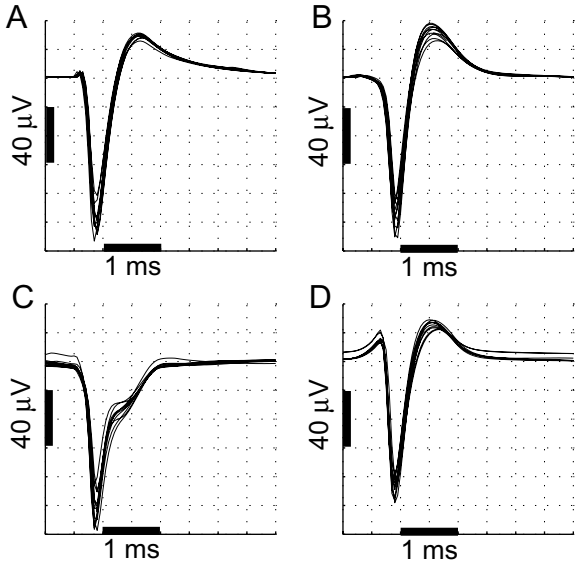

Figure 3.11: Ten examples of EAPs at a location near the soma

For simulations **A**, **B**, **C** and **D** where the $\bar{g}$ values for each conductance in each compartment except the soma is drawn from a random distribution with mean equal to the value for the original simulation. The waveform shapes remain very similar, although the amplitude of negative peak shows somewhat more variability than the overall waveform. The average peak weighted NSMSE values in comparison to the original simulation are: **A**: 5.2% , **B**: 3.4%, **C**: 5.5%, and **D**: 6.2%.

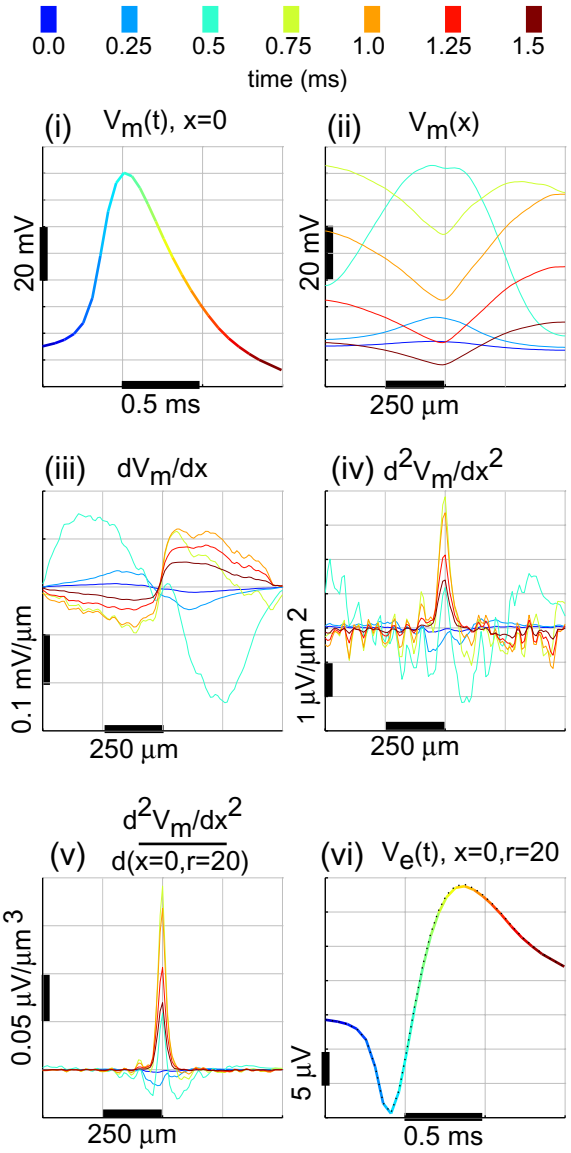

Figure 3.12: V_m, spatial derivatives of V_m, and V_e for a cylinder model with noise in $\bar{g}$

The simulation is based on that of figure 3.8, but with $\bar{g}$ in every compartment a uniform random variable ranging from 50% to 150% of the value used in the simulation of figure 3.8. For a general description, see Figure 3.8. The action potential no longer propagates uniformly to both ends of the cylinder. Both dV_m/dx and d^2V_m/dx^2 are no longer smooth functions, but rather show significant local variability. Nevertheless, because the variability at different locations is uncorrelated the summation over $(1/d(x))d^2V_m/dx^2$ still yields an EAP waveform that is very similar to that for the simulation of Figure 3.8.

3.3.6 Constraining Distal Conductances

I found that it was straightforward to create multiple simulations with different active conductance densities but similar somatic IAPs. At the same time, I found that it was much more difficult to create simulations with different conductance densities but similar EAPs. An example of this is shown in Figure 3.13. The first of these two simulations is **B**; the second is identical except that it has a maximal M type K^+ conductance density of 20 mS/cm^2, rather than 4.5 mS/cm^2 (see table 3.3.) In this case the IAP at the soma is altered by the conductance density change much more so than the EAP: the error between the two IAP traces is 9.8%, while the error between the two EAP traces is 5.0%. The errors at the distal locations considered in Figure 3.3 are similar for both EAP and IAP.

The reason for this result is that the M type K^+ conductance has a much lower threshold of activation than the K type; for review see [Borg-Graham, 1999] and see section 2.2.3.2 for details of the formulation used. Consequently the M type K^+ conductance makes the largest contribution to repolarization in the distal dendrites where the IAP amplitude is small and the K type K^+ conductance is not strongly activated. (For example, see Figure 3.5(i), second row, last column.) The result is that the proximal K^+currents are only slightly altered by the increase in M type K^+conductance and there is little change in the EAP near the soma or apical trunk. However, the net affect of the M type conductance in the distal dendrites leads to a much larger AHP.

This example illustrates the fact that for some differences in distal conductance densities the IAP can be a better measure of error than the EAP. However, in experiments where I made similar alterations to the distal A type K^+ and the distal Na^+ conductance densities there were still larger changes in the EAP than in the IAP. This suggests that for biologically plausible conductance density distributions this example may be the exception rather than the rule. This leads me to conclude that in general the EAP is probably a better model constraint than the IAP even for distal conductance densities. Changes in conductance densities in the soma and proximal dendrites always led to larger changes in the EAP than in the IAP.

3.3.7 Dependence of EAP Waveform on Electrode Position

A serious potential liability of using V_e to tune a compartmental model is the dependence of the EAP on the precise electrode position, which was held constant in Figure 3.3 and table 3.2. One affect of position is that the amplitude of V_e declines with distance from the sources. In fact, the linear decrease in amplitude with distance in eq. 3.3 underestimates the true impact: because the net membrane current summed over the entire neuron is always zero, an amplitude estimate derived from the isolated point source will overestimate the true amplitude from the closed-source loop [De Nó, 1947]. The presence of equal and opposite positive and negative sources make a neuron

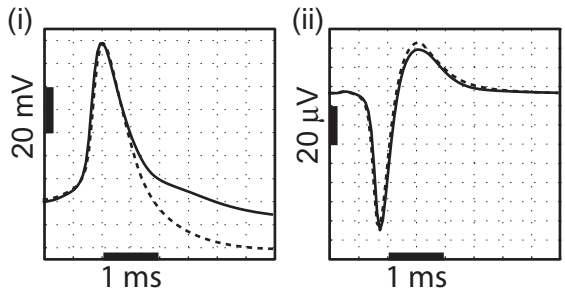

Figure 3.13: Two models with different M type K^+ conductance densities.

The first simulation (solid line) is Simulation **B**, Figure 3.5. The second simulation (dashed line) is identical, except that the maximal M type K^+ conductance density ($\bar{g}$) is 20 mS/cm^2, instead of 4.5 mS/cm^2. **(i)** IAP at the soma. **(ii)** EAP measurements near the soma. The difference between the two conductance densities is more clearly observable in the IAP.

similar to a dipole [Jackson, 1962] or more accurately a tripole, also known as a linear quadrupole [Schwarz, 1973]: in the depolarizing phase of the action potential the basal and apical dendrites form two positive poles and the soma is a negative pole of equal amplitude to the two positive poles combined. During repolarization, the polarity is reversed. At distances much large than the separation between the poles the amplitude of the voltage declines with distance squared for the dipole and with distance cubed for the tripole. These observation explain the bounds on the exponent, $1 < b < 3$, for the distance term in the denominator of eq. 3.6.

However, neuronal measurements are typically made at distances of the same order of magnitude as the distance between the poles. I analyzed the decay of amplitude with distance from the cell body for a variety of cell morphologies and parameter sets. In these experiments I varied the position of the measurement in a direction perpendicular to the apical trunk so as to minimize the effect of proximity to any basal or oblique dendrites. The results, illustrated in Figure 3.14, show that the decay in amplitude is close to distance to a power of -1.2 at ranges of less than 50 μm from the cell. A somewhat better fit is with an exponential decay having a length constant close to 20 μm. At these distances and moving perpendicular to the apical trunk the waveform stays reasonably consistent in shape, although it does tend to widen as previously observed in section 2.3.5.

I also considered the variability in waveform shape that occurs with proximity to the basal and apical dendrites. I have already observed the increase in capacitive phase peak along the apical trunk in section 2.3.2 and 3.3.1. The variability of waveform shape over a wide range of positions is analyzed in Figure 3.15. This analysis compares measurements of the EAP shape that normalize for amplitude, as described in section 3.2.5, for the four simulations of cell D151.

Figure 3.15(i) shows that while the large capacitive peak amplitudes in simulations **A** and **B** vary with position around the neuron, it is still a consistent distinguishing feature in comparison to **B** and **C**. Although the distribution of amplitudes overlap the amplitude for **D** is consistently greater than

the amplitude for **A**. I also looked at the maximum first derivative of the waveform during the rise phase to see if the difference between the rise times to the capacitive peak is a consistent feature. Figure 3.15(ii) shows that **A** displays faster rise times to the capacitive peak than **D**, but the distributions are significantly overlapping and the means are similar. Still, when the two measures of the capacitive current peak are combined it seems that the difference between the rise time and peak amplitude of the capacitive peaks in simulations **A** and **D** is a consistent feature of the EAPs.

Figure 3.15(iii) compares the amplitude of the K^+ current peak in the EAPs. It demonstrates that the lack of a well-defined K^+ peak for **C** distinguishes it at all locations. However, the wide range of K^+ peak amplitudes for **A** suggests that this is not a particularly useful criteria for distinguishing **A** and **B**. The reason for the wide variation in the amplitude of the K^+ peak for **A** is that the C type K^+ conductance which dominates the repolarization is entirely concentrated at the soma. Thus an electrode near the soma will see a high amplitude K^+ peak while an electrode closer to the dendrites will see a much smaller K^+ peak. More useful is the time constant of the decay from the K^+ peak, illustrated in Figure 3.15(iv); in this measure the simulations **A** and **B** are completely non-overlapping and **C** is also easily distinguishable: **A** has the slowest time constant of decay owing to the slow decay of the C type K^+ conductance, **B** has a faster decay resulting from the rapid de-activation of the K type K^+ conductance. Simulation **C** on the other hand typically has a "negative" time constant for the decay, indicating that the membrane potential is increasing in this period.

Another feature distinguishing **C** is the width of the Na^+ peak. As illustrated in Figure 3.15(v) the width of the Na^+ peak for **C** is consistently different from **C** and **D**, although slightly overlapping with **A**. The distribution of widths for simulations **A**, **B** and **D** seem to overlap too much for this to be a useful feature to distinguish them at an arbitrary location. Another useful measure for distinguishing **C** is the minimum first derivative during the repolarization phase, Figure 3.15(vi). A low value for this measure indicates the presence of an inflection point in the repolarization of the EAP.

These results demonstrate that the main features distinguishing EAP waveforms are reasonably consistent throughout the region around a neuron where the amplitude is great enough to record with an extracellular electrode. Although any one feature does vary with position, taken in combination these features form consistent signatures that distinguish waveforms produced by different active conductance densities and different sequences of AP initiation.

3.3.8 Dependence of EAP Waveform on Cell Morphology

Another potentially confounding factor in using EAP recordings to tune a compartmental model under an *in vivo* protocol is uncertainty regarding the morphology of the cell being recorded from. I performed simulations using the parameters of table 3.3 on 16 additional reconstructed morphologies

from [Henze et al., 2000]. The results are illustrated in Figure 3.16. The difference in cellular morphology has a very strong impact on the amplitude of the measured waveform: the difference between the smallest amplitude and largest amplitudes is around a factor of three for each parameter set. However, for the same membrane conductance densities and initiation conditions the shape of the waveform stays consistent. I previously demonstrated in section 2.3.7 that even using the morphology of a non-pyramidal cell leads to the same result: a change in the EAP amplitude but little change in the EAP waveform shape. In my experiments on cortical neurons (chapters 4 and 5) I have found the same rule holds for the wider range of neuronal morphologies found in cortex: morphology primarily influences EAP amplitude, while the balance of active conductances and pattern of AP initiation determines EAP shape.

The impact of neuron size on EAP amplitude is more precisely illustrated in Figure 3.17 which plots peak amplitude as a function of cell size for the 17 cells and 4 parameter sets. The largest cells in the set is around around twice the size of the smallest: The total length of the dendrites range from 7000 μm to 13,000 μm (average 10,200 μm), and the total surface areas for the soma and dendrites combined ranges from 15,000 μm^2 to 28,000 μm^2 (average 22,000 μm^2). The measure which I found most closely correlated to the amplitude of the EAP waveform was the combined surface area of the soma and proximal apical trunk (out to the first branch point). This is because, with conductance *densities* being equal, the total current scales with surface area. The soma and apical trunk make up the largest amount of surface area that can be within range of a recording electrode: while the finely branched distal dendrites make up much of the surface are of a CA1 pyramidal neuron, they are too dispersed in space to make a significant extracellular potential.

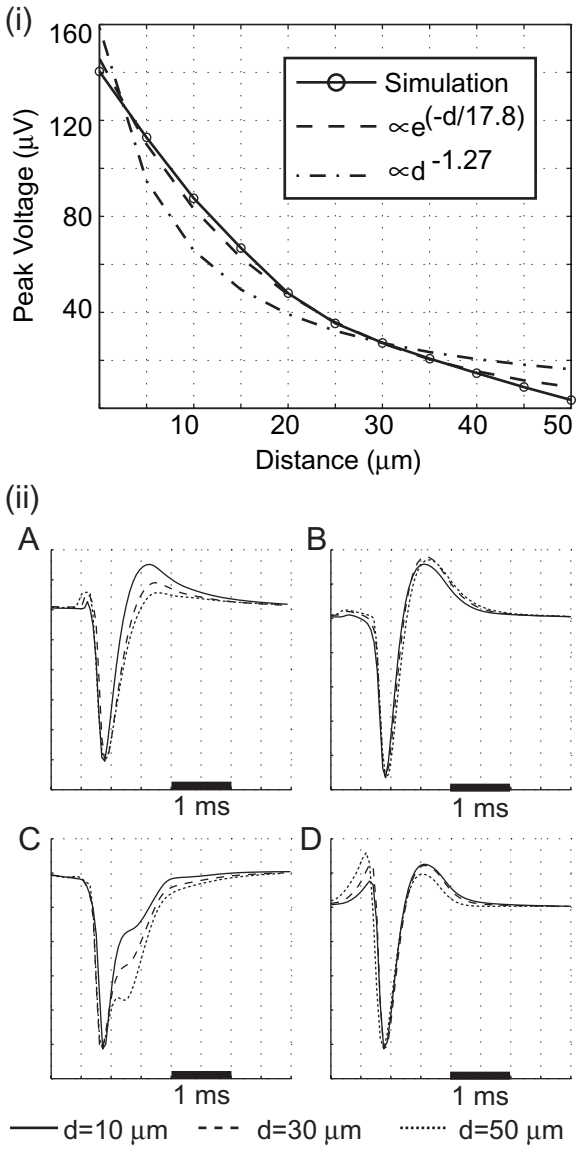

Figure 3.14: Change in EAP amplitude and shape as a function of position.

(i) Amplitude vs. distance in a line of points moving perpendicular to the apical trunk starting at the soma, along with best fits of exponential and power functions (amplitude refers to the amplitude of the negative peak), for cell D151 with parameters **B**; the plot for other cells and parameter sets is similar. For parameter sets A-D and the 17 cell morphologies described in section 3.3.8, the average length constant for the exponential decay fit is 20 μm (std. dev.=3μm), and the average exponent in the power function is -1.2 (std. dev.=0.1). (ii) Comparison of the normalized waveform at positions 10, 30 and 50 μm from the soma, also perpendicular to the apical trunk. The waveform tends to widen with distance, while its shape remains similar.

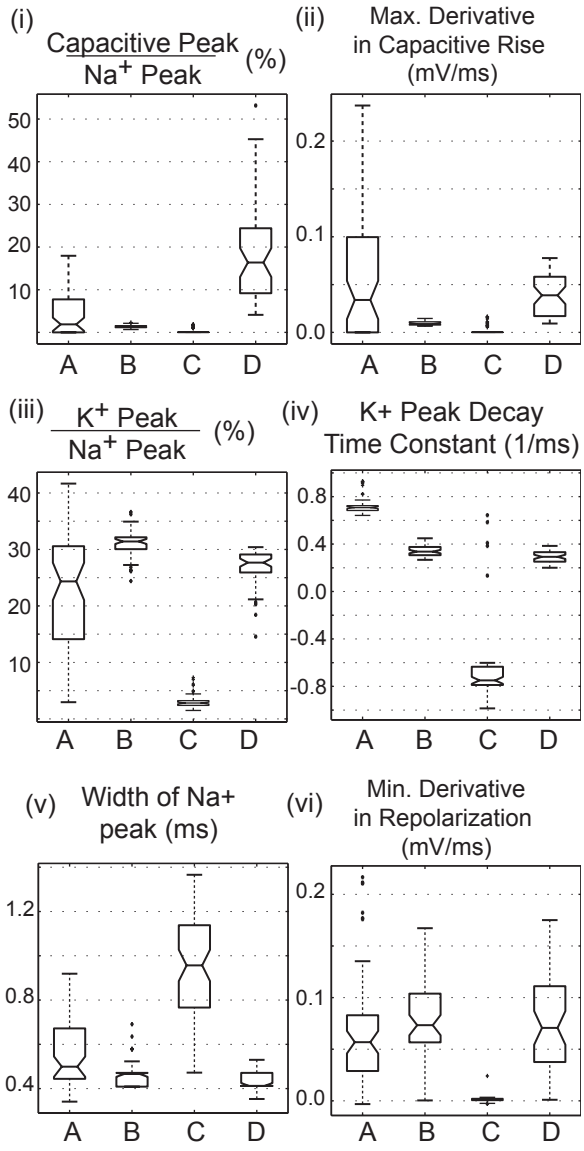

Figure 3.15: Measurement of EAP waveforms.

For description of the measurements see section 3.2.5 and Figure 3.2. Figures show box plots for the measurements of EAPs in a 100 × 100 μm region around the soma spaced on a 10 μm grid. Only EAPs with peak amplitude >40μV were included in the statistics. The boxes have lines at the lower quartile, median, and upper quartile values. The lines extending from each end of the boxes ("whiskers") show the extent of the rest of the data. Outliers are data with values beyond the ends of the whiskers. The notches represent an estimate of the uncertainty about the medians for box-to-box comparison.* **(i)** Ratio of capacitive peak to Na^+peak. **(ii)** Maximum of the first derivative during the rise to the peak of the capacitive current phase. **(iii)** Ratio of K^+peak to Na^+ peak. **(iv)** Decay time constant fit to the K^+ peak. "Negative" decay time constant indicates that there is no K^+ peak and that the waveform is rising during the period of the measurement. **(v)** Width of Na^+ peak at 25% of peak amplitude. **(vi)** Minimum of the derivative during repolarization of the Na^+ dominant phase. *Statistical analysis performed with Matlab^{TM} Statistics Toolbox.

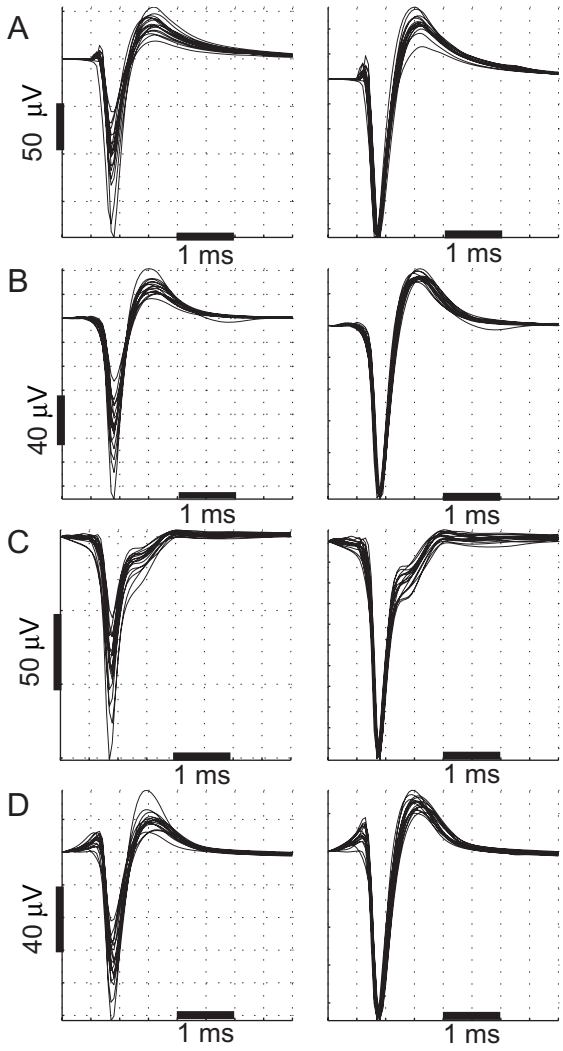

Figure 3.16: Comparison of simulations for varying cell morphology.

Left column: EAP waveforms simulated near the soma for 17 reconstructed CA1 pyramidal neurons using parameter sets A-D. Right column: The same EAP waveforms normalized by the peak amplitude. The difference in cell morphology has a strong impact on the amplitude of the EAP, but the waveform shape is only slightly affected.

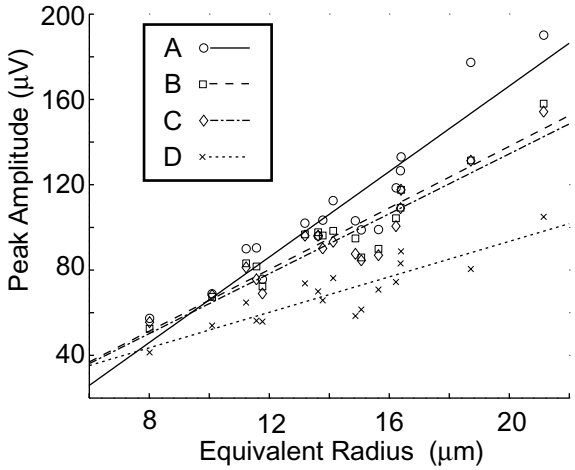

Figure 3.17: Peak amplitude of the negative peak vs. cell size for the 4 parameter sets.

Cell size is plotted as the radius of a sphere with the same surface area as the soma and apical trunk out to the first branch point for each cell. For these cells the combined soma+apical surface area ranges from 300 μm^2 to 2000 μm^2. For the data sets A-D the correlation coefficient between size and amplitude are 0.94, 0.94, 0.93 and 0.88, p<1e-6. Lines fit to each set of points have slopes of 10, 7, 7 and 4 μV/μm for parameters sets A-D respectively.

3.4 Discussion

These results illustrate the fact that single compartment $V_m$measurements underconstrain realistic compartmental models that include non-uniform active conductance densities. Because the EAP waveform is more sensitive to the precise composition of the active ionic conductances, it may provide a suitable means for constraining a compartmental model despite the uncertainty that may arise due to measurement location. An alternative viewpoint of the situation is provided by the relationship between V_e and the second spatial derivative of V_m: the second spatial derivative is sensitive to the overall pattern of activation in the neuron, while the membrane potential waveform in a single compartment is much less so.

That said, it is not true that V_m contains no information about the overall pattern of activation. Close observation of the early rising phase of the AP and the slope during the repolarization phase provide some of the same clues as do measurement of V_e. But standard measurements of V_m, such as the amplitude and duration of the peak and amplitude of the AHP, are insensitive to these subtleties and it is these gross features that dominate an MSE based objective function. This explains the relatively superior performance of objectives functions involving time derivatives of V_m [Hayes et al., 2005]. The advantage of using V_e measurements is that its dependence on $V_m''(x)$ amplifies subtle differences and gives them a more prominent role in a MSE objective function.

The problem with V_m measurements can be mitigated if additional measurements of the IAP are made at multiple, distal locations (i.e., >200 μm from the soma.) These findings agree with those of [Keren et al., 2005], who used genetic algorithms to tune compartmental models. They suggested using multiple membrane potential recordings in the axon and dendrites in order to best constrain the model parameters. [Huys et al., 2006] take this approach to its logical conclusion: if the membrane potential is known for all compartments of a neuron then optimal parameters can be calculated by linear regression without resorting to a search of the parameter space. In practice, however, performing multiple V_m measurements on the same cell is difficult *in vitro* and presently impossible *in vivo*. Voltage imaging technologies also need maturation before the measurements proposed by [Huys et al., 2006] become routine and sufficiently accurate. My results suggest that using extracellular recordings may be an attractive alternative. At the present time, EAP recordings are not routinely made during *in vitro* experiments designed to analyze the properties of active ionic conductances. However, EAP recordings may provide significant additional information in such a context.

In *in vivo* protocols, it is often the case that EAP recordings are the only data available. The results presented in sections 3.3.7 and 3.3.8 demonstrate that variation in morphology and electrode position primarily affect the amplitude of the EAP waveform, but not the EAP waveform shape. This uncertainty over amplitude adds uncertainty due to natural variation in conductance densities

throughout a neuron, as suggested in section 3.3.5. I conclude that a useful approach to constraining a model from *in vivo* data would be to make a model reproduce the features of the EAP waveform *shape(s)* while allowing some freedom in EAP amplitude.

In order to use EAP waveform shapes to tune a model, the individual spikes for each clustered unit must be averaged to produce a low noise average waveform. These can be analyzed and statistics similar to those described in section 3.3.7 can be calculated. Such statistics can be compared to the average measurements from the simulation where the average is taken over both the unknown electrode position and a range of plausible morphologies. Alternatively, the recordings can be normalized and clustered (a second time) to search for prototype shapes in the extracellular recordings. Each prototype shape would suggest a different combination of active conductances or pattern of action potential initiation that may exist side by side in the target neuron population.

At the same time, it can and should be verified that the tuned model reproduces the *range* of EAP amplitudes observed in recordings. In particular, the largest cells in the morphology sample should be able to reproduce the highest amplitude EAP recordings under the assumption of a plausible extracellular resistivity and electrode location. Section 2.3.5 and 3.3.7 demonstrated that the Na^+ dominant phase of an EAP waveform tends to widen as the electrode is moved away from a neuron. But given the high intrinsic variability in waveform width (e.g., Figure 3.15(v)) there is no way of knowing for certain whether a low amplitude EAP recorded *in vivo* comes from a near measurement of a small cell or a distant measurement of a large cell. Therefore, it seems somewhat less useful to check that a model reproduces low amplitude EAP recordings.

These methods will constrain the parameters to plausible ranges, not determine a single "best" value. This is an appropriate approach to *in vivo* modeling: my own experience modeling *in vivo* recordings described in chapter 2 as well as studies of gene expression
[Toledo-Rodriguez et al., 2004] suggest that the active conductance densities for neurons *in vivo* are highly variable. Therefore, any modeling result should be tested over a range of plausible conductance densities to determine the parameter sensitivity. Because of the insensitivity of waveform shape to both position and morphology I believe that this method would give very useful results for any part of the central nervous system, and not only the CA1 region of hippocampus that I have studied here.

When analyzing EAP waveforms recordings should be wideband filtered, 1 Hz - 3 kHz or 5 kHz. While bandpass filtered data must usually be used to detect and cluster spikes, average waveform shapes can be created from the wideband after spike times have been determined. Typical bandpass filter settings used for unit detection and spike sorting (i.e., around 300 Hz to 1 kHz) lead to significant distortion of the waveform shape. Multi-site silicon probes seem preferable to tetrodes as they allow precise knowledge of the relative position of the recording sites. My experiences modeling multi-site silicon probes, described in chapter 2, suggest that this gives a much tighter constraint on

the parameters.

In section 3.3.7 I concentrated on simple and intuitive measurements of the waveform. But more sophisticated means for measuring waveform attributes could be developed; for example, using wavelet decompositions, e.g., [Quiroga et al., 2004]. A related subject that warrants further research is how these types of measurements may change for a single neuron under various conditions such as high firing rate, LTP or influence of neuromodulators. Such knowledge could help to improve clustering algorithms for chronic *in vivo* recordings that must track units over many days and under different conditions.

This study focused on constraining the conductance density of active ionic channels and the conditions of action potential initiation. But the sensitivity of the EAP to changes in the membrane current should also make it suitable for constraining the kinetics of active conductances as well. The contribution of the (positive) capacitive current to the EAP suggests that EAPs may be useful for tuning the membrane capacitance. However, in practice the membrane capacitance is well established [Koch, 1999] and probably does not vary between individual neurons. My results suggest that the EAP may be somewhat less useful in tuning the resting leak conductance. For this purpose, subthreshold measurements of the membrane potential probably remain the most useful technique (e.g. [Spruston and Johnston, 1992].)

In the experiments described in chapter 2, I found that intracellular resistivity, R_i (which determines the individual R_a values based on compartment size), actually had a significant impact on the *amplitude* of the EAP peak. From the point of view of membrane currents, this is because of the role of R_a in determining the input resistance and how much Na^+ current is required to achieve a given peak IAP amplitude. Equation 3.7 demonstrates the importance of R_a for the extracellular potential in terms of the second derivative of the membrane potential. Therefore, simultaneous IAP and EAP measurements at known locations seem to have some value for constraining R_i based on the peak EAP amplitude.

To facilitate further research, I have created a downloadable package of all the NEURON and Matlab code used to perform the experiments described in this study. The code can easily be extended to simulate EAPs from compartmental models of any type of neuron. It is available from the ModelDB on the Internet at *http://senselab.med.yale.edu/senselab/modeldb/*.

Chapter 4

Activity and Sampling Bias in Cortical Recordings

4.1 Introduction

As demonstrated in section 3.3.8 and Figure 3.17, the amplitude of EAPs generated by a neuron are highly dependent on the size of the soma and thick proximal dendrites. This suggests strongly that extracellular recording methods are to some degree biased towards recording from larger neurons. Neurophysiologists making extracellular recordings have been conscious that such a bias must exist for some time (see, e.g.,[Humphrey and Schmidt, 1990]), but there have been few attempts to quantify the magnitude of this bias and its consequences (see, e.g., [Towe and Harding, 1970]).

A related issue is the question of what proportion of cells in any given brain region are responsive to a stimulus during an *in vivo* protocol. In extracellular recordings, neurophysiologists are only studying those units that responded to their stimulus as there is no way to obtain knowledge of those units that did not respond. Finding responsive units that may be reliably recorded for the duration of an experiment tends to be a difficult and time consuming task, leading some neurophysiologists to the conclusion that only a small portion of all neurons are active during a typical protocol. It is suggested in [Shoham et al., 2006] that there is a "dark matter" problem in neuroscience, akin to that found in astronomy: that the lack of active units is so extreme as to call into question neuroscientist's fundamental views of the brain. [Shoham et al., 2006] use estimates for the average detection range to calculate that 90% of neurons, or more, are inactive under a typical protocol. Indeed, blind patch clamp recordings made *in vivo* suggest that arbitrarily selected units are much less responsive than typical units found through extracellular recording[Margrie et al., 2002].

If the proportion of units activated by a stimulus varies between regions of the brain then this may compound (or perhaps ameliorate) bias in recording created by cell size differences. Additionally, an understanding of this question would help to inform theories of neural computation: A recently developed approach is to analyze "sparse" network computations (for review see

[Olshausen and Field, 2004]) which propose that information in the brain is represented by a relatively small number of active neurons.

The model I have developed can be used to directly analyze these questions in a way that has not been possible before now: I can use the model to estimate the range at which neurons of different classes can be detected by considering the spike amplitude predicted by the model and the required amplitude for detection. Combined with measurements of the packing density of neurons I can estimate the number of neurons within range of the electrode in different brain regions. If this estimate is compared to an unbiased measurement of the number of neurons recorded at various points along a path, I can directly calculate the average fraction of neurons that are active. Knowing the detection range and the average proportion of cells that are active in different regions of the brain, I can them determine to what degree recordings may be biased towards these different regions.

For these experiment I focused my efforts on the primary visual cortex of the cat (referred to variously as "V1", "area 17" and "striate cortex"; I will refer to it as "V1"). My choice is dictated by the fact that cat V1 is well studied enough that all the necessary information is available: I have available a large library of reconstructed cortical cells [Binzegger et al., 2004]; sufficient quantitative data on the thickness of the layers and the packing density of neurons [Bealieau and Colonier, 1983]; and collaborators skilled in making the specific type of recording suited to my needs [Girardin et al., 2002].

In neocortex, physiologists typically record from a single area (defined by functional maps of cortical surface), while they typically do not know what layer of cortex their recordings are made from. Further, neurons in the different layers are characterized by markedly different morphological characteristics: spiny neurons in the deeper layers, 5 and 6, are pyramidal with large somas and thick dendrites. Layer 5 contains the largest neuron in all of cortex. Layer 4 contains a majority of spiny stellate cells, while layers 2 and 3 contain smaller pyramidal cells. (for review see, e.g., [Feldman, 1984, Lund, 1984]) For these reasons, the most natural and useful approach for this investigation is to estimate the active proportion of cells in the different layers, and whether there is sampling bias between the different layers.

4.2 Methods

4.2.1 Computational Methods

4.2.1.1 Calculation of Detection Regions and Estimation of Neuronal Activity

The regions in which a simulated neuron would be detected is based on a simulation of a single action potential. After the simulation, EAPs were calculated (as described in section 2.2.1.1) on a 3D spatial grid around the neuron: the grid spacing was 5 μm for L2-4 and smooth interneurons, and 10 μm for pyramidal cells in L5-6 (chosen to reflect the size of the detectable region (as illustrated

in Figure 4.16). I chose an average minimum threshold of 80 μV for detection and clustering, based on my own recording and clustering results (described below), but also analyzed results for higher thresholds.

From the grid of calculated EAPs I used Matlab to generate an isosurface for which the peak EAP amplitude was greater than the minimum threshold. The interior of this region was considered to be the detectable region. The volume of the detection region was determined by dividing volume enclosed by the isosurface into pyramids using custom Matlab scripts (the isosurface routine returned a triangulated surface), and calculating the volume for each pyramid. After the volume of the detection region was computed I describe it by computing the radius of an equivalent sphere having the same volume; although the regions were usually not exactly spherical. Volumes that were typically 1/10,000 or 1/100,000 of a mm^3 are difficult to interpret and an equivalent radius (in μm) provides not only a convenient description but a useful analytic approximation. I refer to the equivalent radius as the detection range, or detection radius.

Because the EAP amplitude depends linearly on the extracellular resistivity (conductivity) it is important to control for this variable. As illustrated in Figure 4.1, the resistivity of cortex is highly variable but has a mean and median both very close to 250 Ωcm (also see [Hoeltzell and Dykes, 1979]). For this reason I used 250 Ωcm as the standard value for my calculations, but also looked at the impact of resistivities ranging from 150 Ωcm to 400 Ωcm.

After calculating the detection range for each cell, I calculated average detection ranges for cells in each layer. The averages were weighted to correct for differences between my morphology sample and what I know of the true distribution of cell sizes, as described in section 4.2.1.2. This average detection range in a given layer is interpreted as the average maximum distance from the recording electrode tip at which neurons in that layer could be detected based on the approximation of spherical detection regions. When the volume of the detection radius sphere is multiplied by the packing density of neurons within each layer it gives the average number of neurons within range for that layer.

[Bealieau and Colonier, 1983] provides cell packing densities separately for the monocular and binocular regions of layers 2, 3A, 3B, 4A, 4B, 5, 6A and 6B. For my calculations I always use the average value of the monocular and binocular regions, and for layers 2/3 I use the average of layers 2, 3A and 3B. For layer 6 I use the packing density and thickness of layer 6A only: my morphology sample consists only of pyramidal neurons of the type found in layer 6A, and histological measurements suggest that my recording penetrations never reached the deeper layer 6B. [Bealieau and Colonier, 1983] provides the packing density of neurons without distinguishing between spiny and smooth cells. Therefore for my packing densities I further multiply by the typical percentage of neurons which are spiny, 80%. In order to determine an average packing density for smooth interneurons, I take the average neuron packing density over all layers and multiply by 20%.

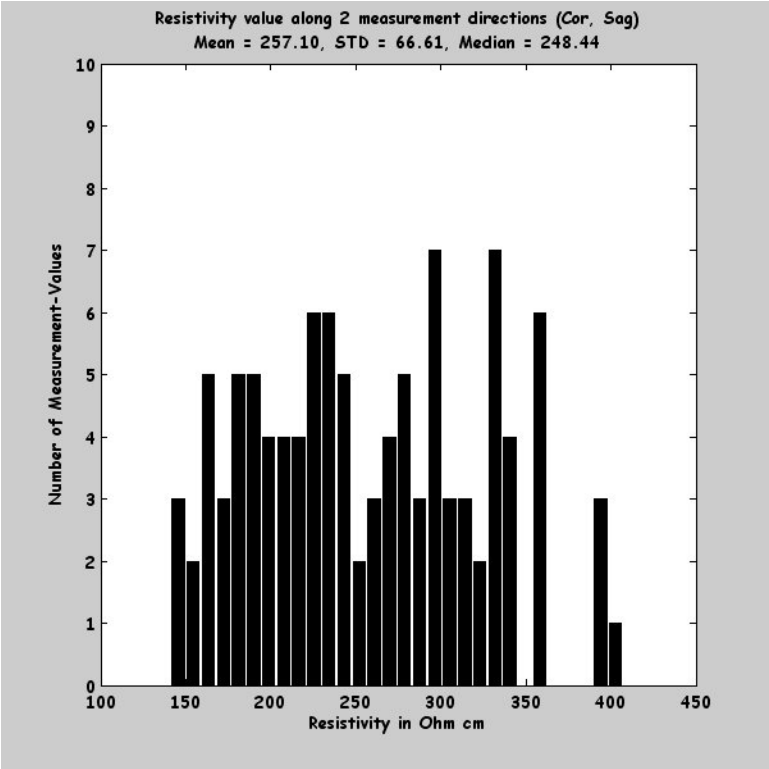

Figure 4.1: Histogram of cortical resistivity measurements.

Measurements from monkey somatosensory cortex. Courtesy of Nikos Logothetis.

Having calculated the average number of neurons within range for each layer, the fraction of neurons active in layer i is:

$$\alpha_i = \frac{N_i^{\text{recorded}}}{N_i^{\text{range}}} \tag{4.1}$$

with N_i^{recorded} the average number of units recorded from each recording site in layer i, and N_i^{range} the model calculation for the number of units within range for layer i.

Note that the simulation detection ranges calculated by this method are radii from the *center* of the soma, not from the soma surface. This is because the detection region volume does not correct for the volume occupied by the soma itself (a relatively small component at the 80 μV threshold.) Consequently this method is appropriate for calculating the neurons within range based on an average packing density, at a low detection threshold. However, care must be taken when applying the same method to a higher threshold: if not corrected the LSA will calculate the potentials that would occur within the confines of the soma itself as if the neural currents were in fact located on a line near its center. This could erroneously provide a non-zero detection region located "inside" the boundaries of the soma at high threshold, when in fact valid potentials calculated outside of the region of the soma are below this threshold. An exact correction for this problem would be

a complex exercise in computational geometry, and would require determining the intersection or enclosure of the detection isosurface with the soma surface. I used a simplification: if the volume of the calculated detection region exceeds the volume of the soma it was interpreted as a valid detection radius from the center of the soma. If the volume of the detection region was less than the volume of the soma it was considered to be zero, meaning no detectable region for that threshold. This was the case for some or all of the neurons in each class at higher thresholds.

4.2.1.2 Correction for Diameter Bias in Morphological Data

Because my goal is to estimate the average detection range for cells in each layer, it is important to ask whether my sample of 68 neuron morphologies based on careful reconstruction is, in fact, representative. [Gabbott et al., 1987] provides the equivalent area diameters for 1350 pyramidal cells in layer 5 of cat V1 sampled randomly with a light microscope. I used this as a basis for comparison with my own sample and the results are summarized in table 4.2. I found that my sample of morphologies is in fact highly biased: more than 50% of neurons in my sample were in the top 10% of size based on the larger sample. This bias most likely results from the process of intracellular labeling with a sharp electrode, which will naturally tend to pick out bigger cells.

To remedy this bias when calculating the average detection region radius for L5 neurons I used a weighted average based on groupings of the cells by size. I grouped the neurons as "small/medium", having diameters smaller than 20 μm, and as "large" having diameters greater than 20 μm. I then calculated an average detection range within each group. For the overall average for L5 neurons I used a weighted average as suggested by the data in [Gabbott et al., 1987]: 90% of the weight went to the small/medium group and 10% of the weight went to the large group.

Size Category	**Diameter Range**	**Literature %**	**Data Samples**	**Data %**
Small	7-14	12%	2	15%
Medium	14-20	78%	4	31%
Large	20+	10%	7	54%

Table 4.2: Layer 5 area equivalent diameters in the literature and morphological data

Diameter Range: Range of equivalent area diameters, in μm. **Literature %**: Percentage of neurons in this category in [Gabbott et al., 1987]. **Data Samples**: Number of cells in this category for my available morphological data. **Data %**: Percentage of cells in this category for the available morphological data.

Unfortunately, I could not find large, unbiased samples of the average neuron size for other layers of cat V1. But based on the results for the layer 5 neurons, I have every reason to expect that my morphology sample for other layers will be similarly biased. Consequently I made an approximate correction by following the results for layer 5: neurons in each layer were divided into

a "small/medium" group containing roughly the smaller 50% of the neurons in my sample and a "large" group containing the larger 50%, as described in table 4.4. When calculating average detection ranges for each layer 90% of the weight was given to the average for the "small/medium" group and 10% of the weight was given to the large group. The impact of the correction is discussed below in section 4.3.7 (in particular see Figure 4.21).

	All			Small/Medium			Large		
Layer	**N**	**Mean**	**Std. Dev.**	**N**	**Mean**	**Std. Dev.**	**N**	**Mean**	**Std. Dev.**
L23	13	17	3.1	6	14.1	1.6	7	19.4	1.3
L4	20	16.9	4.3	8	12.7	1.4	12	19.1	3.7
L5	13	21.7	5.8	6	16.9	2.8	7	25.8	3.4
L6	12	15.8	1.9	6	14.8	1	6	17.5	1.7
Smooth	10	18.5	4.9	5	14.6	3.2	5	22.5	2.1

Table 4.4: Area equivalent diameters in the morphological data

Area Equivalent diameter is the sphere diameter having the same surface area as the actual soma. **All**: All neurons in each layer and also for smooth interneurons from all layers. **Small/Medium**: The neurons comprising the "small/medium" category receive 90% of the weight in determining the average detection range. **Large**: The neurons comprising the "large" category receive 10% of the weight in determining the average detection range.

4.2.1.3 Correction for Multi-Unit Clusters

Because spike amplitude is one of the main criteria for clustering neural units, two neurons which produce EAPs of similar amplitude at the electrode location will normally be clustered together. Such clusters are known as multi-unit clusters. Using my knowledge of the average range at which a neuron in each layer produces a spike of any given amplitude, I construct a model for the probability of recording multi-unit clusters. I can then correct the number of neurons recorded for the purpose of estimating the active cell fraction. I begin by describing an iterative procedure to achieve this, and then show that the result of the iterative procedure is equivalent to a convergent series with a simple analytic solution.

For two spikes to be clustered together, the amplitudes must be within a confined voltage range. I observed that my clustering algorithm ([Quiroga et al., 2004], and see section 4.2.2.2 below) would typically produce separate clusters for spikes with average amplitude that differed by at least 20 μV. This value was relatively independent of the precise background noise level which mostly influence the minimum amplitude for spike clustering. Therefore I make the simple assumption that spikes that are less than around 20 μV apart would be clustered together.

In order to simplify the analysis, I divide all spikes into ranges of 5 μV rather than considering every spike individually. Actual clusters have amplitudes which vary from spike to spike, as discussed

in more detail in section 5.2.8, so little accuracy if any is lost here. I assumed that spikes that are within 10 μV above and below each 5 μV range would be clustered together. For example, a spike whose mean amplitude is between 90 and 95 μV would most likely be clustered together with any any other spikes which had mean amplitude in the range of 80-105μV that were present at the same location. So for convenience and to err on the side of caution I define 25 μV as the range of amplitudes that would be clustered together, rather than 20 μV. I will also analyze the impact if the multi-unit amplitude range were larger in section 4.3.7.

Assuming that the spike amplitude isosurfaces around the neurons are spherical, the probability that a given spike cluster is multi-unit depends on the intersection volume of two pairs of concentric spherical shells, as illustrated in Figure 4.2: the outer of each pair of shells is defined by the minimum voltage for the range, e.g., 80 μV. The inner of the two shells is defined by the maximum spike amplitude for the range, e.g., 105 μV. That is, for a spike to be part of a multi-unit cluster it must be within the same amplitude range of two neighboring neurons, and they both must have been active during the recording. Therefore the (average) probability that a clustered spike in a given amplitude range is multi-unit is the probability that the spike was recorded in a position where a neighboring neuron would have an amplitude in the same range multiplied by the probability that the other neuron was in fact active at the same time. That is:

$$P_{multi} = \frac{V_{overlap}}{V_{detect}} \alpha N_{neighbors} \tag{4.2}$$

where $V_{overlap}$ is the volume of overlap for the detection regions of any single neighboring neuron in the given voltage range, V_{detect} is the total volume of the voltage range detection region for a single neuron, α is the average probability that a neuron in the region is active, and $N_{neighbors}$ is the number of neighboring neurons at the same distance. This is not actually a probability because P_{multi} can be greater than one if $N_{neighbors}$ is large enough – it is better thought of as a ratio, or proportion. When I actually calculate the multi-unit corrections I assume the neurons lie on a cubic lattice so that each neuron has 6 nearest neighbors, 12 near diagonal neighbors (distance of $\sqrt{2}$ times the lattice size) and 8 far diagonal neighbors (distance of $\sqrt{3}$ times the lattice size).

The radii of the two outer (inner) shells for the two neighboring neurons are assumed to be the same, because the neurons under consideration would always be from the same layer and therefore have the same average detection ranges. V_{detect} is calculated as the difference of the volume for the two detection range shells. The next problem is to calculate $V_{overlap}$, the volume of the intersection region. As illustrated in Figure 4.2, this is equivalent to:

$$V_{overlap} = V_{oo} - 2V_{oi} + V_{ii} \tag{4.3}$$

where V_{oo} is volume of overlap for the two outer shells, V_{oi} is the volume of overlap for the outer

and the inner shells, and V_{ii} is the volume of overlap for the two inner shells (Figure 4.2).

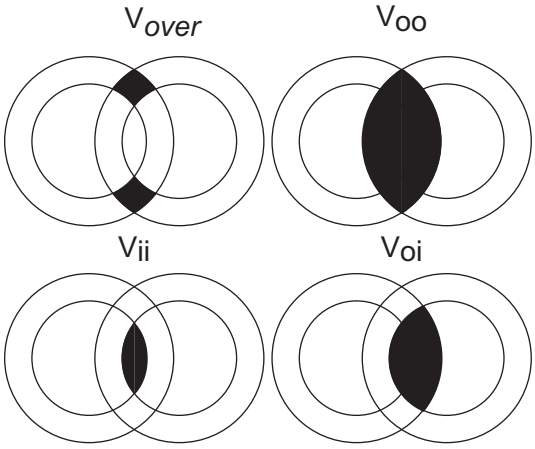

Figure 4.2: Illustration of multi-unit correction calculations.

I determine the intersection volume contained within two pairs of concentric shells, V. This volume is equivalent to the volume of overlap for the outer shells,V_{oo} minus two times the volume of the overlap of the outer shell with the inner shell, V_{oi}, plus the volume of the overlap of the inner shells, V_{ii}.

The volume of the overlapping region for two neighboring spheres of unequal size was calculated in the study of hydration shells of molecules [Kang et al., 1987] which gives the following formula:

$$V_{st} = \frac{\pi}{3}(2r_s^3 + 2r_t^3 + r_{st}^3) - \pi[r_s^2 r_{st}^* + (r_{st} - r_{st}^*)(r_t^2 + r_s r_{st}^*)] \tag{4.4}$$

where r_s and r_t are the radii of the spheres s and t respectively, r_{st} is the distance between the centers of the two spheres, and r_{st}^* is defined as:

$$r_{st}^* = \frac{(r_s^2 - r_t^2 + r_{st}^2)}{2r_{st}}$$

The final piece of information necessary for equation 4.2 is the fraction of neurons that are active. Unfortunately, this is what I am trying to determine. I propose the following iterative procedure to determine the fraction of active units corrected for multi-unit clusters in any given layer of cortex:

1. Calculate the multi-unit overlap fraction $V_{overlap}/V_{detect}$ for each amplitude range, using equation 4.3 and 4.4.

2. Divide the recorded units into amplitude ranges

3. Assume an initial value for the fraction of units active, α

4. Update the number recorded in each range by multiplying the actual number recorded by the multi-unit recording probability, P_{multi}, equation 4.2, using the initial value for α to yield a new value for the total recorded, N^{recorded}

5. Calculate an updated estimate for α using equation 4.1 and the corrected value for N^{recorded}

6. Repeat steps 4-5 until the value for α converges.

Two objections to the proposed procedure could be: 1) that the result may depend on the initial guess for α; and 2) that it is not guaranteed to converge. In fact, the procedure described is equivalent to a simple non-homogeneous, linear recurrent sequence for the activity fraction that converges for all the practical situations I will encounter, no matter what initial guess is used for the activity fraction.

The iterative procedure described above results in a recurrent calculation for the activity fraction.

$$\alpha_n = (R_n/L)/U = \frac{R_n}{LU} \tag{4.5}$$

where α_n is the estimated active neuron fraction on the nth iteration of the correction procedure, R_n is the (corrected) number of units recorded on the nth iteration, L is the number of recording locations, and U is the number of units in electrode range predicted by the model. The update for the number of units recorded, R_n is:

$$\begin{aligned} R_{n+1} &= \sum_s O_s N_s \alpha_n + N & (4.6)\\ &= \alpha_n \Omega + N & (4.7) \end{aligned}$$

where $O_s = \frac{V_{overlap}}{V_{detect}} N_{neighbors}$ is the the total shell overlap proportion for the amplitude range indexed by s (P_{multi} without α), N_s is the number of units recorded in the sth amplitude range, and N is the total number of units recorded ($\sum_s N_s = N$, but note that O_s will go to zero for higher amplitude range.). For a compact notation I have defined $\Omega = \sum_s N_s O_s$. Combining equations 4.5 and equations 4.6 there is a recurrence relationship for α_n:

$$\alpha_{n+1} = \frac{\alpha_n \Omega + N}{LU} \tag{4.8}$$

which is in the form of the simplest linear, non-homogeneous recurrent sequence:

$$x_n = a x_{n-1} + b$$

where $a = \Omega/(LU)$ and $b = N/(LU)$. The general solution for the nth term is

$$x_n = a^n x_0 + \frac{a^n - 1}{a - 1} b$$

which converges whenever $0 < a < 1$, regardless of x_0:

$$\lim_{n \to \infty} x_n = \frac{1}{1 - a} b \qquad 0 < a < 1 \quad \forall x_0$$

Consequently the estimated fraction of active units corrected for multi-unit clusters is:

$$\alpha' = (\frac{1}{1 - \frac{\Omega}{LU}})(\frac{N}{LU}) = \frac{N}{LU - \sum_s N_s O_s} \tag{4.9}$$

Although I began by thinking of the multi-unit correction as an increase to the number of units I found, mathematically speaking it is a reduction in the number I expect to find: the term LU in the denominator is the number of units I think I would record if all were active (the number of locations multiplied by the number in range at each location), and I am reducing it to account for those units I think I would not find because they would be clustered together. The requirement for convergence is

$$\frac{\sum_s N_s O_s}{LU} < 1$$

In practice the criteria is easily met. Note that usually $O_s \leq 1$, meaning that for realistic voltage ranges there is less than 100% overlap with the same ranges of neighboring cells; $U > 1$, as will be shown in section 4.3.6, there are more than one spiny neuron in electrode range; and $L > \sum_s N_s$, because on average I record less than one unit per location, as described in section 4.3.1. In practice the convergence criteria was around 0.15-0.2 for my data in all the layers of cortex. Therefore I conclude that I can calculate the corrected fraction of active units using equation 4.9 without needing an initial "guess" for the active fraction and without actually applying the iterative procedure at all.

4.2.1.4 Calculation of Sampling Bias

Having an estimate for the fraction of active units within each layer I can calculate the probability of sampling from each layer and the resulting sampling bias. For each layer I define the detectable volume fraction ϑ_i as the fraction of the volume of the layer in which the electrode is in range of neurons:

$$\vartheta_i = \frac{(At_i \rho_i)\nu_i \alpha_i}{At_i} = \rho_i \nu_i \alpha_i \tag{4.10}$$

where A is the area of cortex under consideration (i.e., 1 mm^2), t_i is the thickness of cortical layer i, ρ_i is the packing density of neurons in layer i (in cells/mm^3), ν_i is the average detectable volume (in mm^3) around neurons in layer i (i.e., the volume of the sphere having the average detection range), and α_i is the fraction of neurons in layer i that are active. This is the total volume of detection around all active neurons divided by the total volume of the layer. Note that ϑ_i can, in theory, be greater than one if on average more than one active units are in range but this does not turn out to be the case for my data.

After calculating ϑ_i it is straightforward to calculate the Sampling Probability, or the proportion of neurons that would be recorded in each layer:

$$P_i = \frac{t_i \vartheta_i}{\sum_j t_i \vartheta_j} \tag{4.11}$$

P_i can be seen as the probability that a recorded neuron came from layer i if the electrode randomly sampled locations. The thickness of the layers accounts for the probability that the (random) electrode is in each layer to begin with. For a real electrode that travels in a straight path this is the proportion of the total number of units recorded that would come from layer i, *assuming the path of the electrode was perpendicular to the layering of cortex.* As I will show, this assumption is not necessarily valid.

Finally, I define sampling bias, β_i , as the ratio of the sampling probability for layer i to the fraction of cells that are in layer i:

$$\beta_i = \frac{P_i}{C_i} \tag{4.12}$$

where C_i is the fraction of the total cells under a given area of cortex (i.e., 1 mm^2) that are in layer i, as shown in table 4.12. This definition of sampling bias is a measure of how all other factors affecting the detection rate change the sampling probability from what it would be if it depended on the number of neurons alone.

4.2.2 Experimental Methods

4.2.2.1 Recording Methods

Three adult cats were used for this study. The animal was prepared for *in vivo* experiments carried out under authorization of the Cantonal Veterinary Authority of Zurich. For a detailed description of the surgical procedure and animal maintenance see [Girardin et al., 2002]. Briefly, anesthesia was induced with a mixture of xylazine and ketamine and maintained with Saffan (through a venous cannula). Animals were paralyzed and ventilated with 30/70 mixture of O^2/N^2O through a tracheal cannula. Halothane (0.5%) was used for painful procedures (e.g., durotomy) and during initial

surgery (1%-2%). EEG, electrocardiogram, blood pressure, rectal temperature, and expired CO^2 were monitored continuously and kept in physiological ranges. Neutral power lenses and atropine were applied on the eyes. Eyes were refracted and focused at a distance of 114 cm.

Glass pipettes (tip size 2 μm, resistance 10 MΩ) were used for recording extracellularly from primary visual cortex (-3 to -6 mm posterior to inter-aural plane). Pipettes were filled with a recording solution containing pontamine. At least two pontamine injections were made in each penetration in order to reconstruct the electrode track. In each penetration the multi-unit activity was recorded for 3 minutes at each location. The electrode was then moved down by 30 μm and sampling was repeated for the new location. When recording a high amplitude unit recordings were often made at shorter sampling intervals (10-20 μm) and for shorter durations (1-2 min). Recordings of high amplitude units at irregular intervals were not used as part of the statistical sample of cortical activity – these were used in order to characterize the spike waveform shapes only. This process was repeated until the white matter was reached. The extracellular potential was sampled at 20 kHz and band pass filtered (5-8000 Hz). The visual cortex was stimulated by a manually held, high-contrast bar that moved in all orientations and directions during the recording. The receptive field of single cells was occasionally plotted.

4.2.2.2 Spike Clustering

Spikes were clustered from the recordings using wavelet features and superparamagnetic clustering [Quiroga et al., 2004]. For spike detection, the raw data was band pass filtered between 300-1000 Hz, while for clustering the data was band pass filtered between 300 and 3000 Hz. I found that the minimum spike amplitude for clustered neurons was typically around 80 μV. I did not explicitly attempt to split suspected multi-unit spikes (as suggested by ISIs lacking an appropriate refractory period, etc.) Rather I recorded such units as single detections and used a correction in my calculation, as described in section 4.2.1.3.

4.2.2.3 Measurement of EAPs and Classification of Interneurons

After the spikes were clustered an average waveform was made for each cluster. The average was made from data that was high pass filtered above 100 Hz, using the spike times determined by the full clustering algorithm that incorporated narrow band filtering. This removed 50 Hz noise and LFP components while producing waveforms that were virtually unaltered from the wide band recordings. The features of each waveform were measured as described in section 3.2.5 but with two additional measurements: the width of the Na^+ phase at 50% amplitude and the time from the Na^+ peak to the K^+ peak, as illustrated in Figure 4.5. For taking these measurements I excluded spikes that had Na^+ peaks less than 90 μV because the average waveforms for these EAPs were often too noisy to collect meaningful statistics other than the Na^+ peak. (Indeed, for characterizing

the waveform shapes I would have preferred an even higher threshold if only more high amplitude units were available in from the superficial layers.)

I also analyzed measurements for the amplitude of the Na^+ peak of the spikes: Although I argued in sections 3.3.7 and 3.4 that there are too many confounding factors to make this measurement very useful for tuning the conductance densities in a model, it is the most important result of the model when it comes to the question of the detection range of model neurons. For this reason I also measured whether or not a sample of points around the model neurons reproduced the distribution of peak amplitudes observed when recording real neurons. As detailed in section 3.2.5, I made the comparison using all model neurons, and also only those model neurons that were in the "small/medium" size group, as described in section 4.2.1.2.

I classified the spikes as originating from spiny neurons (pyramidal or stellate) or from smooth interneurons using the EAP features suggested by [Barthó et al., 2004]: spikes were classified as originating from a smooth interneuron if they had a 50% amplitude duration less than 0.25 ms, and the time from the Na^+ peak to the K^+ peak was less than 0.4 ms (see Figure 4 in [Barthó et al., 2004]). Because I have shown in section 2.3.5 that EAP waveforms become narrower (shorter in duration) with proximity to the soma, I imposed an additional amplitude criteria on interneuron classification: if the amplitude of the Na^+ peak is greater than 200 μV the spike was classified as spiny, presumably generated by very proximal recording of a large pyramidal cell.

As discussed in section 4.3.1 and detailed in Chapter 5, I excluded spikes with positive peaks from the analysis (those spikes where the positive, capacitive peak exceeded the negative, Na^+peak in amplitude.)

4.2.2.4 Histology Methods

The animals were perfused transcardially with parafolmaldehyde. The brain was sliced with a microtome. Each penetration was reconstructed using the pontamine injections and this was used to reconstruct the path taken by the electrode. The layered structure of cortex was visually identified in the slices and mapped to equivalent depths in each penetration. Using the known depth of penetration for each recording and the approximate layer boundaries each recording was assigned to either layer 2/3, 4, 5, or 6.

4.2.3 Simulation Methods

The simulation methods are similar to those described in sections 2.2.3 and 3.2.1. They are briefly reiterated here, highlighting any differences. Parameters for the cortical neuron model are listed in appendix C.

4.2.3.1 Neuronal Reconstructions

The morphologically reconstructed neurons for the computer simulation were 68 cells including 13 layer 2/3 pyramidal neurons, 20 layer 4 spiny neurons (including 4 pyramidal and 16 stellate), 13 layer 5 pyramidal neurons, 12 layer pyramidal 6 neurons and 10 smooth interneurons from all layers [Binzegger et al., 2004]. The morphological data consisted of coordinates (x, y, z) defining the paths of the dendrites and (in 46 cases) the axon, at intervals of (typically) a few μm.

The soma was outlined in the morphological data with a sequence of coordinates. The soma was converted for the simulation by forming a sequence of center and diameter measurements from pairs of points on opposite sides of the outline. This resulted in somas with the measurements detailed in table 4.4 and discussed in more detail in section 4.2.1.2.

The diameters of the dendrites at each point was provided in a small number cells (2 spiny neurons from each layer, 3 smooth interneurons). Diameters for the dendrites in the remaining cells were defined based on the average diameters for cells from the same layer whose diameters had been measured, corrected by a small factor for varicosity. Layer 4 pyramidal neurons were given the same apical dendrite diameters as the layer 2/3 pyramidal neurons. A varicosity correction factor was formed by taking each neuron that had detailed diameters and comparing its total dendritic surface area calculated using the exact diameters versus the total surface area calculated using its own averages. This resulted in a small correction, always less than 10%. In basal, apical oblique and apical tuft dendrites averages were created for each branching order. For the apical trunk average diameters were created for a set of distance ranges (20 μm intervals close to the soma, expanding with distance.) The final diameters used in the reconstructions are shown in table C.7.

The one exception was for a single Meynert cell from layer 5. Because the Meynert cells have thicker than average dendritic diameters it was not included in defining the average for layer 5. [Feldman, 1984] It was simulated with its own exact diameters. Also, numerous studies have indicated that layer 5 pyramidal cells occur in two varieties: "thick", having thick apical trunks and extensive tuft in superficial layers, and "thin", having narrower apical trunks that reach superficial layers but do not have extensive branching tufts [Peters and Yilmaz, 1993, Larkman, 1991a]. Because my layer 5 pyramidal cells with dendrite diameters appear to be of the thick variety (having extensive apical tuft) I scaled the diameters for layer 5 pyramidal neurons that did not have extensive apical tuft (4 out of 12) by 2/3 [Larkman, 1991a] before performing simulations.

Most of the neurons included very extensive axonal reconstructions and these were used in every simulation when available. The set of axon coordinates closest to the soma were used to define an axon hillock and axon initial segment similar to that described in section 2.2.3.3. For the neurons in layers 2-4 and and smooth interneurons, the axon hillock was defined as 5 μm long and the initial segment was 15 μm long. For layers 5-6 neurons, the axon hillock was 10 μm long and the initial segment 20 μm long. The data also included the location of the axonal boutons to define which

sections of the axon were myelinated and which were not according to the following rules:

1. At every branch point, the axon was non-myelinated for 1 μm before and after the branch point.

2. The axon was always myelinated for the first 50 μm after the initial segment, except for branch points.

3. Each bouton in the data (outside of the initial myelination) created 1 μm of non-myelinated axon around it; non-myelinated sections within 2 μm of each other were merged (i.e., the axon would not "remyelinate" unless there was more than 2 μm between subsequent boutons).

These rules resulted in the majority of the axon being myelinated, around 75%-80% for the spiny neurons, and around 60% for the smooth interneurons.

Because no diameter data was available for any axons, diameters were assigned as follows: non-myelinated axon proximal to the soma was 0.75 μm thick and non-myelinated axon diameters decreased linearly with distance over the first 200 μm to a minimum of 0.25 μm thick, which was used for all non-myelinated axon beyond 200 μm from the soma. Myelinated axon was defined as having double the diameter of an equivalent section of non-myelinated axon. [Mainen et al., 1995]

For neurons that had no axonal data, I used the simplified axon described in section 2.2.3.3.

4.2.3.2 Passive Parameters

The intracellular resistivity was set to R_i =75 Ωcm as suggested by [Stuart and Spruston, 1998]. For the interneuron simulations I used R_i =50 Ωcm, as this gave a superior match to the shape of the EAP waveforms. The membrane resistance was set to R_m =15 kΩcm^2 to account for the net effect of *in vivo* synaptic conductances in reducing the membrane resistance without actually modeling the detailed time-dependency of synaptic activity [Destexhe and Paré, 1999]. The specific capacitance was set to C_m =1 μF/cm^2. The reversal potential for the passive leak mechanism was set to V_{rest}=-65mV. Dendritic spines are accounted for by adjusting the passive membrane parameters and C_m , decreasing the former and increasing the latter by a factor f given by the normalized spine area [Major et al., 1994]. The factor was applied to dendrites more than 40 μm from the soma, and was set independently for the apical and basal dendrites in different layers, reflecting the relative density of spines [Larkman, 1991b]. The correction factors used are shown in table C.1.

4.2.3.3 Ionic Current Model Kinetics

The formalisms used for all of the active channel conductance models, except for the Na^+ conductance, are those described in [Borg-Graham, 1999]. The parameters for the kinetics of the spiny neuron simulations are those given in section 2.2.3.2.

For the Na^+ channel conductance I use a cooperative Markov model based on that of [Naundor et al., 2006]. In the cooperative model, the voltage dependent Closed → Open rate function is shifted in a depolarized direction by an amount proportional to the number of channels already open. Modifications were made so the model was better suited to multi-compartmental simulations rather than a single compartment as used in [Naundor et al., 2006]:

1. The cooperativity level was made a linear function of the maximal Na^+ conductance density ($\bar{g}$) for the compartment. The Na^+conductance density itself was non-uniform, as described below. Consequently compartments with the highest Na^+ density in the cell also had the highest level of cooperativity. Parameters for the minimum and maximum cooperativity parameter J are listed in table C.3.

2. Cooperativity was made to "spread" between compartments by using a weighted average of the channel open fraction in the immediate neighbor compartments to determine the cooperativity level. In dendritic and axonal compartments, the average of cooperativity was weighted by compartment volume. The axon initial segment, the axon hillock and the soma each had equal cooperativity with respect to each other.

3. The Open → Inactivated transition rate was given voltage dependence of the same form as the other transitions, with parameters given in table C.2.

4. For every compartment cooperativity would become inactive after the voltage in the compartment had surpassed $V_{1/2}$ for the Closed → Open transition.

The parameters of the model were tuned to match my *in vivo*extracellular recordings using a multi-compartment model, as well as reproduce the qualitative results described in [Naundor et al., 2006] : a rapid onset of Na^+ current via cooperativity leads to a rapid initiation of the membrane potential spike. As suggested by the results in [Colbert and Pan, 2002] I allowed different parameters for axonal vs. somatic and dendritic portions of the cell, with the axonal variety more excitable at less depolarized potentials, as described in table C.2.

The active ionic conductance model for the smooth interneurons was the same as that for the spiny neurons, but with modified parameters. This was required to match the intra- and extracellular potentials for the spineless interneurons having a higher input resistance and lower effective capacitance. Differences in the Hodgkin-Huxley type channel model for the smooth interneurons are noted in table C.4. The differences are in the K and M type K^+channels, and were required to bring about faster activation of the K^+ conductance than was used in the spiny neuron model. The parameters for the cooperative Na^+ model used for the smooth interneurons are given in table C.5. These changes created a Na^+ window current of briefer duration then for the spiny neuron model,

required to match the narrower duration of both the intra- and extracellular spikes associated with smooth interneurons.

4.2.3.4 Density of Ion Channel Conductance

The simulated cortical neurons had non-uniform ionic channel conductance densities the same as those described in section 2.2.3.2 with a few exceptions, described below. Briefly, the Na^+ channel conductance is the same on the soma and axon hillock and at a moderately raised density on the axon initial segment. For the extensive reconstructed axons described in section 4.2.3.1, I found it was required to use conductance densities that were significantly lower than those in the soma. This is because the narrow axons which were mostly myelinated have a much higher input resistance than the soma or dendrites. Consequently if the axonal Na^+ density were as large as that in soma they would tend to be unstable, as high input resistance amplifies the effect of the Na^+ conductance active at rest. Further, due to the high input resistance, only a small fraction of the somatic Na^+ conductance was required in order for the simulated axons to have complete propagation of *full amplitude* action potentials. While the precise axonal Na^+ conductance density varied from simulation to simulation, the typical values were only around 20% of the density for the soma.

Na^+ channel conductance for the dendrites is at a peak near the soma (though less than the somatic value) and declines with distance from the soma. The minimal value of the Na^+ channel conductance occurred in the most distal compartment of each dendritic branch and the scaling in any given compartment was the proportion of the path distance from the soma to its deepest ancestor compartment, raised to a power. That is, $\bar{g}_{dendrite} = \bar{g}_{soma} \times \{\gamma_{min} + (\gamma_{max} - \gamma_{min}) \times (\frac{d_{max} - d_{comp}}{d_{max}})^p\}$, where γ_{max} and γ_{min} indicate the maximum and minimum dendritic conductance density ratio respectively, d_{comp} is the path distance from the soma to the compartment, and d_{max} is the maximum distance of any ancestor of the current compartment from the soma, and p was a power chosen to control the speed of the decay. I used p around 6 for most simulations and chose the precise value to best match the recording data.

The inactivating A type K^+ channel conductance [Hoffman et al., 1997] is uniform in the proximal dendrites and becomes denser in the distal dendrites, though only 3.5x the proximal value for the cortical pyramidal cells, rather than 7x the proximal value that was used for CA1 pyramidal cells in chapters 2 and 3 [Migliore and Sheperd, 2002]. The C type Ca^{2+} dependent K^+ conductance is located in the soma and proximal dendrites only [Poolos and Johnston, 1999]. The H type, mixed ion, hyperpolarization activated current is 6x more active in distal dendrites than proximal [Magee, 1998]. N and R type Ca^{2+} channel conductance is located in the soma only, while T and L type are located in dendrites only [Fisher et al., 1990, Christie et al., 1995, Magee and Jonston, 1995]. The AHP type slow Ca^{2+}dependent K^+ conductance described in section 2.2.3.2 was not included in these simulations. The D, K and M type K^+ conductances were uniform throughout the simulated

neuron. The maximal conductance densities for each neuron were tuned to achieve the intra- and extracellular spike waveforms.

4.3 Results

4.3.1 Number of Spikes Recorded

My collaborators and I made a total of 8 penetrations in cat V1. In two of these the dye injections could not be found during histology and the recordings made in these penetrations were not used. Examples of two penetration paths with approximate cortical layer boundaries are shown in figure 4.3. In two out of six penetrations the angle of the electrode was such that by the time it reached layer 5 it was nearly parallel to the plane of the layers and made an extended sample of layer 5, never reaching layer 6. In two other penetrations, the electrode became clogged before reaching layer 6. As a result of these factors, I ultimately obtained the largest number of samples from layer 5 (N=104) and the smallest number from layer 6 (N=33) as detailed in table 4.6.

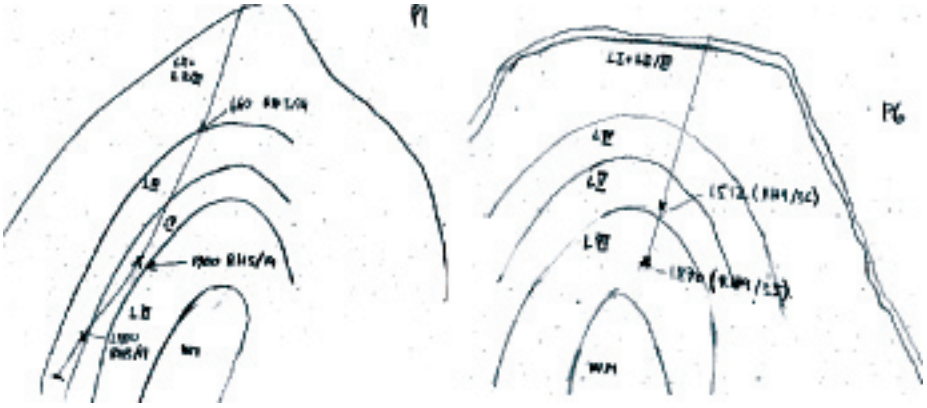

Figure 4.3: Examples of penetrations in cat V1.

In P1 the angle of the electrode and curvature of the electrode path was such that an extended sample was made in layer 5 before the electrode reemerged in layer 4. In P6 the penetration was essentially perpendicular to the layers.

After clustering, a total of 453 units were recorded at 391 locations, including those recording at short electrode advancements (10-20 μm) near a relatively high amplitude unit. Of these, the majority ($\sim$90%) had a dominant negative peak similar to spikes recorded in CA1. Around 10% of all spikes had a dominant positive peak, as illustrated in figure 4.4. Because spikes with positive peaks seem to have a fundamentally different nature of origin from negative peaked spikes I analyze them separately in Chapter 5. Therefore all conclusions in this chapter are based on negative spikes only; I will briefly examine the consequences of this assumption in the discussion, section 4.4.3.

A total of 280 locations were recorded at fixed 30 μm depth increments for the unbiased sample of cortical activity. At these locations a total of 221 negative polarity units were recorded that had negative peaks greater than 80 μV, as detailed in table 4.6. 29 of these units were classified as interneurons according to the criteria described in section 4.2.2.3. Because the number of interneurons

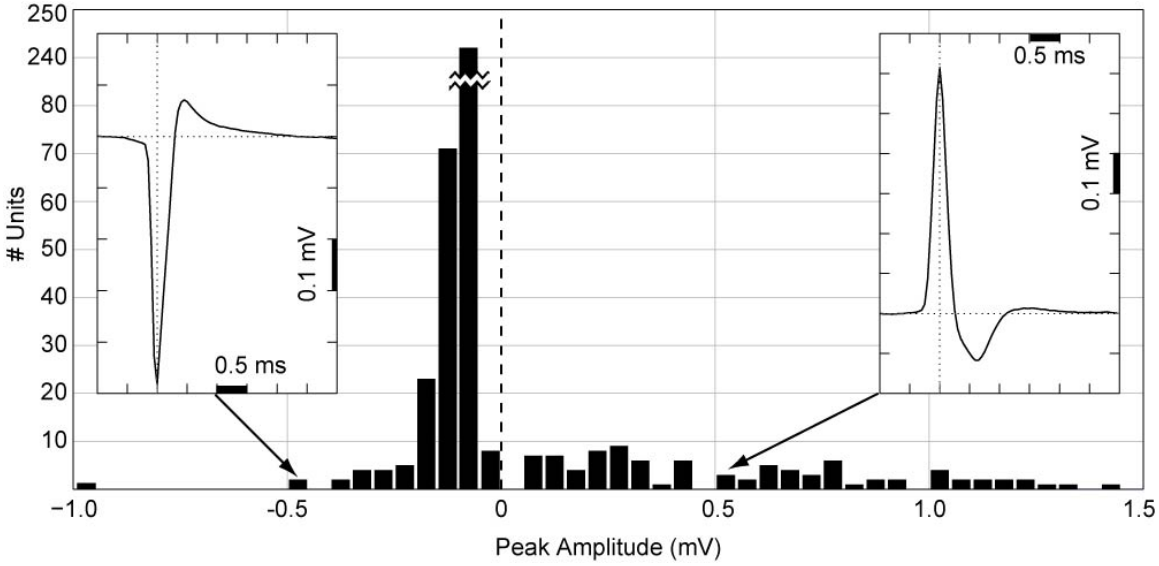

Figure 4.4: Histogram of positive and negative spike recordings

was relatively small (as is my sample of interneuron morphologies) I analyzed them as a group over all layers rather than separating them by layer. Of all locations in the sample, 51% had a single unit (with peak greater than 80 μV), while 36% had no units at all. The remaining locations had either 2 units (10%) or 3 units (3%).

		# Locations with N units					Mean		
	Number					Total	Number	Std.	Std.
Layer	Recorded	0	1	2	3	Units	Units	Dev.	Err.
L23	67	24	41	2	0	45	0.672	0.53	0.06
L4	76	41	34	1	0	36	0.474	0.52	0.06
L5	104	37	54	10	3	83	0.798	0.73	0.07
L6	33	9	20	4	0	28	0.848	0.61	0.11
Smooth	280	255	21	4	0	29	0.104	0.35	0.02

Table 4.6: Number of spike clusters per electrode location

Comparing my observations during the experiment to the results of the clustering I found that units smaller than around 120-150 μV were not clearly discernible on the oscilloscope or over the speaker connected to the amplifier. At these locations I was aware of "hash" but individual spikes were not directly observable. Spikes at amplitude below 120 μV were found only after filtering and clustering.

4.3.2 Recorded EAP Waveforms

Because I use the feature measurements of the recorded EAP waveforms to tune the compartment model (as proposed in section 3.4) it is worth asking whether or not the waveform shapes actually vary between the different layer of cat V1. Figure 4.5 compares the measurements of the recorded spike waveforms from the different layers of cat V1. Using a minimum Na^+ peak of 90 μV, the boxplots in Figure 4.5 represents 29, 19, 74, 13 and 38 examples of waveforms from layer 2/3, 4, 5, 6 and Smooth interneurons respectively.

The deeper layers (5, 6) include many spikes of substantially higher Na^+ peak amplitude than the superficial layers. This is what I would expect, given that cells in the deeper layers tend to be much larger. A result I did not expect was that the spikes classified as originating from interneurons have a higher amplitude than those from cells in superficial layers. This raises the question of whether some proximal recordings from large spiny cells were misclassified as smooth interneuron spikes. However, as shown in table 4.4, the interneurons do tend to be somewhat larger than the spiny cells from superficial layers, and they also tended to have more non-myelinated axon close to the soma. These factors could lead to larger amplitude spikes as well.

The Na^+ peak duration measured at 25% and 50% amplitude are somewhat narrower for deep layer neurons than for superficial layer neurons, although the distributions overlap enough so that the difference is not very significant. The deeper layer spikes also tend to have shorter durations between the Na^+ peak and K^+ peak and somewhat larger K^+ peak ratios. Taken together these features form a consistent picture: deeper layer neurons seem likely to have stronger perisomatic K^+ current than superficial layer neurons. This would explain a narrower Na^+ phase, a shorter time from the Na^+ peak to the K^+ peak and the high amplitude of the K^+ phase.

Naturally, the interneurons have a narrower Na^+ peak and shorter duration from the Na^+ to K^+ peak: the width at 50% amplitude and the time from the Na^+ to K^+ peaks were the features used for their classification. I also find that the spikes classified as originating from smooth interneurons have the largest average K^+ peak amplitude ratio which is what I would expect, given the other measures.

For the amplitude of capacitive peak preceding the Na^+ peak (expressed as a ratio to the Na^+ peak), the most significant difference between the layers is that layer 5 neurons have many more spikes with large capacitive current peaks than in other layers. This is consistent with the prediction that capacitive spikes are generated close to the apical trunk, as discussed in section 2.3.2, and the fact that layer 5 pyramidal cells have very large and thick apical trunks.

The decay time constants for the K^+ peak are similar for the spiny neurons in all layers, while spikes classified as smooth interneurons tend to have much faster decay in the K^+ peak.

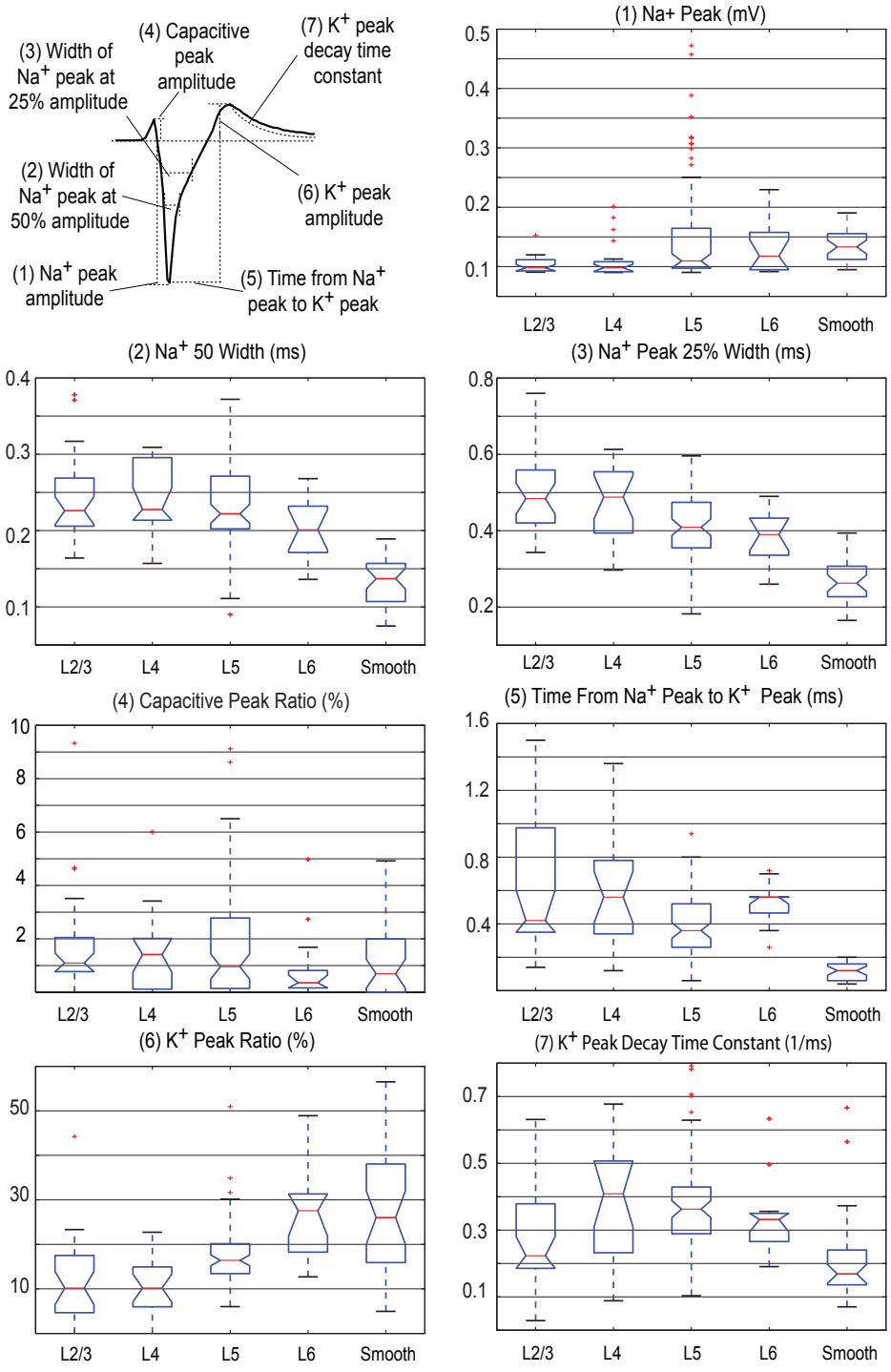

Figure 4.5: Measurement of extracellular spike recordings from cat V1.

The lower and upper boxes show the 25th and 75th percentile, while the central line is the median. Whiskers show which points are considered to be outliers: 1.5x the inter-quartile range. Statistical analysis was performed with the Matlab^{TM} Statistics Toolbox 'boxplot' function using the default parameter settings.

4.3.3 General Properties of the Cortical Model

I found that in order to reproduce the shape of the typical recorded EAP waveform in a simulation, I had to assume that the active Na^+channel conductance is concentrated in the soma, proximal dendrites and axon initial segment and that the action potential fails to fully invade the distal dendrites. In particular, the negative phase of the recorded waveforms has too long a duration and the positive phase of the waveform has too small an amplitude to be matched by a model that produces full backpropagation. The reason that weakly active distal dendrites match this requirement is best understood by considering the relationship between the extracellular action potential and the second spatial derivatives of the membrane potential: The negative phase of the EAP corresponds to the time when soma and proximal dendrites form a maximum in the membrane potential while during the positive phase the soma and proximal dendrites are a minimum (i.e., the second derivative rules for local maxima/minima, as described in section 3.3.4.) Therefore the duration of the negative phase of the EAP corresponds to the time during which the soma has an elevated potential while the dendrites are at a lower membrane potential. The positive phase corresponds to the extent to which the soma leads in the membrane repolarization and forms a local minimum in the membrane potential.

To illustrate these factors, I created two simulations of simplified single cylinder neurons, the results of which are shown in Figures 4.6 and 4.7. In the first simulation, the Na^+ channel conductance density is uniform throughout the cylinder while in the second simulation Na^+ conductance is concentrated in the center. The total amount of Na^+ channel conductance is constrained so that the peak in the membrane potential at the center of the cylinder is the same in each simulation: around 75 mV above the threshold. In the simulation where the Na^+ channel conductance is uniform the AP rapidly spreads to the distal ends of the cylinder. In this scenario the peak membrane potential at the ends of the cylinder is even greater than at the center, due to the high input resistance of the sealed ends. This process accentuates the minimum created at the center during activation of the K^+currents and repolarization. For the simulation with the concentrated Na^+ conductance density, on the other hand, the AP takes longer to spread from the center and the peak membrane potential at the ends of the cylinder are much less than at the center. When the center of the cylinder begins to repolarize in the concentrated Na^+ scenario it is a local but not a global minimum of the membrane potential.

The result of the different patterns of propagation for the EAP is illustrated in Figure 4.7. The cylinder with uniform Na^+ channel conductance has a negative peak that is briefer in duration and weaker than for the cylinder with concentrated Na^+ channel conductance. On the other hand, the positive phase of the EAP for the uniform cylinder is greater in both absolute and relative terms. These directly corresponds to the second spatial derivatives created by the different patterns of activation.

In terms of the components of the membrane current, these differences can be understood by noting two facts: 1) For the uniform cylinder the density of Na^+ channel conductance at the center is much less (approximately 1/2 the density) in comparison to the cylinder with the concentrated density; this fact explains the weakness of the Na^+ peak in the uniform cylinder despite the similarity in the membrane potential peaks. 2) The high amplitude of AP backpropagating to the distal ends in the uniform cylinder activates fast, high threshold K ("DR") type K^+ conductance throughout the cylinder (the conductance density of the K type K^+ conductance is uniform and the same in both simulations.) On the other hand, the weak AP propagation in the cylinder with concentrated Na^+ conductance means that the fast K^+conductance is only strongly activated at the center of the cylinder and low threshold A and M type K^+ currents in the distal ends of the cylinder contribute a greater portion of the repolarization current. The stronger and faster activation of the K type K^+ conductance for the uniform cylinder results in an EAP that has a shorter negative phase as the dominance of the (already weaker) Na^+ current is overwhelmed by the fast onset of the K^+ current. The strong K type K^+ current also creates a much larger positive phase during repolarization.

Based on these theoretical results and the good match of the model to the recording, I conclude that in cortical cells the active Na^+ channel conductance is most likely concentrated on the soma, proximal dendrites, and axon initial segment. As illustrated in the cylinder example, the concentration of the Na^+ on the soma that was required to match the waveform shape increased the peak amplitude of the Na^+ phase over what it would be if the Na^+ conductance were uniformly distributed. These conclusions applied to tuning the model to match the EAPs for all cell types, including the smooth interneurons. Smooth interneurons have waveforms with narrower Na^+ phases and relatively higher amplitude K^+, so based on the preceding examples it might be expected this is evidence for full backpropagation. But smoother interneurons have narrower dendrites with a much lower effective capacitance due to the lack of spines. This alone makes the negative phase of the spike waveforms much shorter in duration and I found that the best match to the recording data was still achieved with a peri-somatic Na^+ concentration and relatively weak distal backpropagation.

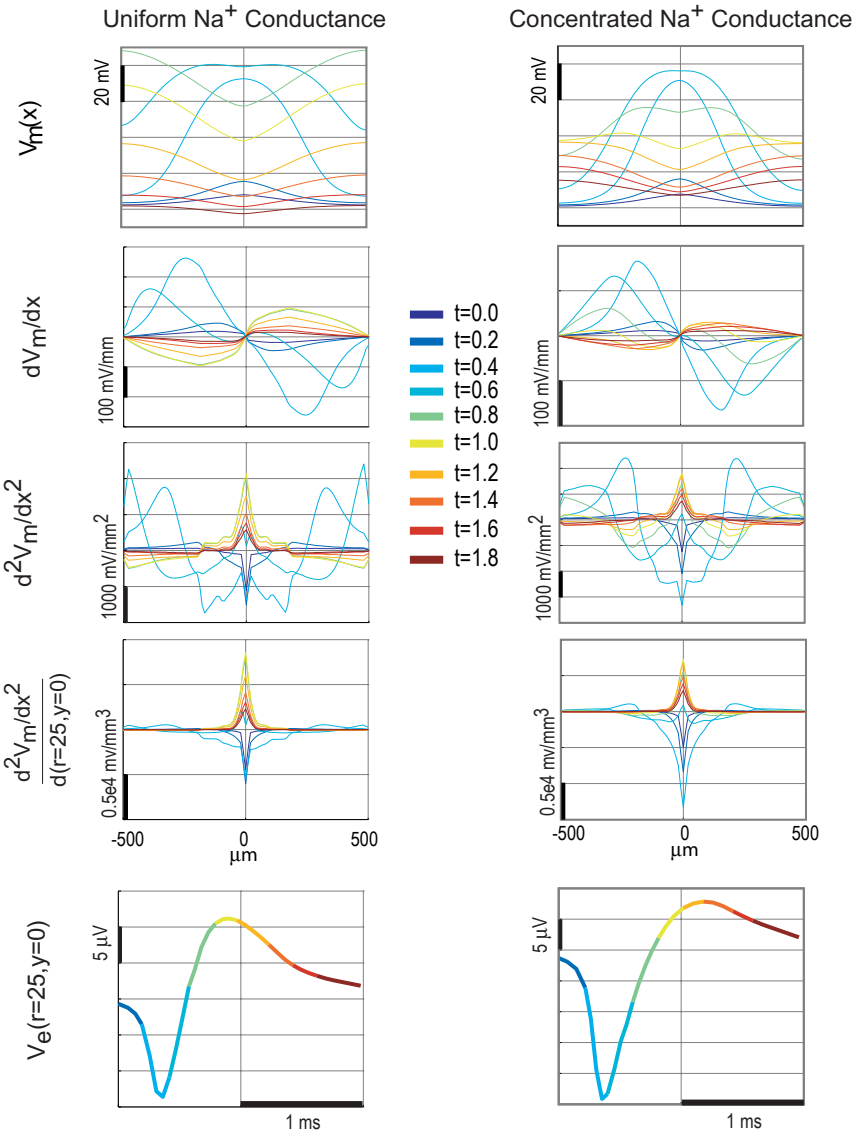

Figure 4.6: Cylinder simulations with uniform and concentrated Na^+

Left: $V_m(x)$ and gradients for a simplified cylinder neuron with uniform Na^+ channel conductance density. After initiating in the center, the AP spreads reaching even higher amplitude at the sealed ends. For a general description see Figure 3.8. Because of the rapid spread of the AP from the center, the central of the cylinder goes from being a maximum to a minimum relatively quickly and the high amplitude of the membrane potential at the distal ends means the minimum at the center is particularly intense. This leads to an extracellular action potential near the center that has a relatively brief negative phase and a particularly strong positive phase. **Right:** $V_m(x)$ and gradients for a simplified cylinder neuron with Na^+ channel conductance density concentrated in the center of the cylinder. The membrane potential at the center of the cylinder is designed to be similar to that for the cylinder with uniform Na^+ channel conductance density. The amplitude of the peak membrane potential falls significantly at the distal ends of the cylinder. As a result, the center of the cylinder remains a maximum for relatively longer than in the cylinder with uniform Na^+ channel conductance and when it becomes a local minimum during repolarization, the extent of the minimum is not very great. Because the EAP is proportional to the second spatial derivatives of the membrane potential, this means that the negative phase of the EAP near the center of the cylinder is relatively long in duration and the positive phase is relatively weak.

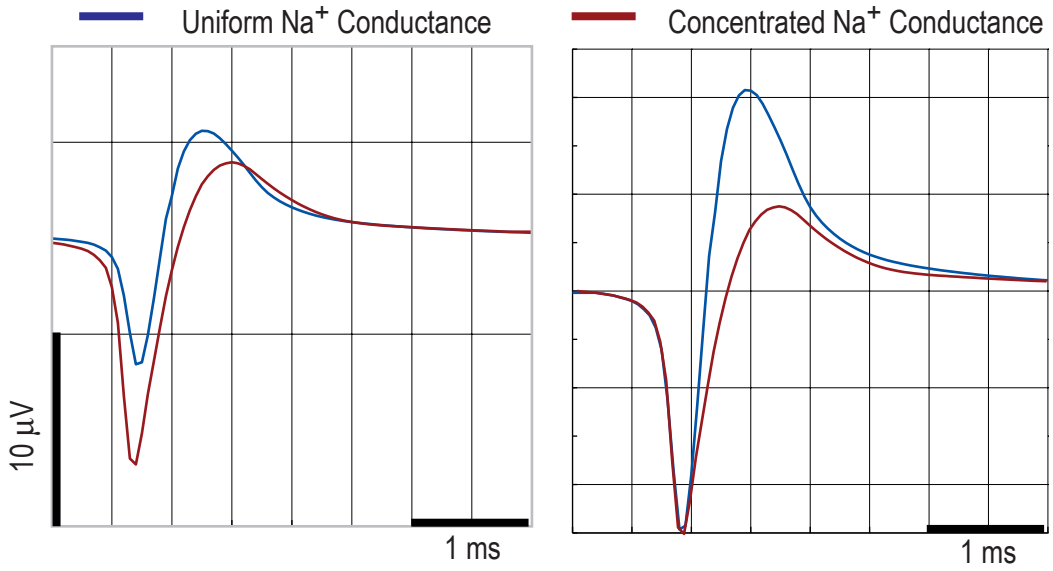

Figure 4.7: Comparison of EAPs for uniform and concentrated Na^+

Comparison of EAP waveforms for the simplified neuron simulations of Figure 4.6. **Left**: Comparison of EAP waveforms at a location 25μm from the center of the cylinder. The simulation with Na^+ channel conductance concentrated at the center has a significantly larger negative phase than the simulation with uniform Na^+ channel conductance, which has a larger positive phase. **Right**: The EAP waveforms normalized according to the negative peak amplitude. This demonstrates the relatively longer duration of the negative phase and the much weaker relative amplitude of the positive phase.

4.3.4 Spikes from a Large Layer 5 Pyramidal Neuron

I made a simulation of a large layer 5 pyramidal cell from cat visual cortex and compared it to a recording of high amplitude negative spike, as illustrated in Figures 4.8 – 4.10. The negative spikes were recorded at 5 locations spanning 90 μm. It was the largest amplitude negative spike I recorded, having a peak amplitude around 1 mV. But the peak amplitude of the spike occurred at only a restricted range of positions: 20 μm before and 10 μm after the peak location, the amplitude was down by 50% or more.

The spikes recorded at the first and last positions in the series have amplitude of only around 100 μV and consequently it is not certain that they actually came from the same unit as the spikes with higher amplitude in the middle of the series. During the recording session they were observed as "hash" and it could not be verified how well they responded to the stimulus in the preferred orientation. Also, they are weak enough that they may well be multi-unit clusters. But the good model match to the sequence of amplitudes suggests they may well have originated from the same neuron as the higher amplitude recordings.

As described in the previous section (4.3.3) the waveform is characterized by a relatively long duration negative (Na^+) phase and small amplitude positive (K^+) phase: the negative (Na^+ current dominant) phase lasts around 0.4 ms (measured at 25% of peak amplitude); the positive (K^+ current dominant) phase amplitude around 13% of the negative peak, and decays with a time constant of around 0.4 ms. These measurements of the waveform are fairly typical of other negative spikes recorded in my experiments. For these reasons, the model best matches the waveform when the Na^+ conductance is concentrated in the soma and proximal dendrites and the AP fails to fully invade the distal dendrites, as illustrated in Figure 4.10.

As illustrated in Figure 4.9, the model matches the sequence of recorded amplitudes with a simulated electrode track that approaches the soma at an oblique angle to the apical trunk, passing within a few μm of the soma near the axon initial segment. The "near miss" with the soma reproduces the high amplitude peak of 1 mV. The angle of approach to the cell is consistent with my histological measurements: in this penetration the electrode entered the cortex nearly perpendicular to the superficial layers, but the cortical folding was such that by the depth of layer 5 the electrode was nearly parallel to the cortical layers (as illustrated in Figure 4.3, P1).

I performed further simulations to estimate the maximum amplitude that could plausibly be generated by a very large layer 5 pyramidal cell in cat V1. In order to do this I used the larger Meynert cell described in detail in section 5.2.5. Starting from the channel conductance density parameters used for the simulation of Figures 4.9-4.10, I increased the Na^+conductance density until the soma had the maximum plausible peak membrane potential, around 95 mV above threshold. [Baranyi et al., 1993] (The peak soma membrane potential for the simulation of Figures 4.9-4.10 is around 65 mV above threshold.) I found that the peak negative spike generated by the simulation is

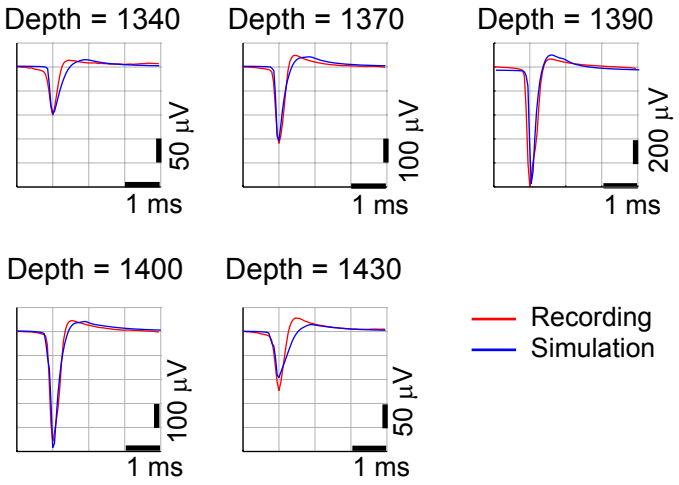

Figure 4.8: High amplitude negative spike – recording and simulation

The spike was recorded over 90 μm of penetration in area V1 with five recording sites separated by 30, 20, 10 and 30 μm respectively. Depths are shown in μm. The identification as a single unit is based on a well defined response to a single preferred orientation at the 3 high amplitude (>100 μV) recording sites; for the first and last recording site the ∼100 μV peak amplitude spike appeared as driven hash during recording and the unit was subsequently identified after filtering and clustering the raw data. The peak amplitude of the unit is 1 mV, at depth 1390, while in the recordings 20 μm before and 10 μm afterward the amplitude is only around 0.35 and 0.45 mV respectively. The simulation is based on a reconstructed layer 5 pyramidal neuron, as illustrated in Figure 4.9.

around -1.5 to -1.75 mV. As in the simulation of Figure 4.9, this peak is achieved in a very restricted region a few micrometers from the soma and near the axon initial segment.

The simulation of Figures 4.9-4.10 assumed an extracellular resistivity of 350 Ωcm resistivity: this is an above average resistivity but not the highest that may be encountered in cortex (see Figure 4.1). Such an assumption seems appropriate for modeling the highest amplitude (negative polarity) spike in my recordings. Because the extracellular resistivity could plausibly be somewhat higher, up to around 400 Ωcm, I expect that high amplitude negative spikes could plausibly range up to around -2 mV in amplitude from a very large layer 5 pyramidal cell that happened to be situated in a region of high resistivity.

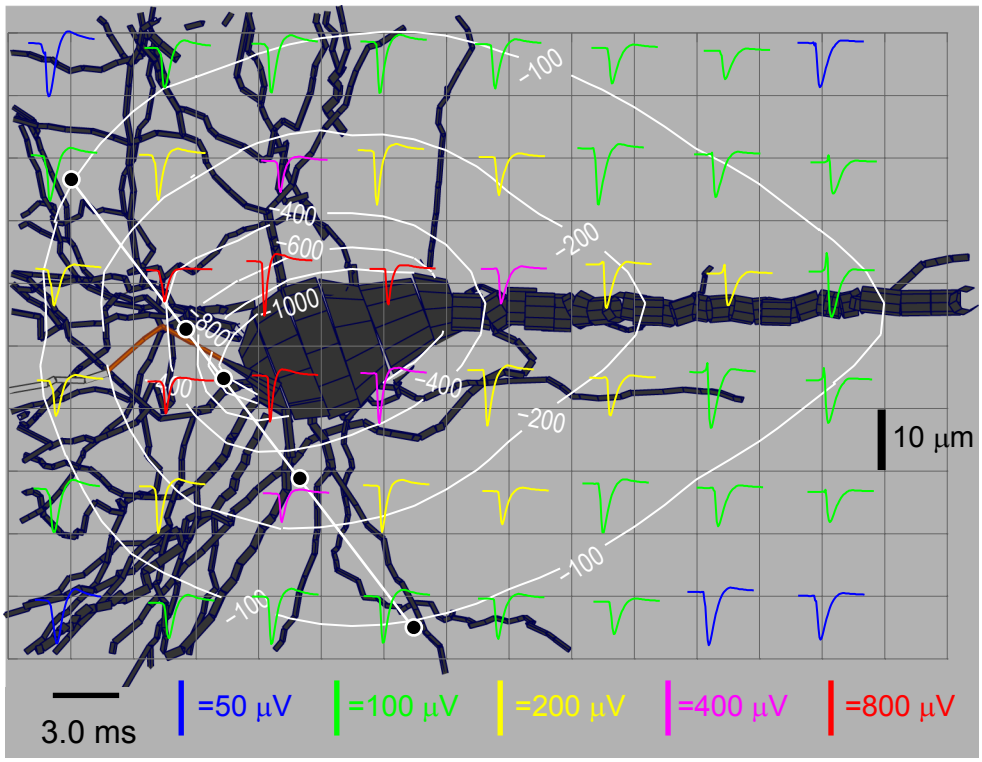

Figure 4.9: Model for high amplitude negative spike – extracellular

Illustration of spike waveforms and amplitude around the soma of a layer 5 cat V1 pyramidal neuron during the simulated action potential. The soma and dendrites are colored blue/black; non-myelinated axon, including the initial segment is brown; myelinated axon is light gray. The peak amplitude, around 1 mV, occurs at positions nearly touching the soma and near the axon initial segment. The sites chosen for the simulated electrode path, detailed in Figure 4.8, are shown as black circles with white outlines. The simulated recording sites chosen for comparison are based on a plausible trajectory of the microelectrode given the angle of penetration where the recording was made, at a shallow angle to the surface of the cortical layers (as illustrated in Figure 4.3, P1). In the simulation, the high amplitude negative spike is reproduced at a point just a few microns from the soma, near the axon hillock and initial segment.

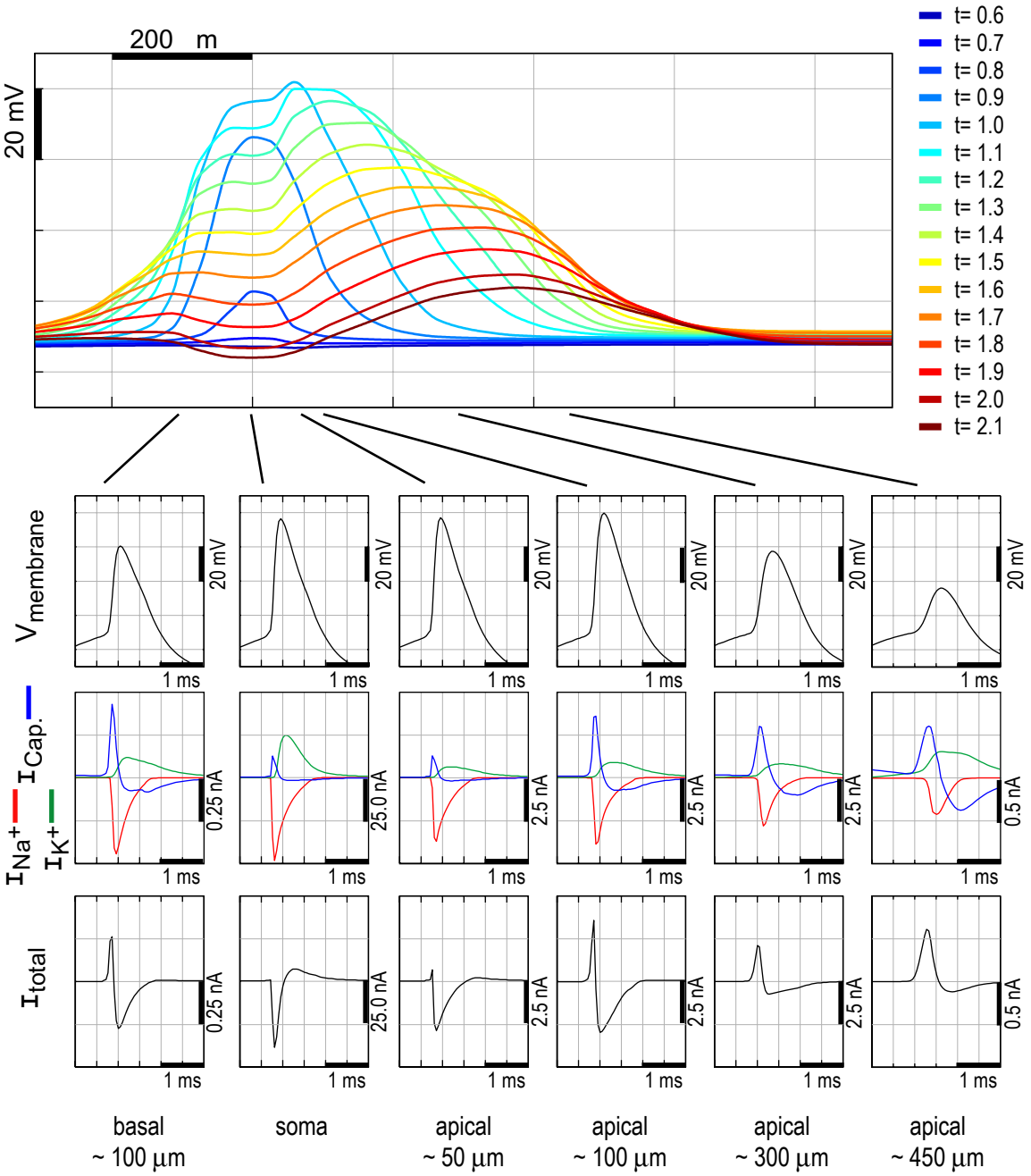

Figure 4.10: Model for high amplitude negative spike – intracellular

Top:Illustration of the membrane potential as function of position at selected times given by the color coded scale. The AP initiates first in the perisomatic region. It falls by 50% amplitude within around 400μm distance in the apical trunk and barely affects the distal apical tuft. **Bottom:** Membrane potential and current vs. time for selected compartments.

4.3.5 Model Match to Recorded EAPs

Measurements of all simulated EAPs are compared to to recordings in Figure 4.11. I find that although the average width of the Na^+ phase for the tuned model is somewhat lower than in the recordings the distributions are very compatible. Models with more uniformly distributed Na^+ conductance had Na^+ phase widths that were much narrower than the recordings. The one measurement in which the model seems a relatively poor match to the recordings is the time from the Na^+ peak to the K^+ peak. In this case the model consistently gives a somewhat longer time in every case. However, a difference of 0.1 ms in a single measure of the EAP waveform shape seems inconsequential, acceptable given the generally good match in the other measures.

Comparison of sample EAPs from the recording and in the model are shown in Figure 4.12. The recorded EAPs were chosen to be close to the average in their various measurements. However, this was difficult in many cases because the recorded waveforms were so varied that there were almost no waveforms that were simultaneously average in all the measurements. The simulated waveforms were chosen to show the generally good match between the model and recordings, as well as to illustrate some of the shortcoming (e.g., several of the comparisons clearly display the discrepancy in the typical time from the Na^+ peak to the K^+ peak.)

A more serious issue in the measurements is that the amplitude of the Na^+ peak in the model is consistently larger than those in the recordings. Because the model Na^+ peak measurements are essentially a random sample (made on a fixed grid around the cell) they should have similar distributions as recordings. There are probably two reasons for this discrepancy: The first reason is that the model measurements are generated from a sample of cell morphologies that is biased and contains unusually large cells, as described in section 4.2.1.2. A second reason is that the measurement of EAP waveforms shown in figure 4.11 allows measurements at points arbitrarily close to the cell body. In *in vivo* measurements it is likely that an electrode within a couple of microns of a neuron would rupture, disrupt, or become fused to the neuron. For this reason I repeated the measurement of the Na^+ peaks using only those model morphologies classified as "small/medium" (as described in section 4.2.1.2) and ignoring sample points that happened to be within 2 μm or less from the cell body. The results are shown in Figure 4.13. This shows that a corrected sample of the simulation amplitudes is reasonably close to the recordings. The simulation of superficial layer spiny cells (layers 2/3 and 4) still have somewhat higher peak amplitudes than the recordings. But the distributions are close enough that the difference may simply reflect the small sample size of the recordings (the sample of recording for the superficial layers consists of only a few dozen points, while the sample from the model consists of hundreds.)

The mean and standard deviation of the conductance density parameters used for cells in each layer are listed in table 4.8. The deeper layer cells had generally higher conductance densities for both Na^+ and K^+ currents due to the fact that the soma (where conductance densities were highest)

was "driving" a much larger dendritic tree. I also note that the cooperative Na^+ conductance model resulted in a much lower fraction of open channels at the peak in comparison to the Hogdkin-Huxley type model used in Chapters 2 and 3, especially for the interneuron channel model. As such the $\bar{g}$ values are much higher and not directly comparable to those from the HH model. Whether or not the fraction of open channels predicted in this model is an accurate reflection of the true conductance *in vivo* is beyond the scope of this study – my concern is that the total *current* the model generates accurately reproduces the EAP waveforms, as well as producing a plausible IAP.

	L23		**L4**		**L5**		**L6**		**IN**	
	Mean	**SD**	**Mean**	**SD**	**Mean**	**SD**	**Mean**	**SD**	**Mean**	**SD**
I_{Na^+}	0.21	0.02	0.21	0.03	0.38	0.06	0.47	0.05	5.4	0.80
I_{Na^+}axon	0.04	0	0.04	0	0.07	0.003	0.05	0.001	3.24	0
I_{Na^+}iseg	1.05	0	0.97	0.03	0.76	0	0.93	0	8.1	0
I_{Na^+}Ap. max	0.21	0	0.21	0	0.26	0	0.22	0	NA	NA
I_{Na^+}Ap. min	0.01	0.003	0.21	0	0.02	0	0.02	0	NA	NA
I_{Na^+}Bas. max	0.21	0	0.21	0	0.28	0	0.15	0	0.27	0
I_{Na^+}Bas. min	0.01	0.003	0.01	0.005	0.02	0	0.02	0	0.27	0
$I_{K^+ADist/Prox}$	0.005	0	0.005	0	0.01	0	0.01	0	0.001	0
I_{K^+C}	0.01	0	0.008	0.002	0.020	0.005	0.03	0	0.03	0
I_{K^+C}Ap. dist	20	0	20	0	150	0	150	0	NA	NA
I_{K^+C}Bas. dist	20	0	20	0	50	0	50	0	20	0
I_{K^+D}	0.003	0.001	0.003	0	0.004	0.001	0.006	0.001	0.003	0
I_{K^+K}	0.01	0	0.009	0.003	0.018	0.012	0.013	0.004	0.05	0
I_{K^+M}	0.00	0	0.002	0.001	0.003	0	0.003	0	0.005	0

Table 4.8: Cortical cell model conductance density parameters

All parameters are maximal conductance densities ($\bar{g}$) except for "I_{K^+C}Ap./Bas. dist" which are the maximum distance from the soma (μm) at which the I_{K^+C} channel is present. "Ap."=Apical. "Bas."=Basal. For layer 4 apical parameters apply to pyramidal neurons only.

In constraining the compartmental model I also considered whether the intracellular action potentials (IAPs) measured at the soma are reasonably close to those described in the *in vivo* physiology literature. This task was complicated by the fact that there are very few detailed measurements of IAPs from cat V1. The only specific measurement in the literature is in [Volgushev et al., 2000] which gives an average IAP amplitude of 55 $\pm$ 3.2 mV. This value is lower than usually reported amplitudes for IAPs in cortex: for example [Baranyi et al., 1993] reports an average value of 74 mV for action potentials in cat motor cortex. However, other studies that illustrate IAPs recorded in cat V1 (without explicitly providing average amplitude measurements) show similarly modest amplitudes, for example [Ahmed et al., 1997] (in particular see Figure 1 which clearly shows IAPs peaking at around 0 mV from a threshold of around -55 mV.)

Based on these reports in the literature I chose to compromise by tuning the model to have an

average IAP amplitude of 60 mV, while also exploring the consequences for the results if the correct IAP amplitude were either 55 mV or 70 mV as suggested by the variety of reports in the literature. As illustrated in Figure 4.14 these amplitudes were very precisely achieved by multiplying the peak Na^+ conductance only by factors of 75% and 150% to achieve average peak IAPs of around 55 mV and 70 mV respectively.

I also examined measurements of the IAP such as the threshold, duration measured at the base and at 50% amplitude, and the size of the AHP. These measurements are presented in Figure 4.15. Because I do not have specific measurements with which to compare these results, I note only that they are all reasonably close to values reported in other areas of cortex and that the measurements vary by layer in a way that is closely related to the EAP characteristics described previously: just as EAPs for spiny cells in deeper layers and interneurons tend to have narrower Na^+ phases and higher amplitude K^+ phases, their respective IAPs are also shorter in duration and have a larger AHP. I note in particular that the smooth interneuron model exhibits IAPs that are briefer in duration than any of the spiny cells, consistent with many observations in the literature (see e.g. [González-Burgos et al., 2005])

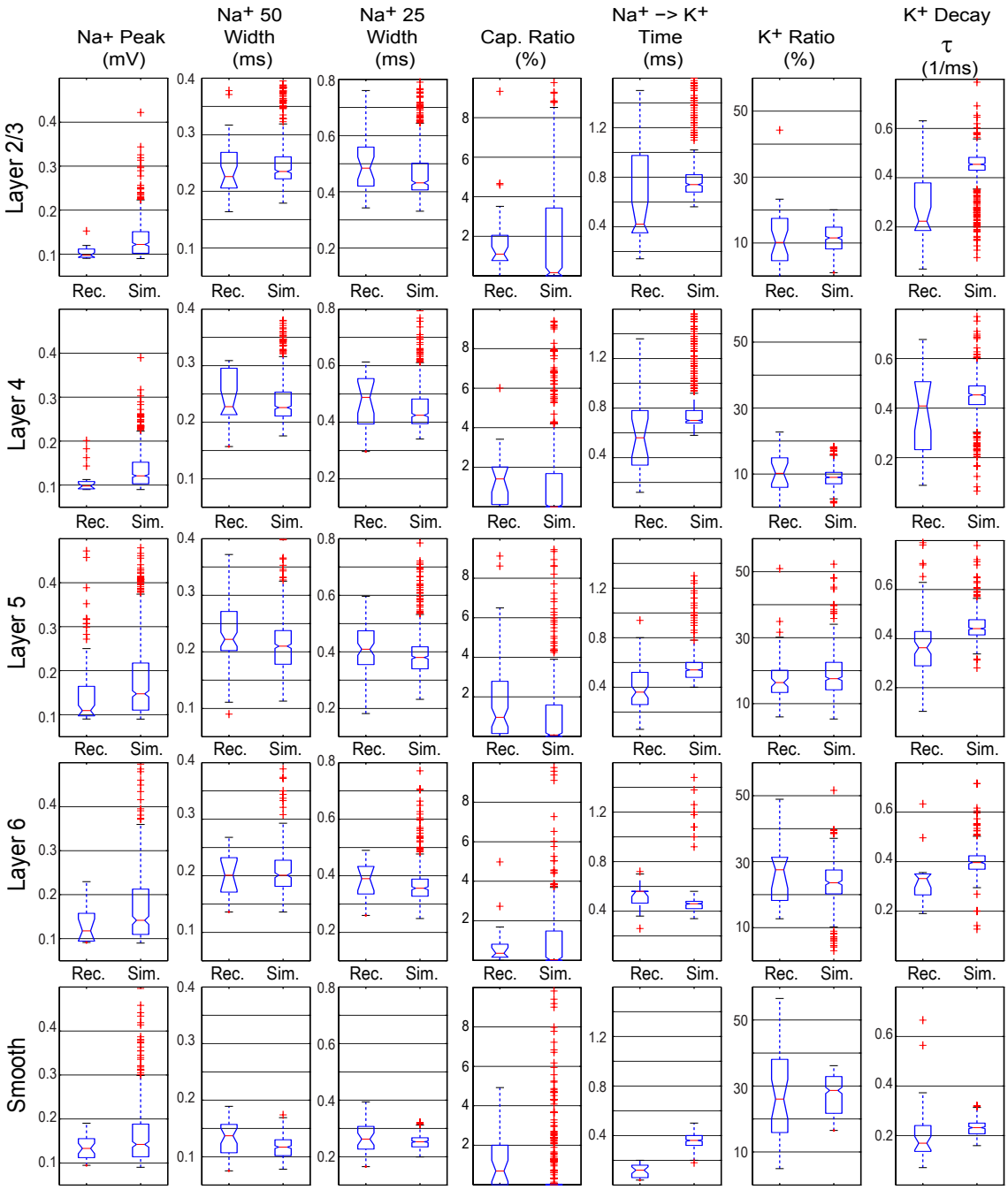

Figure 4.11: Comparison of simulation and recordings

For general description, see Figure 4.5. **Rec**: Measurement of average recorded EAP waveforms reproduced from Figure 4.5. **Sim**: Measurements taken from all the simulated neurons on a 10 μm grid as described in section 3.3.7, using a 90 μV threshold. Note that this procedure for measuring the simulated waveforms results in hundreds of samples for each measurement; as a consequence a relatively large number of samples may be considered "outliers".

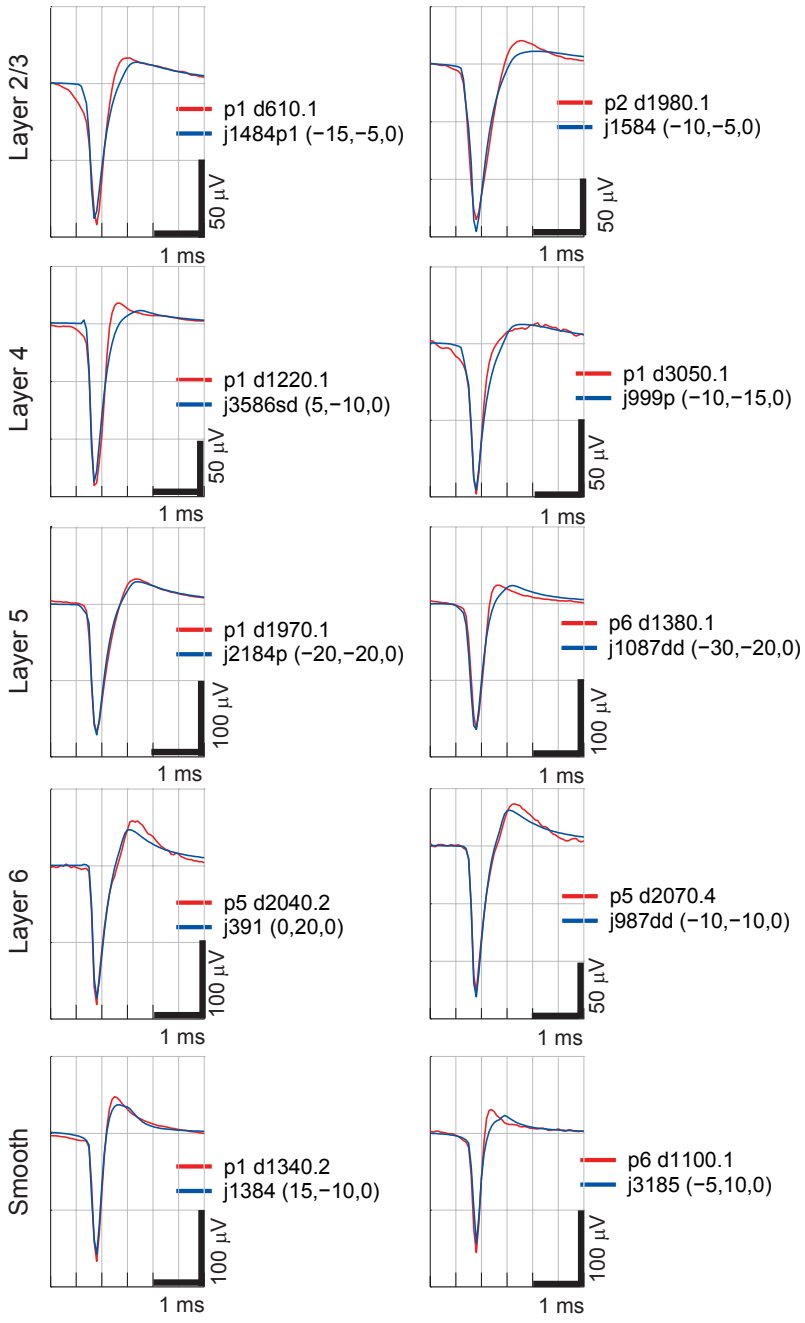

Figure 4.12: Illustration of recordings and simulations

Explanation of legends:
pA d$B.C$ = recording from penetration A made at depth B (μm), cluster number C.
j$name(X,Y,Z)$ = simulation of cell reconstruction *name*, EAP at (X,Y,Z) (μm) from the soma.

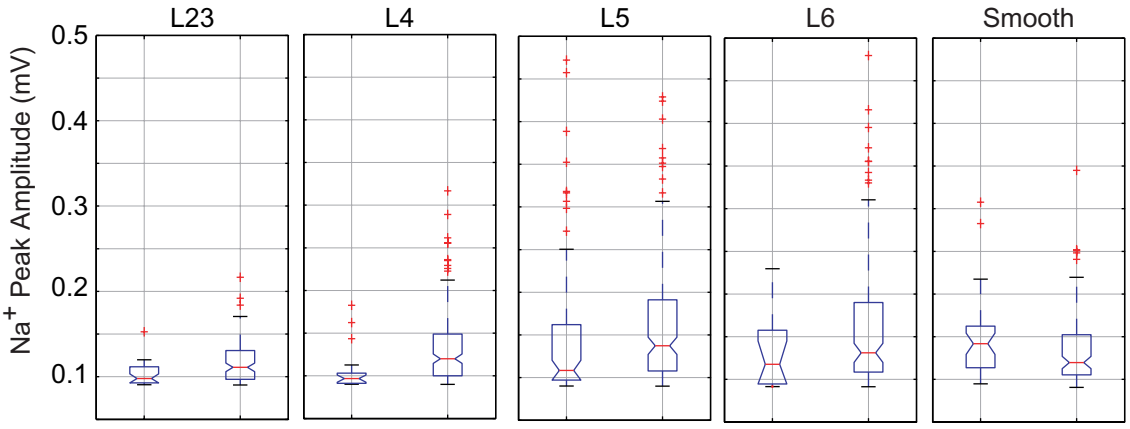

Figure 4.13: Na^+ Peak amplitude comparison with cell size and position correction

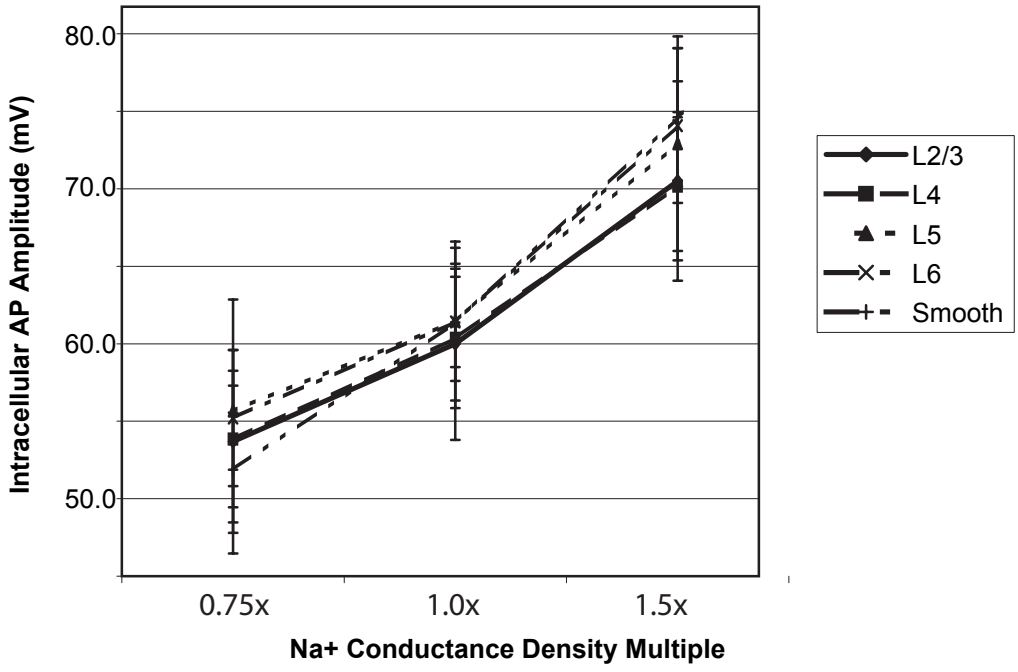

Figure 4.14: Intracellular action potential amplitude

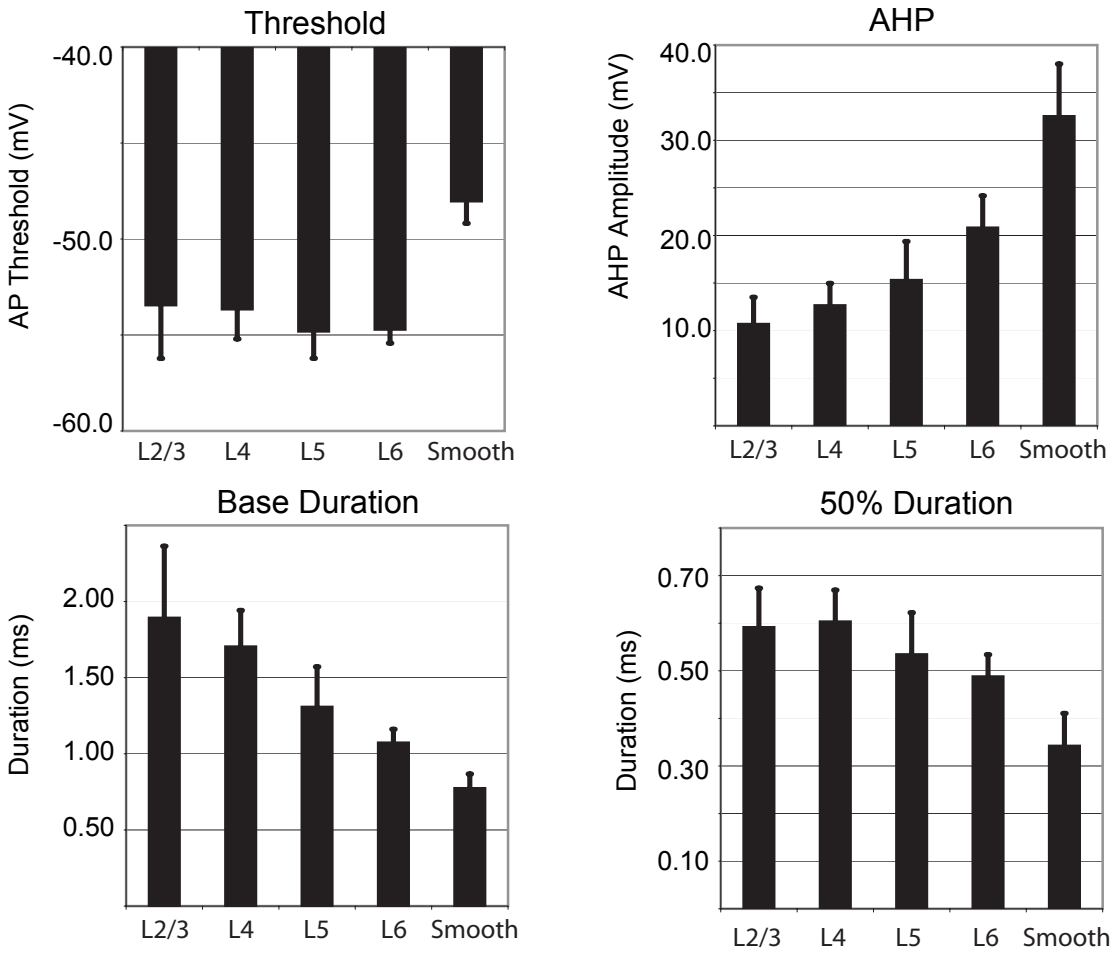

Figure 4.15: Measurements of intracellular action potentials

4.3.6 Spike Detection Range

After being satisfied that the compartmental model provides a reasonable match to the measurements of EAPs recorded in cat V1 *in vivo*, as well as to IAPs reported in the literature, I used the model to predict the region in which an extracellular recording electrode could detect a neuron as described in the methods section 4.2.1.1. Figures 4.16 and 4.17 illustrate the results of the procedure for a minimum detection threshold of 80 μV. The detection regions are nearly spherical, centered around the soma, although they frequently extend somewhat around the apical trunk and axon initial segment.

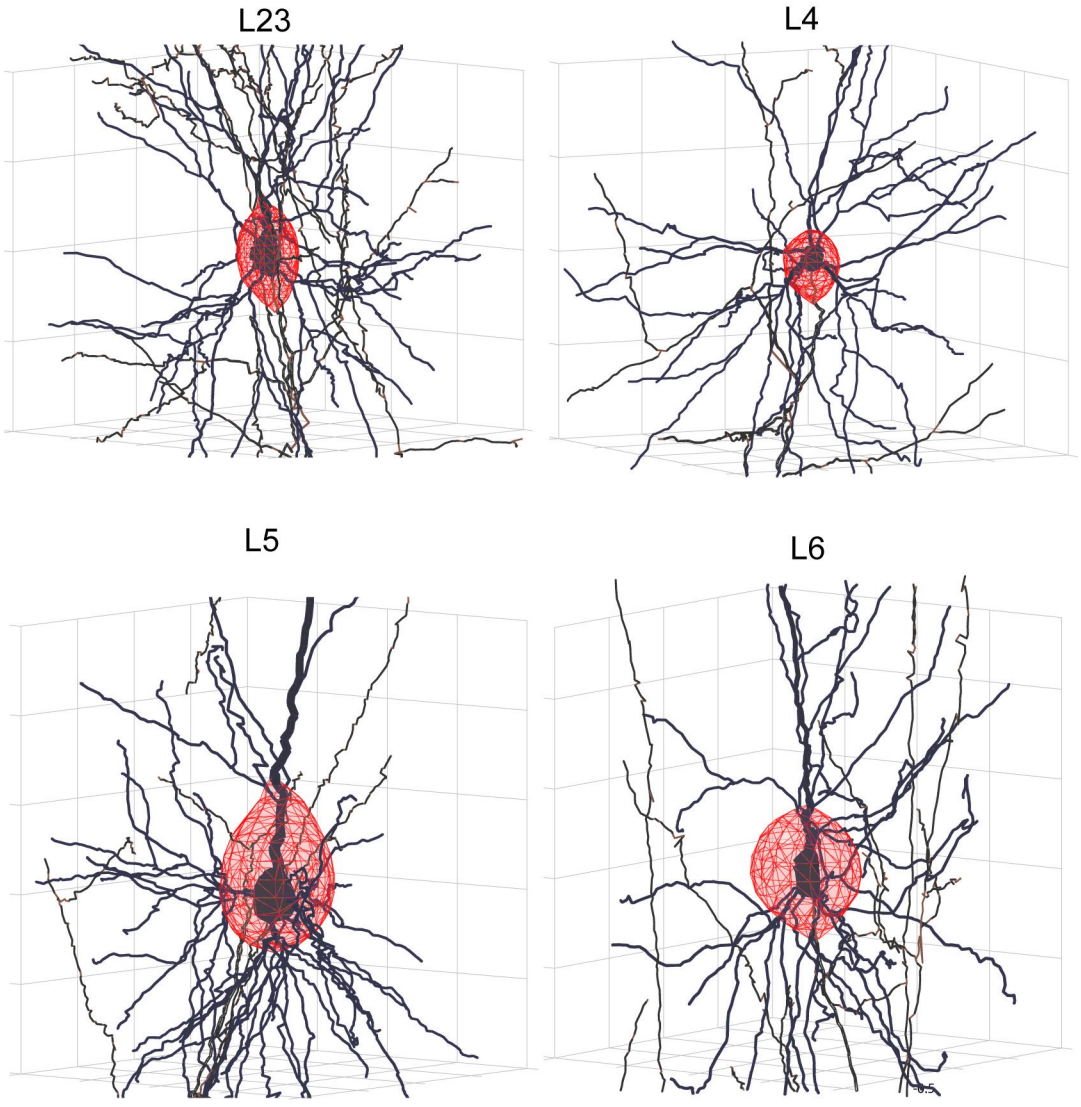

Figure 4.16: Illustration of detection region

Assuming an 80 μV threshold, the neurons have detection region volumes with equivalent radius of around 25, 20 45 and 35 μm for layers 2/3, 4, 5 and 6 respectively. Grid spacing is 20 μm.

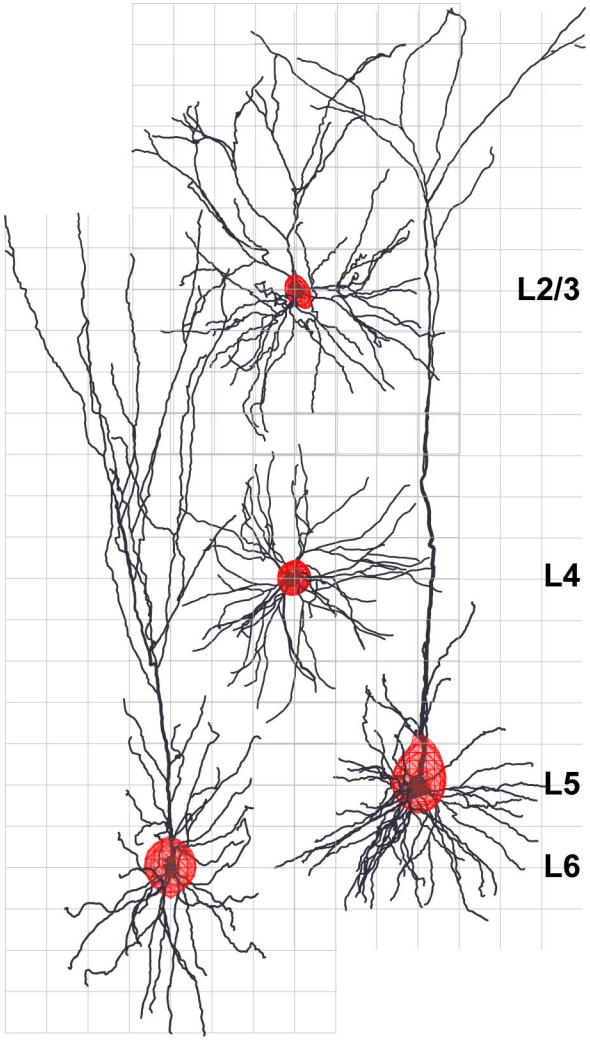

Figure 4.17: Illustration of detection regions at cortical scale

Assuming an 80 μV threshold, the neurons have detection region volumes with equivalent radius of around 25, 20 45 and 35 μm for layers 2/3, 4, 5 and 6 respectively.

Figure 4.18 shows the average detection range (equivalent volume sphere radius) for the different types of cells over a range of thresholds. Neurons in layer 5 have the highest average detection range due to their larger size, but also the highest within-class variability. Neurons from layer 5 and 6 remain detectable even up to a threshold of 500 μV, while neurons in superficial layers 2-4 become essentially undetectable (on average) above a threshold of around 250-300 μV. Smooth interneurons fall somewhere in between the superficial and deep spiny neurons.

Because the amplitude of EAPs is so highly dependent on the extracellular resistivity, I also considered how the detection ranges depend on this important parameter. The results, illustrated in Figure 4.19 show that for all cell classes the detection range varies by around a factor of two from the lowest value of cortical resistivity (150 Ωcm) to the highest value (400 Ωcm.) While I only consider

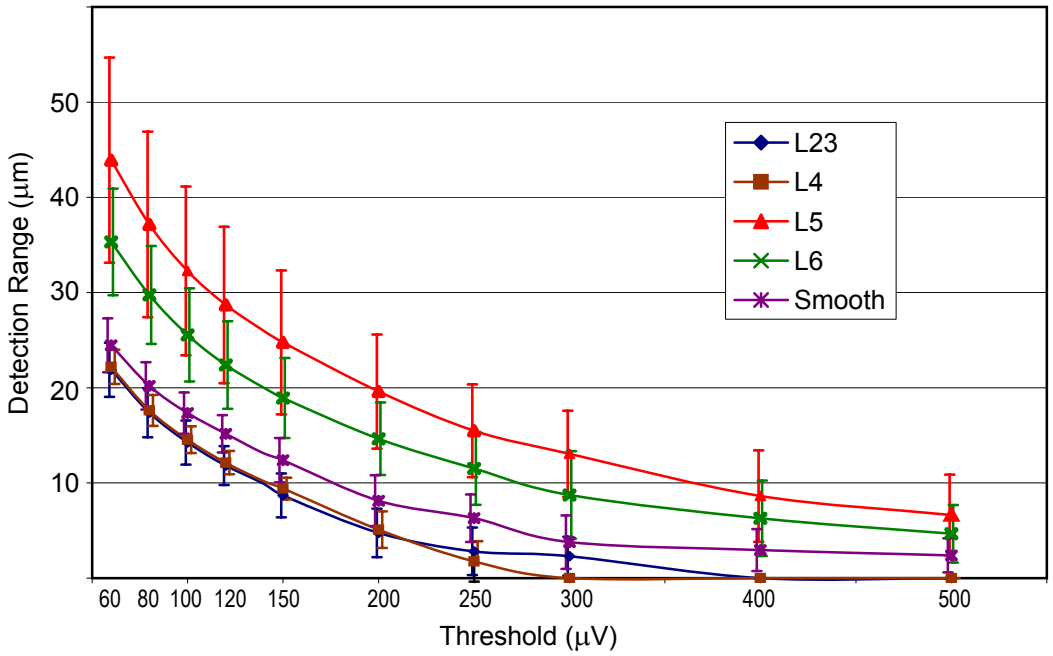

Figure 4.18: Average detection radius vs. threshold

the typical cortical resistivity of 250 Ωcm when I calculate the cortical activity and sampling bias, it is worth bearing in mind that the actual detection range may vary widely for individual cells depending upon not only the properties of the cell itself but also the resistivity of the neuropil that it happens to be located in.

While it is the average detection range that is important for statistical analysis, an interesting question is what is the maximum detection range for cells in each class. To pose an answer to this question I chose the largest cell in each category and increased its Na^+ conductance density until it yield an IAP of 85 mV amplitude – close to the maximum plausible value for cortical cells [Baranyi et al., 1993]. I then calculated the detection range assuming the high resistivity of 350 Ωcm, and a low level of background noise allowing detection and clustering at a threshold of 60 μV. The results are illustrated in table 4.10. They show that the highest plausible detection range for cortical cells is 80 μm for layer 5, around 50 μm for layer 6, and around 40 μm for layers 2/3, 4 and smooth interneurons.

Layer	Soma Diameter (μm)	Total Dendrite Length (μm)	Maximum Detect Radius (μm)
L23	20.5	11,566	41
L4	28.6	5,916	38
L5	33.5	21,257	80
L6	19.2	8,718	49
Smooth	25.6	6,390	42

Table 4.10: Maximum detection ranges for cortical cells
Soma Diameter and Total Dendrite Length: Equivalent sphere diameter of the soma and total length of all dendrites for the neuron used in the simulation. These neurons were chosen for having the largest soma size in their category. **Maximum Detect Radius**: Equivalent radius of the detection region assuming 350 Ωcm resistivity and 60 μV detection threshold.

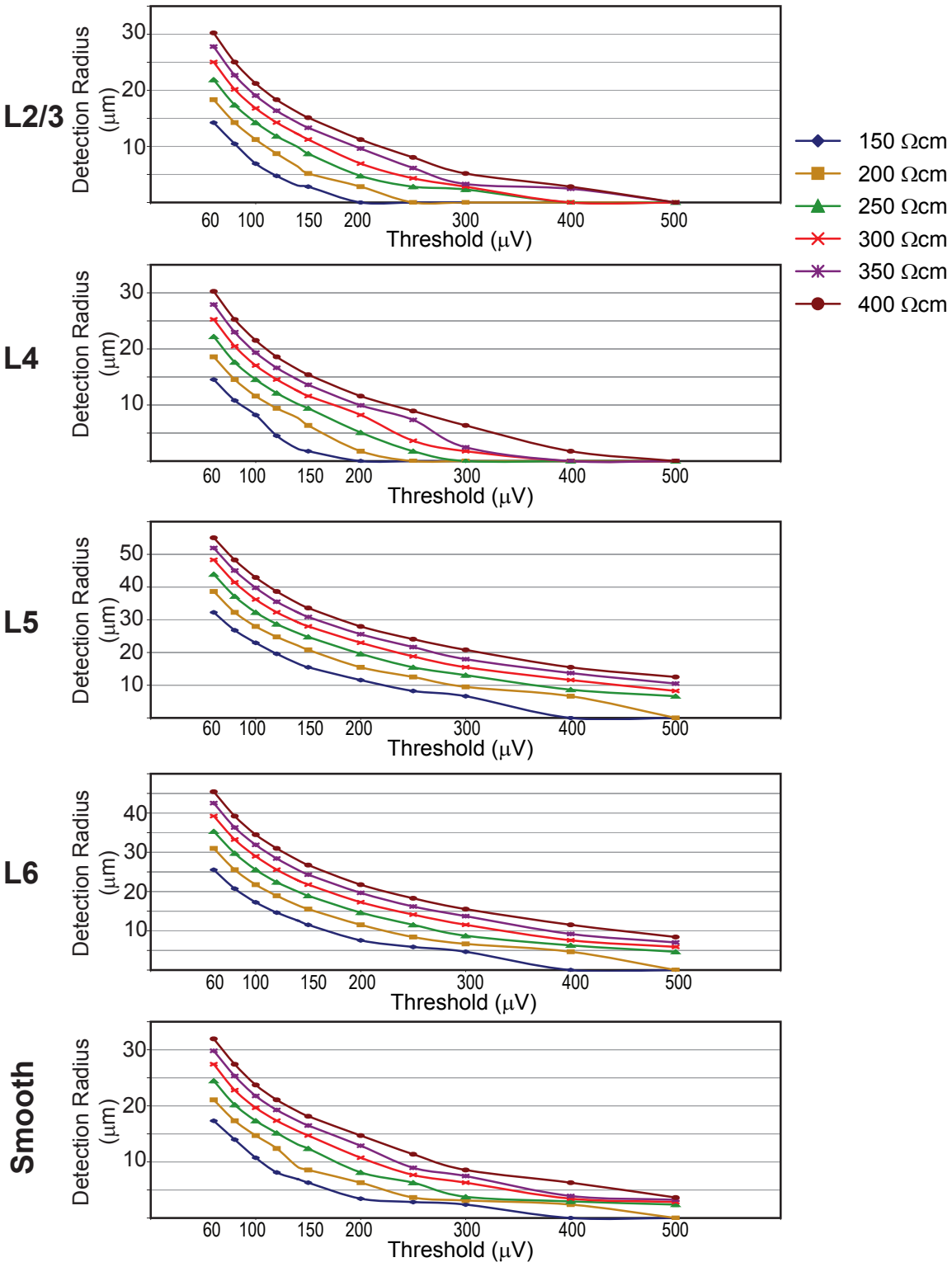

Figure 4.19: Impact of resistivity on average detection radius

4.3.7 Fraction of Neurons Active

In order to simulate the average detection radius and estimate the fraction of active neurons requires the intermediate step of determining the number of neurons typically within range for each layer. This step depends on the packing density of neurons, which are reported in [Bealieau and Colonier, 1983]. The average values I use (as described in the computational methods, section 4.2.1.1) are listed in table 4.12. Layer 5 has the lowest packing density of neurons, although the densities of all cortical layers in cat V1 are relatively close together in comparison to other brain regions. For example, the CA1 region of the hippocampus has a packing density of 300,000 neurons/mm^3 [Aika et al., 1994] – an order of magnitude greater than the cortical packing densities.

layer	width (μm)	volume under 1 mm^2 (mm^3)	Depth Fraction	Spiny Neuron Density (/mm^3)	Equivalent Grid Cell Spacing	Spiny Neurons Under 1 mm^2	Cells Fraction
L2/3	461	0.461	38.0%	4.64×10^4	27.8	2.06×10^4	38.3%
L4	428	0.428	35.3%	4.76×10^4	27.6	1.84×10^4	34.3%
L5	121	0.121	10.0%	3.35×10^4	31.2	4.28×10^3	8.0%
L6a	204	0.204	16.8%	5.08×10^4	27	1.04×10^4	19.4%

Table 4.12: Number of neurons and thickness of layers

Averages values for spiny neurons based on the data reported in [Bealieau and Colonier, 1983]

Figure 4.20 shows the results for the number of neurons within range as well as illustrating the dependence on the IAP amplitude in the model. The results range from only around one neuron in range for the superficial layers (2-4), up to 5 or 10 neurons in range for the deeper layers (5, 6). Figure 4.20 demonstrates that apparently modest differences in the detection radius lead to much greater differences in the number of neurons in range. This is because the volume of a detection sphere is cubic in the radius, so while the detection range (radius) of layer 5 pyramidal neurons is only around two times that for layer 2-4 spiny neurons the volume of the detection region (which determine the number of cells in range) is close to ten times greater. The impact of the Na^+conductance density, as illustrated by the IAP amplitude is significant: for every cell class the 55 mV IAP (75% Na^+ conductance density) yields approximately half the cells in range as the 70 mV IAP (150% Na^+ density).

My estimate of the number of neurons that were active during my protocol (for each cell class) is simply the ratio of the number of neurons recorded per location (table 4.6) divided by the number of neurons within range (Equation 4.1). The results shown at the bottom of Figure 4.20, which do not include the correction for multi-unit recording, suggest that neurons in the superficial layers 2-4 are substantially more active than neurons in the deeper layers, 5 and 6: While I predict that

approximately 50% of neurons in superficial layers are active (∼65% for layers 2/3 and ∼45% for layer 4) I predict only a small minority of neurons are active in the deeper layers (∼10% for layer 5 and ∼15% for layer 6.) The average results for the smooth interneurons seems to be somewhere in between. This difference results from the fact that while I recorded more units per location in deeper layers (e.g., ∼0.8 per location in layer 5 vs. ∼ 0.5 per location in layer 4), these are far short of the difference in the number of neurons in range predicted by the model. An interesting result is obtained if I weight my average activity estimate for each layer (Figure 4.20) with the fraction of total neurons in each layer (table 4.12): this yields an overall activity level of 38% of the neurons in cat V1, assuming a 60 mV IAP amplitude (counting interneurons as 20% of the total number of spiny neurons in all layers).

The precise results for each layer depend strongly on the model IAP amplitude. But this does not affect the qualitative conclusion that the superficial layers are most active. For example, if I assumed that deep layer neurons had 55 mV average IAPs and superficial layer neurons had 70 mV average IAPs I would still predict that superficial layer neurons were around twice as active as deeper layer neurons, rather than the prediction of around four times as active that I make assuming all layers have an average IAP amplitude of 60 mV.

Figure 4.21 illustrates the impact of my correction to the average detection range for the large cell bias in my morphology sample, described in section 4.2.1.2. While the impact in the average detection range is quite modest it leads to a significant difference in the number of neurons in electrode range and the estimate of the fraction of cells that are active. Not surprisingly, I estimate a somewhat higher proportion of cells are active using the correction. This is because weighting the detection range towards the smaller cells in my morphology sample reduces the average detection range. The greatest absolute impact is on the active cells fraction is in layer 2/3. But note that the relative impact for all layers is more similar. The weighting results in about a 30% reduction in the number of neurons within range for both layer 2/3 and layer 5 while the change is about 20% for layers 4 and 6. Consequently the weighting results in an increase in the activity estimate of around 45%-50% for both layers 2/3 and 5, and around 20%-25% percents for layers 4 and 6. The absolute correction is greatest for layer 2/3 mainly because it has the largest estimated activity to begin with.

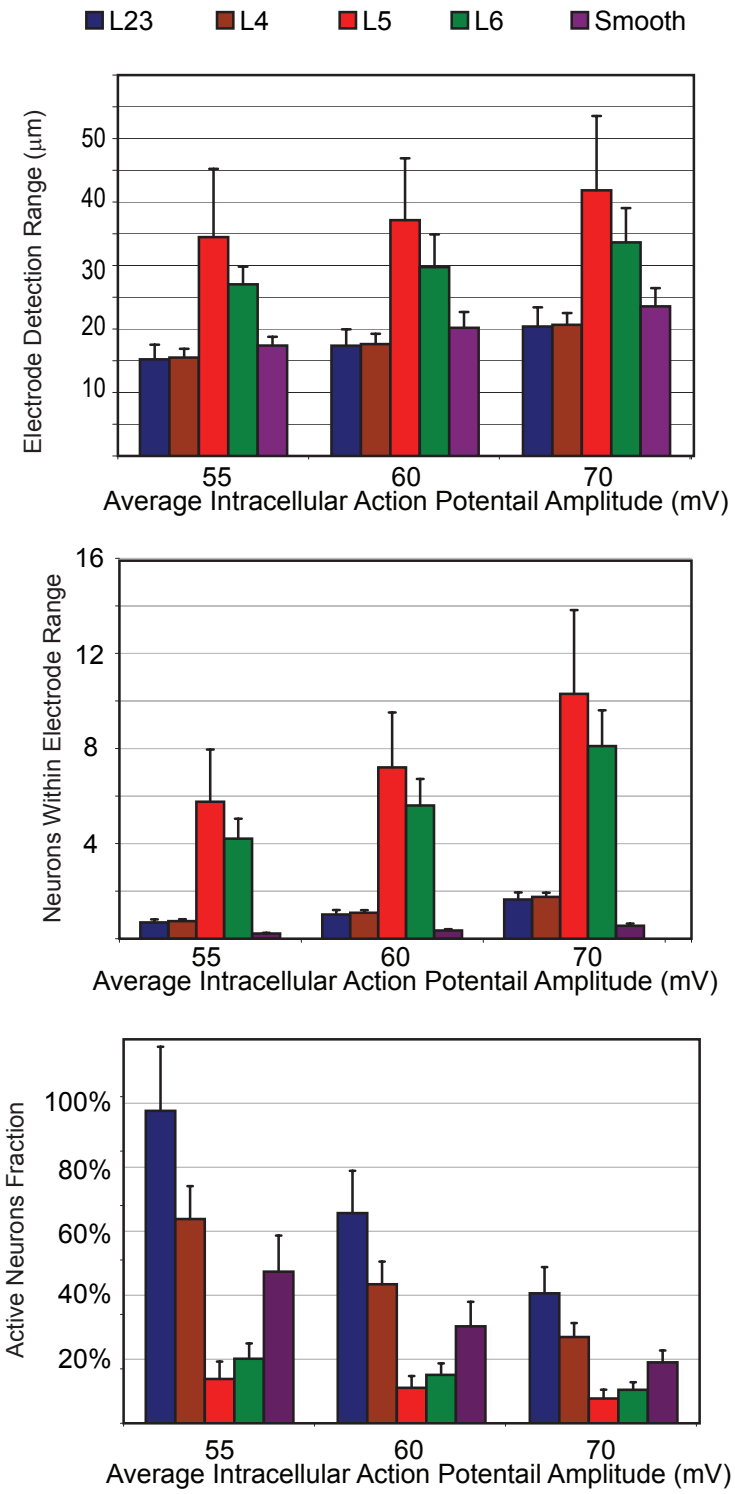

Figure 4.20: Active neurons fraction and AP amplitude

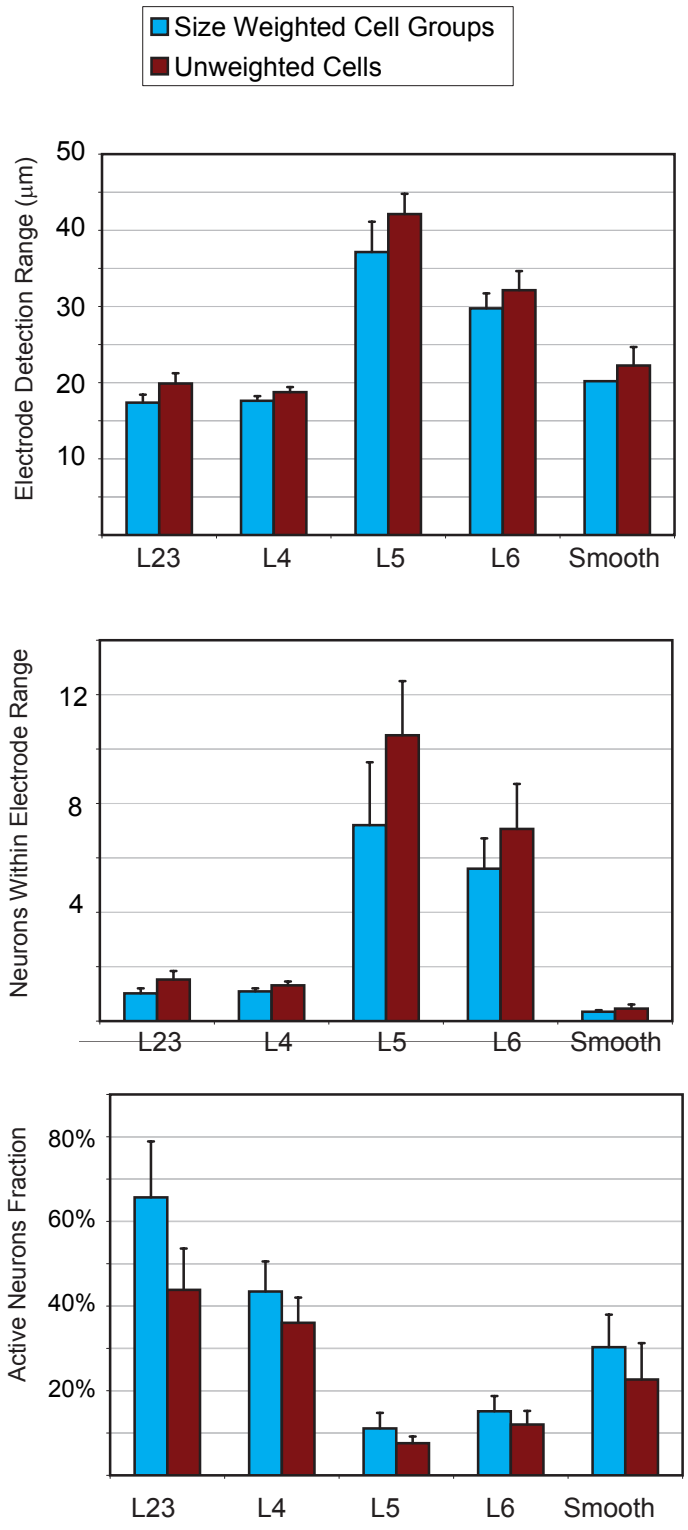

Figure 4.21: Cell size correction

Comparison of the electrode detection range, neurons within electrode range and resulting active neurons fraction when the average detection range is calculated with ("Size weighted cell groups") and without ("Unweighted cells") the correction for the diameter bias in my morphological sample, described in section 4.2.1.2.

4.3.8 Multi-Unit Recording

Figure 4.22 shows the impact of the correction for multi-unit clusters. Like the correction for cell size bias, the correction has the largest absolute impact on the estimated activity for the superficial layers, while it makes less absolute difference for the deeper layers. Note that there is no multi-unit correction for the smooth interneurons because the lower packing density of smooth interneurons leads me to conclude that on average there will not typically be two smooth interneurons in range of the electrode at the same time. Following my correction for multi-unit clusters, I conclude that as many as 85% of layer 2/3 spiny neurons may be active, an increase of 16%, while the number of layer 4 neurons active is around 55%, an increase of 7%. The model predicts less increase in the activity fraction of layer 5 and 6 spiny neurons, increasing to around 12% and 18% respectively, increases of around 1% and 3%. When viewed as a relative increase the impact of the multi-unit correction is more similar across the different layers, but still the greatest for layer 2/3: the active fractions are increased by around 30%, 20%, 10% and 20% over the baseline values for layers 2/3, 4, 5 and 6 respectively. Figure 4.22 also illustrates what the results would be if I had assumed a broader range of amplitudes for the formation of multi-unit clusters. If my clustering algorithm formed multi-unit clusters in a 35 μV range instead of a 25 μV range my estimate for the fraction of active units in layer 2/3 would have to be increased to nearly 100%, while the estimate for activity in layer 4 would be increased to around 60%. Estimates for the deeper layers would increase to around 13% and 19% for layers 5 and 6 respectively. Using these new estimates of activity per layer (with 25 μV multi-unit clustering ranges) to calculate the overall activity level in cat V1, I estimate that an average 48% of all neurons in cat V1 were active in my protocol.

Table 4.14 illustrates the input data to the correction formula, equation 4.9: the number of units recorded in each 5 μV amplitude range, the 25 μV ranges in which multi-unit clusters would be formed, and the average fraction of the volume in which another cell would present a spike of that amplitude ("overlap"). For example, for layer 2/3 6 spikes were recorded in the range of 80-85 μV; I estimate that each of these recordings had a 50% probability of being in a location where another neuron would produce a spike with an amplitude ranging from 70 to 95 μV. For layer 5 the overlap fraction for the same amplitude range is 219%, meaning that on average each of these spikes was recorded in a location where 2.19 other neurons would produce a spike in the Multi-Unit range.

Examples of the overlap calculation are illustrated in 2D in figure 4.22. For all layers, the largest number of recordings were made at the smallest amplitudes, where the overlap fractions are highest. For superficial layers (2-4) the overlap fractions start at around 50% and there is no overlap for spikes greater than 120 μV. For deep layers (5, 6) the overlap fractions at the lowest amplitude are greater than 100%: this is due to the fact that in some regions of the volume defined by the amplitude range there will actually be multiple adjacent neurons that would produce a spike in that amplitude. For deep layer neurons there is a non-zero overlap fraction up to around 250 μV; however, in practice,

the high amplitude range of spike recordings has very little impact on the correction because many fewer neurons are actually recorded at that amplitude. As illustrated in Figure 4.23, this results from the fact that the volume of the amplitude range shells declines sigifnicantly at higher amplitude.

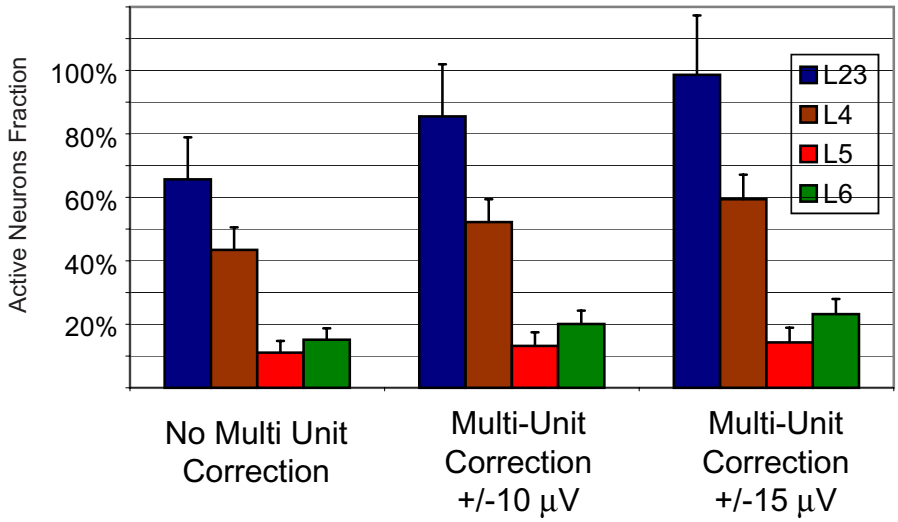

Figure 4.22: Multi-unit cluster correction

Voltage Range (μV)				L23		L4		L5		L6	
Detect		Multi-Unit		#	Ov.	#	Ov.	#	Ov.	#	Ov.
Min	Max	Min	Max	Unit	%	Unit	%	Unit	%	Unit	%
80	85	70	95	6	50%	9	51%	14	219%	11	212%
85	90	75	100	15	46%	9	46%	9	199%	5	197%
90	95	80	105	8	40%	8	40%	12	179%	4	179%
95	100	85	110	7	33%	2	36%	9	165%	0	168%
100	105	90	115	0	22%	4	28%	8	152%	1	156%
105	110	95	120	3	8%	0	15%	6	141%	0	141%
110	115	100	125	4	1%	1	5%	2	132%	1	123%
115	120	105	130	1	0%	0	0%	1	123%	1	103%
120	125	110	135	0	0%	0	0%	2	114%	0	88%
125	130	115	140	0	0%	0	0%	2	104%	0	83%
130	135	120	145	0	0%	0	0%	2	91%	1	79%
135	140	125	150	0	0%	0	0%	1	79%	0	76%
140	145	130	155	0	0%	1	0%	1	71%	0	68%
145	150	135	160	0	0%	0	0%	0	68%	0	55%
150	155	140	165	1	0%	0	0%	0	65%	1	39%
155	160	145	170	0	0%	0	0%	0	63%	0	30%
160	165	150	175	0	0%	1	0%	2	61%	0	27%
165	170	155	180	0	0%	0	0%	1	59%	0	26%
170	175	160	185	0	0%	0	0%	1	51%	0	24%
175	180	165	190	0	0%	0	0%	0	38%	1	23%
180	185	170	195	0	0%	1	0%	1	28%	0	22%
185	190	175	200	0	0%	0	0%	0	24%	0	21%
190	195	180	205	0	0%	0	0%	0	23%	0	20%
195	200	185	210	0	0%	0	0%	0	23%	0	19%
200	205	190	215	0	0%	0	0%	0	25%	0	18%
205	210	195	220	0	0%	0	0%	0	25%	0	17%
210	215	200	225	0	0%	0	0%	0	23%	0	15%
215	220	205	230	0	0%	0	0%	1	22%	0	10%
220	225	210	235	0	0%	0	0%	0	20%	1	4%
225	230	215	240	0	0%	0	0%	0	17%	1	1%
230	235	220	245	0	0%	0	0%	0	17%	0	0%
235	240	225	250	0	0%	0	0%	0	16%	0	0%
240	245	230	255	0	0%	0	0%	0	14%	0	0%
245	250	235	260	0	0%	0	0%	0	10%	0	0%
250	255	240	265	0	0%	0	0%	1	5%	0	0%
255	260	245	270	0	0%	0	0%	0	0%	0	0%

Table 4.14: Illustration of the multi-unit correction

This table shows the data used for the multi-unit correction described in section 4.2.1.3. Recordings are divided into 5 μV amplitude ranges: **Detect Min/Max**; each 5 μV range corresponds to a 25 μV range in which those spikes would be clustered together with spikes from other neurons having similar amplitude, **Multi-Unit Min/Max**. The table lists the number of recordings where the amplitude was in each range, **# Unit**, and the corresponding fractional overlap volume for the spheres defined by multi-unit range, **Ov. %**.

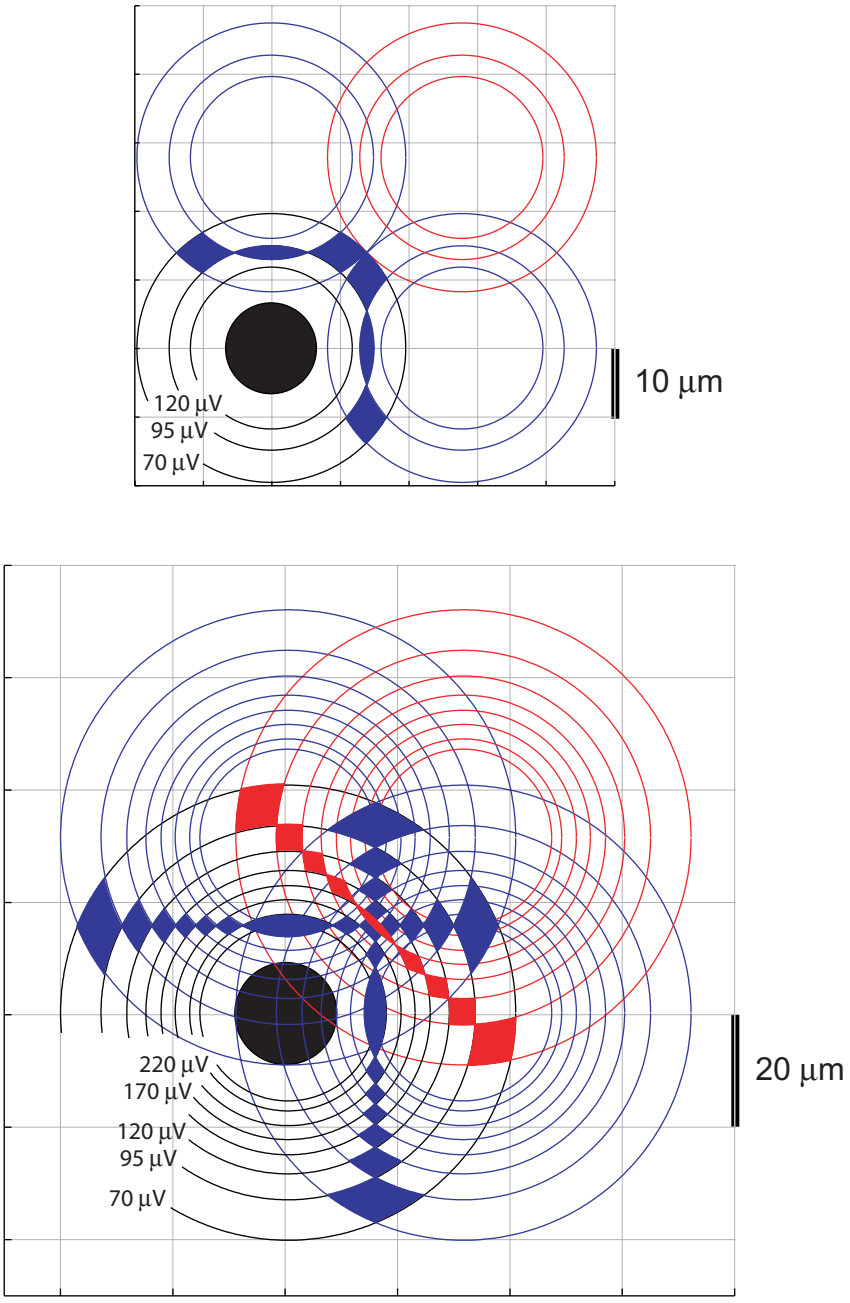

Figure 4.23: Illustration of multi-unit cluster overlap regions

Top: Illustration of adjacent multi-unit overlap regions for an L2/3 neuron, two nearest neighbors, and one near diagonal neighbor. The grid spacing is 27.8 μm (see table 4.12), and detection radii of 19.6, 14.9 and 11.8 μm for 70, 95 and 120 μV thresholds respectively. Because the distance to diagonal neighbors (red) is greater than the maximum detection range they do not contribute. **Bottom**: Illustration of adjacent multi-unit correction for a layer 5 neuron showing two nearest neighbors and one near diagonal neighbor. The grid spacing is 31.2 μm and the detection radii are 40.5 33.3, 28.7, 25.3, 22.6, 20.1, 17.5 and 15.7 μm for thresholds of 70, 95, 120, 145, 170, 195, 220, and 245 μV. Nearest neighbors (blue) contribute the most multi-unit detection regions, and near diagonal neighbors (red) also contribute up to a threshold of 170 μV. For spikes with amplitude greater than 250 μV I expect a single unit recording only.

4.3.9 Sampling Bias

Combining my estimates for the fraction of neurons active (Figure 4.22), the average detection range (volume) for neurons in different layers (Figure 4.18), and the packing density of neurons (table 4.12) I can calculate the sampling probability for spiny neurons in the different layers according to equation 4.11. The results are illustrated in Figure 4.24, which shows estimates for a range of thresholds and different assumptions about the fraction of active neurons and the thickness of the cortical layers. When I combine the recording probabilities for each layer with the fraction of cells located in each layer I calculate sampling bias, according to equation 4.12. These results are illustrated in Figure 4.25.

Using my calculations for cat V1, I predict that at the lowest threshold (80 μV) the largest proportion of recordings should come from layer 2/3 and the smallest from layer 5. Layer 2/3 would produce the largest number of recordings because it is approximately tied with layer 4 for the largest thickness, but is significantly more active than layer 4. While the average detection range for layer 5 is the greatest, the small thickness of this layer combined with the low proportion of cells that are active result in it only producing 10% of recordings. However, even under these circumstances there is some bias towards layer 5: at the 80 μV threshold there is a bias of $\sim$1.7 to record from layer 5 ($\sim$170% as many recordings from layer 5 as there are cells.)

This situation changes dramatically if the threshold for recording is increased. 150 μV is approximately the minimum threshold for which units are readily apparent in an online oscilloscope or a speaker connected to the recording electrode. With this threshold layer 5 and 6 neurons would make up about 20% and 40% of the recordings respectively, while layer 2/3 and 4 decline to around 40% and 20%. At 150 μV threshold I would be biased by around 2.5 times towards layer 5 and 1.5 times towards layer 6. Layer 6 would make a higher proportion of the recordings than layer 5 because, although the average spike detection radius is lower for layer 6, layer 6 is thicker and has a higher packing density of neurons which are more active than those in layer 5.

In practice, recordings may be made with a higher minimum threshold, for example in an attempt to ensure that a unit remains isolated during a long experiment. If a set of recordings used a minimum threshold of 300 μV layers 5 and 6 would completely dominate the recordings, producing around 45% each. Layer 2/3 would produce 10% and layer 4 would most likely produce no recordings. At such a high minimum threshold I would be biased 6 times towards layer 5 and 2.5 times towards layer 6. The higher sampling bias towards layer 5 than towards layer 6 reflects the fact that layer 5 makes up many fewer of the neurons in cat visual cortex, while at the high threshold it would make up an equal number of recordings.

I also looked at how some of my assumptions affected the results – this not only increases my understanding of the factors at work but may have relevance to other regions of cortex. First I looked at how the results would change if all layers of cortex were equally active. (Inspection of

equations 4.10 and 4.11 shows that if all layers are equally active the results do not depend on what the activity fraction actually is.) If all layers were equally active the deeper layers would dominate recording even at the lowest threshold level. Layer 6 would lead layer 5 in the sampling probability at low threshold, but they would equalize at a threshold of around 200 μV. At a 300 μV threshold layer 5 would make up 55% of the recordings, representing a sampling bias of 8x. This calculation illustrates the fact that the difference in activity between layers seems to allow superficial layers to be recorded in reasonable numbers, despite the smaller size of the neurons there.

I next examined how the difference in layer thickness impacts the sampling probabilities and bias. This calculation is definitely relevant to other regions of cortex: examination of a variety of cortical regions in the cat shows that in a sample of 12 different cortical regions the average thickness of the layers 2-6A is, on average, nearly equal. For details, see appendix D. For this reason I recalculated sampling probability and bias under the assumption that layers 2/3 made up 40% of the thickness of cortex and layers 4, 5, and 6A made up 20% each. The results is a substantial increase in the probability of sampling from layer 5, and a decrease in the probability of sampling from layer 4. Layers 2/3 and 6 are not much affected because their relative thickness in area V1 is close to the average value for multiple cortical regions. It is interesting to note that while the sampling probability for layer 5 increases substantially the *bias* towards layer 5 actually decreases slightly in comparison to the calculation for V1: under these conditions the increase in sampling probability is somewhat less than the increase in the fraction of cells contained in layer 5.

Finally, I considered the case of uniform activity combined with uniform cortical layer thickness. If this condition were to hold in some region of cortex layer 5 would make up the largest proportion of samples at any threshold, and a majority at thresholds as low as 150 μV. At a threshold of 150 μV the superficial layers combined would only account for around 15% of all recordings. Bias towards layer 5 would be relatively high, 3 times, even at low thresholds despite the increase in the number of cells in layer 5 due to the uniform layer thickness. At high thresholds deeper layers would completely dominate recordings, with layer 5 producing about twice as many samples as layer 6.

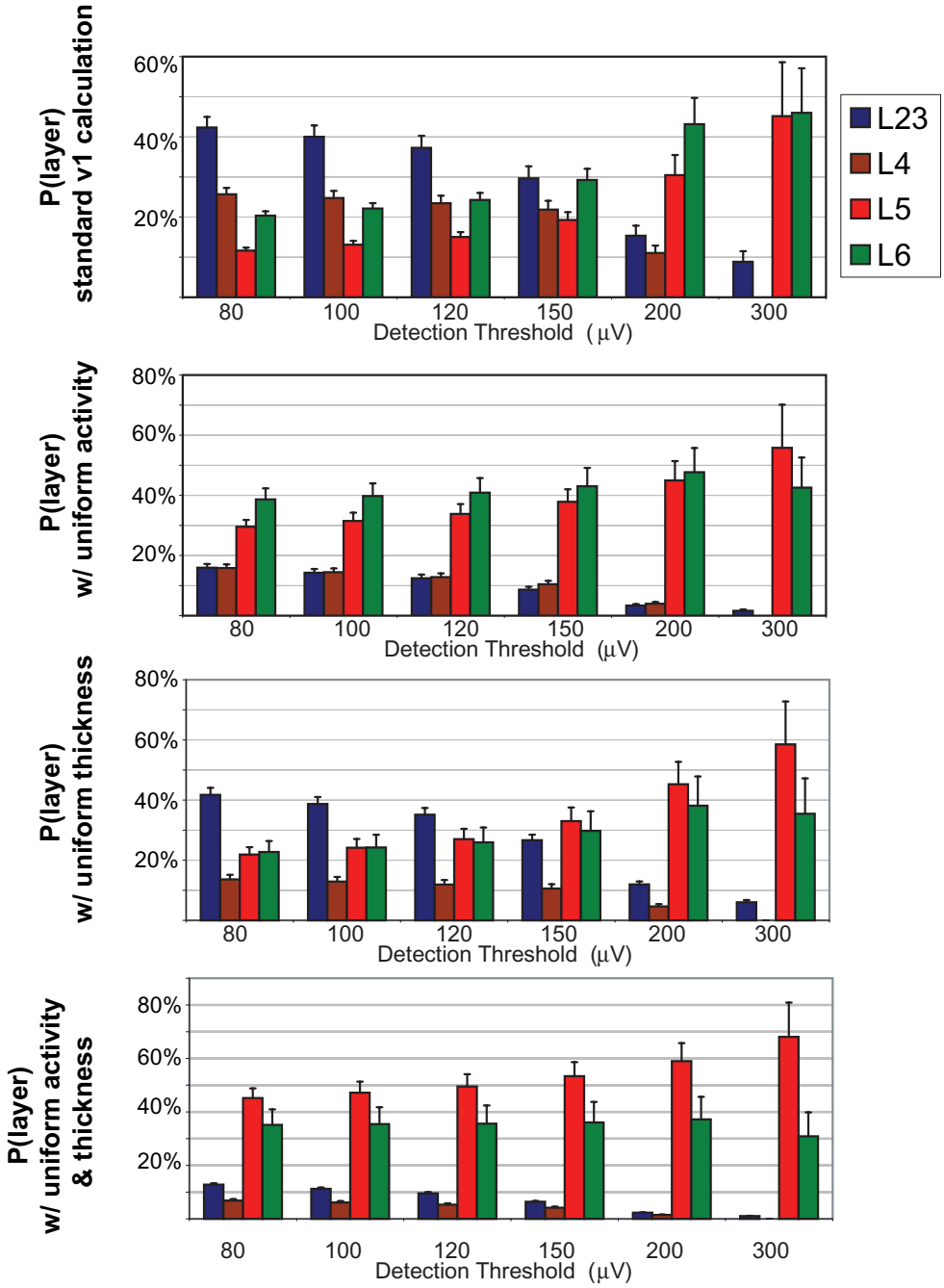

Figure 4.24: Sampling probability

standard v1 calculation: Calculation of the probability of recording from each layer for different detection thresholds, assuming a randomly sampling electrode. Equivalently, the proportion of recordings that would be made with an electrode that penetrated perpendicular to the cortical layering. **w/ uniform activity**: What the probability would be if neurons in all layers were equally active. **w/ uniform thickness**: What the probability would be if all layers of cortex were equally thick with the activity fractions calculated in V1. **w/ uniform activity & thickness**: What the probability would be if all cells in all layers were equally active and all layers had uniform thickness.

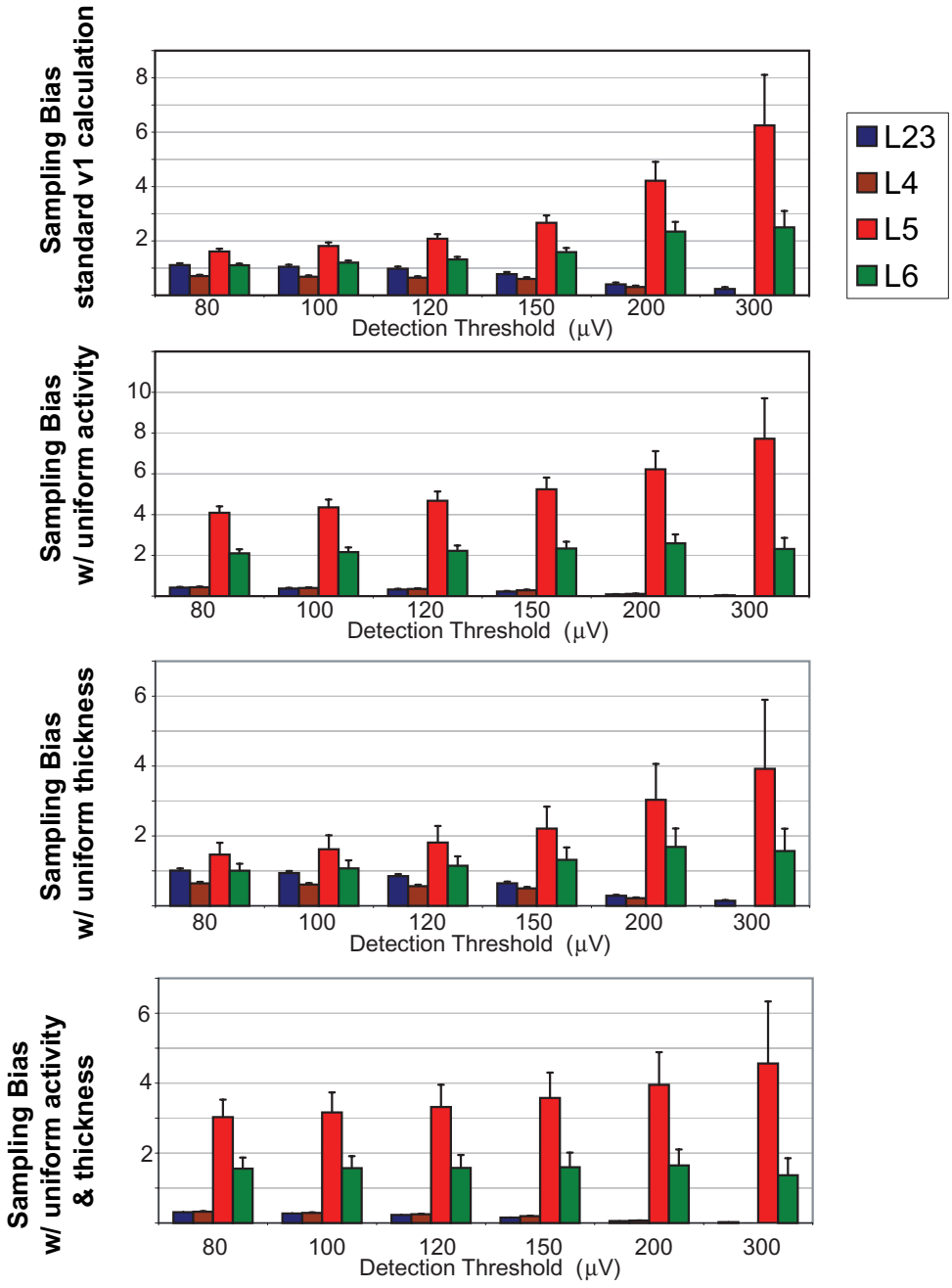

Figure 4.25: Sampling bias

standard v1 calculation: Calculation of the bias in each layer for different detection thresholds. Bias of 1 means that the cells in a given layer would be recorded at the rate predicted by the fraction of cortical cells contained in that layer. **w/ uniform activity**: What the bias would be if neurons in all layers were equally active. **w/ uniform thickness**: What the bias would be if all layers of cortex were equally thick with the activity fractions calculated in V1. **w/ uniform activity & thickness**: What the bias would be if all cells in all layers were equally active and all layers had uniform thickness.

4.4 Discussion

The combined recording and modeling experiments described in this chapter are a novel and exciting approach to answer some outstanding questions about the nature of cortical processing and the dynamics of extracellular recordings. Before now, the basic question of how close an extracellular electrode must be to record a spiking neuron in cortex was largely the domain of speculation and guesswork. With the ability to recreate the extracellular spike generation process in a model it has become a subject for empirical examination. With the question of detection range answered in a meaningful way, it opens the door to examine the bigger questions of cortical activity and sampling bias. Still, it must be acknowledge that the present work represents only a "first pass" with the new techniques and significant questions remain to be answered.

4.4.1 Uncertainty in the Detection Range and Activity Calculations

As outlined in sections 4.3.6 and 4.3.7 there are a number of sources of uncertainty in the calculation of detection ranges and the resulting conclusions about the fraction of active neurons in cortex. The most important source of uncertainty is probably the need for a systematic examination of the amplitude of the intracellular action potential. Ideally, these data would be collected separately for each layer of cortex to note if there is any difference between the different cells types. The resulting uncertainty regarding the Na^+ channel conductance density is probably greater than all other sources of uncertainty regarding the compartmental model.

Another significant problem is the lack of detailed and unbiased data on the size of neurons outside of layer 5. As described in section 4.2.1.2, I applied a correction to all cells in my morphology sample based on data collected in layer 5 alone. Finally, the sources of uncertainty that are directly attributable to my own methods are the error bars on the average number of units per location and on the average detection range for each layer. Reduction in this uncertainty could be achieved with more recordings and more morphology samples.

Unfortunately, all of these proposals for reducing uncertainty would require significant investments in terms of human time and animal sacrifice. In any event, the uncertainty that exists does not cast any doubt on the qualitative conclusions: Substantially more neurons are active in superficial layers than in deeper layers. Probably 50% or more of all neurons are active in superficial layers, while only a small minority of neurons, less than 20%, are active in deeper layers. Probably the best gauge of how well my model matches the reality of cat V1 is the comparison of the Na^+ peak amplitude samples in figure 4.13. This suggests that, if anything, my model is overestimating the amplitude of the spikes, particularly in the superficial layers. Therefore I may have undercorrected for morphology bias, or the 55 mV IAP amplitude estimate [Volgushev et al., 2000] may in fact be correct. If the model spikes are too high in amplitude it means that the real activity fraction

may be somewhat higher than I have predicted. That said, the Na^+ peak amplitude samples for the model and recording are closest for the deeper layers and farthest apart for superficial layers. Therefore the qualitative picture I suggest, that the majority of superficial layer cells are active while a much smaller proportion of neurons in deeper layers are active, remains unchanged. Collection of additional data to reduce the uncertainty may fine tune the estimates but I believe that my current appraisal will prove substantially accurate.

4.4.2 The Multi-Unit Cluster Correction

The method used to correct the recording count for multi-unit clusters is innovative but must be considered somewhat improvised, even as it has demonstrably favorable mathematical properties. Still, it suggests that the existence of multi-unit clusters in no way invalidates my method of analysis. In fact, my analysis suggests that the probable impact of multi-unit clusters is relatively small. The reason this is so can be inferred qualitatively simply by observing the illustration of the amplitude range overlap regions in figure 4.23: for a recorded spike to be from a multi-unit cluster it must fall in a relatively restricted range of radii from two neighboring cells. This is due to strong dependence of spike amplitude on electrode distance from the source. At the same time, it must be recognized that the model assumption of regular neuron spacing holds only in an *average* sense. The probability of recording multi-unit clusters and the likely number of neurons forming a multi-unit cluster are predicted to be very modest. But this does not say anything about the actual number of units that could form a multi-unit cluster for random arrangements of neurons in the neuropil. In any event, the proposed method forms a useful basis for further investigation of this subject.

4.4.3 Positive Spikes

I did not include positive polarity spikes in my calculation of cell activity because, as described in chapter 5, these spikes seem to have a very different and not as yet fully understood form of generation. Positive spikes made up around 22% of all spikes having amplitude greater than 80 μV and were found disproportionately in layer 5. If I had included positive spikes in my count of single units per location I would have counted 0.87, 0.67, 1.30 and 1.30 units per locations for layers 2/3, 4, 5 and 6 respectively, instead of 0.67, 0.47, 0.80, and 0.85 units per location. This would result in activity estimates of 83%, 61%, 18% and 23% for each layer (without multi-unit correction). Thus even if I had included positive spike recordings in my analysis, the result would not change qualitatively: The biggest change is that layer 5 would be estimated to be about the same as layer 6, with around 20% activity.

An interesting possibility discussed in chapter 5 is that high amplitude positive spikes result from synchronized minicolumn spikes, particularly in layer 5. If the synchronization hypothesis is correct

it may explain the low activity fraction for layer 5 based on negative spikes: the reason so few layer 5 pyramidal neurons seem to be generating negative spikes could be that many of them are in a different mode of operation as part of a cluster.

4.4.4 Sampling Bias in Practice

I analyzed the activity of neurons in cortex using a threshold (80 μV) far lower than what is routinely used in neurophysiological experiments (see Figures 4.24 and 4.25). This threshold is the lower limit imposed by an offline clustering algorithm used on data that was collected in an unbiased manner, without regard to whether units were apparent during the recording. It is far more common for neurophysiologists to begin recording only when they know a "good" unit is present based on observation of unfiltered spikes that far exceed the noise threshold. This means that in practice the sampling probability and bias in most experiments are closer to my high-threshold (worst-case) estimates. For most cortical regions (where layer 5 is not so thin as in cat V1) the deeper layers probably form the majority of recordings, while superficial layers must be significantly underrepresented.

An interesting corollary of these deductions is that the best way to improve the yield of responsive units in extracellular recording may be to invest more heavily in noise reduction and online clustering technologies. Instead, the most popular approach seems to be the brute force method of using as many electrodes as possible. But if the addition of microdrives and wiring were to add noise to the system, and if it complicates online processing, the advantage of this approach may be significantly diminished. Reduction of the background noise would translate directly into greater recording range for electrodes and better online processing would allow units in the "hash" to be immediately observed during an experiment. This may prove to be a more cost effective approach to increasing the yield in recording experiments.

4.4.5 Cortical Activity and Computation

I have presented evidence that superficial layers of cortex are significantly more active than deeper layers. While somewhat surprising, it is actually consistent with a widely held view of cortical processing: Layer 4 receives the direct input to cortex, and it would be very surprising if it were not significantly active during visual stimulus. Layer 2/3, or the "associational" layers are believed to perform the first processing on the input, and my results suggest that the processing in layers 2/3 involves the majority of the neurons there. Layers 5 and 6 form the output from each cortical region: layer 5 projects to other parts of cortex and subcortical structures, while layer 6 projects feedback to the LGN. My finding that only a small minority of neurons in the output layers are activated seems logical if I assume that individual neurons in layer 5 and 6 encode different specific

results about the input and only become activated when they are transmitting information about the present stimulus. For example, if an output neuron encodes the presence of an oriented edge at a particular position in the visual field it would only become active when such a stimulus is present.

At the same time, my conclusions regarding sampling bias call into question the most widely held assumption about processing in V1: that what neurons in primary visual cortex "do" is detect oriented edges at different locations in the receptive field [Hubel and Wiesel, 1962]. As most studies do not detail the minimum thresholds for recording and the amplitude of their clustered units I can only guess that they were, in all probability, highly biased towards deeper layers. (Indeed, inspection of the scaleless recording illustrations in [Hubel and Wiesel, 1962] shows spikes that are many times greater than the background noise, suggesting they are very high amplitude.) Thus the standard "story" about the function of V1 neurons is most likely based primarily on deeper layer neurons, and may not apply to neurons in the superficial layers. What exactly the superficial layers do is therefore unknown, while my own results suggest that these layers are in fact the most active during visual processing.

My results bear directly on the question of whether there is a "dark matter" problem in neuroscience, as suggested by [Shoham et al., 2006]. While [Shoham et al., 2006] used relatively simple calculations to suggest that 90% or more of the neurons in cortex are slient, my own more detailed analysis suggests that the overall activity level under my protocol is around 50%. The main reason for this discrepancy is that [Shoham et al., 2006] assume a uniform detection range of 50 μm for all layers. In contrast, I have found that even the large cells in layer 5 are somewhat less detectable than this, and small neurons in superficial layers are significantly less so. Another reason for the discrepancy is that [Shoham et al., 2006] use an estimate for the packing density of neurons in cortex of 60,000-80,000 neurons/mm^3, taken from [Scholl, 1956], and I use the more recent and somewhat lower estimate taken from [Bealieau and Colonier, 1983]. In any event, while my own results still leave me to wonder what the other 50% of the neurons were doing, it does not support the view that there is a "dark matter" problem in neuroscience – rather the problem seems to be that the instruments and practices commonly employed are biased towards the "brightest" objects in the "universe" of the brain.

On the other hand, it is difficult to say whether my results are directly relevant to theories of sparse coding, such as those described in [Olshausen and Field, 2004]. In part this is due to some ambiguity in the sparse coding literature about whether "sparsity" means that neurons fire only a few spikes to transmit information, or whether only a small proportion of neurons respond in processing a stimulus. My results seem to contradict the latter interpretation, or at least show that this type of sparsity pertains only to the output of cortex and not to the input and processing.

My results suggest strongly that the function of the different layers of cortex are significantly different, as reflected by significantly different spiking rates. Further, it is most likely that less

information has been gathered in the past about the function of superficial layers of cortex than about their counterparts in deep layers. In order to improve this situation future studies should do their best to explicitly collect data about what layer of cortex their recordings are made in.

Chapter 5

High-Amplitude Positive Spikes

5.1 Introduction

Using a protocol similar to Hubel and Wiesel [Hubel and Wiesel, 1962] as described in chapter 4, I methodically sampled the average spike waveforms of neurons in V1 of the anesthetized cat. In this process I observed a subset of spike waveforms that had unusual features in comparison to spike waveforms recorded in CA1: In CA1 spikes usually have negative polarity ("negative spikes"), meaning that the leading peak voltage amplitude is negative, while spikes whose leading peak is positive ("positive spikes") typically have only a fraction of the amplitude of negative spikes. In cortex I recorded a significant number of positive spikes whose amplitude is as large or larger than the negative spikes as illustrated in Chapter 4, Figure 4.4. When I tried to recreate high amplitude positive spikes (HAPS) in my biophysical model, I found that the positive polarity is probably due to a process of action potential (AP) initiation in the distal dendrites of the pyramidal cell. The most plausible explanation for the high amplitude is the near simultaneous discharge of a small cluster of neurons.

5.2 Results

5.2.1 Spike Recordings

Recording were made at 391 locations in 6 separate penetrations using a glass pipette electrode as detailed in the methods. My collaborators and I ejected pontamine dye from the pipette at 2-3 locations in each penetration. The path of the penetration was reconstructed during histology, allowing me to estimate with some precision from which layer of V1 each recording was made. I identified 453 units using standard clustering techniques [Quiroga et al., 2004], as described in section 4.2.2.2. The majority (74%) of these were low amplitude spikes (50-200 μV) with a leading and dominant negative peak, as summarized in Figure 4.4. This result is similar to recordings in

rat CA1 (as described in chapter 2) and recordings made in cat V1 using high density silicon probes [Blanche et al., 2005]. The recordings also yielded a small number of units with amplitudes up to around 1.5 mV (6.2% with peak between 0.5 mV and 1 mV; 3.3% with peak $>$ 1 mV). Of the high amplitude spikes nearly all had positive polarity (Figure 4.4) and the majority of these were found in in deep layers, particularly layer 5 (L5): for positive spikes with amplitude above 0.5 mV around 60% were found in L5 and 20% in layer 6 (L6). The mean amplitude of all negative spikes was 0.11 +/- 0.004 mV (sem) , while the mean amplitude of all positive spikes was 0.54 +/- 0.04 mV (sem). Negative spikes accounted for 79% of the total units, while positive spikes were 21%.

As described in Chapters 2 and 3, when spikes are recorded without inverting the polarity during amplification, the negative peak corresponds to Na^+ current entering the neuron during the depolarizing phase of the action potential [Rosenfal, 1969]. Phases of positive polarity result from either a fast capacitive current preceding the Na^+ current phase (i.e., I=C dV/dt), or a much slower K^+ current flowing out from the cell during repolarization of the membrane potential, following the Na^+ current. All high amplitude positive spikes (HAPS) had a fast positive peak, followed by a smaller negative peak (Figures 4.4 (inset) and 5.1), compatible with the conclusion that the positive peak is capacitive in nature. Many of the HAPS also had a slow positive phase after the negative phase, corresponding to K^+current (Figure 4.4, inset). With a high amplitude positive peak followed by a smaller, slower negative phase HAPS appear qualitatively similar to APs recorded intracellularly. But their fast time course indicates that they are most likely not intracellular recordings through the pipette: the mean 50% amplitude duration for positive spikes we recorded was 0.19 +/- 0.09 ms (sd). A sample of neurons recorded intracellularly in cat cortex reported in the literature [Baranyi et al., 1993] had a mean 50% amplitude duration of 0.46 ms; the sample included 48 "fast spiking" cells, presumably interneurons, which had a 50% duration of 0.25 +/- 0.03 ms (sd).

HAPS tended to be very well driven by a preferred orientation of the stimulus, and often exhibited high frequency bursts. I never observed a unit that changed from positive to negative polarity while a recording was made at one or more locations (around 3-15 minutes of recording per unit.) HAPS were often recorded simultaneously with regular amplitude spikes, both positive and negative (Figure 5.2). This rules out the possibility of equipment malfunction. Further, HAPS were typically recorded over tens of microns of electrode penetration, as in Figure 5.1, and showed a progressive increase in amplitude followed by a progressive decrease. I recorded a total of 9 HAPS units that I could track over 3 or more microelectrode positions; in these cases the identification as a single unit is based on a consistent well-defined response to a preferred orientation of the stimulus. The average length of penetration for recording a HAPS was around 100 μm. The average amplitude of a HAPS when first detected was 0.3 mV and the average peak amplitude was 0.8 mV. In 5 out of 9 cases I observed the amplitude decline after the electrode passed a peak location, while in 4 cases the HAPS went silent

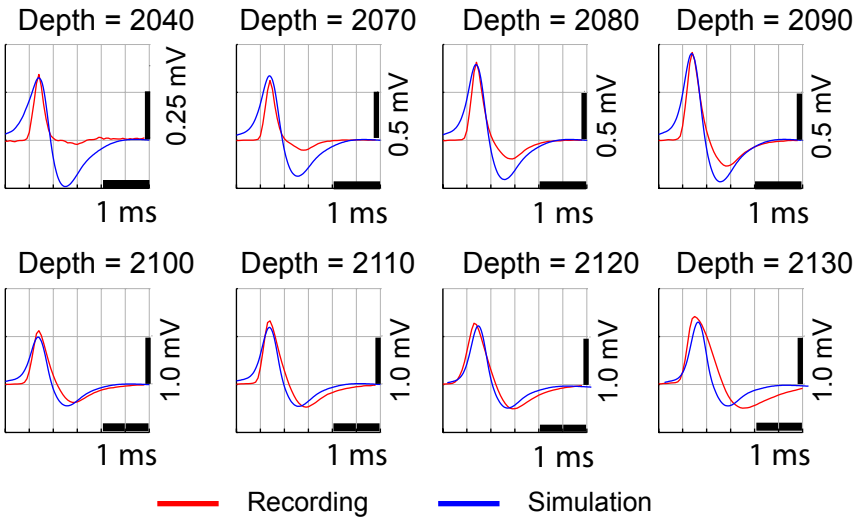

Figure 5.1: High amplitude positive spike, recording and simulation

High Amplitude Positive Spike (HAPS). This HAPS (solid lines) was recorded over 90 μm of electrode penetration with 30 μm between the first and second recording site and 10 μm between each successive recording. Depth is shown in microns. The identification as a single unit is based on a consistent and well-defined response to a preferred stimulus orientation. During recording at the last location, the unit abruptly lost amplitude and then stopped spiking altogether. The spike is characterized by a fast, large and positive phase followed by a longer and smaller, negative phase. It appears qualitatively similar to an action potential recorded intracellularly, while in fact it has around 1/60 the amplitude and is speeded up by a factor of around 2-3 times. The simulated waveforms (dotted lines) are taken from the model for a synchronous layer 5 pyramidal cell cluster spike as illustrated in Figure 5.10.

after its peak amplitude was recorded (as in Figure 5.1). In 2 of the cases where the HAPS was silenced after the peak I observed a discharge pattern compatible with injury: an increased firing rate not driven by the stimulus at the same time as the amplitude declined. In 7 out of 9 cases the amplitude was initially below 0.5 mV and then increased as the electrode moved closer to the source (as in Figure 5.1); in 2 cases the initial amplitude of the identified HAPS unit was greater than 0.5 mV. The low profile of the pipette electrode (2 μm at the tip, as described in the methods) makes it seem unlikely that the presence of a high amplitude spike at multiple subsequent locations resulted from movement of the recorded cell and surrounding tissue by the electrode.

5.2.2 Low Amplitude Positive Spikes in Distal Dendrites

I illustrated in section 2.3.2 that the positive capacitive phase of of the EAP waveform increases with distance in the dendrites. Therefore is natural to ask how large is the EAP peak at a distance from the soma where the spike is completely inverted to positive polarity. Figure 5.3 shows the positive polarity spikes in the distal dendrites for the same simulation as was illustrated in Figures

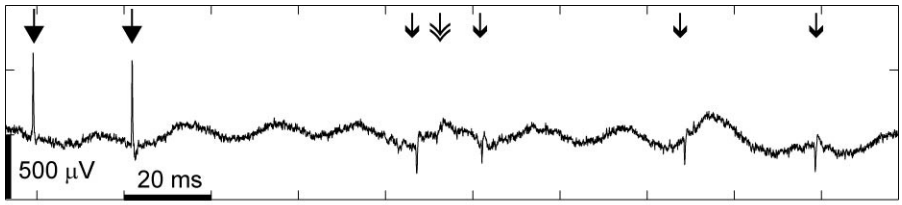

Figure 5.2: Raw data from a high amplitude positive spike recording

This recording was made in layer 5 at a penetration depth of 2070 μm and contains raw spikes for the average HAPS waveform illustrated in Fig 5.1 (filled arrowhead). At the same time two negative spikes of typical amplitude were recorded, one with an average peak amplitude of 120 μV (single open arrowhead) and another with an average amplitude of 90 μV (double open arrowhead.) 50 Hz background noise is visible in this unfiltered recording.

4.9 and 4.10. The positive capacitive peak of the spike increases with distance moving along the apical trunk, similar to the result for CA1 cells in section 2.3.2. At a distance of around 200 μm the positive peak become dominant and the waveform becomes similar in shape to the high amplitude positive spikes illustrated in Figure 5.1. However, the maximum amplitude of these positive spikes is around 100 μV at locations very close to the apical trunk. Therefore I conclude that low amplitude positive spikes, perhaps up to 200 μV peak amplitude, may result from dendritic recording of a somatic AP initiation in cells larger than the one of Figures 4.9 and 5.3.

5.2.3 Juxtacellular Recording

Because reports of juxtacellular recording [Pinault, 1996, Joshi and Hawken, 2006] show high amplitude positive spike I investigated whether the HAPS I recorded were due to unintentional juxtacellular recording. Figure 5.4 shows a circuit model for juxtacellular recording. I assume that a seal resistance, R_{seal}, isolates a small patch of membrane within the small pore at the tip of the electrode. The membrane equivalent circuit is standard, the same as that described in section 3.2.1, Figure 3.1. When membrane current flows during an AP it produces a voltage drop across the seal resistance. The seal resistance also comes between the pore and any external voltage.

5.2.3.1 Estimating the Seal Resistance

I begin by assuming the pipette solution has the same $[K^+]$ and $[Na^+]$ as the extracellular medium, and that V_e is small compared to V_m. Ignoring the pipette capacitance C_p, the juxtacellular potential, $V_j(x)$, is simply $I_j(x)$*R_{seal}. Therefore the voltage is proportional to current, as in the general extracellular case, but I isolate a single compartment. I can estimate R_{seal} because I know $V_j(x)$ from recordings and can estimate $I_j(x)$ from a model. Note that $I_j(x)$ is not the current for a full compartment, only that portion that is within the pore of the electrode, which is around 2 μm in diameter. Both [Joshi and Hawken, 2006] and my own experiments (described in Chapter 4) used

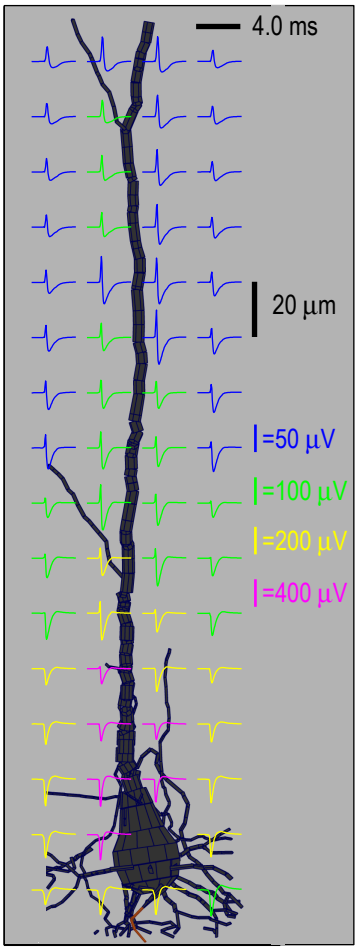

Figure 5.3: EAPs along the apical trunk of a layer 5 pyramidal neuron

EAPs in a plane through the apical trunk for the layer 5 pyramidal cells of Figure 4.9. The plane shown is 15 μm below the plane shown in Figure 4.9. There are positive polarity spikes along the apical trunk around 200-300 μm from the soma but these are weak and would mostly be below the detection threshold.

2μm diameter tips and I neglect the thickness of the glass surrounding the pore. For a 10 μm long and 2.5 μm diameter cylindrical compartment the peak total membrane potential is around 0.5 nA during an action potential, as illustrated in Chapter 3, Figures 3.4-3.7. My tip has area of $\pi\mu$m^2 while the whole compartment has area of around 25π μm^2, so $I_j(x)$ at the peak is around 0.02 nA. I expect juxtacellular recordings to be 1-5 mV, so assuming a 1 mV peak R_{seal}=1e-3/0.02e-9=50MΩ.

But juxtacellular recordings does seem to primarily record positive spikes which means that the patch current is dominated by capacitive current. This suggests that the patch somehow prevents Na^+ and K^+ components of the membrane current: either the patch solution actively blocks the channels, or the $[K^+]$ and $[Na^+]$ inside the pipette becomes equal to that inside the cell and there is no longer a driving potential. Whatever the case, I should use the peak positive capacitive current

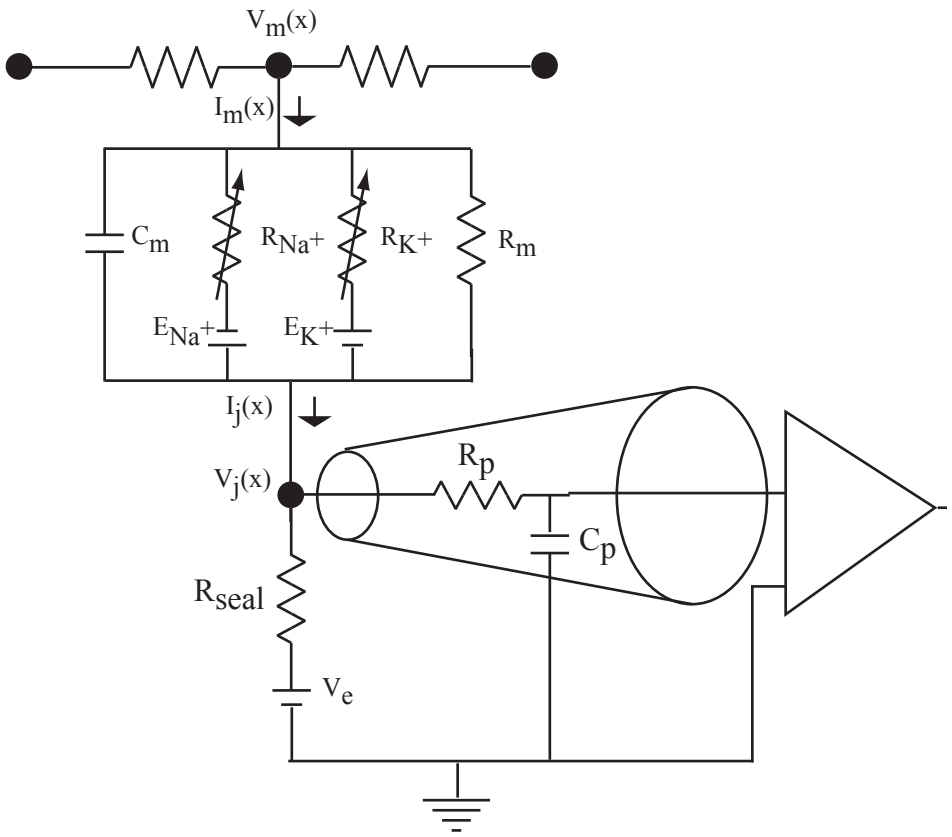

Figure 5.4: Circuit model for juxtacellular recording

Assuming the pipette electrode has attached to a small piece of membrane and a seal resistance R_{seal} forms between the membrane patch current, I_j and external voltages, V_e. The model pipette electrode consists of a simple RC circuit.

to calculate R_{seal} and not the peak negative current. This is around 0.25 nA rather 0.5 nA for a standard compartment (Chapter 3, Figures 3.4-3.7) so I reestimate that R_{seal} is 100 MΩ. The same estimate for the capacitive current can be reached without using the compartmental model result by noting that the capacitance of a 2 μm diameter section of membrane having a capacitance per unit area of 1 μm F/cm^2 will be 1e-6 μF/cm^2 * (1e-8π)cm^2 $\sim$ 31 fF. The maximum first derivative of the membrane potential during an action potential is around 300 V/s [Naundor et al., 2006]. Therefore peak capacitive current is 31e-15 * 300 = 0.009 nA. So to have a 1 mV peak potential gives a seal resistance R_{seal}=1e-3/0.009e-9=110 MΩ. The small difference in the estimates results from the fact that the maximum dV/dt in my model was somewhat less than 300 V/s. Note that, if anything, the 100 MΩ estimate must still be low because in fact the seal resistance is in parallel with the RC circuit of the pipette which would have lower total impedance (meaning the seal must have higher resistance to have recorded the peak that I did). Still, this estimate seems reasonable because ordinary patch clamping is considered to have a seal of around a gigaOhm or more, and I am considering "loose

patch" recording.

Unfortunately, the literature provides no direct measurements of the seal resistance for a juxtacellular patch. [Joshi and Hawken, 2006] states that the electrode resistance increases by around 4 times as the electrode comes into contact with a cell, and increases 3-10 times when a seal is formed through the application of suction. Given that the electrode starts around 10 MΩ
[Joshi and Hawken, 2006] I expect a resistance of around 40 MΩ when the electrode is merely in contact with a cell, and 120-400 MΩ after a seal has formed.

5.2.3.2 Measurements of Electrode Resistance During HAPS Recording

In order to determine whether the HAPS I recorded were produced by juxtacellular recordings my collaborators measured the resistance through the electrode at locations where a HAPS was recorded. The electrode resistance was measured with the bridge balancing circuit in the usual way. At 28 locations where a positive spike with minimum amplitude of 0.8 mV was recorded we found the resistance of the electrode was 19.3 +/- 5.1 MΩ. In comparison, at 15 locations where no HAPS were present, the resistance was 13.4 +/- 5.4 MΩ. While the difference between the mean of the two resistance samples is significant (Student's t-Test, p=0.005), the electrode resistance tended to increase as the electrode proceeded in a penetration, presumably due to miscellaneous matter clogging the tip. This phenomena alone probably explains the slightly higher resistance found during HAPS recording, as the non-HAPS resistance measurements were typically made at the start of a penetration, or in some cases immediately after the electrode was cleared by passing a current. In any event, the measured resistances are significantly below the level I expect for an electrode in contact with a cell (40 MΩ), let alone the seal that would be required to produce a 1 mV positive spike during an action potential (∼100 MΩ). For this reason I consider the electrode resistance measurements to be strong evidence that the HAPS I recorded did not result from a juxtacellular recording.

In another set of experiments my collaborators sent 0.5 nA current pulses through the electrode and measured the resulting voltage in order to check for any resistance change as the electrode approached a high amplitude unit. This is the procedure typically used to detect the presence of a cell against the electrode in order to know when to apply suction [Joshi and Hawken, 2006]. In three separate trials where the moving electrode came into range of a HAPS unit while current pulses were measured there was no significant change in the magnitude of the voltage recorded. These tests provide additional evidence that the HAPS I recorded were not juxtacellular recordings.

5.2.3.3 Extracellular Recording in the Juxtacellular Configuration

It is interesting to note that a juxtacellular seal, if present, would not necessarily block recording extracellular spikes. Consider the circuit of Figure 5.4 and assume that $V_m(x)$ is at rest so that

$R_{Na^+}$and $R_{K^+}$are very large. Under these conditions a good approximation for the circuit is to simply ignore the attached membrane and consider recording of V_e through R_{seal}: for a 0.5 μm patch the leak resistance will be 15e3 Ωcm / (0.25e-8π)cm^2 = 2 TΩ (Tera ohms). At the same time the capacitance will be 1e-6 μF/cm^2 * (1e-8π)cm^2 = 31 fF (Femto Farads). With such a high resistance and low capacitance the membrane patch at rest can safely be ignored leaving V_e to be recorded through a simple RC circuit (a low-pass filter) with a combined resistance of R_{seal}+R_p and a capacitance of C_p.

[Schanne et al., 1968] studied the properties of glass pipette microelectrodes and found a value of 10 MΩ for R_p which happens to be the same as my typical bridge resistance measurement. Therefore R_{seal} will dominate the resistive component. C_p, assuming 1-2 mm of pipette immersion, will be in the range of 0.25-1 pF. If I assume a capacitance of 0.5 pF and a seal resistance of 400 MΩ the RC circuit will have a time constant of 0.2 ms, equivalent to a filter with a 3 dB down frequency of 800 Hz. Because most of the power in an extracellular spike is well below this frequency the seal-pipette filter would not completely block the amplifier from following V_e and it is not obvious whether this effect would be easily observable during recording. Because the filter is at the borderline of having a noticeable impact it would depend upon the precise value of the seal resistance and pipette capacitance. But I conclude that in general an electrode in the juxtacellular patch configuration may very well record extracellular spikes during times when the attached cell is quiescent. For this reason the presence of small amplitude spikes during a HAPS recording, as illustrated in Figure 5.2, is evidence of a properly functioning electrode but cannot be considered evidence for whether or not a juxtacellular seal has formed.

5.2.4 High Amplitude Positive Spikes in a Simplified Model

Having concluded that my HAPS recordings probably do not result from a juxtacellular electrode configuration I proceeded to analyze the generation of such spikes in the extracellular model. My model for extracellular recordings in CA1 suggested that positive spikes should exist in the neighborhood of distal apical dendrites of pyramidal neurons, but only at amplitudes below the detection threshold (see e.g. Figure 2.2). To better understand how positive spikes could be generated at higher amplitudes, I analyzed positive and negative spike generation in a simplified model of a single, long (1 mm) cylinder (Figures 5.5 and 5.6). Its central compartments are defined as "somatic" in that it has half the membrane capacitance of the "dendrites" (>20 μm from the center in either direction), mimicking the absence of spines in the perisomatic region of a real pyramidal neuron. In the first of two simulations, Na^+ channels are concentrated at the soma (center) of the cylinder and the AP initiates there before spreading to the distal ends. In a second simulation, the same total amount of Na^+ channels are concentrated in the distal dendrites (ends) of the cylinder, resulting in an AP that initiates in both ends before invading the center as detailed in the simulation methods,

section 5.4.

Figure 5.5 (left) demonstrates that when the AP initiates in the center of the neuron, the negative second derivatives associated with the maximum in the spatial V_m profile create a negative spike. At the same time, positive second derivatives dominate at the distal ends, corresponding to positive spikes in the extracellular potential, although at lower amplitude. This is similar to CA1 neurons where positive spikes of low amplitude occur outside distal dendrites, as described in chapter 2. The positive spikes are lower in amplitude than the negative spikes for two reasons: because the absolute amplitude of the second derivative at the distal ends is less than in the center, and because the zones of positive second derivatives are separated at either end of the cylinder and do not combine to any significant extent with each other through superposition, because of the large separating distance.

The amplitude of the positive spike is maximized in the second simulation where the AP initiates simultaneously from both ends of the simplified neuron (Figure 5.5, right). This condition creates a single global minimum in V_m rather than two separated local minima, and the negative spikes are separated. But the positive spikes are still of lower absolute amplitude than the negative spikes in the first simulation. One reason for this difference is that the lower capacitance (lack of spines) at the center (soma) of the cylinder favors negative spike generation: low capacitance allows the soma membrane to be rapidly driven to high potential by concentrated Na^+ channel conductance, while the high capacitance of the spiny dendrites slows the rate at which they can follow. This creates ideal conditions for a large local maximum, leading to negative spikes In the situation of distal dendritic initiation, the soma can rapidly follow the voltage in the dendrites, reducing the gradient which produces positive spikes. In simulations of the cylinder neuron with an uniform membrane capacitance, the amplitude of positive and negatives spikes generated at the center are approximately equal, although the highest amplitude still occurs for the negative spikes.

A second reason that the centralized initiation yields negative spikes of greater absolute amplitude than the positive spikes in the distal initiation scenario has to do with the nature of the currents involved in each type of spike. Negative spikes result from Na^+ current which is an active current flowing through discrete channels. As such they can be concentrated in a small region of the neuron. Positive spikes result from capacitive current which, although fast, is fundamentally a passive current and will naturally be distributed over the membrane. In the central initiation scenario in Figure 5.6 (left), very high amplitude negative spikes are concentrated very close the center, while in Figure 5.6 (right) a high amplitude exists over a longer section of the cylinder but there is no very high amplitude at the center. A final reason that positive spikes may be weaker than negative spikes in real neurons is that achieving the maximum positive spike amplitude as in my second simulation depends on symmetric initiation in different parts of the neuron. Simulations of the single cylinder neuron with distal initiation showed that if the synaptic input driving the AP is unbalanced by more than around 10%, the positive spike amplitude fell significantly. This would probably be closer to

the situation in a real neuron.

These cartoon simulations lead me to the following expectations for the generation of HAPS in real neurons: HAPS are most likely driven by some form of distal dendritic AP initiation, and the maximum amplitude of a positive spike will be somewhat lower than the maximum amplitude for a negative spike from the same neuron undergoing a somatic AP initiation.

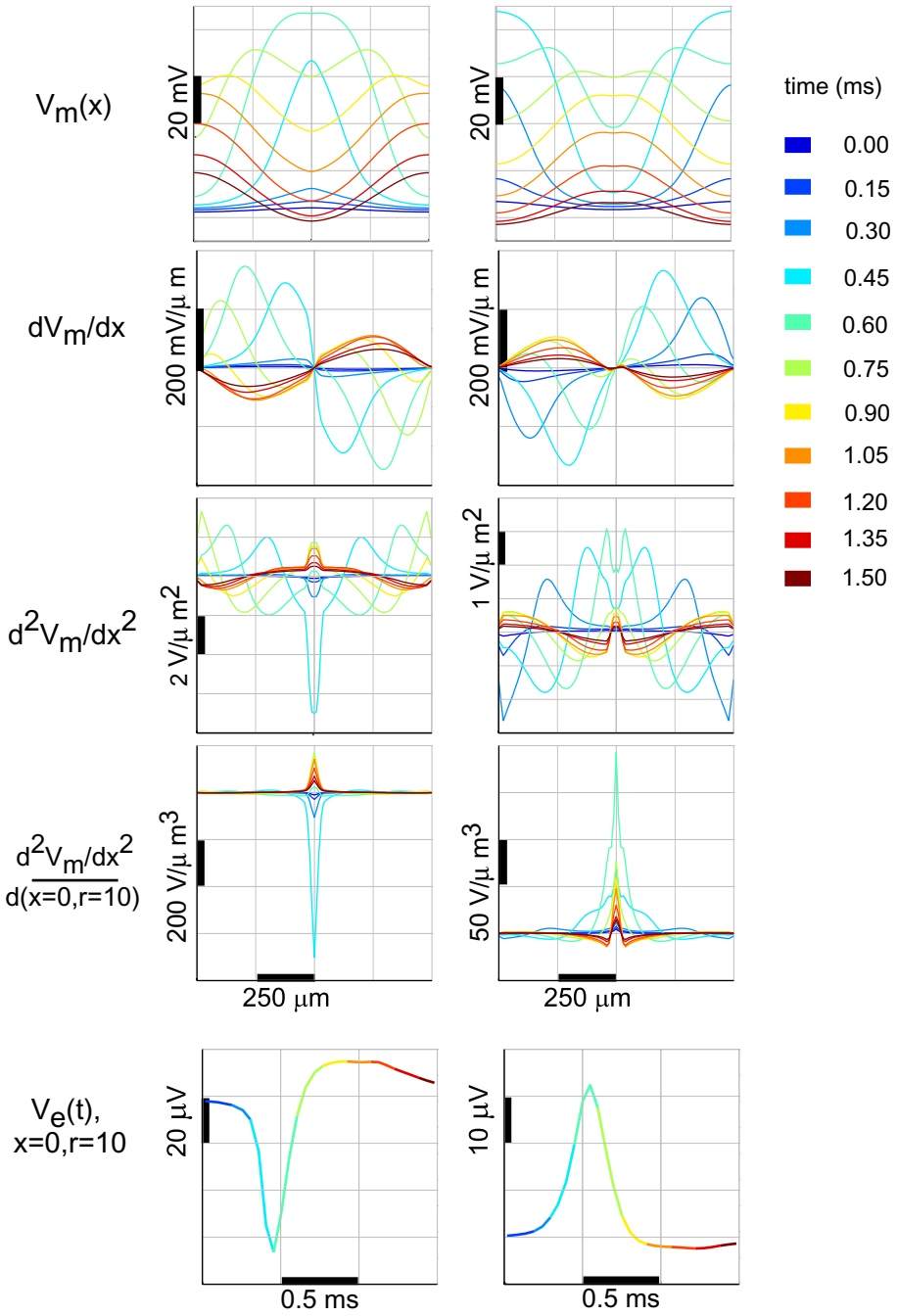

Figure 5.5: Cylinder simulation of positive and negative spikes – intracellular

For a general description see Figure 3.8. **First column**: Na^+ channel conductance is concentrated in the middle of the cylinder and the AP initiates in the center and spreads to the ends. **Second column**: Na^+ channel conductance is concentrated in the ends of the cylinder and the AP initiates in the end and then spreads to the center. The centralized Na^+ channel conductance and action potential initiation results in a negative extracellular spike near the center of the cylinder, while the distal Na^+ channel conductance concentration results in a distal AP that then invades the center producing a positive spike near the center of the cylinder. For further illustration of the extracellular potentials see Figure 5.6.

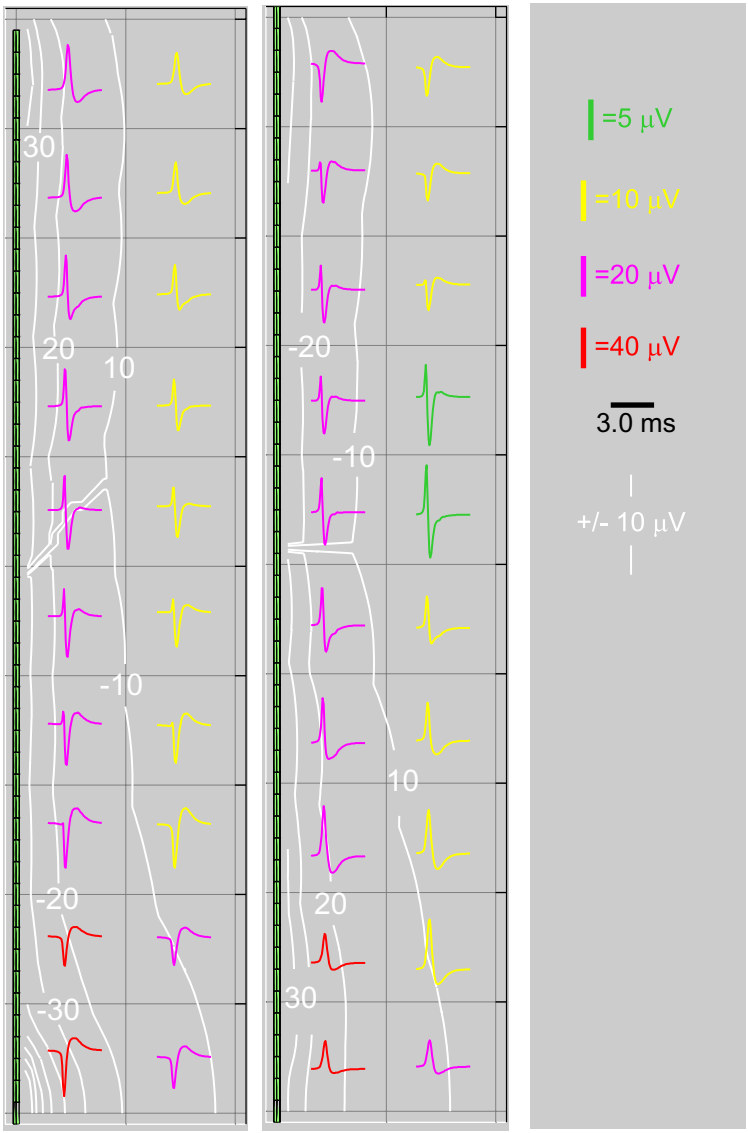

Figure 5.6: Cylinder simulation of positive and negative spikes – Extracellular

Left: Extracellular potential amplitude and waveforms in a single quadrant around the cylinder with central Na^+ and AP initiation (Figure 5.5 (left)) The axis of the cylinder is plotted vertically. Negative spikes of relatively high amplitude occur at the center of the cylinder. Positive spikes at lower amplitudes occur at the distal end of the cylinder. Midway down the cylinder the spikes include fast positive and negative phase of approximately equal amplitude. The highest amplitude of negative spikes occur in a small region very close to the center of the cylinder, near the highest density of Na^+ conductance. **Right:** Extracellular potential amplitude and waveform around the cylinder with distal Na^+ and AP initiation (Figure 5.5 (right)). Relatively high amplitude positive spikes occur around the center of the cylinder, but the amplitude is less than that of the central negative spikes due to central initiation. The spikes at the exact center are not much higher in amplitude than those nearby. Negative spikes occur at the distal ends.

5.2.5 Positive Spikes from a Single, Layer 5 Pyramidal Neuron

Based on these principals I modeled a HAPS using a reconstruction of large layer 5 pyramidal cell from cat visual cortex, as illustrated in Figure 5. The cell is a reconstructed Meynert cell (as described in section 4.2.3.1) and is representative of one of the largest neurons in all of cortex: The soma surface area is around 3500 μm^2, equivalent to a sphere with diameter of 33.5 μm. The apical trunk starts thicker than 10 μm and maintains an average diameter greater than 6 μm for approximately 150 μm. Because the amplitude of any spike is proportional to the size of the soma and proximal apical trunk (as illustrated in Figure 3.17), I expect that the results of the simulation are representative of positive spikes that could be generated by the largest cells in cat V1, if not in all of cortex. As suggested by the simulation of the cylinder in section 5.2.4, I assume that the neuron has high densities of active Na^+ and K^+ channels in the distal dendrites while the soma and proximal dendrites have lower densities (as detailed in the section 5.4.) The model is constrained so that the somatic IAP has amplitude around 80 mV above threshold even though the IAP in some distal compartments is much larger.

The simulation predicts that for an layer 5 pyramidal neuron undergoing distal AP initiation, positive spikes will be generated near the soma and apical trunk, with amplitudes up to a few hundred microvolts. Such positive spikes are well above the detection threshold (50-100 μV) but far short of the level seen in the HAPS recordings. In contrast a single layer 5 pyramidal cell, even one of only average size, could produce a negative spike up to around 1 mV during a perisomatic AP initiation, as illustrated in Figure 4.9. A model cell as large as the one in Figure 5.7 generates a negative spike greater than 1.5 mV.

A second way in which the simulation fails to reproduce the HAPS recording is that the maximum positive spike potential (400 μV) is restricted to a very small zone within a few μm of the cell. The simulation predicts that the amplitude would fall by 50% within 10-20 μm. In contrast, the HAPS recording illustrated in Figure 5.1 shows that a peak amplitude of greater than 1 mV was present over 40 μm of electrode movement. A large spatial extent for the high amplitude peak was typical of HAPS recordings – in one case a HAPS greater than 1 mV was recorded over more than 100 μm of electrode movement.

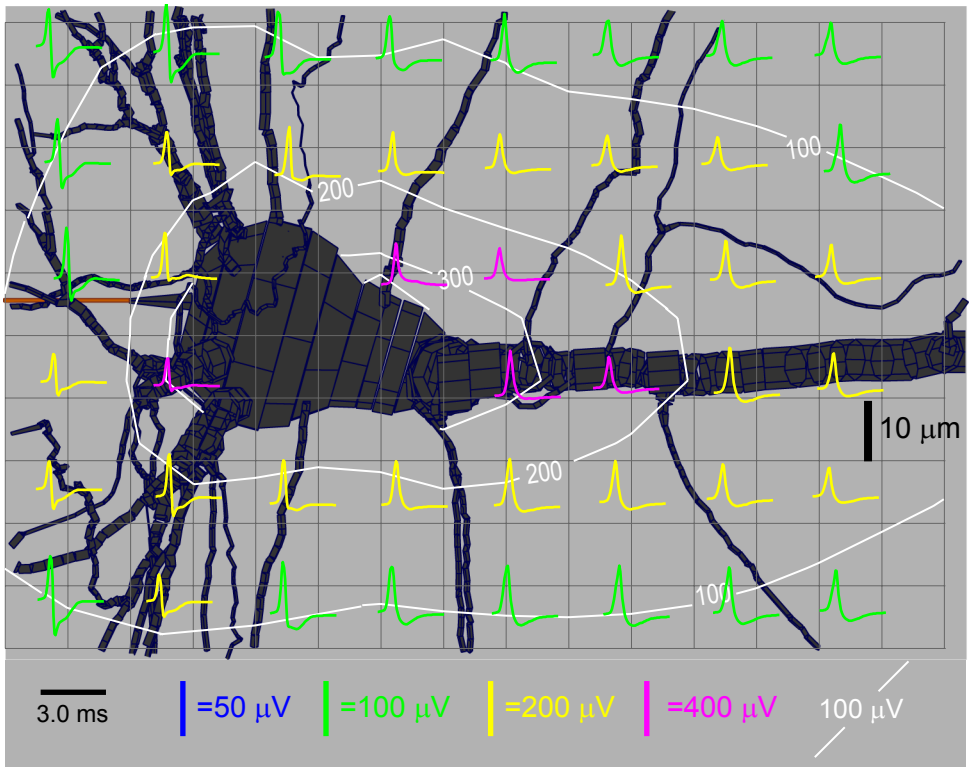

Figure 5.7: Positive spikes in a layer 5 pyramidal cell model – extracellular

Illustration of spike waveforms and amplitude around the soma of a layer 5 cat V1 Meynert cell during a simulated action potential initiating in the distal dendrites (see Figure 5.8). The soma and dendrites are colored blue/black; non-myelinated axon, including the initial segment is brown. The peak amplitude, around 400 μV, occurs in a small region close to the soma and decays rapidly with distance.

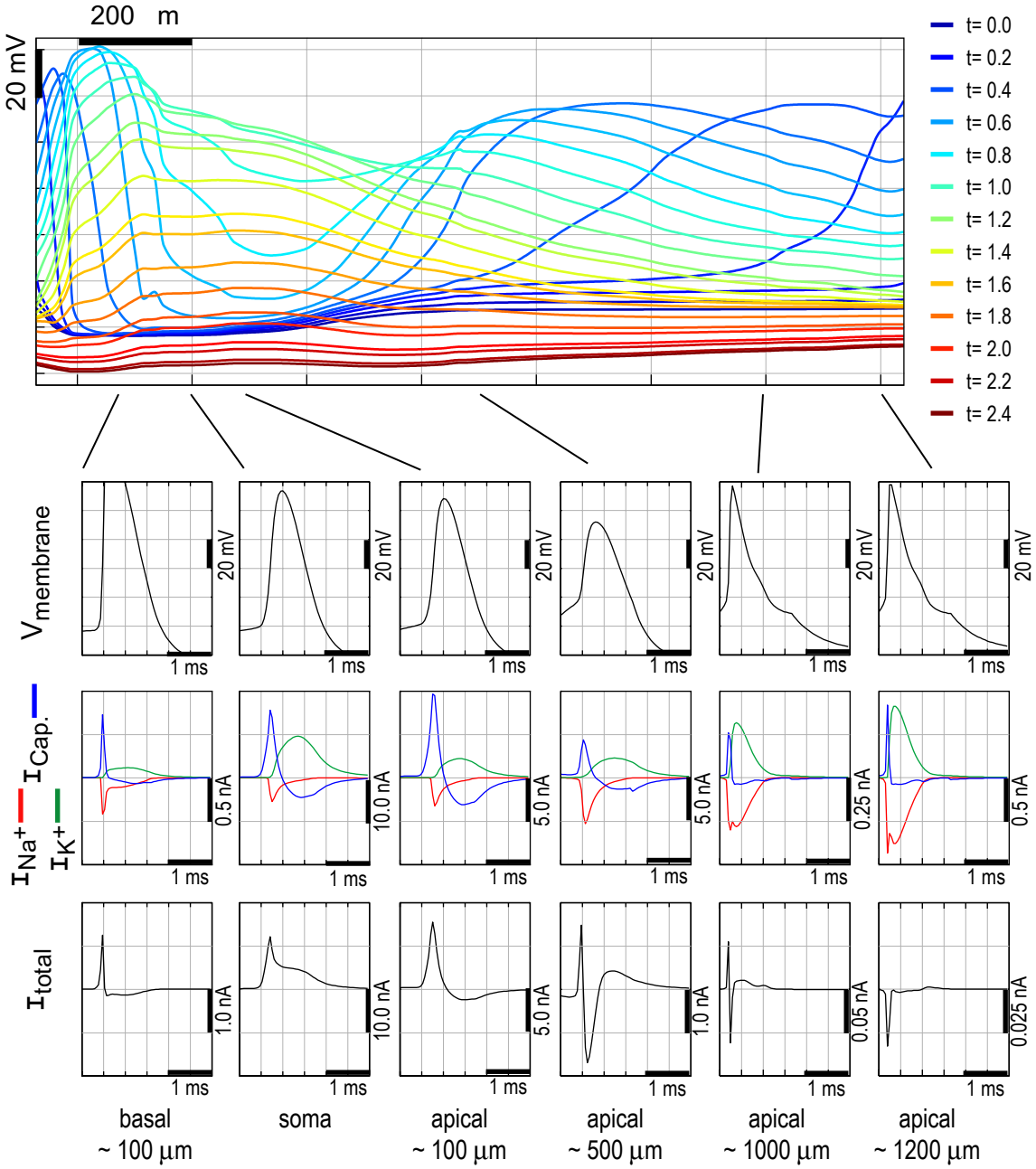

Figure 5.8: Positive spikes in a layer 5 pyramidal cell model – intracellular

Top:Illustration of the membrane potential as function of position at selected times given by the color coded scale. The AP initiates first in the distal dendrites before spreading to the perisomatic region. **Bottom:** Membrane potential and current versus time for selected compartments.

5.2.6 Analytic Model of the Maximum Positive Spike Amplitude

The same conclusion derived from detailed the compartmental model can be reached from a simple analytic model consisting of a passive spherical soma. I have $V = \frac{I\rho}{4\pi R}$, where R is the distance from the center of the soma to the measurement, $I = C\frac{dV_m}{dt}$, $C = C_m A$, where A is the surface area of the membrane, and for a sphere $A = 4\pi R^2$. Hence I can write:

$$V_{\max} = \rho R C_m [dV_m/dt]_{\max} \tag{5.1}$$

where for simplicity I have assumed that the measurement is made directly at the surface of the soma (without formation of a juxtacellular seal.) Equation 5.1 shows that the maximum positive spike is linearly dependent on the soma size, the capacitance per unit area of the membrane, the maximum derivative of the membrane potential, and the extracellular resistivity.

Figure 5.9 illustrates the result as a function of soma size, ranging from a radius of 5 to 25 μm. In fact, the largest L5 pyramidal cells have a soma equivalent to a sphere with diameter 20 μm [Gabbott et al., 1987] (the neuron of Figure 5.7 has an equivalent radius of around 17 μm), so by including radii up to 25 μm I have made a generous allowance for the additional surface area of proximal dendrites. To estimate the maximum positive spike I choose values for the remaining parameters that put them at the boundary of biological plausibility:

- C_m is assumed to be 1.5 $\mu F/cm^2$. In fact, $C_m \sim 1\mu F/cm^2$ but the presence of spines may effectively raise C_m to as high as 2 $\mu F/cm^2$ in the dendrites. However, the majority of the cell surface area in the perisomatic portion of the neuron is the spineless soma, so a value of 1.5 $\mu F/cm^2$ is probably above and beyond the true average for the soma and proximal dendrites.

- $[dV_m/dt]_{\max}$ is assumed to be 400 mV/ms. For cortical pyramidal neurons the maximum dV_m/dt is normally in the range of 250 to 300 mV/ms [Naundor et al., 2006].

- I assume the maximum cortical resistivity of 400 Ωcm (Figure 4.1), while the average is in fact 250 Ωcm.

Assuming a soma radius, membrane capacitance, dV_m/dt, and resistivity that are all at the limit of biologically plausible values I find a maximum positive spike that is only 0.6 mV, less than half the amplitude of the largest HAPS which I recorded. And this amplitude decreases linearly with distance from the soma and could not therefore be maintained for 10's of μm, let alone 100 μm or more.

Interestingly, the compartmental model Meynert neuron in Figure 5.7 has virtually the same peak amplitude as predicted by the analytic model for its soma radius of 17 μm: around 0.4 mV. But it should be noted that this equality is due to a rough balance between factors that are different

in the compartmental model and the analytic calculation of Figure 5.9: the Meynert neuron actually has greater effective area due to its dendrites, particularly the thick apical trunk, while the other parameters (dV_m/dt, C_m, σ) are all somewhat less conducive to high positive spike amplitude in the Meynert cell. Of course, this analytic model is highly idealized because it does not provide any mechanism to drive the soma through such a rapid depolarization. But it is useful to show that a simple calculation gives essentially the same result as the much more complicated compartmental model.

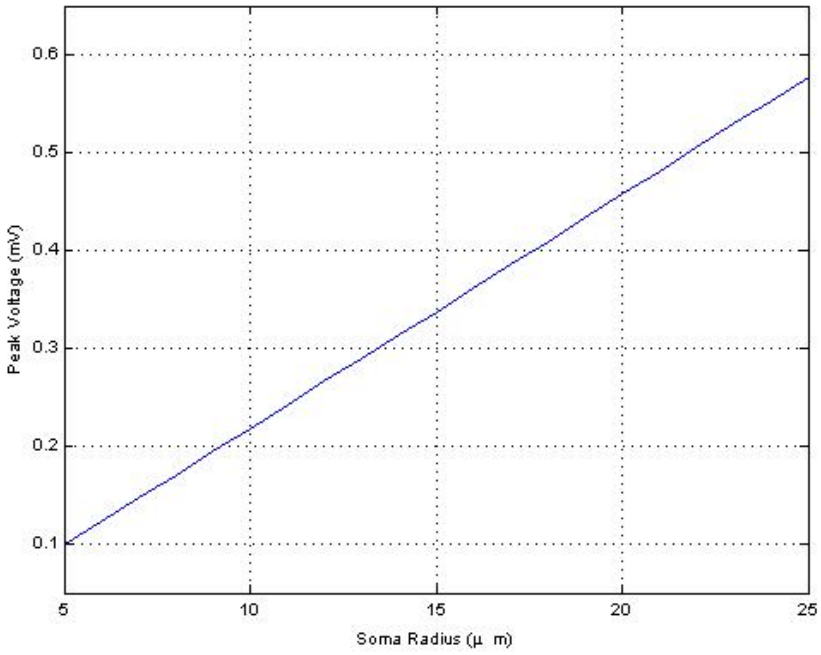

Figure 5.9: Positive spikes in an analytic model

The measurement is assumed to be made 1 μm distant from the surface of the spherical soma.

5.2.7 Positive Spikes from a Synchronized Cortical Minicolumn

Because potentials arising from multiple sources in the extracellular space combine linearly via superposition, it is possible that HAPS could be the result of multiple neurons spiking in near synchrony. Indeed, artificially induced population spikes can be formed by stimulating efferent axons in the hippocampus [Varona et al., 2000], although these population spikes are typically much larger and longer in duration than any ordinary spikes and possibly involve hundreds or more neurons. Near simultaneous APs superimposing to create spikes like the HAPS would require that a small number of synchronized neurons be located in close proximity so as to generate superposition of relatively high amplitude potentials and to allow whatever physical connections may facilitate the synchronization. An anatomical feature of the neocortex that meets these requirements is the so called "minicolumn" which includes a "cluster" of layer 5 pyramidal cells at its base [Peters and Yilmaz, 1993]. These arrangements, which compromise the majority of layer 5 pyramidal cells in cat visual cortex, consist of anywhere from a 5 to 30 pyramidal cells (mean of 12 cells per cluster). The cell bodies are grouped into vertical clusters approximately 40 μm in diameter, and the apical trunks come close together and ascend through layer 4 to the superficial layers of cortex in parallel. Spiny stellate cells, smooth interneurons and pyramidal cells in layers 2-4 are situated around the ascending apical trunks from layer 5, giving the appearance of a vertically arranged functional unit. Minicolumns are present in all mammalian cortex that has been studied [Mountcastle, 1997]. Their functional role remain unclear [Buxhoeven and Casanova, 2002].

I created a model layer 5 cluster consisting of 26 neurons as detailed in the method section, 5.4, and simulated the positive spike that would be generated if the neurons of the cluster fired in near synchrony (Figure 5.10). The neurons in the cluster are simulated so that they fire distally initiated APs similar to the one in Figures 5.7 and 5.8. The combined cluster spike is modeled by an average of 100 trials in which each individual neuron's spike is offset by a random time drawn from a normal distribution with standard deviation of 0.1 ms before being combined in the superposition for that trial. Thus, the majority of spikes occur with 0.2 ms of each other and $\sim$95% are within a 0.4 ms window. The result of the model is a very good approximation to the recorded HAPS (Figure 5.1). The synchronized cluster simulation is a good match to both the peak amplitude of the HAPS and the spatial extent of the high amplitude region.

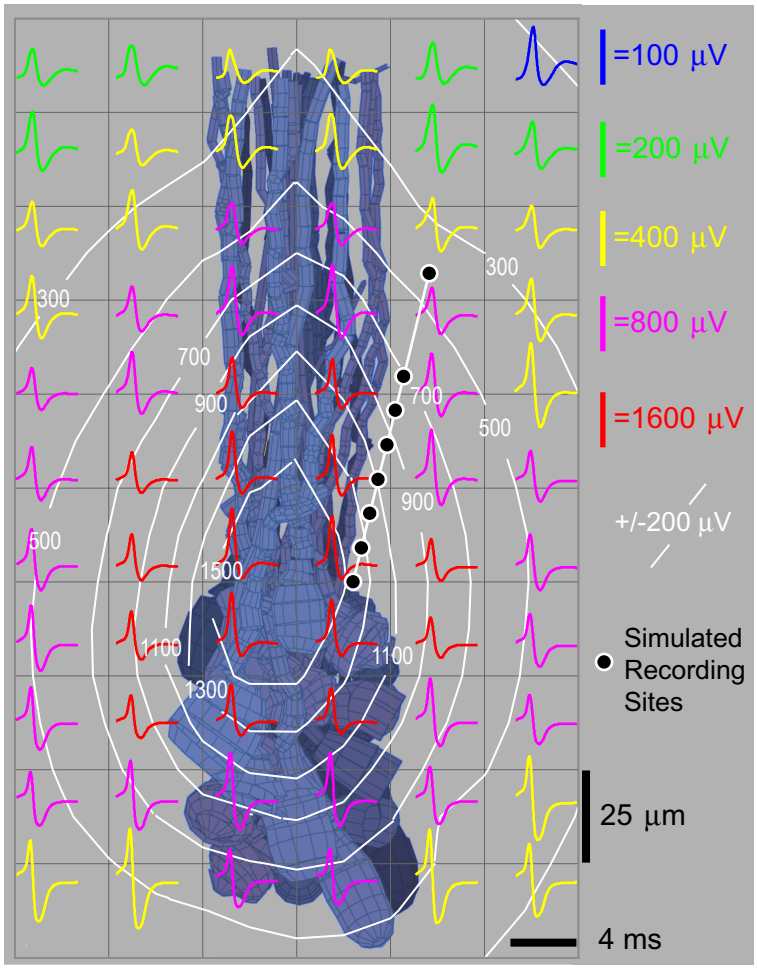

Figure 5.10: Positive spikes from a synchronized layer 5 pyramidal cell cluster

The cluster consists of 25 reconstructed L5 pyramidal cells [Peters and Yilmaz, 1993]. The cell bodies are arranged in a columnar pattern with a diameter of 40 μm. Each cell has dense distal Na^+ and K^+ channel conductance and fires a distally initiated AP similar to the one illustrated in Figures 5.7 and 5.8. The combined cluster spike is modeled by an average of 50 trials in which each neuron's spike is offset by a random time drawn from normal distribution with 0.1 ms standard deviation before being combined in the superposition. The simulated electrode path recording sites that created the waveforms of Figure 5.1 are illustrated with filled circles.

5.2.8 Variability of Positive Spike Amplitude

If HAPS result from synchronized spikes in a cluster of neurons then I would expect the amplitude to show a high level of variability: not only due to the combination of the variability of the amplitude of the individual neurons, but also due to the occasional failure of some members of the cluster to fire. I analyzed the variability of the amplitude of HAPS and found the evidence to be consistent with this hypothesis. Figure 5.11 illustrates the amplitude variability of a few HAPS and the single negative spike I recorded with amplitude ∼1 mV.

For example, in one highly variable positive spike the amplitude distribution seems to show two peaks as if the spikes were generated by two separate units (Figure 5.11(ii)c). However, the shape of the spikes are so similar (Figure 5.11(ii)b) and the amplitude distributions so overlapping that the units could not be separated either by a clustering algorithm or by any analysis of the raw data I know of. Another explanation for this phenomena is that there is a single unit that generates a broad distribution of spike amplitudes with two peaks. This explanation is consistent with the synchronized cluster hypothesis.

I measured the amplitude for *individual* spikes and calculated the variability of the amplitude for a single unit and recording location. This analysis was only possible for spikes with sufficient amplitude that they could be detected by a simple threshold crossing without clustering (∼0.15 mV), and with sufficient firing rate to make meaningful statistics. I found that the average of the standard deviation for HAPS with amplitude greater than 0.15 mV (N=45) is 0.084 mV (average of the mean amplitude is 0.82 mV). In comparison, negative spikes with amplitude greater than 0.15 mV (N=18) have standard deviation of, on average, 0.04 mV (average of the mean amplitude is 0.42 mV). This shows that the amplitude of HAPS is in fact highly variable, but not clearly greater than that for negative spikes.

I analyzed the variability of HAPS amplitude more rigorously by comparing the *variance* of the amplitude to the mean: for independent random variables the variance of the sum is the sum of the variances. Therefore if HAPS result from a synchronized cluster spike with occasional AP failures I would expect the variance of the amplitude to grow superlinearly with respect to the mean of the amplitude. That is, the combination of variance in the spike amplitude of the individual neurons should lead to the variance of synchronized cluster amplitude growing *at the same rate* as the mean synchronized cluster amplitude. But occasional failures of neurons in the cluster should create additional variance not explained by the simple summation. The results of this analysis are shown in Figure 5.12. I find that for positive spikes not only does the variance increase with spike amplitude, but also the normalized variance (divided by the mean amplitude). The increase in the normalized variance is consistent with the hypothesis that these spikes result from a superposition with occasional failures. For negative spikes the variance of spike amplitude also increases with the mean spike amplitude, but the normalized variance does not.

Another expectation I might have if the synchronized cluster hypothesis is correct is that the duration of HAPS should be negatively correlated with amplitude. This would be because if, in a given synchronized spike, the individual APs in the cluster neurons were poorly synchronized then it would result in a lower peak amplitude for the superposition but a longer duration. In contrast, if the individual APs were tightly synchronized it would result in a higher amplitude superposition of shorter duration. Note that this is different from the correlation discussed in section 2.3.5: in that case I analyzed the correlation for duration and amplitude of *average* waveforms from different units. In this case I am analyzing the correlation for individual spikes from the same unit.

In fact, I do find that for positive spikes the duration and amplitude are usually negatively correlated, while for negative spikes the amplitude and duration are positively correlated as illustrated in Figure 5.13. For 36 positive spiking units with amplitude greater than 0.5 mV ("high amplitude") 23 had a negative correlation between the amplitude and duration with significance $P<0.01$ (correlation coefficient -0.44 +/- 0.18), 7 had a positive correlation between amplitude and duration (correlation coefficient 0.29 +/- 0.22), and 6 had no significant correlation ($P > 0.01$). For positive spiking units with mean amplitude less than 0.5 mV ("low amplitude", N=10) 5 had positive correlation (0.49 +/- 0.14) and 5 had no significant correlation. For 17 negative spiking units with mean amplitude greater than 0.15 mV all had positive correlation between the amplitude and duration of the spike (correlation coefficient of 0.35 +/- 0.18.) I conclude that high amplitude positive units have significantly more negative correlation between the amplitude and duration of their spikes than either low amplitude positive units or negative spiking units of all amplitudes.

When I experimented with creating variability of amplitude and duration for positive and negative spikes in the model, I found that *individual* positive spiking neurons also showed negative correlation between the amplitude and duration of their spikes. Beginning with the simulations of positive and negative spikes illustrated in Figure 4.9 and Figure 5.7 I ran 50 additional trials where in each simulation the $\bar{g}$ for each conductance in each compartment was varied by the addition of a small amount of noise (uniform distribution with amplitude +/-10% of base value, similar to what was described in section 3.3.5.) I found that with conductance density noise the positive spiking Meynert cell (Figure 5.7) showed a predominantly negative correlation between between the amplitude and duration of the spikes from each trial, while the negative spiking pyramidal cell (Figure 4.9) showed a predominantly positive correlation.

Based on these results I cannot conclude whether or not the mainly negative correlation seen in the recordings is strong evidence for a synchronized cluster at this time: if I was confident that the model accurately recreated the causes of variability in spike amplitude and duration in real neurons then I could look to see if recorded HAPS showed "excess" correlation in comparison to what I could reasonably expect for individual neurons. At present I conclude that the negative correlation between amplitude and duration in the HAPS recordings is consistent with the synchronization

hypothesis.

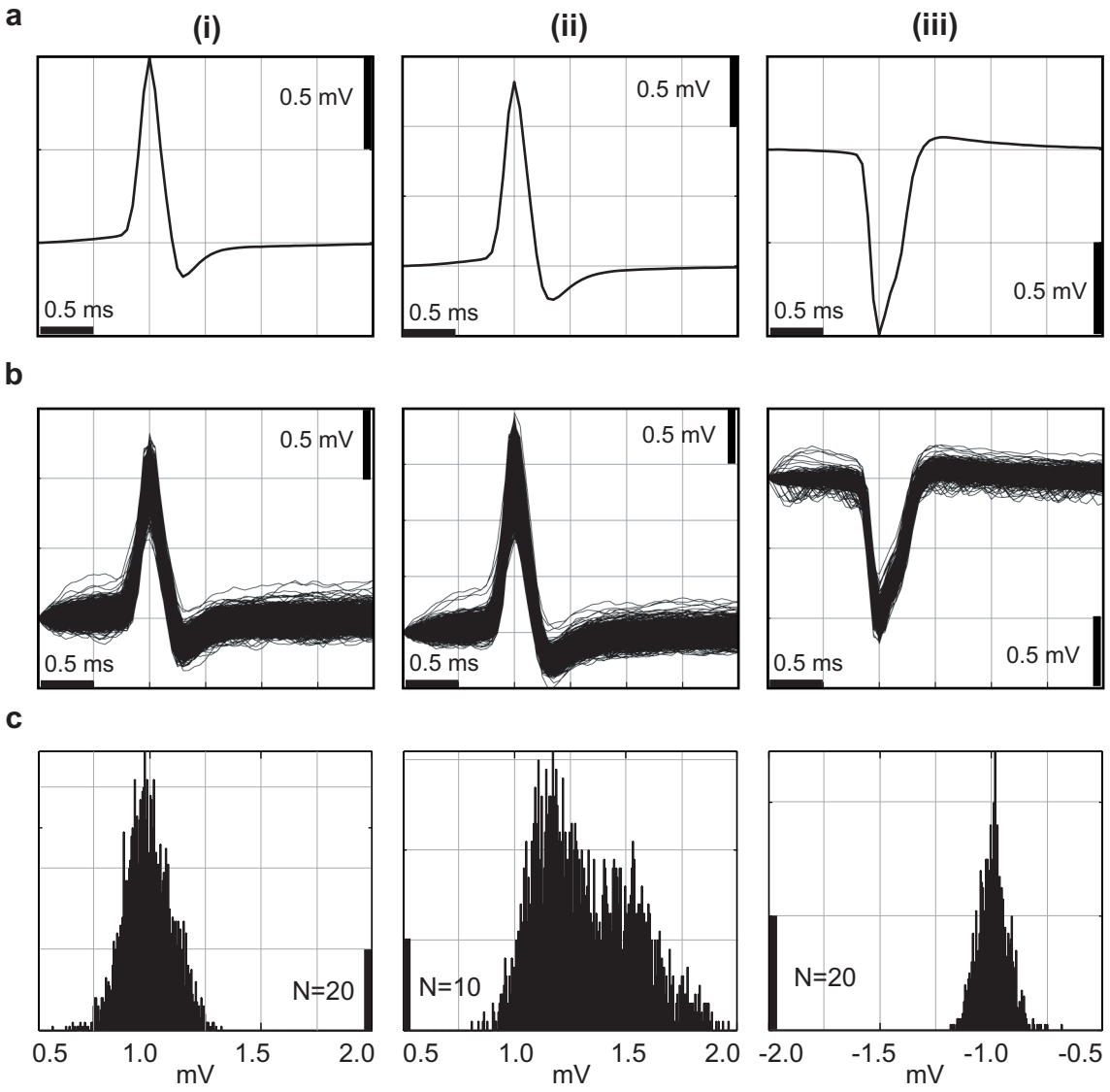

Figure 5.11: Illustration of spike amplitude distribution

(a) Average spikes for two examples of high amplitude positive spikes, **(i)** and **(ii)**, and the single high amplitude negative spike in my data set, **(iii)**. **(b)** Individual traces making up the averages shown in **a**, for **(i)** N=2813, **(ii)** N=2312, **(iii)** N=991. **(c)** Histogram of peak amplitudes. **(i)** has average variability for HAPS in my data set, σ=0.11 mV; **(ii)** has the highest variability of all HAPS which I recorded σ=0.22 mV; **(iii)** has σ=0.07 mV.

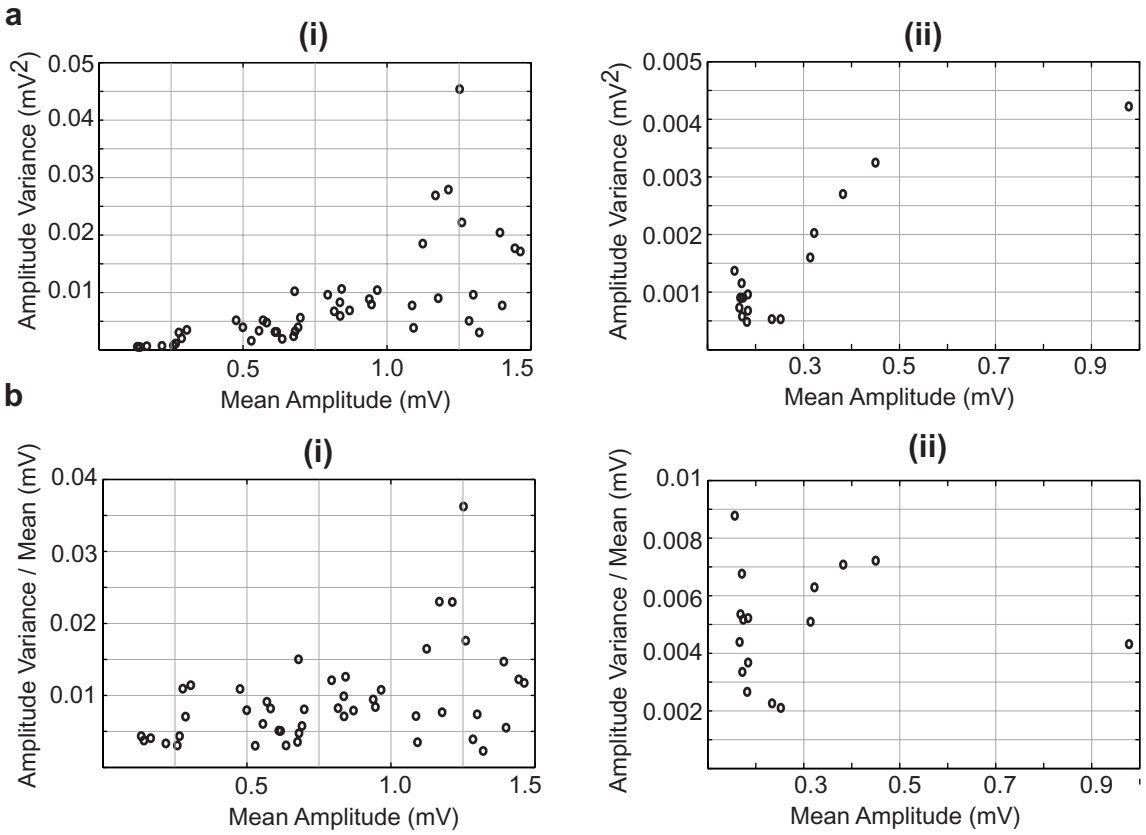

Figure 5.12: Analysis of spike amplitude variance

(a) Variance of the amplitude plotted against the mean spike amplitude for positive spikes **(i)** and negative spikes **(ii)**. Each data point represents spikes from one recording location. Both positive and negative spikes show spike amplitude variance that increases with the mean amplitude. **(b)** Variance of the amplitude divided (normalized) by the mean amplitude, plotted against the mean amplitude. For positive spikes (**i**) there is a clear positive trend in the normalized variance (correlation coefficient=0.42, P=0.003) while for negative spikes (**ii**) there is not a significant correlation (correlation coefficient=0.04, P=0.88)

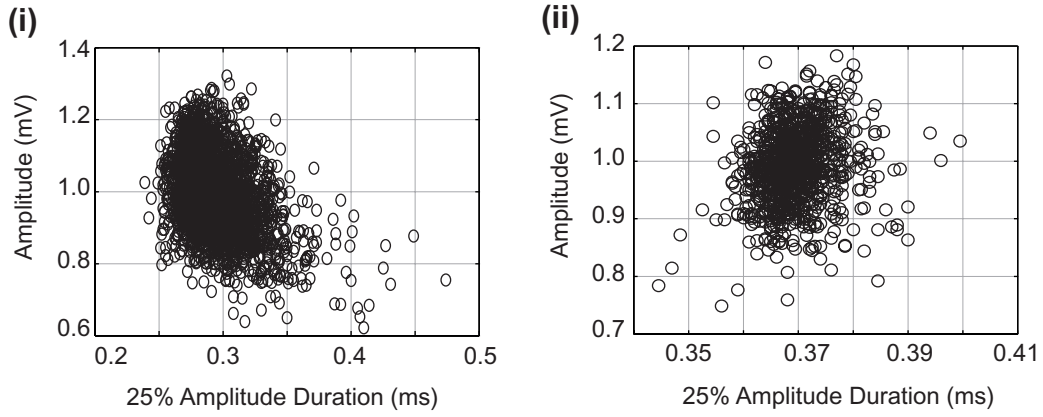

Figure 5.13: Spike amplitude and duration

Duration of individual spikes measured at 25% of peak amplitude for an example high amplitude positive, **(i)**, and negative, **(ii)** spike. The positive spike amplitude and duration have a correlation coefficient of -0.37 (P=2.2e-93) while the negative spike amplitude and duration have a correlation coefficient of 0.17 (P=1e-7).

5.3 Discussion

5.3.1 HAPS are Not a Measurement Artifact

I believe that high amplitude spikes with a leading positive phase (HAPS) are a real neuronal phenomena and are generated by quite different biophysical mechanism that the much more common spikes with a leading negative phase. HAPS are unlikely to be intracellular spikes recorded through the pipette because they are much too fast. Juxtacellular recording with a patch electrode can explain high amplitude spikes (up to around 5 mV), and often show positive spike waveforms [Pinault, 1996, Joshi and Hawken, 2006]. However, my protocol involved none of the careful techniques normally associated with forming and maintaining juxtacellular patches. When I measured the resistance of the electrode during a HAPS recording I found no evidence of the heightened resistance which should result from a membrane seal. Also, I apparently recorded the same unit over tens or even a hundred microns of electrode movement and recorded multiple other units (both positive and negative) over the same period. For the recording of Figure 5.1 to be a juxtacellular recording, I would have to assume that by accident and without applying suction through the pipette a loose patch was formed, whose quality of seal gradually improved by advancing the electrode by 90 μm. This would require that an electrode with a 2 μm tip diameter could drag a 10+ μm neuron and surrounding tissue for 90 μm without rupturing the cell, with the cell remaining well driven by an external stimulus, and actually improving the quality of the patch seal in the process. This hypothetical scenario seems to contradict the previous descriptions of juxtacellular recording as a relatively delicate process requiring careful maintenance of electrode suction, and in which sudden electrode movements tend to rupture a cell to which a seal is already formed [Joshi and Hawken, 2006].

Additionally, similar spikes have been recorded with multi-site silicon probe electrodes which are not known to exhibit any form of direct membrane coupling. For example, HAPS were recorded in cat V1 using high density silicon probe electrodes [Blanche et al., 2005]. In these recordings, positive spikes made up about 15% of the total and included instances at all amplitude levels. Positive spikes were typically recorded on a few neighboring channels of the multi-site electrode array. (T. J. Blanche, personal communication). Taken together these facts suggest that my HAPS recordings are probably neither intracellular nor juxtacellular in nature.

5.3.2 HAPS May be Due to Near-Simultaneous Spikes in a Cluster of Nearby Neurons

Analysis of the biophysics of spike generation demonstrates that single cell action potentials can generate positive spikes in both weak and strong varieties, depending on whether the AP initiates in the soma or in the dendrites. But my model also predicts that for plausible values of the biophysical

parameters the highest amplitude positive spikes are still weaker than the highest amplitude negative spikes: the maximum amplitude for positive polarity spike from a single neuron is probably around 0.5 mV, compared to around 2 mV for negative spikes. Thus, small amplitude positive spikes are probably caused by a dendritic extracellular recording of a somatic AP initiation, and medium amplitude positive spikes (up to a few hundred microvolts) may be a somatic recording of a dendritic AP initiation in a single neuron. But it does not seem possible that high amplitude positive spikes may originate from a single cell under any realistic conditions. The same model accurately predicts that high amplitude negative spikes are well explained by a single unit action potential initiating in the axon and soma.

The superposition principle of extracellular fields allows the possibility that synchronized action potentials could form a high amplitude spike in a cluster of neurons. The model predicts that a synchronized spike in an anatomically realistic cluster consisting of a small number of cells would have the correct peak amplitude and spatial extent of the high amplitude region to match the recordings. And there is evidence for the required millisecond time scale synchronization in thalamo-cortical processing [Bruno and Sakman, 2006]. But there is at this time no direct evidence that clusters of layer 5 pyramidal neuron do in fact synchronize their spiking with natural mechanisms as I propose. I therefore consider the hypothesis that synchronized layer 5 cell clusters generate HAPS to be unproven but the most plausible of all the alternatives I know. To confirm or deny this hypothesis requires that positive polarity extracellular spikes be identified *in vitro* and the mechanism of their generation probed under controlled conditions.

5.3.3 Frequency of Different Spike Waveforms

As illustrated in Figure 4.4, the majority of the high amplitude spikes in my recordings have positive peaks. However, in [Blanche et al., 2005] high amplitude positive and negative spikes were recorded in approximately equal proportions (T. J. Blanche, personal communication). Each sample consists of hundreds of recordings, but high amplitude units form only a small fraction. So it is possible that the difference is due to the random electrode placement. If it is not accidental, possible explanations for the discrepancy include differences resulting from the anesthesia and stimulation protocols. A more interesting possibility is that if HAPS depend on network activity for synchronization, then the smaller size of the pipette electrode may be less disruptive to the cortical circuitry than the silicon probes used in [Blanche et al., 2005]. Unfortunately, spike polarity and amplitude are rarely reported in extracellular recording studies and it is not possible to make a more systematic comparison with the literature. Comparison of the types of spike recorded with different electrodes and under different protocols is an interesting topic for further study.

5.3.4 Concentrations of Active Currents

My simplified model demonstrated that the maximum amplitude of positive spikes should occur when the distal dendrites contain the highest density of active Na^+ channel conductance. On the other hand, as described in section 4.3.3, the best model match for the duration of negative spikes in cat V1 requires that active Na^+ channel conductance be concentrated in the axon initial segment, soma and proximal dendrites. In contrast to both of these results, *in vitro*patch clamp studies of neocortical neurons have found that the density of Na^+ channels is uniform throughout the soma and thick dendrites [Migliore and Sheperd, 2002].

To resolve this apparent conflict, I propose that apparent differences in conductance densities might be due to neuromodulators and second messenger cascades active under *in vivo* conditions [Tsubokawa, 2000]. In this framework, proximal vs. distal concentrations of active currents may correspond to different modes of operation for the pyramidal cell. When active currents are proximally concentrated, the pyramidal cell operates as a classical integrate and fire computational unit at the soma. With distally concentrated active currents, the pyramidal cell would fire an AP with only a modest amount of input in a single dendritic branch, due to the combination of highly active Na^+ channels conductance and the high input resistance in narrow dendrites. In such a state each dendrite could act as an independent coincidence detector and the neuron would be primed to transmit the occurrence of even a small amount of excitatory input.

5.3.5 Mechanism of Synchronization

The proposed explanation for HAPS requires a cluster of layer 5 pyramidal cells to fire distally initiated APs within a relatively short time window, less than 0.5 ms. It remains a question what mechanism could provide such tight synchronization. It has been suggested that gap junctions exist between layer 5 pyramidal neurons based on evidence from both computer models [Traub et al., 2005] and *in vitro* physiology [Roopun et al., 2007]. However, conclusive evidence of gap junctions between layer 5 pyramidal cells remains lacking. It should be noted, however, that the generation of HAPS seems to require dendritic AP initiation; so while axonal gap junctions may provide synchronization, it is necessary that these axons in turn synapse onto the dendrites of the cluster neurons.

An alternative possibility is that the synchronization could be due to synchronized synaptic inputs. Sensory events evoke tightly synchronized thalamic input to cortex [Bruno and Sakman, 2006] and it is therefore possible that the output of cortical processing in the superficial layers of a minicolumn may lead to synchronized inputs to L5 pyramidal neuron clusters at the base. Because HAPS generation requires high levels of active dendritic Na^+ channel conductance, the required amount of synchronized synaptic input to trigger an AP would be modest. Both of these explanations are consistent with anatomical analysis of the excitatory input to L5 pyramidal neurons: the largest

source of excitatory input to L5 pyramidal neurons is from nearby L2/3 pyramidal neurons and the second largest source is from the axons of other L5 pyramidal neurons [Binzegger et al., 2004].

5.3.6 Minicolumn and Cluster Function

The cluster of layer 5 pyramidal neurons at the base of minicolumn forms the output of the cluster, projecting to other parts of cortex and to subcortical structures [Buxhoeven and Casanova, 2002]. If neurons in layer 5 pyramidal cell clusters fire with submillisecond precision as implied by my HAPS model, it suggests that the cluster is a mechanism that allows precisely timed outputs to be sent simultaneously to multiple remote brain regions for further processing. Whether or not spike timing is an important aspect of neural information processing has been a subject of furious debate [Buzsaki et al., 1994]. If layer 5 pyramidal cell clusters do, in fact, discharge with submillisecond precision it would strongly support the notion that the precise timing of spikes contains essential information used by neural computation.

5.3.7 Conclusion

Whether or not my hypothesis about synchronized layer 5 pyramidal clusters is correct, it is remarkable that after decades of recording extracellular spikes from cortex the dichotomy between positive and negative spikes has not previously been considered worthy of analysis. This may have been a reasonable approach in the past due to the lack of analytic tools to make such information meaningful. But the recent advances in the necessary modeling techniques combined with the publication of the core portions of my own model code[1] argues that this potentially useful information should no longer be ignored. If my theory is not correct then another explanation for high amplitude positive spikes in cortex should be formulated and tested. The brain is a complex system which neuroscientists still understand poorly – there is no reason to be complacent about any unexplained phenomena.

5.4 Methods

The recording methods are the same as those described in section 4.2.2.1. The negative polarity spikes considered in chapter 4 were recorded in the same sessions as the positive spikes considered in the present chapter.

The simulations of simplified cylinder neurons in section 5.2.4 are based on the simulation of cylinder **B** described in section 3.3.4. The negative and positive spike generating cylinders are modified so that they have the same *total* Na^+conductance on their surface, concentrated in the

[1]Extracellular Action Potential Simulations code package available for download from http://senselab.med.yale.edu/senselab/modeldb/

center to create the negative spike and concentrated in the ends to make the positive spike. For the negative spike cylinder, the peak Na^+ $\bar{g}$ is 0.05 and it declines (linearly) to 2% of that amount in the distal dendrites. For the positive spike cylinder the density is reversed.

The simulations of L5 pyramidal cells use the same model described in chapter 4. The parameters were altered so that the maximal Na^+ $\bar{g}$ occurred in the distal dendrites rather than the proximal dendrites. The ratio of distal to proximal Na^+ conductance density was typically around 45 times for apical dendrites and around 60 times for basal dendrites. I used the same method for the non-uniform distribution as described in section 4.2.3.4: the density was scaled in proportion to each compartments distance to its deepest (farthest from the soma) ancestor, raised to a power, albeit with the densest values occurring in the deepest compartments. The power for scaling the distance was 2.

I also made some modifications to the density of the K^+ conductance to give a better match to the waveform of the positive spike recordings. The K type K^+ conductance was also made densest in the distal dendrites, though the ratio was only around 10 timesthe somatic density. The M type K^+ current was made densest in the medial apical trunk and declined to lower densities in both the distal apical dendrites and the basal dendrites, typically 10%-30% of the maximum value.

In comparison to the negative spike simulations, the positive spike simulations are more reliant on the M and K type K^+ conductance for repolarization, and the total Na^+ conductance is higher. The maximum conductance densities for the positive spike simulations are listed in table 5.1.

Conductance	Meynert Cell	Cluster
I_{Na+} *	1.03	0.83 +/- 0.08
$I_{K+AProx}$	0.001	0.001
I_{K+C}	0.001	0.001
I_{K+D}	0.001	0.001
I_{K+K}	0.06	.03
I_{K+M}	0.03	0.02
I_{HSoma}	0.0005	0.0005
I_{Ca2+L}	0.0002	0.0002
I_{Ca2+N}	0.0002	0.0002
I_{Ca2+R}	0.0002	0.0002
I_{Ca2+T}	0.0001	0.0001

Table 5.1: Maximal conductance densities for the positive spike model.

All units are mS/cm^2. * For the Na+ conductance density the value for distal apical dendrites is shown. For cells used in the cluster simulation the Na+ conductance density was varied for each cell and the average and standard deviation are shown.

The arrangement of the layer 5 pyramidal neuron cluster was based on the descriptions in [Peters and Yilmaz, 1993]. The simulation was made using 11 detailed neuronal reconstructions. Four of these neurons are medium-sized and have thinner apical trunks as described in section 4.2.3.1 ("thin"). The four medium-sized pyramidal cells are each repeated 5 times in the cluster so

that most of the neurons in the cluster are medium in size (my morphology sample lacked enough medium size neurons to achieve this without repeating morphologies.) The remaining six neurons are large and have the thicker dendrites described in section 4.2.3.1. The cells were organized around a cylinder 40 μm in diameter and around 75 μm high, spaced so that no somas were within around 20 μm of each other. The morphology of each neuron was slightly modified to make the apical trunks ascend in parallel, as described in [Peters and Yilmaz, 1993]: a bend of about 10°-15° was placed in each apical trunk so that after the cell bodies were arranged the apical trunks were reasonably close to parallel.

To create the simulation of the synchronized spike each neuron was simulated once. 50 trials were performed in which each spike was offset in time by an amount drawn from a Normal distribution with zero mean and sigma = 0.1 ms.

Chapter 6

Conclusion

I have examined the biophysics of extracellular action potentials (EAPs) and analyzed a number of questions pertaining to the interpretation of EAP recordings. I conclude by briefly reviewing the questions posed in the introduction, and the answers I have suggested.

- *Why do EAPs waveforms show so much variability when viewed at a short (e.g. millisecond) time scale, while intracellular action potentials (IAPs) are so stereotyped? And is this variability essentially random, or can it be used to identify different neuron classes or intracellular phenomenon?* As explained in chapters 2 and 3, EAPs result from membrane currents which are proportional to the second derivative of the spatial profile of the membrane potential (IAP). As such, EAPs reflect the variability of action potential initiation and propagation scenarios – information that is less apparent in the IAP at any isolated recording location. The pattern of AP initiation and propagation primarily results from the distribution of active ionic currents. The detectable EAP primarily reflects the ionic conductances dominant in the perisomatic region (e.g., Figures 2.1, 2.3 and 2.2). But very different distributions of ionic conductances still have relatively stereotypes IAPs (e.g., Figure 3.3). Alternatively, second derivatives amplify small differences in the spatial profile, leading to the result that superficially similar IAPs can have significantly different EAPs (e.g Figures 3.8, 3.9 and 3.10). The precise dendritic morphology of different neurons in the same class makes very little difference in the EAP waveform but the size of the neuron contributes to the amplitude (e.g., Figures 3.16 and 3.17). The same is also true of electrode position relative to the soma: it influences EAP amplitude far more than the waveform (e.g., Figure 3.15 and 3.14). Taken as a whole, it is evident that variability of the EAP is only random to a small degree and that the randomness is primarily in factors determining the amplitude (i.e., electrode position and neuron size are typically unknown *in vivo*). The waveform itself contains a significant amount information that can be used to make conclusions about the class of neuron, its composition of ionic channels, and how its action potential initiates and propagates.

- *How does the amplitude of the EAP depend on factors like the size of the neuron and the distance of the recording electrode, and at what range can an electrode reliably record different types of neurons?* A wide variety of factors influence in the amplitude of the EAP, primarily the electrode position (e.g., Figure 3.14), the size neuron (e.g., Figure 3.17), active Na^+conductance density (e.g., Figure 4.20), and local resistivity (conductivity) of the neuropil (e.g., Figure 4.19). Electrode position affects the amplitude of any EAP with a decay with distance from the neuron that is faster than linear. Aside from electrode position, the greatest impact seems to be due to neuron size: the plausible change of Na^+ conductance density from lowest to highest only leads to about 33% change in detection radius, while the plausible variation in resistivity and cell size each leads to about 100% change in detection range. But while extremes of resistivity occur, the variance is relatively low in comparison to the variance of neuron size. Also, local resistivity is essentially random while neuron size is systematically related to the brain region and type of cell. All of these factors combine to create a very wide range of detection distances. Small neurons with low Na^+ conductance density may be undetectable unless the recording electrode practically touches the cell, while the largest neurons with relatively high Na^+ density may be detectable as much as 80 μm away. Another factor which strongly influences the detection range is the prevalent background noise and the SNR required by the clustering algorithm. An interesting question for further research is, for given recording conditions, what proportion of the noise is due to background biological sources (unavoidable), how much is due to intrinsic properties of the electrode (i.e., thermal noise; potentially improvable) and how much is due to stray noise in the environment (almost always correctable).

- *How likely is it that different neurons in range of the electrode produce similar amplitude spikes and thus create multi-unit clusters?* I found that this depends on the spike amplitude and the typical size of the neurons in question. For low amplitude spikes in cortex there are from 0.5 to 2 other neurons present at a distance that would produce a spike of similar amplitude, depending on the layer of the recordings (i.e., size of the neurons; see table 4.14 and 4.23). But this number decays rapidly with the amplitude of the spike under consideration. Also, even if another neuron is present at the correct range to result in a multi-unit cluster it must be firing action potentials to do so. The net result is a relatively modest impact on quantitative measurements of cortical recordings (e.g., Figure 4.22).

- *Are extracellular recordings biased towards different classes of cells due to differences in their resultant EAP amplitudes?* I found that the answer to this question depends heavily on the recording setup and procedure in use: If recordings are made in such a way that very low amplitude spikes (i.e., <100 μV) are recorded (e.g., using unbiased sampling or online clustering procedures to locate units) then in practice there will be only very modest bias towards larger

cells. But if recordings only consider high amplitude units (e.g., if such units are deliberately sought out so as to ensure stability during a long recording session) then bias towards larger neurons is likely to be substantial, and small neurons will only make up a small fraction of those recorded (e.g., see Figures 4.24 and 4.25). Interestingly, my answer to this question was heavily influenced by my answer to the question of activity (below): I found that in cat V1 the largest neurons were also the least active, reducing the probability of recording larger neurons. If neurons in all layers (i.e., of all sizes) had been equally active there would have been significant bias even for recording spikes of the lowest amplitude. Another important factor turned out to be the relative thickness of the cortical layers: in cat V1 layer 5 is the thinnest layer, making up the fewest number of cells – this also reduced the probability of recording from large cells. It remains a question how well these findings match the circumstances in other brain regions.

- *What portion of neurons in the brain are actually active during recordings?* Using my sample of cortical recordings, calculation for detection ranges and the known densities of cortical neurons I estimated that the fraction of neurons that were active during my protocol. Surprisingly, the result was very different for the different layers of cortex with superficial layers apparently much more active than deeper layers. The spiny neurons in layers 2/3 and 4 seem to be 50% to 80% active, while neurons in layers 5 and 6 were only 10% and 20% active, respectively (see Figure 4.20 and 4.22). An interesting question for further study is how much these answers depend on the protocol I used. For example, I stimulated V1 with simple oriented edges and it is not known how this result would change for a more natural stimuli.

A final question I did not anticipate at the outset of this study was whether or not certain EAP recordings were in fact generated by single neurons, as is commonly supposed. As described in Chapter 5, the biophysical model predicts that the high amplitude positive spikes I recorded could not possibly be generated by single neurons. I showed that it possible that synchronized spikes, initiated in the distal dendrites in clusters of layer 5 pyramidal neurons could produce spikes with correct amplitude and waveform. But confirmation of this hypothesis would require further experiments, most like *in vitro*. Exactly what produces these positive spikes remains a very interesting question for further research.

Taken together, these results show that a biophysical model of extracellular action potentials provides a great deal of useful information about the brain. The techniques I have used here could be applied equally well to other areas of the brain and to analyze other questions regarding extracellular recordings. To this end the core part of my modeling code has been made available on the Internet at the ModelDB web site: *http://senselab.med.yale.edu/senselab/modeldb/*. At the present time, neuroscientists are still unable to answer many important questions about the brain.

My thesis research has helped to answer some questions, raised new questions, and provided a few new tools with which to search for answers.

Appendix A

Method of Images for Nonhomogeneous Resistivity

My model accounts for the impact of the higher resistivity of the CA1 pyramidal cell body layer [López-Aguado et al., 2001] using the Method of Images; for review, see e.g., [Jackson, 1962] [Maxwell, 1881]. In the method of images the impact of *planar* discontinuities in a volume conductor on the voltages resulting from current sources[1] can be calculated analytically using so-called "image" sources.

A.1 A Single Planar Discontinuity

I begin by reviewing the simple case of a point source of current and a single planar boundary separating two semi-infinite regions with conductivities σ_1 and σ_2, as illustrated in Figure A.1. Assuming that region 1 contains a point source of current, the voltage within region 1 is given by adding an image source at an equal distance from the discontinuity on the opposite side (in region 2) having magnitude:

$$I_{\text{image}} = I_{\text{original}}(\frac{\sigma_1 - \sigma_2}{\sigma_1 + \sigma_2}) \tag{A.1}$$

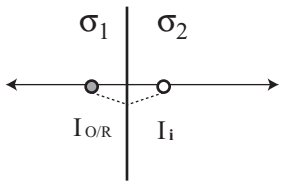

Figure A.1: Method of images for a single planar discontinuity

Note that the image source always has a magnitude less than that of the original source (because

[1]The problem is dual to the problem of static electrical charges in a dielectric medium.

$\sigma_1, \sigma_2 > 0$) and the sign of the image depends on the relative conductivities. If region 2 has conductivity less than region 1, the image source will have the same sign and thus increase voltages within region 1. The intuitive explanation is that region 2 resists the flow of current leaving more current in the higher conductivity region 1. If region 2 has a higher conductivity than region 1 the sign of the image will be opposite the sign of the original, reducing the voltage in region 1. The intuitive explanation in this case is that region 2 draws current away from region 1. The voltage in region 1 is given by:

$$\Phi_1 = \frac{1}{\sigma_1}\left(\frac{I_{\text{original}}}{R_1} + \frac{I_{\text{image}}}{R_2}\right) \tag{A.2}$$

where R_1 and R_2 are distances from the original source and the image source respectively. At the same time, in order to solve for the impact of the discontinuity on the opposite side of the boundary from the original source (region 2), the original source is replaced with a new source having magnitude:

$$I_{\text{replacement}} = I_{\text{original}}\left(\frac{2\sigma_2}{\sigma_1 + \sigma_2}\right) \tag{A.3}$$

In this case the replacement source always has the same sign as the original source, but the magnitude will be less than the original if region 2 has lower conductivity than region 1, or greater than the original if region 2 has higher conductivity. The voltage on the opposite side of the boundary from the source is given by:

$$\Phi_2 = \frac{1}{\sigma_2}\left(\frac{I_{\text{replacement}}}{R_1}\right) \tag{A.4}$$

This approach satisfies Gauss' law in both regions separately (note that in each region the solution involves fictitious charges only in the other region) and must satisfy the condition of continuity of the Electric flux at the boundary.

If I use cylindrical coordinates and define the boundary to be at $z = 0$ and place the original charge at $z = d$ (so region one is the positive half of the z-axis) I have $R_1 = \sqrt{r^2 + (d-z)^2}$ and $R_2 = \sqrt{r^2 + (d+z)^2}$. The boundary condition is:

$$\begin{aligned} \lim_{z \to 0^+} \sigma_1 E_z &= \lim_{z \to 0^-} \sigma_2 E_z \\ \lim_{z \to 0^+} E_r &= \lim_{z \to 0^-} E_r \end{aligned}$$

Note that

$$\begin{aligned}\frac{\partial}{\partial z}(\frac{1}{R_1})|_{z=0} = -\frac{\partial}{\partial z}(\frac{1}{R_2})|_{z=0} &= \frac{d}{(r^2+d^2)^{3/2}} \\ \frac{\partial}{\partial r}(\frac{1}{R_1})|_{z=0} = \frac{\partial}{\partial r}(\frac{1}{R_2})|_{z=0} &= \frac{-r}{(r^2+d^2)^{3/2}}\end{aligned}$$

For the z direction I have:

$$\begin{aligned}\sigma_1\frac{\partial}{\partial z}\frac{1}{\sigma_1}(\frac{I_{\text{original}}}{R_1}+\frac{I_{\text{image}}}{R_2}) &= \sigma_2\frac{\partial}{\partial z}\frac{1}{\sigma_2}(\frac{I_{\text{replacement}}}{R_1}) \\ \frac{d}{(r^2+d^2)^{3/2}}(1+\frac{\sigma_2-\sigma_1}{\sigma_1+\sigma_2}) &= \frac{d}{(r^2+d^2)^{3/2}}(\frac{2\sigma_2}{\sigma_1+\sigma_2}) \\ \frac{2\sigma_2}{\sigma_1+\sigma_2} &= \frac{2\sigma_2}{\sigma_1+\sigma_2}\end{aligned}$$

And for the radial direction:

$$\begin{aligned}\frac{\partial}{\partial r}\frac{1}{\sigma_1}(\frac{I_{\text{original}}}{R_1}+\frac{I_{\text{image}}}{R_2}) &= \frac{\partial}{\partial r}\frac{1}{\sigma_2}(\frac{I_{\text{replacement}}}{R_1}) \\ \frac{-r}{(r^2+d^2)^{3/2}}\frac{1}{\sigma_1}(1-\frac{\sigma_2-\sigma_1}{\sigma_1+\sigma_2}) &= \frac{-r}{(r^2+d^2)^{3/2}}\frac{1}{\sigma_2}(\frac{2\sigma_2}{\sigma_1+\sigma_2}) \\ \frac{1}{\sigma_1}(\frac{2\sigma_1}{\sigma_1+\sigma_2}) &= \frac{1}{\sigma_2}(\frac{2\sigma_2}{\sigma_1+\sigma_2}) \\ &= \frac{2}{\sigma_1+\sigma_2}\end{aligned}$$

which completes the proof of the solution. For further details see [Jackson, 1962], on which my explanation is based.

A.2 Two Planar Discontinuities

With two discontinuities the solution is somewhat more complicated. Consider three regions with conductivities σ_1, σ_2 and σ_3, where regions 1 and 3 are semi-infinite and region 2 is a finite region sandwiched in the middle. I will first consider the solution for a point source of current in the middle region, region 2, as illustrated in Figure A.2. [Weber, 1950] gives a solution for the case where $\sigma_1 = \sigma_3$. The voltage in region 2 is given by adding two infinite series of sources in regions 1 and 3. The series of image sources in region 1 has magnitude:

$$I_n^1 = [\frac{\sigma_2-\sigma_1}{\sigma_1+\sigma_2}]^{\overline{(n/2)}}[\frac{\sigma_2-\sigma_3}{\sigma_2+\sigma_3}]^{\underline{(n/2)}} \tag{A.5}$$

where $(\overline{x})$ and $(\underline{x})$ indicate the ceiling and floor of the argument, respectively. Similarly, the

sequence of image sources in region 3 have magnitudes given by:

$$I_n^3 = [\frac{\sigma_2 - \sigma_3}{\sigma_2 + \sigma_3}]^{(\overline{n/2})}[\frac{\sigma_2 - \sigma_1}{\sigma_1 + \sigma_2}]^{(\underline{n/2})} \tag{A.6}$$

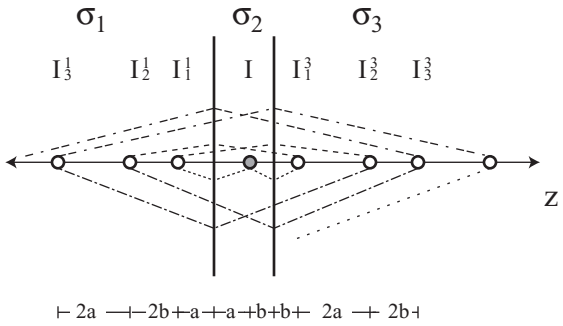

Figure A.2: Method of images for two planar discontinuities — middle Source

The location of the images is given by a sequence of reflections across the two boundaries, as illustrated in Figure A.2. The first image in each outer region is a direct reflection of the original source and thus is at an equal and opposite location across the appropriate boundary. The second image in each region is a reflection of the first image in *the other region* and hence is at a location that is opposite from that image, as reflected across the near boundary (i.e., the second image in region 1 is the reflection of the first image in region 3 across the 1/2 boundary). The sequence of alternating reflections across the two boundaries explains the increasing powers of the reflection coefficients $(\frac{\sigma_2-\sigma_1}{\sigma_1+\sigma_2})$ and $(\frac{\sigma_2-\sigma_3}{\sigma_2+\sigma_3})$ in the image magnitudes. Consequently the exact solution for the electric potential in the interior region (region 2) at an arbitrary location is given by:

$$\begin{aligned}\Phi^2 \quad = \quad & \frac{I_{\text{original}}}{\sigma_2} \times \{\frac{1}{R_0} + \\ & \sum_{n=1}^{\infty} \frac{[\frac{\sigma_2-\sigma_1}{\sigma_1+\sigma_2}]^{(\overline{n/2})}[\frac{\sigma_2-\sigma_3}{\sigma_2+\sigma_3}]^{(\underline{n/2})}}{R_n^1} + \\ & \sum_{m=1}^{\infty} \frac{[\frac{\sigma_2-\sigma_3}{\sigma_2+\sigma_3}]^{(\overline{m/2})}[\frac{\sigma_2-\sigma_1}{\sigma_1+\sigma_2}]^{(\underline{m/2})}}{R_m^3}\}\end{aligned} \tag{A.7}$$

where R_0 denotes the distance from the original source to the location of the measurement, and R_n^i denotes the distance from n*th* charge in region i ($i \in \{1, 3\}$) to the measurement location.

The solution in either one of the outer regions $\{1, 3\}$ is obtained by taking the infinite sequence of sources in the opposite region, along with the original source, and multiplying by a factor of either $(\frac{2\sigma_2}{\sigma_1+\sigma_2})$ or $(\frac{2\sigma_2}{\sigma_2+\sigma_3})$, for the solution in region 1 and 3 respectively. This is similar to the solution described for the single discontinuity in equation A.1. Consequently, the voltage in region 1 is given

by:

$$\Phi^1 = \frac{I_{\text{original}}}{\sigma_1} \times (\frac{2\sigma_2}{\sigma_1+\sigma_2}) \times \{\frac{1}{R_0} + \sum_{m=1}^{\infty} \frac{[\frac{\sigma_2-\sigma_3}{\sigma_2+\sigma_3}]^{\overline{(m/2)}}[\frac{\sigma_2-\sigma_1}{\sigma_1+\sigma_2}]^{\overline{(m/2)}}}{R_m^3}\} \tag{A.8}$$

and, similarly, the voltage in region 3 is given by:

$$\Phi^3 = \frac{I_{\text{original}}}{\sigma_3} \times (\frac{2\sigma_2}{\sigma_2+\sigma_3}) \times \{\frac{1}{R_0} + \sum_{n=1}^{\infty} \frac{[\frac{\sigma_2-\sigma_1}{\sigma_1+\sigma_2}]^{\overline{(n/2)}}[\frac{\sigma_2-\sigma_3}{\sigma_2+\sigma_3}]^{\overline{(n/2)}}}{R_n^1}\} \tag{A.9}$$

Proof that the solution satisfies the boundary conditions at each of the two boundary is made in the same way as the proof for the single-layer case of section A.1, although with somewhat greater complexity and I omit it for the sake of brevity. Note that the terms in the infinite series of equations A.7, A.8 and A.9 decay in amplitude because $\sigma_1, \sigma_2, \sigma_3 > 0$. In practice only a few (< 5) terms are required to achieve a reasonable degree of accuracy for conductivities typically found in the brain.

The solution for the case where the voltage is one of the outer regions is illustrated in Figure A.3. The method is first proposed in [Maxwell, 1881], also in the context of current sources in volume conductors.

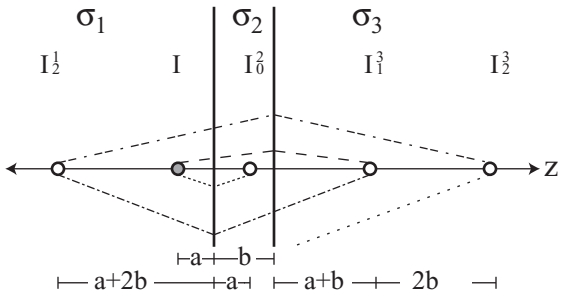

Figure A.3: Method of images for two planar discontinuities — outer source

For the voltage in the middle layer I require two infinite series of charges in the outer layers:

$$I_n^1 = \frac{2\sigma_2}{\sigma_1+\sigma_2}[(\frac{\sigma_2-\sigma_1}{\sigma_1+\sigma_2})(\frac{\sigma_2-\sigma_3}{\sigma_2+\sigma_3})]^{(n-1)} I_{\text{original}} \tag{A.10}$$

$$I_n^3 = \frac{2\sigma_2}{\sigma_1+\sigma_2}[\frac{\sigma_2-\sigma_1}{\sigma_1+\sigma_2}]^{(n-1)}[\frac{\sigma_2-\sigma_3}{\sigma_2+\sigma_3}]^{n} I_{\text{original}} \tag{A.11}$$

For the voltage in layer 1 the solution uses the original charge, the infinite series in layer 3 multiplied by $\frac{2\sigma_1}{\sigma_1+\sigma_2}$ plus a single image source in layer 2:

$$I_0^2 = I_{\text{original}}(\frac{\sigma_1-\sigma_2}{\sigma_1+\sigma_2}) \tag{A.12}$$

The solution in layer 3 uses the infinite series in layer 1 multiplied by $\frac{2\sigma_2}{\sigma_2+\sigma_3}$.

Appendix B

Parameters for the CA1 Model

Region, Type	ρ (spines/μm)	Compartment Classification[1]
oriens, proximal	0.64	$\Delta < 50$
oriens, distal	3.4	$\Delta > 50$
radiatum, thick proximal	0.03	$d > 1.5$, $\Delta \leq 50$
radiatum, thick medial	2.3	$d > 1.5$, $50 < \Delta < 150$
radiatum, thick distal	6.9	$d > 1.5$, $\Delta \geq 150$
radiatum, thin	3.5	$d < 1.5$, $\Delta \leq 300$
lacunosum-moleculare, thick	1.72	$1 < d < 1.5$, $\Delta > 300$
lacunosum-moleculare, medium/thin[2]	0.6	$d \leq 1$, $\Delta > 300$

Table B.1: Variable parameters for the spine model of section 2.2.3.1.

[1] All units are in μm. [2]Represents an average of the values for lacunosum-moleculare/medium and l-m/thin from [Megias et al., 2001]

Current	Variable	Order	$V_{1/2}$ (mV)	z	γ	K (1/msec)	τ_0 (msec)
$I_{Na^+Ax.}$	m	3	-51	-4.6	0.05	100	0.04
	h	1	-50	12.6	0.2	2	0.25
I_{Na^+SD}	m	3	-46	-4.2	0.05	100	0.04
	h	1	-50	12.6	0.2	1.33	0.25
I_{HSoma}	m	1	-82	6.3	–	–	100
I_{HDend}	m	1	-90	6.3	–	–	100
I_{K^+AProx}	m	4	-40	-3.2	–	–	0.2
	h	2	-50	3.2	0.5	0.67	0.3
I_{K^+ADist}	m	4	-50	-3.2	–	–	0.2
	h	2	-60	3.2	0.5	0.67	0.3
I_{K^+D}	m	4	-63	-3.0	0.5	1.0	0.25
	h	2	-73	2.5	0.5	–	1000
I_{K^+K}	m	1	-5	-5.1	0.5	0.25	0.25
	h	1	-65	1.7	0.5	1.0	100
I_{K^+M}	m	2	-45	-6.3	0.5	0.5	2
$I_{Ca^{2+}L}$	m	2	5	-3.2	0.5	0.5	2.0
$I_{Ca^{2+}N}$	m	2	-14	-3.9	0.2	0.2	1
	h	1	-40	2.5	0.5	1.0	50
$I_{Ca^{2+}R}$	m	2	0	-3.2	0.5	0.33	3
	h	1	-40	2.8	0.5	1.0	50
$I_{Ca^{2+}T}$	m	2	-30	-3.6	0.1	0.2	2.0
	h	1	-60	5.1	0.5	1.0	25

Table B.2: Parameter values for non-Ca^{2+} dependent active current kinetics

Note that for all current types activation particles are denoted m and inactivation particles are denoted h

Variable	Order	α ($msec^{-1}$ mM^{-n})	β (1/msec)	n	τ_0 (msec)
m	8	1e31	0.2	2	5

Table B.3: Parameters for the I_{K^+AHP} current model

.

Transition	$1/\tau_{max}$ (1/msec)	k (mV)	$V_{1/2}$ (mV)	$1/\tau_{min}$ (1/msec)	α (mM^{-n})	n
O → I	0	12	-30	0.67	–	–
I → C	0	-10	-120	10	–	–
C → O	0.02	6	-45	50	2.5e10	3
O → C	0	-3	-40	0.67	–	–

Table B.4: Parameters for the I_{K^+C} current model

	I_{K^+AHP}						
	$\bar{g}_{high}$	$\bar{g}_{low}$	$I_{Ca^{2+}L}$	$I_{Ca^{2+}N}$	$I_{Ca^{2+}R}$	$I_{Ca^{2+}T}$	$I_{HSoma/Dend}$
$\bar{g}$	0.1	0.05	0.2	0.2	0.2	0.1	0.4

Table B.5: Conductance density parameters for AHP type K^+ currents, Ca^{2+}currents, and mixed-ion H type currents.

As these currents had less impact on the extracellular waveform, they were made constant for all cells. All units are mS/cm^2.

Appendix C

Parameters for the Cortex Model

Layer	Apical	Basal
L2/3	1.5	1.25
L4	NA	1.25
L5	2.5	1.75
L6	1.75	1.25

Table C.1: Spine correction factors for the spiny cortical neurons.

	Somatic/Dendritic			Axonal		
Transition	$V_{1/2}$	K	τ	$V_{1/2}$	K	τ
Closed → Open ("A")	-30	3	0.3	-30	4.5	0.5
Open → Inactivated ("I")	-40	1	0.15	-30	1	0.3
Inactivated → Closed ("CI")	-55	-3	1.0	-50	-3	2

Table C.2: Kinetics parameters for the cooperative Na^+ channel.

Used in the spiny neurons model based on the formalism of [Naundor et al., 2006].

	Dendritic	Axonal
J_{min}	0.05	0.1
J_{max}	0.5*	1.0

Table C.3: Cooperativity parameters for the cooperative Na^+ channel model.

Used in the spiny neurons model based on the formalism of [Naundor et al., 2006]. *The cooperativity for the soma and axon hillock was the same as the maximal value for the axon.

Conductance	Gate	Variable	Value
I_{K+K}	m	γ	0.95
I_{K+K}	m	K	3.33
I_{K+K}	m	τ_0	0.1
I_{K+M}	n	τ_0	1

Table C.4: Differences between the Hodgkin-Huxley kinetics for the spiny neurons and the smooth interneurons.

Parameters not listed use the same values as for the spiny neurons, described in section 2.2.3.2.

	Somatic/Dendritic			Axonal		
Transition	$V_{1/2}$	K	τ	$V_{1/2}$	K	τ
Closed - Open ("A")	-35	2	0.8	-35	2.75	0.3
Open - Inactivated ("I")	-45	1	0.15	-45	1	0.08
Inactivated - Closed ("CI")	-55	-3	0.2	-55	-3	0.2

Table C.5: Kinetics parameters for the cooperative Na^+ channel used in the smooth interneurons

Model based on the formalism of [Naundor et al., 2006].

Apical Trunk							
Distance:	**0-20**	**20-40**	**40-60**	**60-80**	**80-100**	**100-150**	**150-200**
L2/3	3.7	1.5	1.4	1.2	1.0	0.8	0.7
L5	5.9	4.4	4.2	4.1	4.0	4.0	3.7
L6	4.7	3.3	2.8	2.6	2.6	2.6	2.5

Apical Trunk							
Distance:	**200-300**	**300-400**	**400-500**	**500-600**	**600-700**	**700-800**	**800-1000**
L2/3	0.6	NA	NA	NA	NA	NA	NA
L5	3.5	3.4	2.1	1.8	1.6	1.5	0.7
L6	2.4	2.0	2.4	1.3	1.3	1.1	0.7

Apical Oblique							
Order:	**1**	**2**	**3**	**4**	**5**	**6**	**7**
L2/3	1.0	0.9	0.9	0.9	0.7	0.5	NA
L5	1.3	1.2	1.1	0.8	0.7	NA	NA
L6	1.0	1.0	1.0	0.7	0.7	0.7	0.7

Apical Tuft							
Order:	**1**	**2**	**3**	**4**	**5**	**6**	**7**
L2/3	1.0	0.9	0.9	0.9	0.7	0.5	NA
L5	0.8	0.7	0.6	0.5	0.4	0.4	NA
L6	0.7	0.7	0.6	0.6	0.6	0.6	0.5

Basal							
Order:	**1**	**2**	**3**	**4**	**5**	**6**	**7**
L2/3	1.4	1.0	0.8	0.8	0.7	0.7	NA
L5	1.6	1.0	1.0	0.9	0.9	0.8	0.8
L6	1.4	1.0	0.8	0.8	0.7	0.7	NA

Stellate							
Order:	**1**	**2**	**3**	**4**	**5**	**6**	**7**
L4 Stellate	1.7	0.9	0.7	0.7	0.6	0.6	0.5
Smooth	1.0	0.8	0.7	0.7	0.6	0.4	0.4

Table C.7: Dendrite diameters used for the morphological reconstructions

All length and diameters are in μm.

Appendix D

Relative Thickness of Cortical Regions in the Cat

	Anterior Coronal Sections			Mid-Coronal Sections		Posterior Coronal Sections			
area	prae-	parobit-	post-	insularis	tempor-	occip-	occip-	pari-	
layer	centralis (4)	alis ext- ernal(8)	centralis (1-3)	granu -laris 13	alis sup- erior 22	italis 18	italis 17	etalis 7	Mean
L2/3	18%	48%	37%	48%	41%	33%	27%	47%	37%
L4	21%	11%	12%	15%	6%	24%	25%	19%	17%
L5	31%	24%	28%	13%	21%	15%	27%	15%	22%
L6A	31%	18%	23%	25%	31%	28%	21%	19%	24%

Table D.2: Relative thickness of cortical regions in the cat

Measured from plates in [Snider, 1911]

Bibliography

[Ahmed et al., 1997] Ahmed, B., Allison, J. D., Douglas, R. J., and Martin, K. A. C. (1997). An intracellular study of the contrast-dependence of neuronal activity in cat visual cortex. *Cerebral Cortex*, 7:559–570.

[Aika et al., 1994] Aika, Y., Ren, J. Q., Kosaka, K., and Kosaka, T. (1994). Quantitative analysis of gaba-like-immunoreactive and parvalbumin-containing neurons in the ca1 region of the rat hippocampus using a stereological method,. *Experimental Brain Research*, 99:267–276.

[Baranyi et al., 1993] Baranyi, A., Szente, M. B., and Woody, C. D. (1993). Electrophysiological characterization of different types of neurons recorded in vivo in the motor cortex of the cat. ii. membrane parameters, action potentials, current-induced voltage response and electrotonic structures. *Journal of Neurophysiology*, 69(6):1865–1879.

[Barthó et al., 2004] Barthó, P., Hirase, H., Monconduit, L., Zugaro, M., Harris, K. D., and Buzsáki, G. (2004). Characterization of neocortical principal cells and interneurons by network interactions and extracellular features. *Journal of Neurophysiology*, 92:600–608.

[Bealieau and Colonier, 1983] Bealieau, C. and Colonier, M. (1983). The number of neuronsin the different laminae of the binocular and monocular region of area 17 in the cat. *Journal of Comparative Neurology*, 217:337–344.

[Bédard et al., 2006] Bédard, C., Kroeger, H., and Destexhe, A. (2006). Model of low-pass filtering of local field potentials in brain tissue. *Physical Review E*, 73(051911).

[Binzegger et al., 2004] Binzegger, T., J.Douglas, R., and Martin, K. A. (2004). A quantitative map of the circuit of cat primary visual cortex. *Journal of Neuroscience*, 24(39):8441–8453.

[Blanche et al., 2005] Blanche, T. J., Spacek, M. A., Hetke, J. F., and Swindale, N. V. (2005). Polytrodes: High-density silicon electrode arrays for large-scale multiunit recording. *Journal of Neurophysiology*, 93:2987–3000.

[Borg-Graham, 1999] Borg-Graham, L. J. (1999). Interpretations of data and mechanisms for hippocampal pyramidal cellmodels. *Cerebral Cortex*, 13:19–138.

[Bruno and Sakman, 2006] Bruno, R. M. and Sakman, B. (2006). Cortex is driven by weak but synchronously active thalamocortical synapses. *Science*, 312:1622–1627.

[Buxhoeven and Casanova, 2002] Buxhoeven, D. P. and Casanova, M. F. (2002). The minicolumn hypothesis in neuroscience. *Brain*, 125:935–951.

[Buzsáki and Kandel, 1998] Buzsáki, G. and Kandel, A. (1998). Somadendritic backpropagation of action potentials in cortical pyramidal cells of the awake rat. *Journal of Neurophysiology*, 79(3):1587–1591.

[Buzsaki et al., 1994] Buzsaki, G., Llinas, R., Singer, W., Berthoz, A., and Christen, T. (1994). *Temporal Coding in the Brain*. Springer-Verlag, Berlin.

[Buzsáki et al., 1996] Buzsáki, G., Penttonen, M., Nadasdy, Z., and Bragin, A. (1996). Pattern and inhibition-dependent invasion of pyramidal cell dendrites by fast spikes in the hippocampus in vivo. *Proceedings of the National Academy of Sciences (USA)*, 93:9921–9925.

[Christie et al., 1995] Christie, B. R., Eliot, L. S., Ito, K., Miyakawa, H., and Johnston, D. (1995). Different Ca^{2+} channels in soma and dendrites of hippocampal pyramidal neurons mediate spike-induced Ca^{2+} influx. *Journal of Neurophysiology*, 73(6):2553–2557.

[Colbert and Johnston, 1996] Colbert, C. M. and Johnston, D. (1996). Axonal action-potential initiation and Na^{+} channel densities in thesoma and axon initial segment of subicular pyramidal-neurons. *Journal of Neuroscience*, 16(21):6676–6686.

[Colbert et al., 1997] Colbert, C. M., Magee, J. C., Hoffman, D. A., and Johnston, D. (1997). Slow recovery from inactivation of Na^{+} channels underlies the activity-dependent attenuation of dendritic action potentials in hippocampal CA1 pyramidal neurons. *Journal of Neuroscience*, 17(17):6512–6521.

[Colbert and Pan, 2002] Colbert, C. M. and Pan, E. (2002). Ion channel properties underlying the axonal action potential initiation in pyramidal neurons. *Nature Neuroscience*, 5(6):533–538.

[Csicsvari et al., 2003] Csicsvari, J., Henze, D. A., Jamieson, B., Harris, K. D., Sirota, A., Bartho, P., Wise, K. D., and Buzsáki, G. (2003). Massively parallel recording of unit and local field potentials with silicon-based electrodes. *Journal of Neurophysiology*, 90(2):1314–1323.

[Csicsvari et al., 1999] Csicsvari, J., Hiráse, H., Czurko, A., Mamiya, A., and Buzsáki, G. (1999). Oscillatory coupling of hippocampal and pyramidal cells and interneurons in the behaving rat. *Journal of Neuroscience*, 19(1):274–287.

[De Nó, 1947] De Nó, R. L. (1947). Action potential of the motoneurons of the hypoglossus nucleus. *J. Cell. Comp. Phsiol.*, 29:207–287.

[Destexhe and Paré, 1999] Destexhe, A. and Paré, D. (1999). Impact of network activity on the integrative properties of neocortical pyramidal neurons *in vivo*. *Journal of Neurophysiology*, 81:1531–1547.

[Feldman, 1984] Feldman, M. L. (1984). Morphology of the neocortical pyramidal neuron. *Cerebral Cortex*, 1:123–200.

[Fisher et al., 1990] Fisher, R. E., Gray, R., and Johnston, D. (1990). Properties and distributions of single voltage-gated calcium channels in adult hippocampal neurons. *Journal of Neurophysiology*, 64(1):91–104.

[Forsyth and Ponce, 2003] Forsyth, D. A. and Ponce, J. (2003). *Computer Vision: A Modern Approach*. Prentice Hall, Saddle River, NJ.

[Frick et al., 2004] Frick, A., Magee, J., and Johnston, D. (2004). Ltp is accompanied by an enhanced local excitability of pyramidal neuron dendrites. *Nature Neuroscience*, 7(2):126–135.

[Frick et al., 2003] Frick, A., Magee, J., Koester, H. J., Migliore, M., and Johnston, D. (2003). Normalization of Ca^{2+} signals by small oblique dendrites of CA1 pryramidal neurons. *Journal of Neuroscience*, 23(8):3243–3250.

[Gabbott et al., 1987] Gabbott, P. L., Martin, K. A., and Whitteridge, D. (1987). Connections between pyramidal neurons in layer 5 of cat visual cortex (area 17). *Journal of Comparative Neurology*, 259(3):364–381.

[Girardin et al., 2002] Girardin, C. C., Kiper, D. C., and Martin, K. A. C. (2002). The effect of moving textures on the responses of cells in the cat's dorsal lateral geniculate nucleus. *European Journal of Neuroscience*, 16(11):2149–2156.

[Gold et al., 2007] Gold, C., Henze, D. A., and Koch, C. (2007). Using extracellular action potential recordings to tune compartmental models. *Journal of Computational Neuroscience*, 23(1).

[Gold et al., 2006] Gold, C., Henze, D. A., Koch, C., and Buzsáki, G. (2006). On the original of the extracellular action potential waveform: A modeling study. *Journal of Neurophysiology*, 95:3113–3128.

[González-Burgos et al., 2005] González-Burgos, G., Krimer, L. S., Povysheva, N. V., and Barrionuevo, G. (2005). Function properties of fask spiking interneurons and their synaptic connections with pyramidal cells in primate dorsolateral prefrontal cortex. *Journal of Neurophysiology*, 93:942–953.

[Gray et al., 1995] Gray, C. M., Maldonado, P. E., Wilson, M., and McNaughton, B. (1995). Tetrodes markedly improve the reliability and yield of multiple single-unit isolation from multi-unit recordings in cat striate cortex. *Journal of Neuroscience Methods*, 63:43–54.

[Gulyas et al., 1999] Gulyas, A. I., Megias, M., Emri, Z., and Freund, T. (1999). Total number and ratio of excitatory synapses converging into single interneurons of different types in the ca1 area of rat hippocampus. *Journal of Neuroscience*, 19(22):10082–10097.

[Halliwell and Adams, 1982] Halliwell, J. V. and Adams, P. R. (1982). Voltage-clamp analysis of muscarinic excitation in hippocampal neurons. *Brain Research*, 250:71–92.

[Harris and Stevens, 1989] Harris, K. M. and Stevens, J. K. (1989). Dendritic spines of CA1 pyramidal cells in the rat hippocampus: serial electron microscopy with reference to their biophysical characteristics. *Journal of Neuroscience*, 9(8):2982–2997.

[Hayes et al., 2005] Hayes, R. D., Byrne, J. H., Cox, S. J., and Baxter, D. A. (2005). Estimation of single-neuron model parameters from spike train data. *Neurocomputing*, 66:517–529.

[Henze et al., 2000] Henze, D. A., Borhegyi, Z., Csicsvari, J., Mamiya, A., Harris, K., and Buzsáki, G. (2000). Intracellular features predicted by extracellular recordings in the hippocampus *in vivo*. *Journal of Neurophysiology*, 83:390–400.

[Henze and Buzsáki, 2001] Henze, D. A. and Buzsáki, G. (2001). Action potential threshold of hippocampal pyramidal cells *in vivo* is increased by recent spiking activity. *Neuroscience*, 105:121–130.

[Hines and Carnevale, 1997] Hines, M. L. and Carnevale, N. T. (1997). The neuron simulation environment. *Neural Computation*, 9:1179–1209.

[Hines and Carnevale, 2001] Hines, M. L. and Carnevale, N. T. (2001). Neuron: A tool for neuroscientist. *The Neuroscientist*, 7:123–135.

[Hoeltzell and Dykes, 1979] Hoeltzell, P. B. and Dykes, R. W. (1979). Conductivity in the somatosensory cortex of the csy – evidence for cortical anisotropy. *Brain Rsearch*, 177:61–82.

[Hoffman et al., 1997] Hoffman, D. A., Magee, J. C., Colbert, C. M., and Johnston, D. (1997). K^+ channel regulation of signal propagation in dendrites of hippocampal pyramidal neurons. *Nature Neuroscience*, 387:869–875.

[Holt, 1998] Holt, G. (1998). A critical reexamination of some assumptions and implications of cable theory in neurobiology. PhD thesis, California Insitute of Technology.

[Holt and Koch, 1999] Holt, G. and Koch, C. (1999). Electrical interactions via the extracellular potential near cell bodies. *Journal of Computational Neuroscience*, 6:169–184.

[Hubel and Wiesel, 1962] Hubel, D. and Wiesel, T. (1962). Receptive fields, binocular interaction and functional architecture in the cat's visual cortex. *Journal of Physiology (London)*, 160:106–154.

[Humphrey and Schmidt, 1990] Humphrey, D. R. and Schmidt, E. M. (1990). Neurophysiological techniques: Basic methods and concepts. In Boulton, A. A., Baker, G. B., and Vanderwolf, C. H., editors, *Neurophysiological Techniques: Basic Methods and Concepts*, chapter 1, pages 1–64. Humana Press.

[Huys et al., 2006] Huys, Q. J. M., Ahrens, M. B., and Paninski, L. (2006). Efficient estimation of detailed single-neuron models. *Journal of Neurophysiology*, 96:872–890.

[Jackson, 1962] Jackson, J. D. (1962). *Classical Electrodynamics*. Wiley, New York.

[Jaffe et al., 1994] Jaffe, D. B., Ross, W. N., Lisman, J. E., Lasser-Ross, N., Miyakawa, H., and Johnston, D. (1994). A model for dendritic Ca^{2+} accumulation in hippocampal pyramidal neurons based on fluorescene imaging measurements. *Journal of Neurophysiology*, 71(3):1065–1077.

[Joshi and Hawken, 2006] Joshi, S. and Hawken, M. J. (2006). Loose-patch-juxtacellular recording in vivo-a method for functional characterization and labeling of neurons in macaque v1. *Journal of Neuroscience Methods*, 156:37–49.

[Kamondi et al., 1998] Kamondi, A., Acsády, L., and Buzsáki, G. (1998). Dendritic spikes are enhanced by cooperative network activity in the intact hippocampus. *Journal of Neuroscience*, 18:3919–2928.

[Kang et al., 1987] Kang, Y. K., Nemethy, G., and Scheraga, H. A. (1987). Free energies of hydration of solute molecules. 1. improvement of the hyrdation shell model by exact computations of overlapping volumes. *Journal of Physical Chemistry*, 91:4105–4109.

[Keren et al., 2005] Keren, N., Peled, N., and Korngreen, A. (2005). Constraining compartmental models using multiple voltage recordings and genetic algorithms. *Journal of Neurophysiology*, 94:3730–3742.

[Klee et al., 1995] Klee, R., Ficker, E., and Heinemann, U. (1995). Comparison of voltage-dependent potassium currents in rat pyramidal neurons acutely isoluated from hippocampal regions CA1 and CA3. *Journal of Neurophysiology*, 74(5):1982–1995.

[Koch, 1999] Koch, C. (1999). *Biophysics of Computation*. Oxford University Press, Oxford, UK.

[Koch and Segev, 1999] Koch, C. and Segev, I., editors (1999). *Methods in Neuronal Modeling: From Ions to Networks*. Bradford, Cambridge, Massachusetts.

[Lancaster and Nicoll, 1987] Lancaster, B. and Nicoll, R. A. (1987). Properties of two calcium-activated hyperpolarizations in rat hippocampal slices. *Journal of Physiology*, 389:187–203.

[Larkman, 1991a] Larkman, A. U. (1991a). Dendritic morphology of pyramidal neurones of the visual cortex of the rat: I. Branching patterns. *Journal of Comparative Neurology*, 306(2):307–319.

[Larkman, 1991b] Larkman, A. U. (1991b). Dendritic morphology of pyramidal neurones of the visual cortex of the rat: III. spine distributions. *Journal of Comparative Neurology*, 306(2):332–343.

[López-Aguado et al., 2001] López-Aguado, L., Ibarz, J. M., and Herreras, O. (2001). Activity-dependent chanes of tissue resistivity in the CA1 region in vivo are layer specific: Modulation of evoked potentials. *Neuroscience*, 108(2):249–262.

[Lund, 1984] Lund, J. S. (1984). Spiny stellate neurons. *Cerebral Cortex*, 1:201–254.

[Magee, 1998] Magee, J. C. (1998). Dendritic hyperpolarization-activated currents modify the integrative properties of hippocampal CA1 pyramidal neurons. *Journal of Neuroscience*, 18(19):7613–7624.

[Magee and Jonston, 1995] Magee, J. C. and Jonston, D. (1995). Characterization of single voltage-gated Na^+ and Ca^{2+} channels in apical dendrites of rat CA1 pyramidal neurons. *Journal of Physiology*, 487(1):67–90.

[Mainen et al., 1995] Mainen, Z. F., Joerges, J., Huguenard, J. R., and Sejnowski, T. J. (1995). A model of spike initiation in neocortical pyramidal neurons. *Neuron*, 15:1427–1439.

[Major et al., 1994] Major, G., Larkman, A. U., Jonas, P., Sakmann, B., and Jack, J. J. B. (1994). Detailed passive cable models of whole-cell recorded CA3 pyramidal neurons in rat hippocampal slices. *Journal of Neuroscience*, 14(8):4613–4638.

[Malmivuo and Plonsey, 1995] Malmivuo, J. and Plonsey, R. (1995). *Bioelectromagnetism*. Oxford University Press, New York, Oxford.

[Margrie et al., 2002] Margrie, T. W., Brech, M., and Sakmann, B. (2002). In vivo, low-resistance, whole-cell recordings from neurons in the anaesthetized and awake mammalian brain. *Pflugers Arch – European Journal of Physiology*, 444:491–498.

[Martina and Jonas, 1997] Martina, M. and Jonas, P. (1997). Functional difference in Na^+ channel gating between fast-spiking interneurones and principal neurones of rat hippocampus. *Journal of Physiology*, 505(3):593–603.

[Maxwell, 1881] Maxwell, J. C. (1881). *A Treatise on Electricity and Magnetism*. Clarendon Press, Oxford, England.

[Megias et al., 2001] Megias, M., Emri, Z., Freund, T. F., and Gulyas, A. I. (2001). Total number and distribution of inhibitory and excitatory synapse on hippocampal CA1 pyramidal cells. *Neuroscience*, 102(3):527–540.

[Migliore and Sheperd, 2002] Migliore, M. and Sheperd, G. M. (2002). Emerging rules for the distributions of active dendritic conductances. *Nature Reviews Neuroscience*, 3:362–370.

[Mountcastle, 1997] Mountcastle, V. B. (1997). The columnar organization of the neocortex. *Brain*, 120:701–722.

[Mountcastle et al., 1969] Mountcastle, V. B., Talbot, W. H., Sakata, H., and Hyvarinen, J. (1969). Cortical neuronal mechanisms in flutter-vibration studied in unanesthetized monkeys. Neuronal periodicity and frequency discrimination. *Journal of Neurophysiology*, 32:452–484.

[Naundor et al., 2006] Naundor, B., Wolf, F., and Volgushev, M. (2006). Unique features of action potential initiation in cortical neurons. *Nature*, 440(20):1060–1063.

[Olshausen and Field, 2004] Olshausen, B. and Field, D. J. (2004). Sparse coding of sensory inputs. *Current Opinion in Neurobiology*, 14:481–487.

[Peters and Yilmaz, 1993] Peters, A. and Yilmaz, E. (1993). Neuronal organization in area 17 of cat visual cortex. *Cerbral Cortex*, 3:49–68.

[Pinault, 1996] Pinault, D. (1996). A novel single-cell staining procedure performed in vivo under electrophysiological control: Morpho-functional features of juxtacellularly labeled thalamic cells and other central neurons with biocytin or neuro-biotin. *Journal of Neuroscience Methods*, 65:113–36.

[Plonsey, 1969] Plonsey, R. (1969). *Bioelectric Phenomena*. McGraw-Hill, New York.

[Poirazi et al., 2003] Poirazi, P., Brannon, T. M., and Mel, B. W. (2003). Arithmetic of subthreshold synaptic summation in a model CA1 pryamidal cell. *Neuron*.

[Poolos and Johnston, 1999] Poolos, N. P. and Johnston, D. (1999). Calcium-activated potassium conductances contribute to action potential repolarization at the soma but not the denrites of hippocampal CA1 pyramidal neurons. *Journal of Neuroscience*, 19(13):5205–5212.

[Quirk et al., 2001] Quirk, M. C., Blum, K. I., and Wilson, M. A. (2001). Experience-dependent changes in extracellular spike amplitude may reflect regulation of dendritic action potential back-propagation in rat hippocampal pyramidal cells. *Journal of Neuroscience*, 21(1):240–248.

[Quiroga et al., 2004] Quiroga, R. Q., Nadasdy, Z., and Ben-Shaul, Y. (2004). Unsupervised spike sorting with wavelets and superparamagnetic clustering. *Neural Computation*, 16:1661–1687.

[Rall, 1962] Rall, W. (1962). Electrophysiology of a dendritic neuron model. *Biophysics Journal*, 2:145–167.

[Roopun et al., 2007] Roopun, A. K., Middleton, S. J., Cunningham, M. O., LeBeau, F. E. N., Bibbig, A., Whittington, M. A., and Traub, R. D. (2007). A beta2-frequency (20-30 hz) oscillation in non-synaptic networks of somatosensory cortex. *Proceedings of the National Academy of Sciences*, 103(42):15646–15650.

[Rosenfal, 1969] Rosenfal, P. (1969). Intra- and extracellular potential fields of active nerve and muscle fibres - a physico-mathematical analysis of different models. *Acta Physiologica Scandinavica S*, 9.

[Schanne et al., 1968] Schanne, O. F., Lavallee, M., Laprade, R., and Gagne, S. (1968). Electrical properties of glass microelectrodes. *Proceedings of the IEEE*, 56:1072–1082.

[Scholl, 1956] Scholl, D. A. (1956). *The Organization of the Cerebral Cortex*. Methuen, London.

[Schwarz, 1973] Schwarz, W. M. (1973). *Intermediate Electromagnetic Theory*. Robert E. Kreiger Publishing Company, New York.

[Shoham et al., 2006] Shoham, S., O'Connor, D. H., and Segev, R. (2006). How silent is the brain: si there a "dark matter" problem in neuroscience? *Journal of Comparative Physiology*, 192:777–784.

[Snider, 1911] Snider, R. S. (1911). *A Stereotaxic Atlas of the Cat Brain*. University of Chicago Press, Chicago.

[Spruston and Johnston, 1992] Spruston, N. and Johnston, D. (1992). Perforated patch-clamp analysis of the passive membrane properties of three classes of hippocampal neurons. *Journal of Neurophysiology*, 67(3):508–529.

[Storm, 1988] Storm, J. F. (1988). Temporal integration by a slowly inactivating K^+ current in hippocampal neurons. *Nature*, 336:379–381.

[Stuart and Spruston, 1998] Stuart, G. and Spruston, N. (1998). Determinants of voltage attenuation in neocortical pyramidal neuron dendrites. *Journal of Neuroscience*, 18(10):3501–3510.

[Stuart et al., 2001] Stuart, G., Spruston, N., and Hausser, M. (2001). *Dendrites*. Oxford University Press, Oxford, U.K.

[Toledo-Rodriguez et al., 2004] Toledo-Rodriguez, M., Blumenfeld, B., Wu, C., Luo, J., Attali, B., Goodman, P., and Markram, H. (2004). Correlation maps allow neuronal electrical properties to be predicted from single-cell gene expression profiles in rat neocortex. *Cerebral Cortex*, 14(12):1310–27.

[Towe and Harding, 1970] Towe, A. L. and Harding, G. W. (1970). Extracellular microelectrode sampling bias. *Experimental Neurology*, 29:366–381.

[Traub et al., 2005] Traub, R. D., Contreras, D., Cunningham, M. O., Murray, H., LeBeau, F. E. N., Roopun, A., Bibbig, A., Wilent, W. B., Higley, M. J., and Whittington, M. A. (2005). Single-column thalamocortical network model exhibiting gamma oscillations, sleep spindles, and epileptogenic bursts. *Journal of Neurophysiology*, 93(4):2194–2232.

[Trayanova and Henriques, 1991] Trayanova, N. and Henriques, C. S. (1991). Modification of a cylindrical bidomain model for cardiac tissue. *Mathematical Biosciences*, 104(1):59–72.

[Tsubokawa, 2000] Tsubokawa, H. (2000). Control of Na^+ spike backproagation by intracellular signaling in the pyramidal neuron dendrites. *Molecular Neurobiology*, 1(3):129–141.

[Vanier and Bower, 1999] Vanier, M. C. and Bower, J. M. (1999). A comparative survey of automated parameter search methods for compartmental models. *Journal of Computational Neuroscience*, 7(2):149–171.

[Varona et al., 2000] Varona, P., Ibarz, J. M., Lopez-Aguado, L., and Herreras, O. (2000). Macroscopic and subcellular factors shaping population spikes. *Journal of Neurophysiology*, 83:2192–2208.

[Volgushev et al., 2000] Volgushev, M., Pernberg, J., and Eysel, U. T. (2000). Comparison of the selectivity of postsynaptic potentials and spike responses in cat visual cortex. *European Journal of Neuroscience*, 12:257–263.

[Weber, 1950] Weber, E. (1950). *Electro Magnetic Fields, Theory and Aplications*. John Wiley and Sons, New York.

[Williamson and Alger, 1990] Williamson, A. and Alger, B. E. (1990). Characterization of an early afterhyperpolarization after a brief train of action potentials in rat hippocampal neurons in vitro. *Journal of Neurophysiology*, 63(1):72–81.

[Yoshida et al., 1991] Yoshida, A., Oda, M., and Ikemoto, Y. (1991). Kinetics of Ca^{2+}-activated K^+ channel in rat hippocampal neurons. *Japanese Journal of Physiology*, 41:297–315.